Jordan Journal of
PHYSICS
An International Peer-Reviewed Research Journal

Volume 15, No. 1, March 2022, Shaban 1443 H

Jordan Journal of Physics (*JJP*): An International Peer-Reviewed Research Journal funded by the Scientific Research and Innovation Support Fund, Jordan, and published quarterly by the Deanship of Research and Graduate Studies, Yarmouk University, Irbid, Jordan.

Manuscripts should be submitted to:

Prof. Mahdi Salem Lataifeh
Editor-in-Chief, Jordan Journal of Physics
Deanship of Research and Graduate Studies
Yarmouk University-Irbid-Jordan
Tel. 00 962 2 7211111 Ext. 2075
E-mail: *jjp@yu.edu.jo*
Website: *http://Journals.yu.edu.jo/jjp*

Jordan Journal of
PHYSICS
An International Peer-Reviewed Research Journal

Volume 15, No. 1, March 2022, Shaban 1443 H

The Hashemite Kingdom of Jordan

Yarmouk University

Jordan Journal of PHYSICS

An International Peer-Reviewed Research Journal

Funded by the Scientific Research and Innovation Support Fund

Volume 15, No. 1, March 2022, Shaban 1443 H

Instructions to Authors

Instructions to authors concerning manuscript organization and format apply to hardcopy submission by mail, and also to electronic online submission via the Journal homepage website (http://jjp.yu.edu.jo).

Manuscript Submission

1- **E-mail to** : jjp@yu.edu.jo

2- **Online**: Follow the instructions at the journal homepage website.

Original *Research Articles*, *Communications* and *Technical Notes* are subject to critical review by minimum of two competent referees. Authors are encouraged to suggest names of competent reviewers. *Feature Articles* in active Physics research fields, in which the author's own contribution and its relationship to other work in the field constitute the main body of the article, appear as a result of an invitation from the Editorial Board, and will be so designated. The author of a *Feature Article* will be asked to provide a clear, concise and critical status report of the field as an introduction to the article. *Review Articles* on active and rapidly changing Physics research fields will also be published. Authors of *Review Articles* are encouraged to submit two-page proposals to the Editor-in-Chief for approval. Manuscripts submitted in *Arabic* should be accompanied by an Abstract and Keywords in English.

Organization of the Manuscript

Manuscripts should be typed double spaced on one side of A4 sheets (21.6 x 27.9 cm) with 3.71 cm margins, using Microsoft Word 2000 or a later version thereof. The author should adhere to the following order of presentation: Article Title, Author(s), Full Address and E-mail, Abstract, PACS and Keywords, Main Text, Acknowledgment. Only the first letters of words in the Title, Headings and Subheadings are capitalized. Headings should be in **bold** while subheadings in *italic* fonts.

Title Page: Includes the title of the article, authors' first names, middle initials and surnames and affiliations. The affiliation should comprise the department, institution (university or company), city, zip code and state and should be typed as a footnote to the author's name. The name and complete mailing address, telephone and fax numbers, and e-mail address of the author responsible for correspondence (designated with an asterisk) should also be included for official use. The title should be carefully, concisely and clearly constructed to highlight the emphasis and content of the manuscript, which is very important for information retrieval.

Abstract: A one paragraph abstract not exceeding 200 words is required, which should be arranged to highlight the purpose, methods used, results and major findings**.**

Keywords: A list of 4-6 keywords, which expresses the precise content of the manuscript for indexing purposes, should follow the abstract.

PACS: Authors should supply one or more relevant PACS-2006 classification codes, (available at http://www.aip.org/pacs/pacs06/pacs06-toc.html)

Introduction: Should present the purpose of the submitted work and its relationship to earlier work in the field, but it should not be an extensive review of the literature (e.g., should not exceed 1 ½ typed pages).

Experimental Methods: Should be sufficiently informative to allow competent reproduction of the experimental procedures presented; yet concise enough not to be repetitive of earlier published procedures.

Results: should present the results clearly and concisely.

Discussion: Should be concise and focus on the interpretation of the results.

Conclusion: Should be a brief account of the major findings of the study not exceeding one typed page.

Acknowledgments: Including those for grant and financial support if any, should be typed in one paragraph directly preceding the References.

References: References should be typed double spaced and numbered sequentially in the order in which they are cited in the text. References should be cited in the text by the appropriate Arabic numerals, enclosed in square brackets. Titles of journals are abbreviated according to list of scientific periodicals. The style and punctuation should conform to the following examples:

1. Journal Article:

a) Heisenberg, W., Z. Phys. 49 (1928) 619.
b) Bednorz, J. G. and Müller, K. A., Z. Phys. B64 (1986) 189
c) Bardeen, J., Cooper, L.N. and Schrieffer, J. R., Phys. Rev. 106 (1957) 162.
d) Asad, J. H., Hijjawi, R. S., Sakaji, A. and Khalifeh, J. M., Int. J. Theor. Phys. 44(4) (2005), 3977.

2. Books with Authors, but no Editors:

a) Kittel, C., "Introduction to Solid State Physics", 8th Ed. (John Wiley and Sons, New York, 2005), chapter 16.
b) Chikazumi, S., C. D. Graham, JR, "Physics of Ferromagnetism", 2nd Ed. (Oxford University Press, Oxford, 1997).

3. Books with Authors and Editors:

a) Allen, P. B. "Dynamical Properties of Solids", Ed. (1), G. K. Horton and A. A. Maradudin (North-Holland, Amsterdam, 1980), p137.
b) Chantrell, R. W. and O'Grady, K., "Magnetic Properities of Fine Particles" Eds. J. L. Dormann and D. Fiorani (North-Holland, Amsterdam, 1992), p103.

4. Technical Report:

Purcell, J. "The Superconducting Magnet System for the 12-Foot Bubble Chamber", report ANL/HEP6813, Argonne Natt. Lab., Argonne, III, (1968).

5. Patent:

Bigham, C. B., Schneider, H. R., US patent 3 925 676 (1975).

6. Thesis:

Mahmood, S. H., Ph.D. Thesis, Michigan State University, (1986), USA (Unpublished).

7. Conference or Symposium Proceedings:

Blandin, A. and Lederer, P. Proc. Intern. Conf. on Magnetism, Nottingham (1964), P.71.

8. Internet Source:

Should include authors' names (if any), title, internet website, URL, and date of access.

9. Prepublication online articles (already accepted for publication):

Should include authors' names (if any), title of digital database, database website, URL, and date of access.

For other types of referenced works, provide sufficient information to enable readers to access them.

Tables: Tables should be numbered with Arabic numerals and referred to by number in the Text (e.g., Table 1). Each table should be typed on a separate page with the legend above the table, while explanatory footnotes, which are indicated by superscript lowercase letters, should be typed below the table.

Illustrations: Figures, drawings, diagrams, charts and photographs are to be numbered in a consecutive series of Arabic numerals in the order in which they are cited in the text. Computer-generated illustrations and good-quality digital photographic prints are accepted. They should be black and white originals (not photocopies) provided on separate pages and identified with their corresponding numbers. Actual size graphics should be provided, which need no further manipulation, with lettering (Arial or Helvetica) not smaller than 8 points, lines no thinner than 0.5 point, and each of uniform density. All colors should be removed from graphics except for those graphics to be considered for publication in color. If graphics are to be submitted digitally, they should conform to the following minimum resolution requirements: 1200 dpi for black and white line art, 600 dpi for grayscale art, and 300 dpi for color art. All graphic files must be saved as TIFF images, and all illustrations must be submitted in the actual size at which they should appear in the journal. Note that good quality hardcopy original illustrations are required for both online and mail submissions of manuscripts.

Text Footnotes: The use of text footnotes is to be avoided. When their use is absolutely necessary, they should be typed at the bottom of the page to which they refer, and should be cited in the text by a superscript asterisk or multiples thereof. Place a line above the footnote, so that it is set off from the text.

Supplementary Material: Authors are encouraged to provide all supplementary materials that may facilitate the review process, including any detailed mathematical derivations that may not appear in whole in the manuscript.

Revised Manuscript and Computer Disks

Following the acceptance of a manuscript for publication and the incorporation of all required revisions, authors should submit an original and one more copy of the final disk containing the complete manuscript typed double spaced in Microsoft Word for Windows 2000 or a later version thereof. All graphic files must be saved as PDF, JPG, or TIFF images.

Allen, P.B., "…….", in: Horton, G.K., and Muradudin, A. A., (eds.), "Dynamical…….", (North……..), pp….

Reprints

Twenty (20) reprints free of charge are provided to the corresponding author. For orders of more reprints, a reprint order form and prices will be sent with the article proofs, which should be returned directly to the Editor for processing.

Copyright

Disclaimer

Indexing

JJP is currently indexing in:

Scopus	ULRICHSWEB GLOBAL SERIALS DIRECTORY

Jordan Journal of
PHYSICS
An International Peer-Reviewed Research Journal

Volume 15, No. 1, March 2022, Shaban 1443 H

Table of Contents:

Articles	Pages
Nanofibers of Palladium (Pd)-sensitized SnO2 Encapsulated with Polyaniline for Effective Hydrogen Gas Sensing A. M. More, S. B. Kondawar and S. P. Dongre	1-8
Solvent Extraction and Separation of Silver(I) in Real Sample Using Hexaacetato Calix[6]arene Y. S. Thakare	9-19
Impact of La on Structural, Morphological and Magnetic Properties of $NiCoFe_2O_4$ Nano Ferrites P. K. Nagpure, A. K. Nandanwar, V. M.Nanoti and K. G. Rewatkar	21-27
Structural and Electrical Studies of Aluminium-doped Nickel-Cobalt Ferrite Nanoparticles S. P. Waghmare, D. M. Borikar, M. A. Borikar and K. G. Rewatkar	29-36
Optical, P-XRD & U-V Properties by Varying the Concentration of L-valine Amino Acid in Pure KDP Nitesh D. Shambharkar and Vijay R. Raghorte	37-42
Study of Acoustic Behaviour of Thiamin Hydrochloride with Methanol at 303K S. P. Dange and O. P. Chimankar	43-48
Optical, Structural and Electrical Properties of CuS Thin Film on Dielectric Substrate by Spray Pyrolysis Technique Avish K. Patil, Sachin H. Dhawankar, Nishant T. Tayade	49-56
Study of Structural and Magnetic Properties of Co-doped M-Type Sr-Hexaferrite Nanoparticles Sunil N. Kamde, Amar K. Nandanwar, Purushottam G. Agone and Kishor G. Rewatkar	57-60
A Brief Review on Structural, Morphological, Magnetic and Dielectric Behavior of Divalent Cation-substituted Nanocrystalline Cobalt Ferrite Y. S. Bopche, A. M. Shahare, A. V. Bagde and D. S. Choudhary	61-66
Natural Extracts-mediated Biosynthesis of Zinc Oxide Nanoparticles and Their Multiple Pharmacotherapeutic Perspectives A. G. M. Haldar, D. Kar Mahapatra, K. M. Dadure and R. G. Chaudhary	67-79

Articles	Pages
Half a Decade Progress of Biomass-assisted Development of Zirconium Nanomaterials: Anti-microbial Potentials D. Kar Mahapatra, A. G. M. Haldar, K. M. Dadure and R. G. Chaudhary	81-88
Utilization of Mother Nature's Gift for the Biofabrication of Copper/ Copper Oxide Nanoparticles for Therapeutic Applications K. M. Dadure, D. Kar Mahapatra, A. G. M. Haldar, A. K. Potbhare and R. G. Chaudhary	89-99
Two-color Emission in Dy^{3+}-activated $CaZnP_2O_7$ Pyrophosphate for White LED R. L. Kohale, A. N.Yerpude and S. J. Dhoble	101-106

Volume 15, Number 1, 2022. pp. 1-8

Jordan Journal of Physics

ARTICLE

Nanofibers of Palladium (Pd)-sensitized SnO_2 Encapsulated with Polyaniline for Effective Hydrogen Gas Sensing

A. M. More[a], **S. B. Kondawar**[b] and **S. P. Dongre**[c]

[a] *Department of Physics, D. B. Science College, Gondia-441614, India.*
[b] *Department of Physics, R.T. M. Nagpur University, Nagpur, India.*
[c] *Department of Physics, Bhalerao Sc. College, Saoner, Dist- Nagpur, India.*

Doi: **https://doi.org/10.47011/15.1.1**

Received on: 01/08/2020; *Accepted on: 12/12/2020*

Abstract: In this paper, we have successfully synthesized Pd-doped SnO_2 nanofibers encapsulated with Polyaniline (PANI). The morphology of nanofibers was investigated using Scanning Electron Microscopy (SEM) technology. SEM study suggested that the diameter of Pd-doped SnO_2 encapsulated with polyaniline (PSP) nanofibers was found in the range 200-400 nm. The average diameter of PSP nanofibers was estimated using ImageJ software. XRD study of pure FIBRESSnO_2 and PSP nanofibers shows perfect matching of major peaks corresponding to Tin Oxide (SnO_2). EDAX pattern depicted weight percentage of constituent elements indicated the presence of Palladium (Pd) in nanofibers. The study revealed that PSP nanofibers were more sensitive as compared to pristine SnO_2 nanofibers. The working temperature of PSP nanofibers was found 32°C. The low working temperature provokes the use of PSP nanofibers as a promising hydrogen gas sensor. Response and recovery time of 34 seconds and 63 seconds respectively has been observed for PSP nanofibers. Palladium (Pd) could have played a major role in higher response towards hydrogen gas sensing. The mesoporous PSP electrospun nanofibers exhibited excellent response and recovery behavior, with much higher sensitivity to H_2 as compared with pure SnO_2 nanofibers. It could be understood that the high gas sensing performance of PSP nanofibers is obtained from the high surface area, with more activity at Pd active sites of nanofibers. Highly porous nature of electrospun nanofibers led to effective surface interaction between the hydrogen gas molecules and SnO_2 active site mediated by palladium for electron transfer through the matrix of nanofibers.

Keywords: Nanofibers, Hydrogen sensing, Pd-doped SnO_2 Polyaniline (PSP), Electrospinning, Polyaniline.

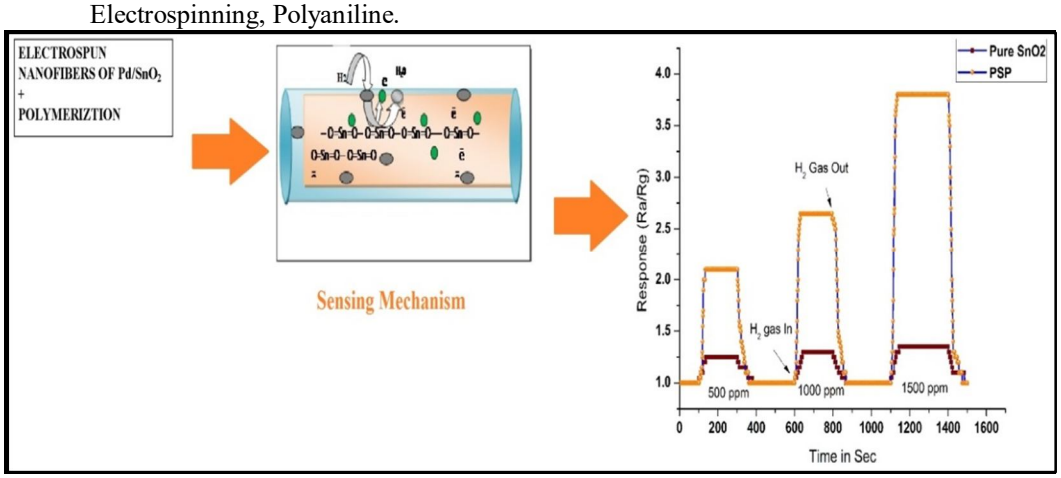

Corresponding Author: A. M. More **Email**: more_phy@rediffmail.com

Introduction

Today, we face drastic changes in atmospheric condition due to uncontrolled variation in the concentration of atmospheric gases like Hydrogen, CO_2, Methane, Oxygen and Nitrogen. Monitoring of these highly flammable and atmospheric gases is essential. Many techniques are employed for sensing these gases. The sensing devices use different parameters of sensing materials, such as their conductivity, optical property and mechanical strength. [1-2]. Wide variety of sensors, such as electrochemical sensor, optical sensor, chemo-resistive sensor is used for sensing important gases [3-4]. Semiconducting Gas Sensors are operated upon warming or heating metal oxides. Semiconducting Metal Oxides are used for measurement of gas concentration by measuring the electrical resistance of the device. Variation in the electron concentration over the surface of SMO in the presence of analyte gas is the key parameter in the detection of gas [5-6]. Sensors using semiconducting oxides (SMO) and Conducting Polymer are commonly used for the detection of gases, such as CO, CO_2, H_2, NH_3, H_2S, O_2, Ar and the presence of moisture in air [7]. However, high operating temperature, low selectivity, humidity dependence, low response and recovery time are the drawbacks of Semiconducting Oxides. It has been observed that reduction in the dimensions to nano-range can improve the ability of sensors of sensing gases to a great extent. Many researches indicate that doping of noble metals, such as Palladium (Pd), Silver (Ag), Gold (Au), Copper (Cu), Aluminium (Al) catalyses the sensor response of SnO_2 [6, 10, 11-14]. These metal elements provide more active site for the redox reaction between the target gas and the sensing material. SnO_2 is the most promising member in the series of semiconducting metal oxides, like ZnO, TiO_2, WO_3, In_2O_3, because it has considerable variation in the resistance in the presence of reducing gases like H_2, H_2S and oxidizing gases like NH_3, O_2 [15-19]. Electrospun nanowires of SnO_2 could provide larger surface area for interaction with target gas. Pd-functionalized nanostructures exhibited a dramatic improvement in sensitivity toward oxygen and hydrogen due to the enhanced catalytic dissociation of the molecular adsorbate on the Pd nanoparticle surfaces and the subsequent diffusion of the resultant atomic species to the oxide. Further, another approach suggested that the receptor for the analyte gas has been drastically modified by the introduction of foreign receptors, in particular Pd and Ag, on the surface of SnO_2 [9]. Pd and Ag promoters form oxides in the presence of air. These oxides of Pd or Ag interact with the SnO_2 electrospun nanofibers and form an electron-deficient space-charge layer which contributes much to promoting the gas sensitivity. Electrospinning is an important technique to obtain nanofibers of 1D hierarchical formats with enhanced reactivity due to availability of active site for the reaction of the gas over the matrix of nanofiber [20]. Polyaniline (PANI)-based SMO has a relatively high sensitivity to gases due to its conductive nature.

In this paper, we have interpreted the sensing response of Pd-doped SnO_2 embedded polyaniline (PSP) to the hydrogen gas at low temperature.

Experimental Details

Preparation of Pd-doped SnO_2 Embedded Polyaniline Nanofibers (PSP)

Fig. 1 shows the schematic diagram of preparation of nanofibers of Pd-doped SnO_2 encapsulated with Polyaniline [21]. In the first step, 0.2 g of Stannous Chloride ($SnCl_2.2H_2O$) and 0.002g of $PdCl_2$ (1% by weight) were dissolved in 2.3 ml (2.2 g) Dimethyl formamide (DMF) and 2.6ml (4.4 g) ethanol solution. The resulting gel - solution was stirred for half an hour with magnetic stirring to get proper viscosity. Afterwards, 0.6g Poly (vinylpyrrolidone) PVP was added to the solution. The solution was stirred for the next 30-35 minutes to attain proper viscosity. For electrospinning, the solution was firstly filled in 10ml syringe. The potential of 18 kV was provided between the tip of the spinning nozzle and the collector which were kept at a distance of 25 cm apart. The solution flow rate was kept at 0.5 ml/h. Nanofibers collected on the electrode were dried at about 70-80°C overnight. The dried nanofibers were peeled off. The dried nanofibers were calcined at 350 °C for 5 hours. In the second step, calcined nanofibers were dip-coated during the polymerization of aniline. The coated fibers were dried at about 100 °C. The nanofibers so formed were used for gas-sensing purposes.

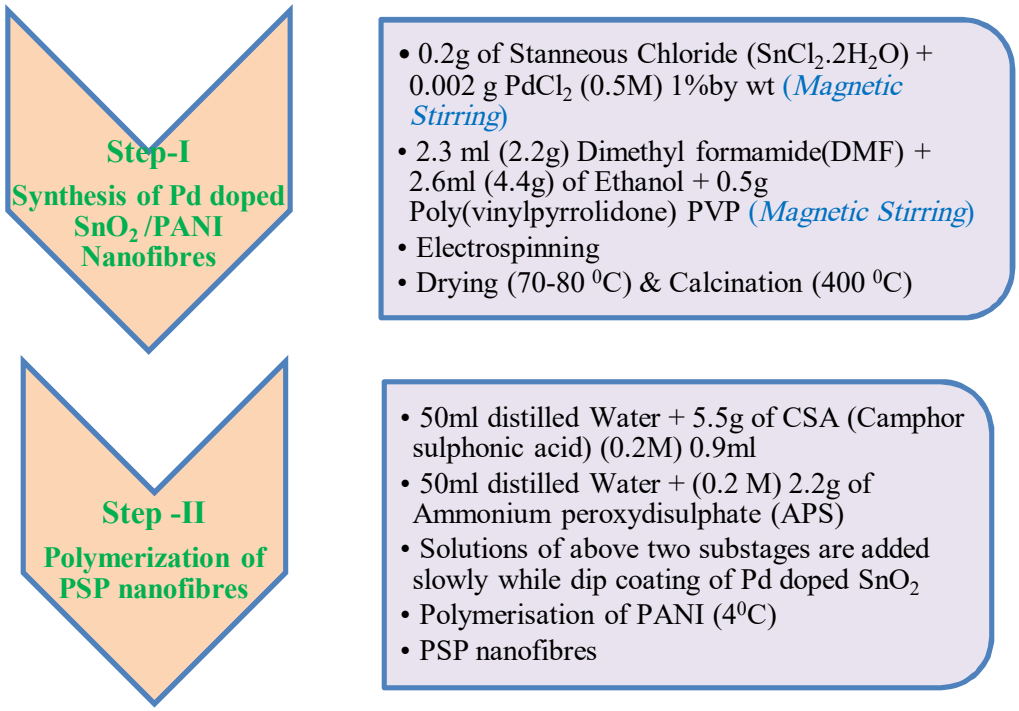

FIG. 1. Synthesis of Pd-doped SnO_2 encapsulated with PANI (PSP) nanofibers.

TABLE 1. List of chemicals with details of suppliers.

S.N.	Chemicals	Supplier	Purification Grade
1.	Poly(vinylpyrrolidone)PVP(M.W. 130,000gm/mol)	Sigma-Aldrich	A.R.
2.	Silver Nitrate($AgNO_3$)	HI- MEDIA	A.R.
3.	N-N Dimethylformamide (DMF)	HI- MEDIA	A.R.
4.	Ehanol(C_2H_5OH)	HI- MEDIA	A.R.
5.	Camphor Sulphonic acid (CSA)	HI- MEDIA	A.R.

Results and Discussion

SEM Analysis of the Samples

The SEM micrographs of pure SnO_2 and Pd-doped SnO_2 polymerized by aniline are analysed using Scanning Electron Microscopy (SEM), (Carl Zeiss Model EVO-18, JSM-7600F) which depict that the diameters of the nanofibers of pure SnO_2 and Pd-SnO_2-PANI (PSP) composite fibers are about 400-500 nm. The average diameters were estimated using ImageJ software. Many fibres were chosen at different positions of nanofibers for collecting data for diameter. Fig. 2a and Fig. 2b show the typical SEM images of pure SnO_2 and Pd-SnO_2/ PANI (PSP) composite nanofibers, respectively. The diameter distribution of PSP fibers also shown in the adjoining Fig. 2a and Fig. 2b indicated that most probable diameters of nanofibers are found in the 200-400 nm range. SEM image reveals the hierarchical branched structure of PSP nanofibers. The trend to increase the diameter of PSP nanofibers after polymerisation is because of encapsulation of Pd-doped SnO_2 by polyaniline (PANI).

XRD Analysis of the Samples

XRD analysis is the plot between number of counts having Arbitrary Unit (AU) and diffraction angle (2θ). Fig. 3a shows the XRD pattern for pure SnO_2 and Pd-doped SnO_2 encapsulated with PANI (PSP) nanofibers. The major diffraction peaks are confirmed for SnO_2 and PSP nanofibers with standard data. The diffraction peaks have been identified for SnO_2 at 2θ =26.6^o, 33.8^o, 52.4^o corresponding to (110), (101), (211) which can be perfectly indexed as the tetragonal rutile structure of SnO_2 by comparing with JCPDS 41-1445. The prominent peak of Polyaniline is seen at 25.4^o with (110). A small shift in peak positions has been observed for Pd-doped SnO_2 /PANI (PSP) nanofibers. The peaks of Palladium (Pd) are not prominent because of very little concentration of dopent Pd

in the sample. The constituent elements Pd, Sn, N, O, C have been detected by EDAX pattern which is clearly seen in Fig. 3b. The crystal size of SnO_2 molecule has been estimated using Debye-Scherrer's relation for grain size. Mathematically, Debye-Scherrer relation is given as:

$$\tau = \frac{0.9\,\lambda}{\beta\, Cos\theta}$$

where, τ = Crystal size, λ = X-ray wavelength used for diffraction ($\lambda = 1.53$ Å), β = Full width at Half Maxima (FWHM), θ = Diffraction angle. From Table 2, it is evident that the average crystal size of SnO_2 is found to be 5.60nm.

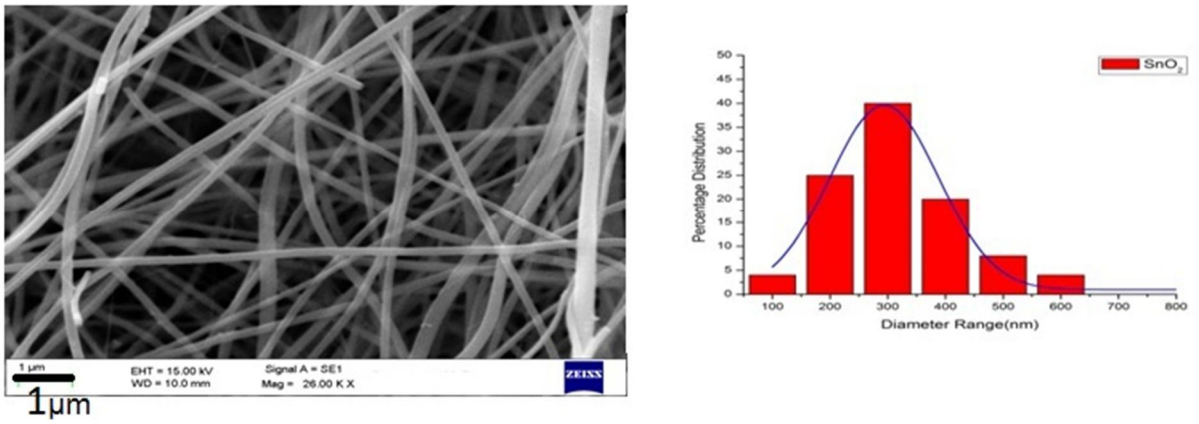

FIG. 2a. SEM image and diameter distribution of SnO_2 nanofibers.

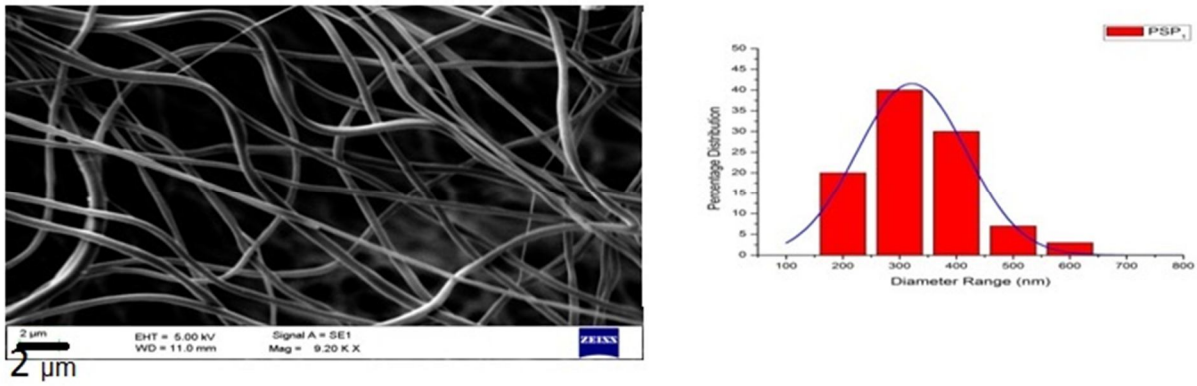

FIG. 2b. SEM image and diameter distribution of Pd-doped SnO_2 encapsulated with PANI (PSP) nanofibers.

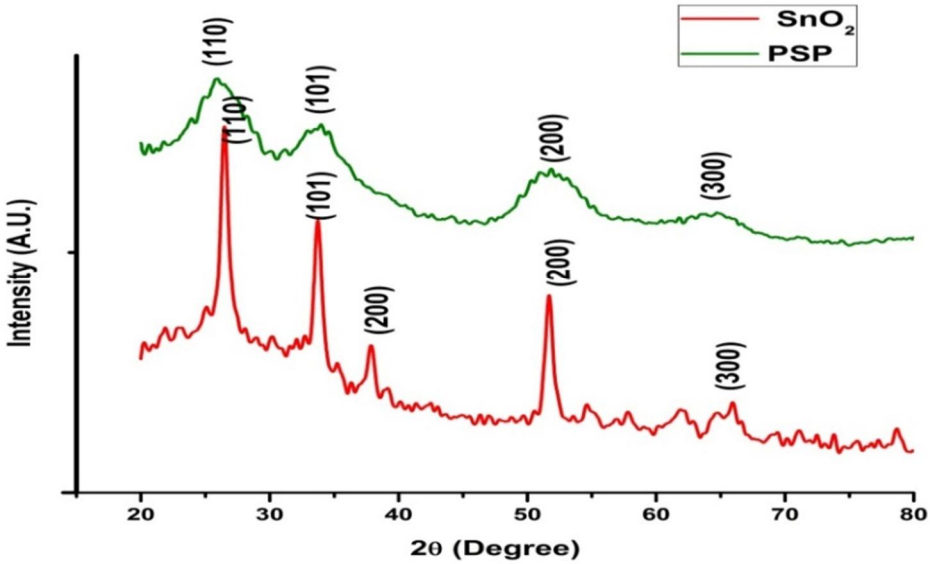

FIG. 3a. XRD pattern for pure SnO_2 and Pd-doped SnO_2 encapsulated with PANI (PSP) nanofibers.

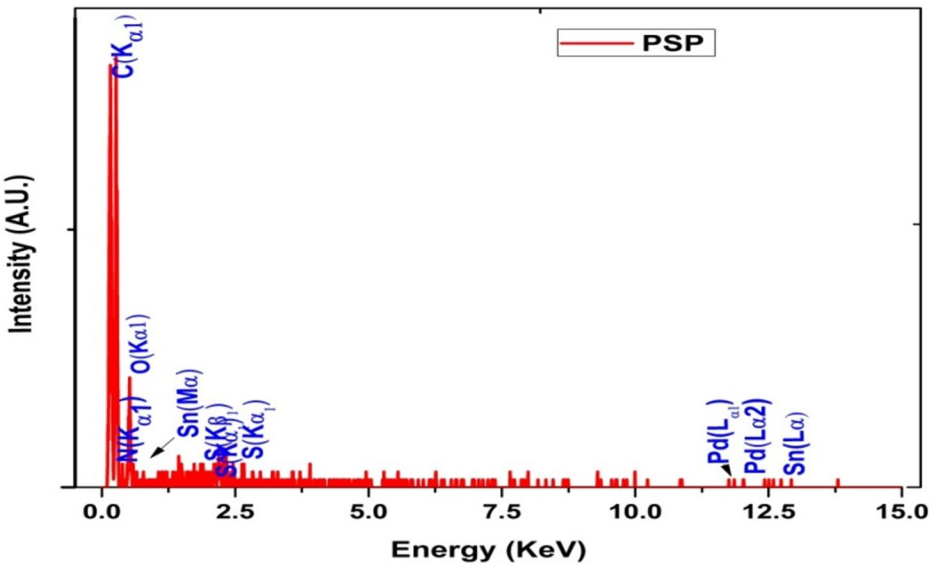

FIG. 3b. EDAX pattern of Pd-doped SnO_2 encapsulated with PANI (PSP) nanofibers.

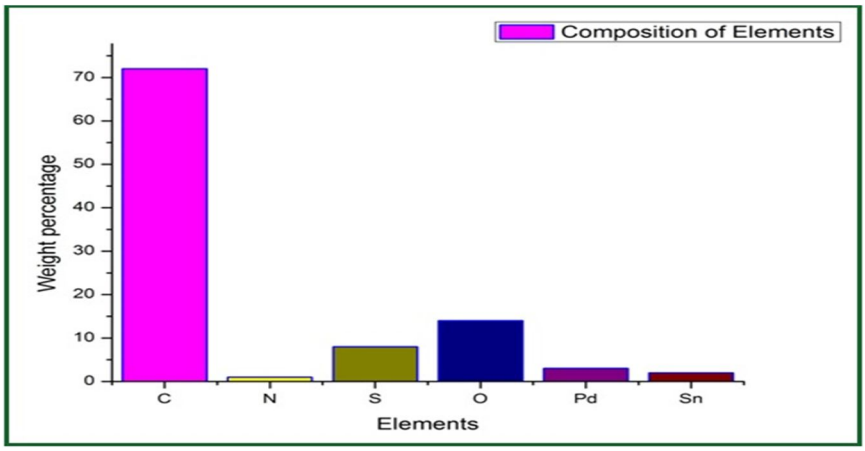

FIG. 3c. Composition of elements of Pd-doped SnO_2 encapsulated with PANI (PSP) nanofibers from EDAX pattern.

XRD and SEM study showed that nanocrystalline SnO_2 had been synthesized. SEM images estimate size of nanofibers of SnO_2 and PSP to be in the range of 200-400 nm. It is evident from the different sizes of nanofibers calculated from Debye-Scherrer's formula and SEM microgram that nanofibers are of multi-layered, polycrystalline nature. Further encapsulation of Pd-doped SnO_2 nanofibers by polyaniline (PANI) shows an enhancement in diameter.

TABLE 2. Determination of crystal size of SnO_2 by Debye- Scherrer formula.

Diffraction Angle (2θ)	Miller Indices (h k l)	Interplanar Spacing ($\tau = \frac{0.9\,\lambda}{\beta\, Cos\theta}$) for Each Plane (nm)	Mean Size for SnO_2 Crystal (nm)
26.56	110	5.34	5.60
33.7	101	5.04	
37.82	200	4.8	
51.7	211	7.23	

Gas Sensing of Samples

Pristine SnO_2 and PSP nanofibers were utilized for hydrogen gas sensing. The percentage sensitivity, which is given as {[(Rg-Ra)/Ra] x 100}, is evaluated for 1000 ppm of hydrogen gas and plotted against temperature. The variation of percentage sensitivity with temperature is shown in Fig. 4. Nanofibers were found to have maximum sensitivity at 32°C for PSP than pristine SnO_2. The sensitivity rises to

170% of its initial conductivity value. The higher sensitivity may be attributed to the presence of Palladium (Pd) in the PSP nanofibers. Pd nanoparticles form oxides in the presence of air. These oxides of Palladium (Pd) interact with the SnO_2 electrospun nanofibers and form an electron-deficient space-charge layer which contributes much to enhancing hydrogen gas sensitivity. The response (Ra/Rg) of the SnO_2 and PSP plotted against time shows that response time and recovery time are 34 seconds and 63 seconds, respectively. Fig. 5 shows the response of nanofibers for 500 ppm, 1000ppm, 1500ppm of hydrogen gas. The low-temperature high sensitivity of the PSP nanofibers is due to a large spill-over of the Pd nanoparticles. The variation of the response with the concentration of hydrogen gas at different ppm values reveals maximum response for PSP over pristine SnO_2. PSP has been studied for selectivity using different gases for 1000 ppm at 35 °C. It has been observed that PSP is more selective towards hydrogen gas as compared with NH_3, ehanol, LPG and CO_2 gases.

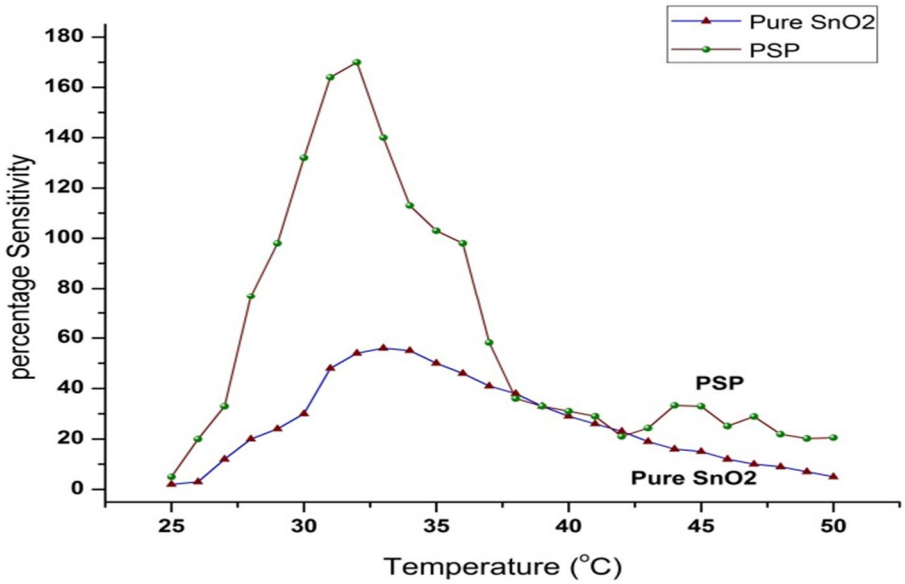

FIG. 4. Sensitivity study of pure SnO_2 and Pd-doped SnO_2 encapsulated with PANI (PSP) nanofibers for hydrogen gas.

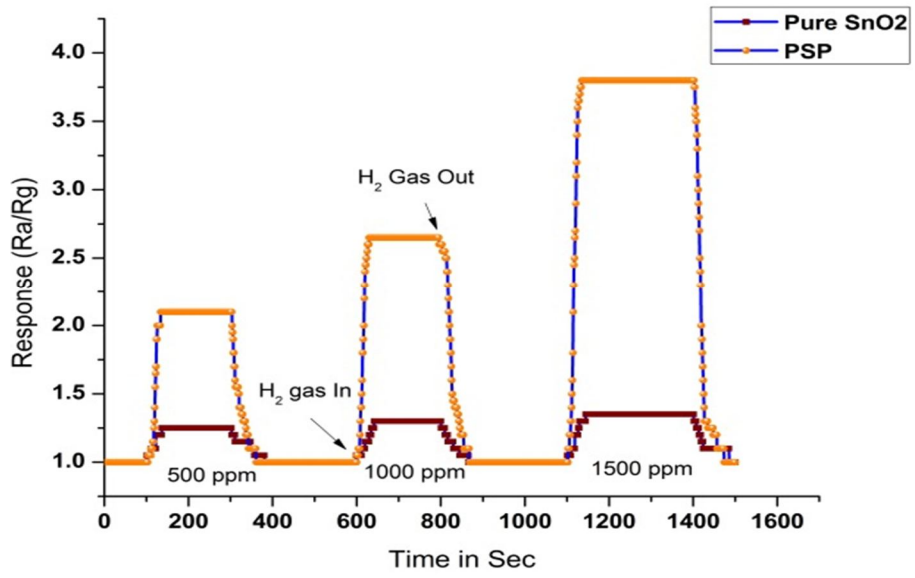

FIG. 5. Response study of pure SnO_2 and Pd-doped SnO_2 encapsulated with PANI (PSP) nanofibers for different parts per million (ppm) of hydrogen gas.

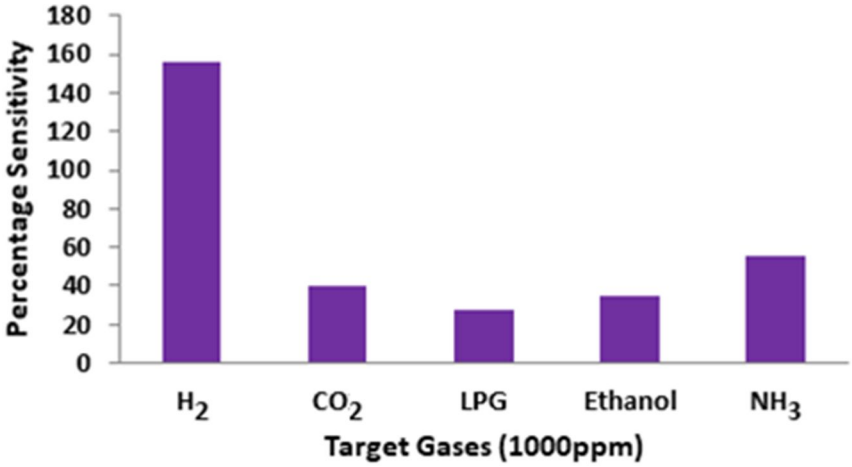

FIG. 6. Selectivity study of Pd-doped SnO_2 encapsulated with PANI (PSP) nanofiber for 1000 ppm of different gases.

Conclusions

PSP nanofibers have been synthesized successfully. The formation of PSP nanofibers includes two steps. In the first step, Pd-doped SnO_2 nanofibers were synthesized, followed by step two in which dip coating of Pd-doped SnO_2 nanofibers is achieved during polymerization of aniline. The XRD study of the nanofibers indicates the formation of crystalline SnO_2 with an average grain size of 5.60 nm. The prominent peaks of SnO_2 show good agreement with the standard peaks from JCPDS file. EDAX pattern depicts the composition of constituent elements. SEM images with diameter distribution of pristine SnO_2 and PSP nanofibers indicate that the average diameters are approximated to 200-400 nm. The average diameter of nanofibers is different from crystal size of SnO_2 due to poly-crystalline nature of nanofibers. The remarkable sensitivity of PSP nanofibers for hydrogen gas has been observed near 32 °C. This indicates that PSP could be used to sense hydrogen gas efficiently near room temperature. The response and recovery times of 34 and 63 seconds respectively promote the practical use of PSP nanofibers for hydrogen gas sensing. The higher percentage of Pd doping could enhance the sensor response. Selectivity of PSP is outstanding for hydrogen gas compared with other gases, like NH_3, CO_2, ethanol vapours. Future work with PSP nanofibers may be advanced with multiple directions, such as different doping percentages of palladium, different polymers for conductivity and modeling of sensitivity study.

References

[1] Matsuguchi, M., Io, J., Sugiyama, G. and Sakai, Y., Synth. Met., 128 (2002) 15.

[2] Adam, H., Stanisław, G. and Folke, I., Pure Appl. Chem., 63 (1991) 1274.

[3] Christie, S., Scorsone, E., Persaud, K. and Kvasnik, F., Sens. Actuators B, 90 (2003) 163.

[4] Kocemba, C. and Renkowisky, J., Sensors and Actuators B: Chemical, 150 (2011) 659.

[5] Khodadadi, A., Mohajerzadeh, S.S., Mortazavi, Y. and Miri, A.M., Sensors and Act. B: Chemical, 80 (3) (2001) 267.

[6] Hubezt, T., Hoon-Brett, L., Black, G. and Banach, U., Sensors and Act. B: Chemical, 157 (2011) 329.

[7] Kolmakov, A., Klenov, D.O., Lilach, Y. and Stemmer, S., Nano Lett., 5 (4) (2005) 667.

[8] Yamazoe, N., Sensors and Act. B: Chemical, 5 (1991) 7.

[9] More, A.M., Sherma, H.J., Kondawar, S.B. and Dongre, S.P., J. Mat. Nanoscience, 4 (1) (2015) 14.

[10] Yang, Z., Miao, Y.E. and He, S., Electrochimica Acta, 99 (2013) 117.

[11] Sharma, H.J., Jamkar, D. and Kondawar, S.B., Proc. Mater. Sci., 10 (2015) 186.

[12] Sharma, H.J., Salorkar, M.A. and Kondawar, S.B., Advance Material Process, 2 (1) (2017) 61.

[13] Xu, X., Sun, J., Zhang, H., Wang, Z., Dong, B., Jiang, T., Wang, W., Li Z. and Wang, C., Sens. Act. B Chem., 160 (1) (2011) 858.

[14] Matsushima, S., Teraoka, Y., Miura, N. and Yamazoe, N., The Japan Society of App. Phys., 1 (27) (2008) 10.

[15] Baik, J.M., Kim, M.H., Larson, C., Yavuz, T., Stucky, G.D., Wodtke, A.M. and Moskovits, M., Nano Letters, 9 (12) (2009) 3980.

[16] Zang, H., Li, Z., Li, L., Xiuru, X., Wang, Z. and Wang, W., Sensors and Actuators B: Chemical, 147 (2010) 111.

[17] Jimenez, G., Candena, J. and Rius, F., Analyst, 132 (2007) 1083.

[18] Joong, C., Hawang, I. and Kim, S., Sensors and Act. B: Chemical, 150 (2010) 191.

[19] Joshi, R.K., Krishnan, S., Yoshimura, M. and Kumar, A., Nanoscale Res. Letters, 4 (2009) 1191.

[20] Ding, B., Wang, M., Yu, J. and Sun, G., Sensors, 9 (2009) 1610.

[21] More, A.M., Ph.D. Thesis, Nagpur University, (2017).

Volume 15, Number 1, 2022. pp. 9-19

Jordan Journal of Physics

ARTICLE

Solvent Extraction and Separation of Silver(I) in Real Sample Using Hexaacetato Calix[6]arene

Y. S. Thakare

Department of Chemistry, Shri Shivaji Science College, Amravati, 444 603, India.

Doi: **https://doi.org/10.47011/15.1.2**

Received on: 01/08/2020; *Accepted on: 16/12/2020*

Abstract: In this study, silver(I) was extracted at pH 11.5 into organic phase using 0.0001 M hexa-*p*-t-butyl-hexaacetato calix[6]arene solution in xylene after a five min equilibration period. Silver(I) was back extracted with 1 M HNO_3 and determined photometrically. Log-log plot gives 1:1 stoichiometry of extracted species indicating that one ligand reacts with one mole of silver(I). The values of ΔG, ΔH and ΔS were determined by studying the extraction equilibrium at different temperatures. Quantitative separation of binary and synthetic mixtures of silver from associate elements was effectively carried out. The extraction and separation of silver(I) from real and multicomponent samples were also studied. The RSD was $\leq 0.5\%$.

Keywords: Solvent extraction, Acetyl derivative, Calix[6]arene, Separation, Silver(I).

Introduction

Ores of copper, copper-nickel, lead-zinc, argentite, chlorargyritepyrargyrite and alloys with gold are main sources of silver.Their compounds have been widely used in pharmaceuticals, industrial, printed circuitry, superconductors, electroplating, brazing, soldering, solar energy, photovoltaic cells, photographic films, water purification and microbiocides. In the medical field, silver has been used as an antiseptic and disinfectant in medical appliances [1-3].

Calixarene is the macrocyclic compound having hydrophobic cavity which can form host-guest type of complex. Cavity size of calixarene can be varied by substituting lower rim. Acetyl derivatives of calix[6]areneare formed by acylation of calix[6]arene and have a variety of applications. The present study deals with the extraction and separation of silver(I) using acetyl derivative of calix[6]arene. Also, it is applied to determine trace level quantity of silver present in real samples.

There are very few methods available for the selective separation and extraction of silver(I) using supramolecular compounds, like calixarenes, cryptands and crown ethers. Liquid-liquid extraction of Ag(I) was carried out using tetraspirocyclohexylcalix[4]pyrrole, calix[4] arenetetramide and its thio analog [4-6]. However, for the quantitative extraction, high reagent concentrations were required and stripping efficiency was low. The structural effects of the three isomers, 2, 3 and 4-pyridino calix[4]arenes on the extraction of silver have been examined. It was observed that the position of the pyridyl nitrogen, conformation and the size of calix[4]arene affect the quantitative extraction [7]. A new calix[4]arene-based podand incorporating two 2, 2'-bipyridine and two benzyl units in alternate positions at the lower rim showed quantitative extraction of silver(I) from neutral aqueous solution containing a mixture of lead and silver nitrates [8].

Makrlik groups reported the extraction of Ag(I) using the two-phase water/nitrobenzene system and determined the stability constant of the5,11,17,23-tetra-*tert*-butyl-25,27-bis[2-methyl thio)ethoxy]calix[4]arene)-Ag(I)complex in

Corresponding Author:Y. S. Thakare **Email**: yogitathakare_2007@rediffmail.com

nitrobenzene saturated with water [9]. Also, studies have been carried out on the extraction of silver using ionic liquids containing calixarene [10]. The calix[4]arene bearing four pyridine groups in the lower rim was used for the solvent extraction of silver and it was observed that this compound showed 230-fold enhancement of the extractability of Ag(I) in ionic liquid over that in chloroform [11]. Ketonic derivatives of calixarenes were found to be selective extractants for Ag(I) over Pd(II), but the extraction of both metals was found to be suppressed in highly acidic media [12,13]. The extraction capacity of tetraallyloxy and tetrabenzyloxy derivatives of calix[4]arenes in the cone and 1,3-alternate conformations was also investigated to extract thallium(I) and silver(I) ions [14].

The kinetics of complicated ion-pair extraction was studied by using Ag(I)-specific thia-crown ether compounds as ion-association reagents by adding fluorescent anions [15,16]. It was found that the extraction capacities of poly cyclic crown ethers were higher than for monocyclic crown ethers.

A simple and practical extraction method of supramolecular solvent was developed for separation and enrichment of trace amounts of palladium (Pd) and silver (Ag) in water samples,where the limits of detection were 2.8 and 1.9 μg/L for Pd and Ag [17].

Newly synthesized chelating resins have been used for on-line solid-phase extraction and preconcentrationfor the determination of trace levels of Ag(I) from water, by flame atomic absorption spectrometry. The detection limits for Ag(I) were found to be2.4 μg/L and 0.3 μg/L [18-19].

Experimental

Reagents and Chemicals

All reagents used in this study were purchased from Merck and Sd-fine. A standard solution of silver(I) was prepared by dissolving 0.03175 g of silvernitrate in double distilled water containing 1 mL HNO_3 and diluted to 500 mL. 0.1 M EDTA was prepared by dissolving 3.73 gm of di-sodium salt of EDTA in 100 mL. 0.001M 1,10phenanthroline was prepared by dissolving 0.020 g in 100 mL. 20% ammonium acetate was prepared by dissolving 20 g in 100 mL. 0.0001M bromopyragallol red was prepared by dissolving 0.006 g in 100 mL. All these solutions were diluted to adequate volume using double distilled water.For extraction of silver(I), 1 x 10^{-4} M solution of reagent was prepared in xylene. Working solutions were prepared by appropriate dilution.

Apparatus

A systronics UV-Visible spectrophotometer (Model No-108) with matched 10 mm quartz cuvettes was used for the absorbance measurements. The calibration of the spectrophotometer was checked by measuring the absorption spectrum of 0.004% solution of potassium chromate in 0.05 M KOH solution and also with 0.0058 % solution of $KMnO_4$ in 1M H_2SO_4. The observed spectra are reported in literature.

A digital pH meter (Systronics Model No-361) with combined glass and calomel electrodes was used to measure the H^+ ion concentration. The pH meter was standardized using the buffer of pH 4.01, 6.0, 7.0, 9.2 at room temperature.

Experimental Procedure for Determination of Silver(I)

For solvent extraction of silver(I), 25 ppm of 10 mL aqueous solution at pH 11.5 and10 mL of 0.0001 M of hexa-*p*-t-butyl-hexaacetato calix[6]arene (HR) in xylene were shaken vigorously for five min in a 60 mL separatory funnel. After equilibrium, two phases allowed to settle and separate. The amount of silver(I) present in the organic phase was back extracted with 10 mL of 1 M nitric acid solution. It was evaporated to dryness and concentration of silver(I) presentwasdeterminedspectrophotometricallywithbromo-pyragallolred [20]. From the concentration of silver in each phase, distribution ratio and percentage extraction values were calculated.

$$D = \frac{\text{Total concentration of solute in the organic phase}}{\text{Total concentration of solute in the aqueous phase.}}$$

where, D=Distribution ratio, assuming that there is no association, dissociation or polymerization in the phases, under idealized condition K_D =D.

UV-Visible spectrophotometer (Systronics-108) and digital pH meter (Systronics-361) were used during the study.

Results and Discussion

Effect of pH on Extraction of Silver(I)

To study the effect of pH, silver(I) was extracted at pH varying from 1.0 to 13.5 with acetyl derivative of calix[6]arene. It was observed that pH over 11.0 -12.0 gives maximum extraction. Hence, for routine work, pH of 11.5 was ensured (Fig. 1).

Effect of Contact Time

The contact time also affects the extraction of silver. It was studied by equilibrating aqueous silver from 30 sec to 15 min with organic phase-containing ligand. It was found that at four min, the percentage extraction was more. In general, five min contact time was taken for further extraction studies (Fig. 2).

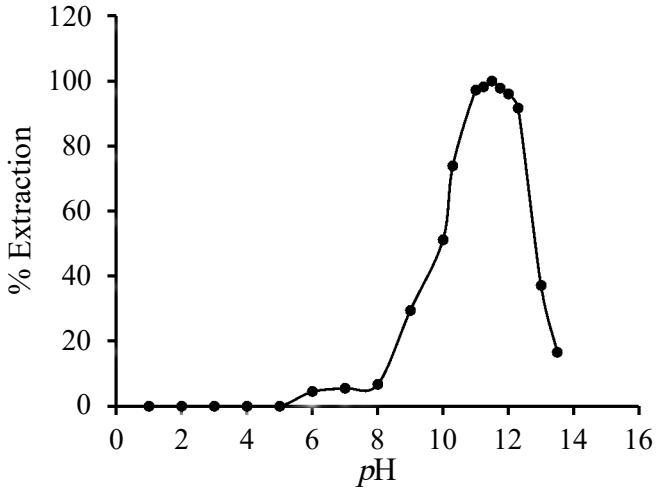

FIG. 1. Effect of pH on the percentage extraction of silver(I) with hexaacetato calix(6)arene.

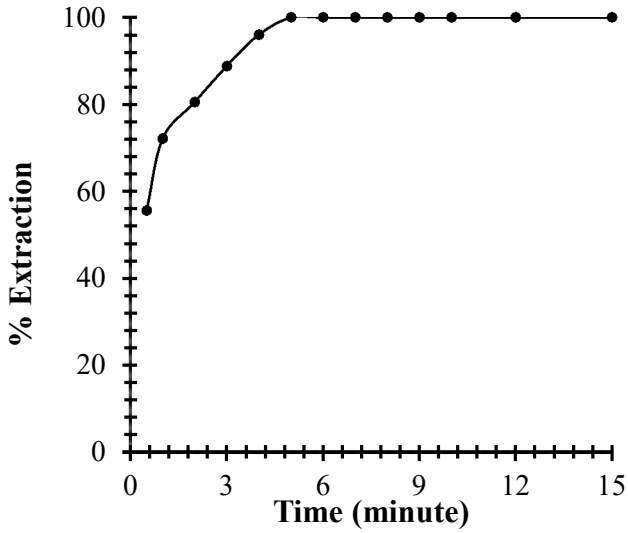

Fig.2. Kinetic study of silver extraction with hexaacetatocalix(6)arene in xylene; pH = 11.5; Ag(I) = 25 ppm; O/A = 1:1.

Effect of Polar and Non-polar Solvents

In non-polar solvents toluene, xylene and cyclohexane, extraction was found to be quantitative. Distribution ratio has a high value (∞). We know that a very high value of distribution ratio indicates the formation of the ion–pair complex. On the other hand, chloroform (22.22%), dichloromethane (3.33%) and 1,2 dichloroethane (5.56%) were found to be poor solvents. The percentage of extraction was more for the non-polar solvent having lower dielectric constant with aromatic nature. The present study was carried out using xylene as an extraction solvent.

Effect of Extractant and Loading Capacity

Varying reagent concentration distribution ratio shows different values. The extraction of silver(I) from 1 x 10^{-6} M to 5 x 10^{-6} M was in the range of 25-50%. For 1 x 10^{-5} M, extraction was

57.22 %. For the reagent concentration 0.2 x 10^{-4} M, it was found to be 69.45%. In the reagent concentration range of 0.4 x 10^{-4} to 0.85 x 10^{-4},the percentage extraction was in the range of 80-90%. For 0.95 x 10^{-4},it was found to be 92.22. The percentage extraction was found to be quantitative from 1x10^{-4} and above reagent concentration (Fig.3). The loading capacity of proposed concentration of reagent was found to be 100 ppm of metal ion (Fig. 4).

The stoichiometry of the extracted species can be depicted by conventional slope analysis method [21]. The graph between log *D* and log of the ligand concentration (Fig. 3) shows a slope of 0.96. Therefore, the expected nature of extracted species is 1:1; i.e., $[Ag(HR)]_{org}$ indicating that one ligand reacts with one mole of silver(I) ions. Again, the graph of log *D*versuspH (Fig. 5) shows a linear plot with a slope of 1.01 nearly equal to integer one, which clearly shows that one ligand is being associated with one mole of metal ion in the organic phase [22].Hence, we can conclude that the probable structure of complex in the organic phase is $AgNO_3$. (HR); where HR is the acetyl derivative of calix(6)arene. The overall reaction can be represented as:

$$Ag^{+}+NO_3^{-} + HR \rightarrow AgNO_3.\ (HR)$$

The equilibrium constant for the extraction of silver in the basic medium (pH 11.5) is given by:

$$\{[Ag(HR)]^{+}, OH^{-}\}_{aq} \rightleftharpoons \{[Ag(HR)]^{+}, OH^{-}\}_{org}$$

The equilibrium constant K_{ex} is defined as:

$$K_{ex} = \frac{\{[Ag(HR)]^{+}, OH^{-}\}_{org}}{[Ag^{+}]_{aq}\,[HR]_{org}[OH^{-}]_{aq}}.$$

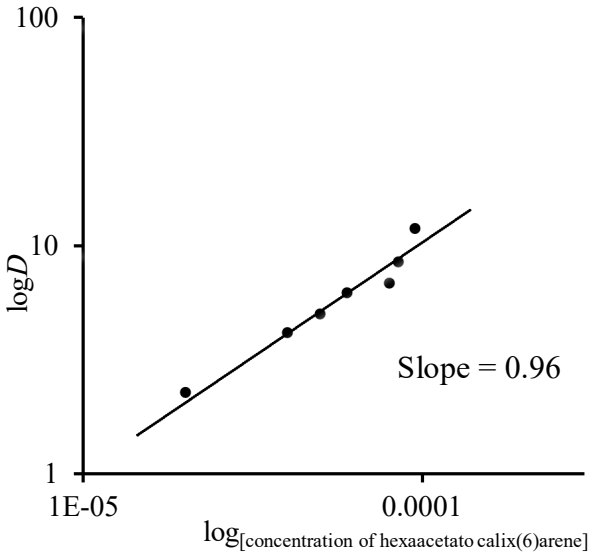

FIG. 3.Effect of reagent concentration on the extraction of silver(I).

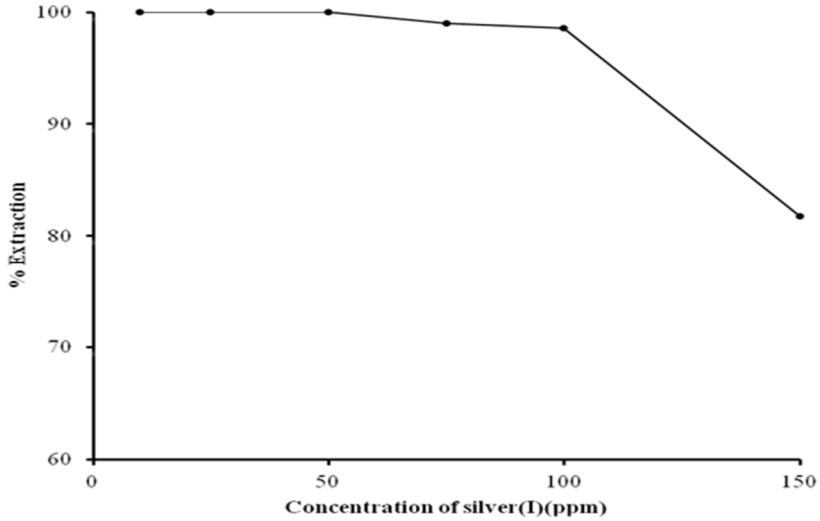

FIG.4. Effect of metal loading on percentage extraction of silver(I)

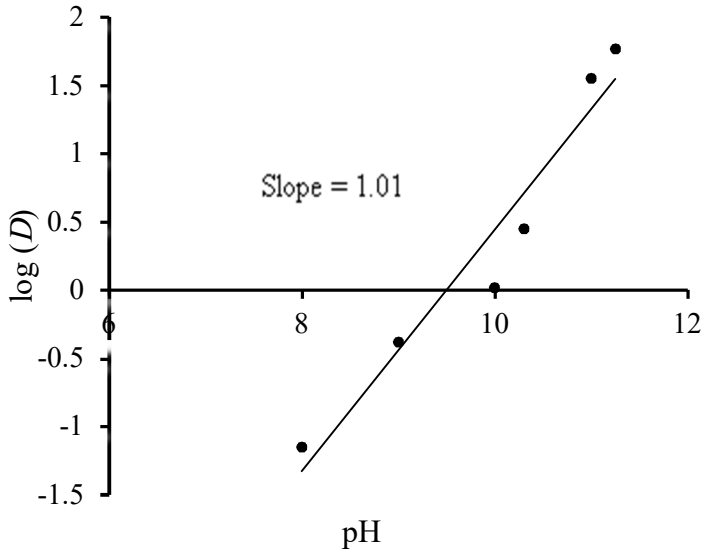

FIG 5. Plot of log *D* against pH for the extraction of silver(I).

Thermodynamic Study

The extraction of Ag(I) with hexaacetato calix[6]arene was carried out in the range of 298 to 328 K. The extraction of Ag(I) decreases with increased temperature. According to Van't Hoff, the K'_{ex} related with temperature is expressed by the equation, $\frac{d\ln K'_{ex}}{d\left(\frac{1}{T}\right)} = \frac{-\Delta H^0}{R}$. The graph of $\ln K'_{ex}$ against 1000/T was linear with a slope of 18.69. The values of thermodynamic parameters ΔG^0 = -111.26 kJ mol^{-1}, ΔH^0 = -155.39 kJ mol^{-1}, and ΔS^0 = -148.07 J K^{-1} mol^{-1} (Table 1) for the solvent extraction of Ag(I) were calculated. Formation of ion–pair complex is favored by a high negative value of standard Gibb's free energy. The reaction was favored with decrease of temperature supported by a negative value of entropy. The negative value of enthalpyindicated the exothermic reaction.

TABLE1. Effect of temperature on solvent extraction of silver(I) with hexaacetato calix[6]arene.

Temp / (K)	log K_D	dlogK'_{ex}	ΔH kJ mol^{-1}	ΔG kJ mol^{-1}	ΔS J K^{-1} mol^{-1}
298	3.999	19.50		-111.26	-148.07
308	1.771	17.271		-101.85	-173.82
313	1.279	16.779	-155.39	-100.55	-175.2
318	0.954	16.454		-100.19	-173.59
323	0.415	15.915		-98.426	-176.35
328	0.196	15.696		-98.578	-173.2

Effect of Back Extracting Agents

Solvent extraction of silver(I) was carried out at pH 11.5 using ligand in xylene witha contact time of five min. Then, the metal ions in the organic phase were back extracted using various concentrations of mineral acids from 0.1 to 2 M. For nitric acid and hydrochloric acid from 0.1 M to 0.5 M, the extraction was incomplete. For 1 M, it was found to be quantitative and for 1 M and 2 M, it was 77.78 and 75.0, respectively. It was found that with increase in the concentration the percentage extraction was decreased. For acetic acid, the percentage extraction was incomplete from 0.1 M to 0.5 M and from 1 M to 2 M, it was found to be quantitative. When perchloric acid was used as a stripping agent, then for 0.1 M, the extraction was found to be quantitative and again with increasing concentration up to 2 M, it was found that the percentage extraction was decreased. Using sulphuric acid, it was found that from 0.1 M to 2 M, the extraction was incomplete. Hence, for the ease of extraction, stripping was carried out by using 1 M nitric acid (Table 2).

TABLE 2. Effect of concentration of back extractant on percentage extraction of silver(I).

Stripping agents /Concentration	% Extraction				
	0.1 M	0.25 M	0.5 M	1 M	2 M
HNO_3	13.89	29.45	48.89	100	77.78
HCl	32.22	40.56	55.0	100	75.0
CH_3COOH	58.33	64.45	71.11	100	100
$HClO_4$	100	69.45	60.56	52.78	40.0
H_2SO_4	28.89	36.67	38.89	51.67	78.33

Mass Spectrometric Analysis

Hexaacetatocalix[6]arene was synthesized in laboratory by reported mehod. It is the cone-shaped compound having cavity inside and its anular space varring from 1.0 A^0 to < 4.8 A^0 [23]. The ionic radii of silver(I) fall under this range, so that it was easily trapped in the cavity of hexaacetatocalix[6]arene through ion-pair interaction. The stoichiometry of the extracted species was determined by LCMS spectra of the pregenant organic phase. The acetyl derivative of calix[6]arene (HR) has m/e 1226.9 and its complex with silver(I) supposed to be [Ag(HR)] in the organic phase has m/e 1326.9. This enhanced the value of the complex formed in the organic phase clearly supporting 1:1 metal:ligand stoichiometry in the organic phase. Mass: m/z, 1326.9 (M+2) parent ion. 1324.6 (M+1), 1282 (M+2)-$COCH_3$,1267.3 (M+1)-$COCH_3$, (M. F. Ag-$C_{78}H_{96}O_{12}$). The comparative mass spectra of acetyl derivative of calix[6]arene and its complex with silver(I) are depicted below in Figs. 6 and 7,respectively. Also, the possible structure of the complex is shown in Fig. 8.

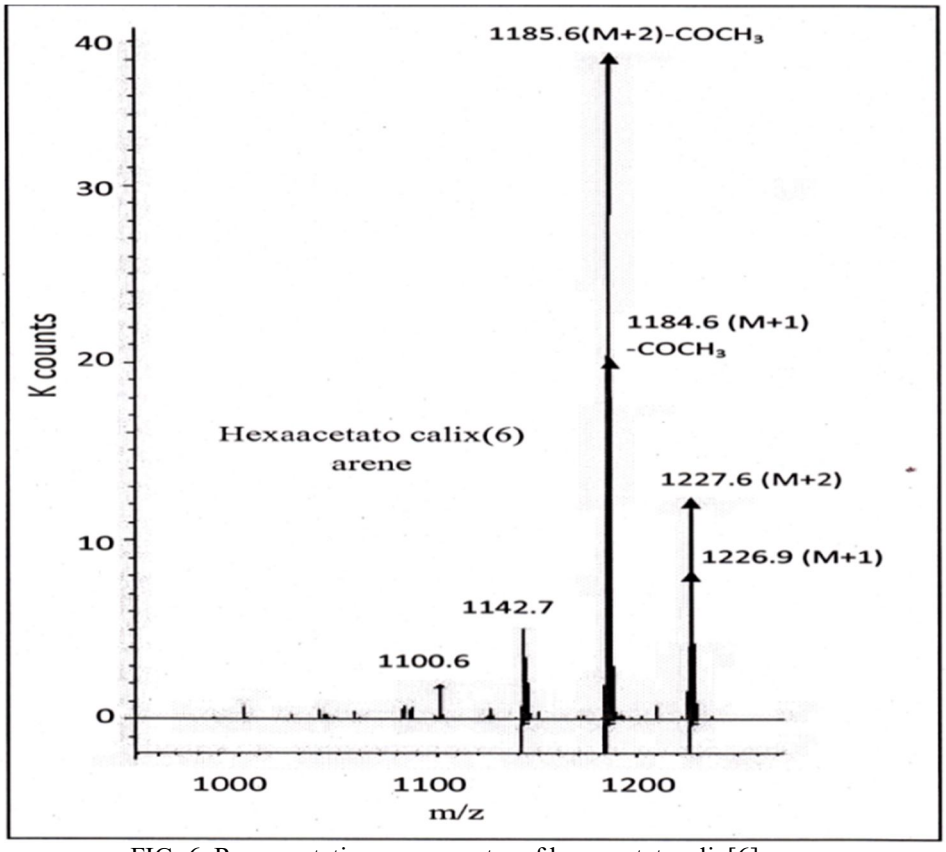

FIG. 6. Representative mass spectra of hexaacetatocalix[6]arene.

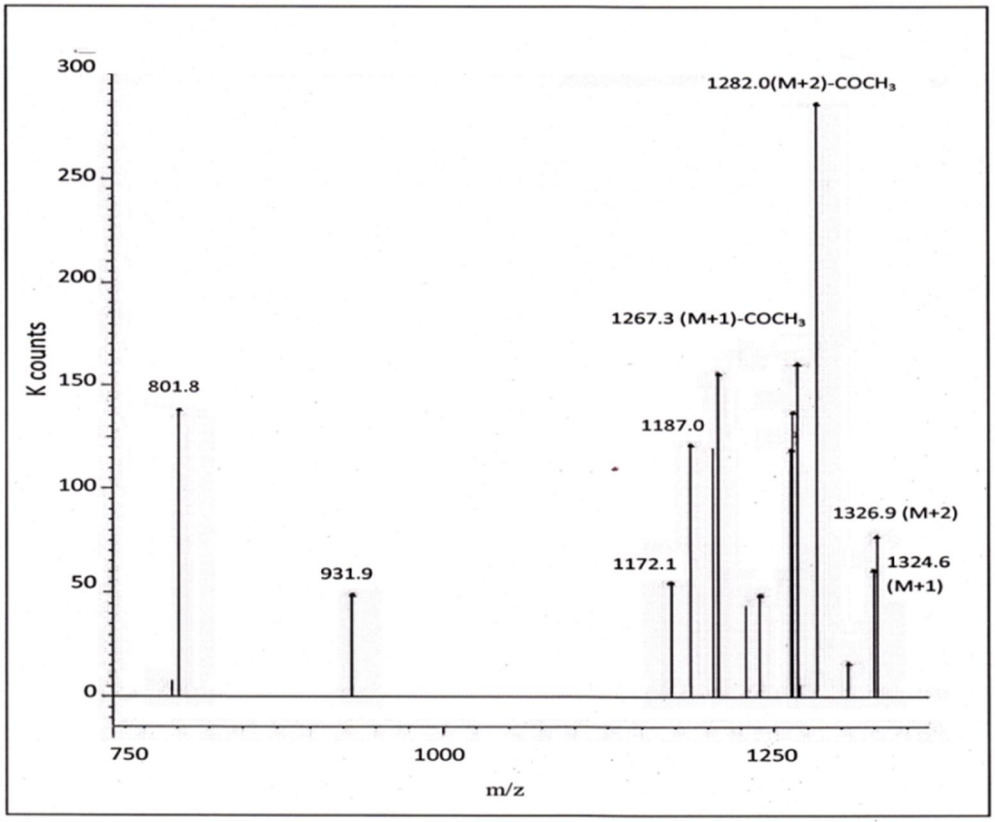

FIG. 7. Representative mass spectra of hexaacetatocalix[6]arene with silver(I).

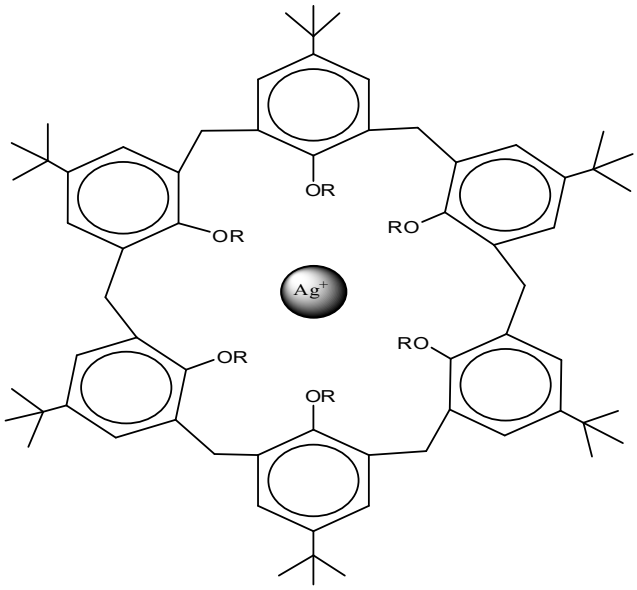

FIG 8.Possible structure of hexaacetatocalix[6]arene with the silver(I) (R = -$COCH_3$).

Applications

Foreign Ions Effect

After successful extraction and stripping of silver using the proposed experimental conditions,the effect of large number of foreign ions on its extraction was studied. Initial interference was studied by adding large excess of foreign ions (say 500 ppm), then theconcentration was decreased up to the tolerance limit. It was observed that the method is free from interference of large number of transition, non-transition metal ions and anions. Only some metal ions Cd^{2+}, Hf^{4+}, Au^{3+}, Hg^{2+}, Ga^{3+} and In^{3+} interfered strongly. Also, the anions Br^-, I^-, thiocynate, thiosulphate and EDTA ions strongly interfered during the extraction (Table 3).

TABLE 3. Effect of diverse ions on the extraction and determination of silver(I).

Forgien ion	Added as	Tolerance limit	Forgien ion	Added as	Tolerance limit
Li^{+}	LiCl	200	Th^{4+}	$Th(NO_3)_4.5H_2O$	50
Na^{+}	NaCl	150	Al^{3+}	$AlK(SO_4)_2.12H_2O$	50
K^{+}	KNO_3	350	Ga^{3+}	$GaCl_3$unhydrous	Interfere
Be^{2+}	$BeCl_2.2H_2O$	350	In^{3+}	$InCl_3$unhydrous	Interfere
Mg^{2+}	$MgCl_2.6H_2O$	150	Sn^{2+}	$SnCl_2.2H_2O$	10
Ca^{2+}	$CaCl_2.2H_2O$	250	Pb^{2+}	$Pb(NO_3)_2$	10
Ba^{2+}	$BaCl_2.2H_2O$	100	As^{3+}	As_2O_3	100
Sc^{3+}	Sc_2O_3	30	Sb^{3+}	$SbCl_3$	30
V^{5+}	V_2O_5	10	Bi^{3+}	$Bi(NO_3)_3.5H_2O$	10
Cr^{3+}	$Cr(NO_3)_3.9H_2O$	10	Cl^{-}	Potassium chloride	350
Mn^{2+}	$MnCl_2.4H_2O$	30	Br^{-}	Potassium bromide	Interfere
Fe^{3+}	$Fe(NO_3)_3.9H_2O$	50	I^{-}	Potassium iodide	Interfere
Fe^{2+}	$FeSO_4.7H_2O$	30	Nitrite	Sodium nitrite	200
Co^{2+}	$Co(NO_3)_2.6H_2O$	30	Nitrate	Sodium nitrate	350
Ni^{2+}	$Ni(NO_3)_2.6H_2O$	30	*o*-phosphate	Sodium dihydrogen*o*-phosphate	100
Cu^{2+}	$CuSO_4.5H_2O$	50	Thiocynate	Ammthiocynate	Interfere
Zn^{2+}	$Zn(NO_3)_2.6H_2O$	50			
Y^{3+}	Y_2O_3	30	Thiosulphate	Sodium thiosulphate	Interfere
Zr^{4+}	$ZrOCl_2.8H_2O$	30	Acetate	Sodium acetatetrihydrate	50
Mo^{6+}	$(NH_4)_6Mo_7O_{24}.4H_2O$	30	Oxalate	Potassium oxalate	10
Rh^{3+}	$RhCl_3.H_2O$	10	Tartaret	Sodium potassium tartaret	10
Cd^{2+}	$CdCl_2.2H_2O$	Interfere	EDTA	Di sodium salt of EDTA	Interfere
La^{3+}	LaO_3	30	Carbonate	Sodium bicarbonate	100
Ce^{4+}	$(NH_4)_4Ce(SO_4)_42H_2O$	50	Sulphate	Potassium sulphate	350
Sm^{3+}	Sm_2O_3	50	Fluoride	Sodium fluoride	10
Hf^{4+}	$HfCl_4$	Interfere	Bisulphite	Sodium bisulphite	100
Au^{3+}	$HAuCl_4.xH_2O$	Interfere	Citrate	Trisodium citrate	30
Hg^{2+}	$HgCl_2$	Interfere			

Determination of Silver(I) in Synthetic Mixtures

Silver is a precious metal on earth. The synthetic mixture was prepared according to its composition in the real samples or natural source. A solution containing 25 ppm ofAg(I) was taken and a known amount of other metal ions was added. Extraction of silver was carried out using the developed method. The RSD was found to be $\leq$ 0.5%(Table 4).

TABLE 4. Extraction separation and determination of silver(I) from synthetic mixtures.

Composition (ppm)	Silver(I) found (µg)	Mean (µg)	% Recovery	% [a]RSD
Ag(25)+As(25)+Ni(25)	24.86, 24.86, 24.86, 24.72,24.58	24.78	99.11	0.50
Ag(25)+Cu(25)+Pb(25)	24.87, 24.75, 2462,24.75, 24.87	24.77	99.09	0.43
Ag(25)+Cu(25)+Zn(25)	24.85, 24.85, 24.71, 24.71, 24.85	24.79	99.17	0.33
Ag(25)+Ni(25)+Zn(25)	24.72, 24.72, 24.86, 24.86, 24.72	24.77	99.09	0.32
Ag(25)+Pb(25)+As(25)	24.75, 24.87, 24.87, 24.87, 24.62	24.80	99.19	0.46

[a]Average of five determinations.

Separation and Determination of Silver(I)from Binary Mixtures

This method permits the extraction and separation of Ag(I) from commonly associated metal ions Al(III), Mn(II), Cr(III),Zr(IV) and Y(III) by taking the advantage of differences in the extraction conditions, like pH, equilibration time and stripping agents of the other metal ions. Below pH 6, silver(I) was not extracted; therefore, separation of it from the other metal ions was easily carried out. For the analysis, the mixture of Ag(I) with other metal ions Al(III) or Mn(II) or Cr(III) or Zr(IV) or Y(III)) was taken and its respective pH was maintained at 5.0, 6.0, 6.5, 3.0 and 6.0, respectively and allowed to equilibrate for 10 min. The added metal ionswere quantitatively extracted in the organic phase and silver(I) quantitatively remained in the aqueous phase. The extracted metal ions from the organic phase were stripped by using 1 M HCl, 2 M H_2SO_4, 4 M HCl, 4 M HNO_3 and 1 M HNO_3 as stripping agents, respectively. The aqueous phase was evaporated to moist dryness and the amount of Al(III) or Mn(II) or Cr(III) or Zr(IV) or Y(III) was determined spectro photometrically by using eriochrome cynine-R, periodate, xylenol orange and arsenazo(III), respectively. The concentration of Ag(I) present in the aqueous phase was determined by the recommended procedure (Table 5).

TABLE 5. Extraction separation of binary mixtures.

Metal ion	Amount taken(µg)	pH	Stripping agent	% Recovery	Determination method	Wavelength (nm)
Ag(I)	25	11.5	1 M HNO_3	99.99	b	650
Al(III)	20	5.0	1 M HCl	99.71	c	535
Ag(I)	25	11.5	1 M HNO_3	99.99	b	650
Mn(II)	25	6.0	2 M H_2SO_4	99.50	d	545
Ag(I)	25	11.5	1 M HNO_3	99.99	b	650
Cr(III)	30	6.5	4 M HCl	99.50	e	520
Ag(I)	25	11.5	1 M HNO_3	99.99	b	650
Zr(IV)	20	3.0	4 M HNO_3	99.66	e	560
Ag(I)	25	11.5	1 M HNO_3	99.99	b	650
Y(III)	10	6.0	1 M HNO_3	99.35	f	620

[b]Bromopyragallol red at 650 nm, [c]Eriochromecynine-R, [d]Periodate, [e]Xylenol orange, [f]Arsenazo(III).

Analysis of Real Samples

The applicability of the proposed method was used to extract and separate silver(I) from real samples. The results obtained by this present method were in good agreement with the certified values. The stock solution of samples was prepared as follows.

Pharmaceutical Samples

The silver ion is bioactive and in sufficient concentration readily kills bacteria *in vitro*. For the analysis of amount of silver(I) present in the antibacterial creams, 0.125 g of Silhex (CadilaHealth Care limited) and 1.25 g of Silverex^{TM} ionic (Virchow Biotech limited) were dissolved in 5 mL of 4 M HNO_3 and evaporated to moist dryness. Then, the residue was dissolved in minimum quantity of water and filtered. After that the filtrate was evaporated to moist dryness and finally diluted to 25 mL.

Silver Dental Alloy

Silver dental alloy (0.2 g) used in teeth feeling was dissolved in 10 mL of 4 M HNO_3 and evaporated to moist dryness. Then, the residue was dissolved in minimum quantity of water and filtered. After that,the filtrate was evaporated to moist dryness and diluted to 25 mL.

Silver Alloy

For the analysis of the silver(I) present in the silver alloy, 0.085 g sample was dissolved in 8 mL of 4 M HNO_3 and evaporated to moist drynessThen, the residue was dissolved in minimum quantity of water and filtered. After that,the filtrate was evaporated to moist dryness and diluted to 25.0 mL.

Waste Liquid during Photographic Film Processing

The waste liquid was collected during the photographic film processing. For the analysis, 20 mL of waste liquid was treated with 10 mL of 4 M HNO_3. The solution was kept overnight in dark. Then, it was evaporated to moist dryness, taken into minimum quantity of water and filtered to remove undissolved impurities. Finally, the solution was diluted to 50.0 mL.

Silver Foil (Vark)

Traditional Indian dishes sometimes include the use of decorative silver foil known as vark. For the determination of the amount of silver(I) in the silver foil, one leaf of nearly 0.005 g (Meera brand guaranteed pure silver leaves and company, Delhi) was dissolved in minimum quantity of HNO_3 and kept overnight. Then, the solution was evaporated to moist dryness and taken into minimum quantity of water. Finally, it was filtered and diluted to 50.0 mL.

All the solutions were acidified with drop ofconcentrated HNO_3 before dilution. An aliquot of each of the above solution was taken and then its pH was maintained to 11.5 and extracted with 10 mL of 1 x 10^{-4} M of acetyl derivative of calix[6]arene and determined spectrophotometrically by complexation with bromopyragallol red at 650 nm (Table 6).

TABLE 6.Analysis of silver(I) in real samples.

Samples	Amount found by proposed method (µg)	Mean (µg)	Certified value (µg)	% Recovery	% [a]RSD
Silhex (Cadila Health Care limited)	14.83 15.10 14.96 14.96 14.96	14.96	15.10	99.09	0.65
Silverex™ ionic (Virchow Biotech limited)	63.12 62.93 63.31 63.12 62.74	63.05	63.50	99.29	0.34
Silver dental alloy	24.86 24.86 24.72 24.58 24.72	24.75	25.00	99.00	0.47
Silver alloy	48.86 49.05 48.86 49.05 48.67	48.90	49.24	99.31	0.33
Waste liquid (during photographic film processing)	46.97 47.16 47.16 46.97 46.78	47.01	47.35	99.28	0.34
Silver foil (vark)	79.86 80.06 79.86 79.47 79.67	79.78	80.25	99.42	0.29

[a]Average of five determinations.

Conclusions

Acetyl derivative of calix[6]arene was found to be a novel extractant for analysis of silver(I)in a variety of real samples, binary mixtures and synthetic mixtures. This study was carried out using very low concentration reagent, relatively less toxic solvent and low concentration of back extracting reagent. The values of thermodynamic parameters were also evaluated. Silver complex was formed with the ligands in the organic phase with the stoichiometric formula $[Ag(HR)]_{(org)}$. The large numbers of foreign ions were tolerated in high ratios. The method was free of interference from a large number of foreign ions which were often associated with naturally occurring silver(I). The time required for the extraction and separation was very short, which indicates a high distribution ratio of the complex involved in the quantitative recovery of silver(I). The proposed method involves quantitative extraction in a single step within a very short time.

References

[1] Atiyeh,B.S., Costagliola,C., Hayek,S.N. and Dibo,S.A., Burns,33(2007) 139.

[2] Qin,Y., Int. Wound J.,2 (2005) 172.

[3] Hermans,M.H., Am. J. Nurs., 106 (2006) 60.

[4] Ghiasvand,A.R., Moradi,F., Sharghi,H. and Hasaninejad,A.R., Anal. Sci., 21 (2005) 387.

[5] Stankovic,V., Outarra,L., Zonnevijlle,F. and Comninellis,C., Sep. Purif. Technol., 61 (2008) 366.

[6] Stankovic,V., Duo,I., Comninellis,C. and Zonnevijlle,F., J. Appl. Electrochem., 37 (2007) 1279.

[7] Ohto,K., Higuchi,H. and Inoue,H.K.,SolventExtr. Res. Dev. Jpn.,8 (2001) 37.

[8] Regnouf-de-Vains,J.B., Dalbavie,J.O., Lamartine,R. and Fenet,B., TetrahedronLett., 42 (2001) 2681.

[9] Makrlik,E., Dybal,J., Svorcikova,J., Budka,J. and Vanura,P., Monatsh. Chem., 141 (2010) 507.

[10] Shimojo,K. andGoto,M., Anal. Chem., 76 (2004) 5039.

[11] Shimojo,K. and Goto,M., Chem. Lett., 33 (2004) 320.

[12] Ohto,K., Murakami,E., Shiratsuchi,K., Inoue,K. and Iwasaki,M.,Chem. Lett., 2 (1996)173.

[13] Ohto,K., Murakami,E., Shinohara,T., Shiratsuchi,K., Inoue,K. and Iwasaki,M., Anal. Chim. Acta, 341 (1997) 275.

[14] Chester,R.T., Couton,D., Lobler,R., Mocerino,M., Ogden,M.I.,Pettersen,J.K., Skelton,B.W. and White,A.H.,J. Inclusion Phenom. MacrocyclicChem., 71 (2011) 471.

[15] Nagai,H., Miwa,N., Segawa,M., Wakida,S.I. and Chayama,K., J. Appl. Phys., 105 (2009) 102015/1.

[16] Miwa,N. and Chayama,K., Mem. Konan Univ. Sci. Ser., 52 (2005) 147.

[17] Meng,L., Cheng,J. and Yang,Y., Water Sci. Technol., 69 (2014) 580.

[18] Cetin,T., Tokalioglu,S., Ulgen,A., Sahan,S., Ozenturk,I. and Soykan,C., Talenta, 105 (2013) 340.

[19] Dasbasi,T., Sacmaci,S., Sahan,S., Kartal,S. and Ulgen,A., Talenta, 103 (2013) 1.

[20] Snell,F.D., "Photometricand FluorometricMethodsof AnalysisMetals",Part 1, (WileyIntersciencePublication, New York, 1978), p. 76.

[21] Thakare,Y.S., Alochana Chakra J., 9 (2020) 523.

[22] Swamidoss,C., Ramaswamy,K. and Tallam,V., Mater. Today:Proce., 21 (2020) 954.

[23] Thakare,Y.S. and Malkhede,D.D., Sep. Sci. Technol., 49 (2014) 1198.

Volume 15, Number 1, 2022. pp. 21-27

Jordan Journal of Physics

ARTICLE

Impact of La on Structural, Morphological and Magnetic Properties of $NiCoFe_2O_4$ Nano Ferrites

P. K. Nagpure[a], **A. K. Nandanwar**[b], **V. M.Nanoti**[c] and **K. G. Rewatkar**[b]

[a] *Department of Physics, D.B. Science College, Gondia-441614, Maharashtra, India.*

[b] *Department of Physics, Dr. Ambedkar College, Deekshabhoomi Nagpur-440010, Maharashtra, India.*

[c] *Department of Physics, PIET, Nagpur-440019, Maharashtra, India.*

Doi: **https://doi.org/10.47011/15.1.3**

Received on: 01/08/2020; *Accepted on: 16/12/2020*

Abstract: $Ni_{0.2}Co_{0.8}Fe_{2-x}La_xO_4$ (x = 0.02, 0.06, 0.10) nano ferrites have been synthesized by Sol-gel auto combustion method using urea as a fuel. The sample calcinations have been performed at 800 ^oC for 4 hours. The synthesized samples were subjected to study X-ray diffraction spectroscopy (XRD) for structural investigations. All the samples were found to constitute Face Centered Cubic (FCC) spinel structure belonging to the Fd3m space group. The XRD results show the single cubical phase formation in the heated samples. Energy-dispersive X-ray spectra confirmed the presence of Ni, Co, La Fe and O elements with no existence of any impurity. The average crystallite size was decreased by varying the concentration of La from 10 to 8 nm. The Field Emission Gun Scanning Electron microscopy (FEG-SEM) and Field Emission Gun transmission electron microscopy (FEG-TEM) have given the morphological study of the samples. It is also found that the value of the lattice constant decreases with increases in La concentration. The magnetic properties of the samples were investigated by using a vibrating sample magnetometer (VSM). The results obtained from VSM show that the value of both magnetization (Ms) and coercivity (Hc) decreases with an increase in diamagnetic La concentration.

Keywords: Spinel ferrites, Sol-gel, SEM, TEM, VSM.

Introduction

The physical, electrical and magnetic properties of ferrites enable their use in various types of technologies. Spinel ferrite nanoparticle materials are highly preferred in engineering and technology applications, like biomedecine, pharmaceuticals, sensors, magnetic resonance imaging, drug delivery, microwaves, high-frequency devices, information storage and electronic chips [1, 2, 3, 4]. The structure and electromagnetic properties of nano-spinel ferrites can be modified by the substitution of different cations. Rare earth substitutions are highly valuable for reducing the particle size and intensification of the lattice parameter [5]. In this respect, substituting rare earth (RE) cations into the spinel ferrite structure plays an important role in enhancing the dielectric, magnetic and electric properties due to the Fe–Fe interactions caused by the spin coupling effect of 3d electrons [6]. Therefore, when rare earth and iron interactions (3d–4f coupling) of the spinel ferrites occur, they can vary the structural, electrical, spectral and magnetic properties of spinel ferrites. In our study, structural changes, such as decreases in lattice constant due to the transfer of an equivalent number of Fe^{3+} ions (0.64 Å) from tetrahedral (A) site to octahedral [B] site to relax strain at the octahedral site, are observed. Magnetic parameters, such as

Corresponding Author: Priti K Nagpure **Email**: pritinagpure1979@gmail.com

coercivity (Hc), saturation magnetization (Ms) and retentivity (Mr), decrease with an increase in La concentration. Different RE substitutions have proven to have different results on the ferrite structure [7,8,9]. Some researchers have investigated the effects of La substitution into cobalt-doped nickel ferrite [10-14].

Materials and Methods

Nano-sized ferrite particles with the composition $Ni_{0.2}$ $Co_{0.8}$ $Fe_{2-x}La_xO_4$ (x = 0.02, 0.06, 0.10) were prepared using sol-gel auto combustion method using urea as a fuel. The high-purity AR grade ferric nitrate ($Fe(NO_3)_3.9H_2O$), Nickle nitrate ($Ni(NO_3)_2.6H_2O$), Cobalt nitrate ($Co(NO_3)_2.6H_2O$), Lanthanum nitrate ($La(NO_3)_3.6H_2O$) are dissolved in distilled water. This solution was then heated at 80^0 C for 4 to 5 hrs, to form sol to viscous brown gel. After that, it was kept in a microwave oven (Model IFB 17 PM – MEC1); within 2 to 3 min. auto combustion takes place and yields fine powder of $Ni_{0.2}$ $Co_{0.8}$ $Fe_{2-x}La_xO_4$ ferrite nanoparticles. The powder was sintered at 800^0 C for 4 hrs.

Results and Discussion

X-ray Diffraction Analysis

The X-ray diffraction pattern for $Ni_{0.2}$ $Co_{0.8}$ $Fe_{2-x}La_xO_4$ (x = 0.02, 0.06, 0.10) synthesized by sol-gel auto combustion method is shown in Fig. 1. The XRD pattern confirmed the formation of single-phase cubic spinel with space group Fd3m, which is in agreement with ICSD 174321. Measurements were performed using Cu Kα radiation having a wavelength, λ = 1.5406 Å. Fig. 1 shows that the most intense diffraction peak (311) is slightly shifted towards a higher angle with increasing La substitution. The peak shift towards a higher angle can be attributed to a decrease in lattice parameter the reason behind which is that the lattice parameter is inversely proportional to the diffraction angle $\sin\theta$. When the diffracting angle (θ) increases, lattice constant (a) goes on decreasing.

The broadening of XRD peaks is related to the nano-sized particle and lattice strain. The value of lattice constant 'a' and particle size for each sample are given in (Table 1).

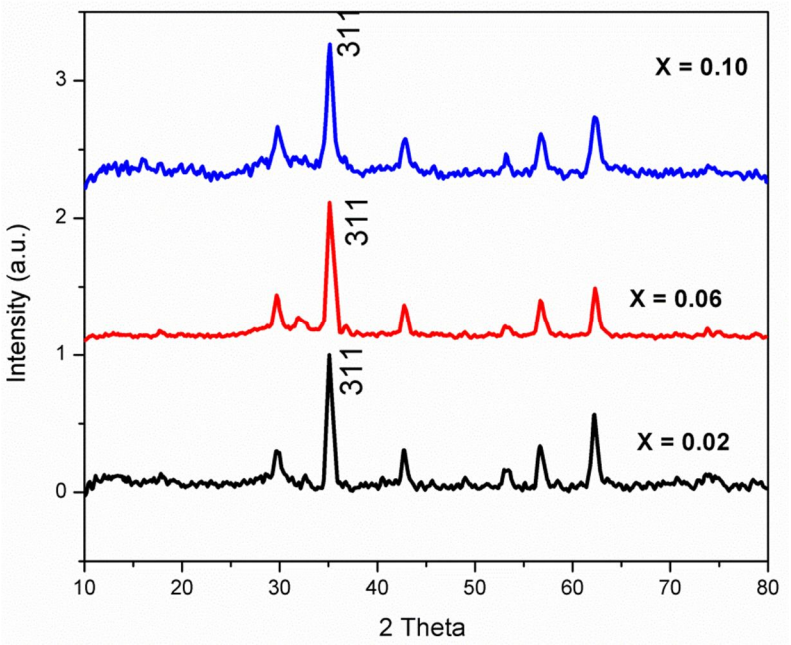

FIG. 1. XRD pattern of $Ni_{0.2}$ $Co_{0.8}$ $Fe_{2-x}La_xO_4$.

TABLE 1. Average particle size (D) and lattice constant (a).

Composition (X)	Average particle size (D) nm	Lattice constant (a) Å
X = 0.02	10.34	8.48024
X = 0.06	11.89	8.47431
X = 0.10	8.56	8.46290

Note: Variation of average particle size (D) and lattice constant (a) of $Ni_{0.2}$ $Co_{0.8}$ $Fe_{2-x}La_xO_4$.

Morphological Analysis

The Field Emission Gun scanning electron microscopy (FEG-SEM) of $Ni_{0.2}Co_{0.8}Fe_{2-x}La_xO_4$ (x = 0.02, 0.06, 0.10) nanoparticles is shown in Fig 2. The image exhibits a higher agglomeration cubic shape with an average grain size of 39 nm. The existence of agglomeration may be due to the interaction between the magnetic particles [12].

The EDX spectrum confirmed the existence of Ni, Co, Fe, La and O in composition X = 0.02, 0.06 and 0.10, as shown in Fig 3. The EDX spectra illustrate that La peak intensities increase with an increase in La content. The TEM pattern of $Ni_{0.2}Co_{0.8}Fe_{2-x}La_xO_4$ (x = 0.02) nanoparticles is shown in Fig. 4. The image confirms the cubic spinel structure. Fig 5 shows the Selected Area Electron Diffraction (SAED) image which also confirms the formation of poly-nanocrystalline form.

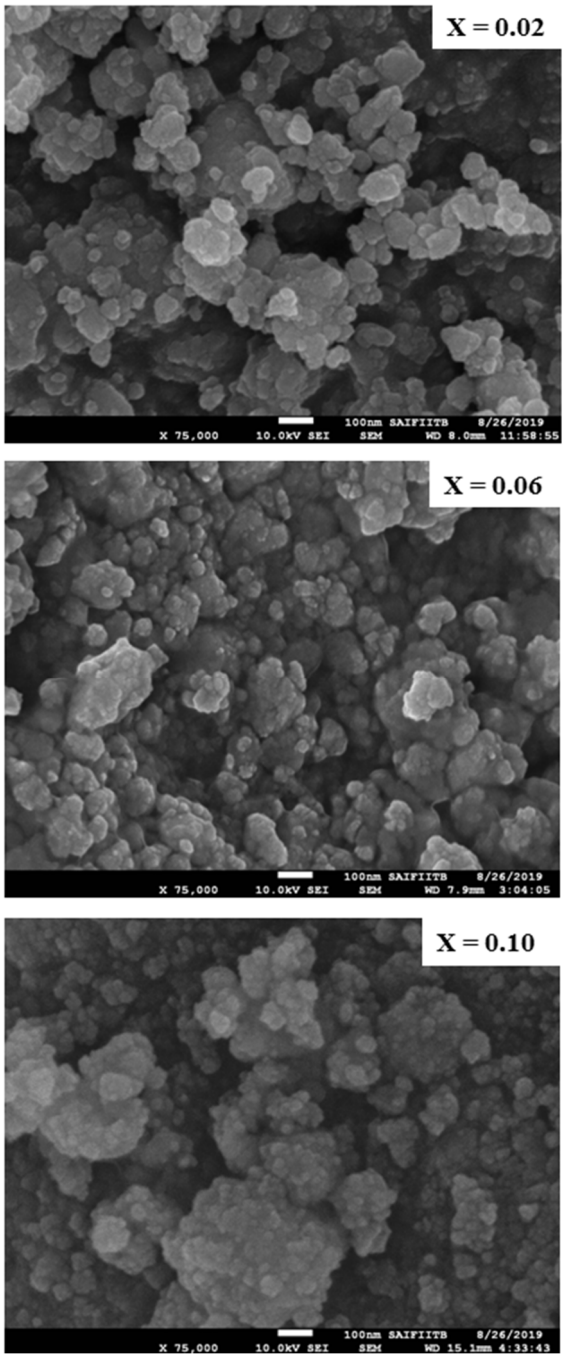

FIG 2. Field emission gun scanning electron microscopy (FEG- SEM) of $Ni_{0.2}Co_{0.8}Fe_{2-x}La_xO_4$ for different concentrations of X.

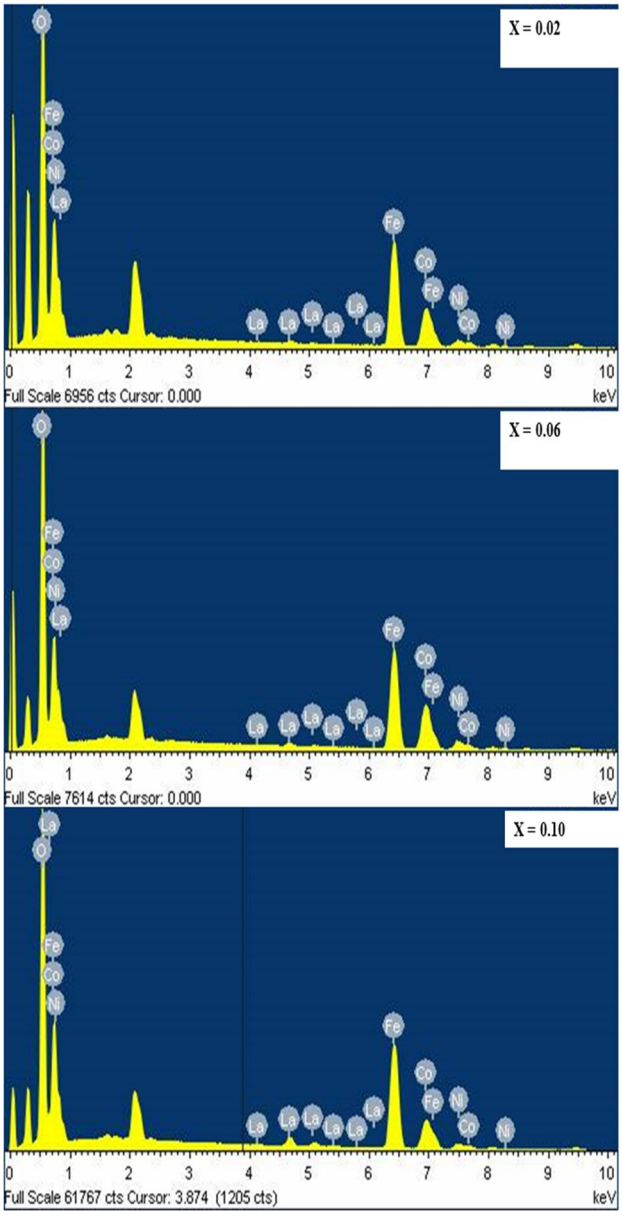

FIG. 3. EDX of $Ni_{0.2}$ $Co_{0.8}$ $Fe_{2-x}La_xO_4$ for different concentrations of X.

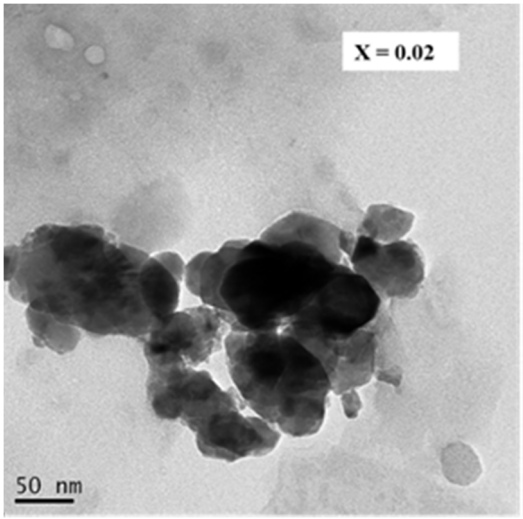

FIG. 4. The field emission gun transmission electron microscopy (FEG- TEM) of $Ni_{0.2}$ $Co_{0.8}$ Fe_{2-x} La_xO_4 for (X = 0.02).

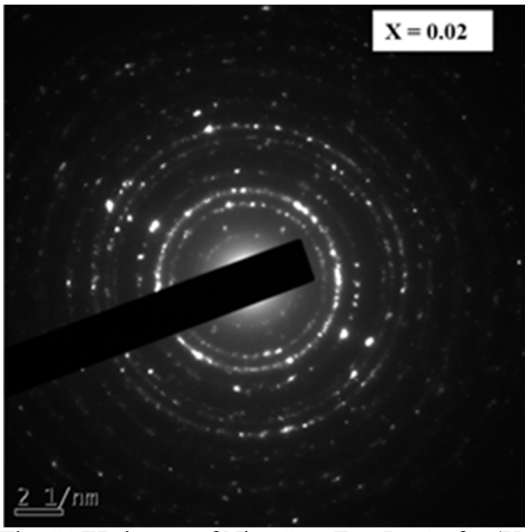

FIG. 5. The SAED image of $Ni_{0.2}Co_{0.8}Fe_{2-x}La_xO_4$ for (X = 0.02).

Magnetic Properties

At room temperature, magnetization as a function of the applied magnetic field is shown in Fig. 6 for different samples. All samples show a typical magnetic characteristic of ferrites with a difference in the value of saturation magnetization (Ms). The saturation magnetization value (Ms) and coercivity (Hc) have been found to decrease with the increase in La concentration. In the rare-earth substituted ferrites, the rare-earth ions have a strong preference for the octahedral lattice site (B) of the spinel lattice. Neel has explained the magnetic behavior of these spinels based on the exchange interaction that occurs between metal ions at A & B sites spinel. Fig. 7a and Fig. 7b show tetrahedral A sites and octahedral B sites, respectively. [15-18]. It was expected that a fraction of La ion enters into octahedral sites and creates distortions as well as a decrease in lattice constant. This is in agreement with the findings in this work (Table1). Thus, the observable decreases in coercivity (Hc) and saturation magnetization (Ms) may be attributed to the larger lattice distortion and smaller crystalline size. The values of saturation magnetization (Ms), coercivity (Hc) and retentivity (Mr) for all three samples are tabulated in (Table 2).

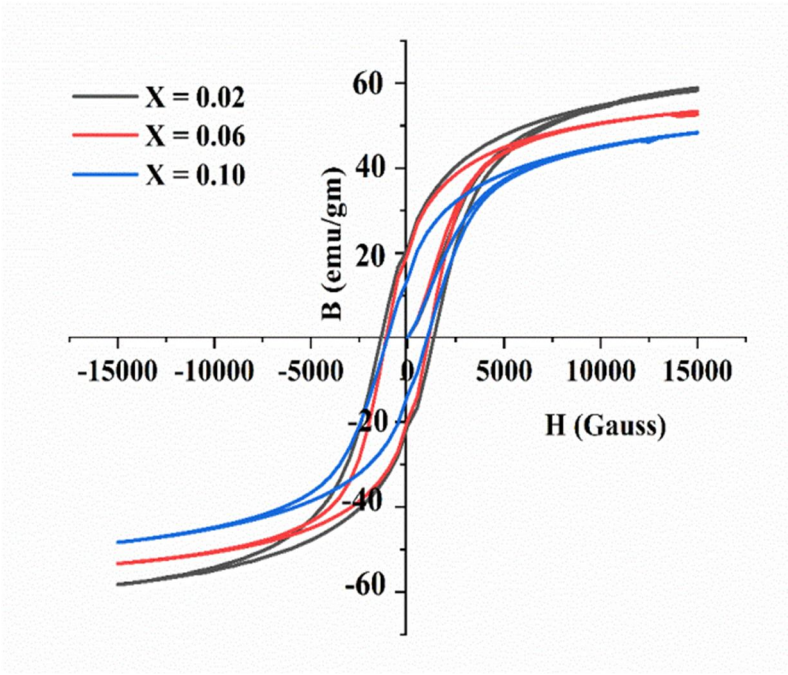

FIG. 6. Hysteresis loop for $Ni_{0.2}Co_{0.8}Fe_{2-x}La_xO_4$.

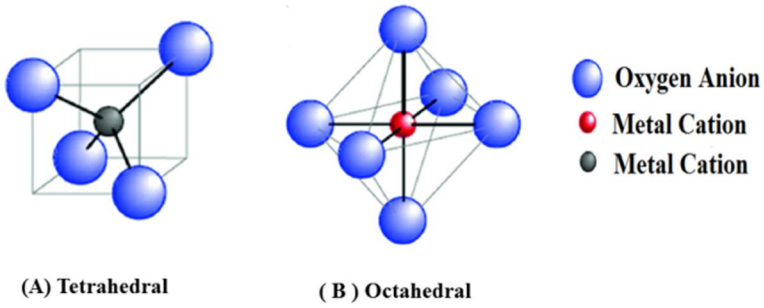

FIG. 7. (a) Tetrahedral (A) sites and (b) Octahedral (B) sites.

TABLE 2. Values of coercivity (H_C), retentivity (Mr) and saturation magnetization (Ms) for $Ni_{0.2}Co_{0.8}Fe_{2-x}La_xO_4$.

Composition (X)	H_C (G)	Mr (emu/gm)	Ms (emu/gm)
X = 0.02	1366.2	20.92	58.58
X = 0.06	1105.0	19.67	53.34
X = 0.10	1031.6	13.75	48.36

Conclusion

In this work, a series of $Ni_{0.2}Co_{0.8}Fe_{2-x}La_xO_4$ (X = 0.02, 0.06 and 0.10) powders and sintered samples were successively prepared by sol-gel auto combustion method using oxide as precursor and urea as fuel. The structural properties were investigated by XRD. XRD confirmed the formation of the FCC spinel phase for all the samples. The EDX spectrum shows that no additional impurity is present in the sample. It also shows that the lattice constant 'a' decreases with the increase in La concentration. The particle size calculated from X-ray diffraction is approximately constant. The SAED image also confirms the formation of a poly-nanocrystalline sample. Further, La-substituted $NiCoFe_2O_4$ ferrite shows a definite hysteresis loop at room temperature. The presence of non-magnetic La in $NiC_OFe_2O_4$ ferrite results in a reduction of coercivity (Hc), saturation magnetization (Ms) and retentivity (Mr), which could be due to dilution in the magnetic interaction.

References

[1] Chen, Q. and Zhang, Z.J., Appl. Phys. Lett., 73 (1998) 3156.

[2] Zhao, L., Yang, H., Yu, L., Cui, Y., Zhao, X. and Feng, S.J., Mater. Sci., 42 (2007) 686.

[3] Kumar, E.R., Kamzin, A.S. and Janani, K.J., J. Magn. Magn. Mater., 417 (2016) 122.

[4] Kumar, E.R., Jayaprakash, R. and Patel, R., Superlattices and Microstructures, 62 (2013) 277.

[5] Das Calu, G., Popescu, T., Feder, M. and Caltun, O.F., J. Magn. Magn. Mater., 333 (2013) 69.

[6] Shah, M.S., Ali, K., Ali, I., Mahmood, A., Ramay, S.M. and Farid, M.T., Mater. Res. Bull., 98 (2018) 77.

[7] Junaid, M., Khan, M.A., Iqbal, F., Murtaza, G., Akhtar, M.N., Ahmad, M., Shakir, I. and Warsi, M.F., J. Magn. Magn. Mater., 419 (2016) 338.

[8] Boda, N., Boda, G., Naidu, K.C.B., Srinivas, M., Batoo, K.M., Ravinder, D. and Reddy, A.P., J. Magn. Magn. Mater., 473 (2019) 228.

[9] Kokare, M.K., Jadhav, N.A., Singh, V. and Rathod, S.M., Opt. Laser Technol., 112 (2019) 107.

[10] Kumar, P., Sharma, S.K., Knobel, M., Chand, J. and Singh, M., J. Electroceram., 27 (2011) 51.

[11] Mansour, S.F., Hemeda, O.M., El-Dek, S.I. and Salem, B.I., J. Magn. Magn. Mater., 420 (2016) 7.

[12] Vadivel, M, Ramesh Babu, R., Arivanandhan, M. and Ramamurthi, K., Journal of Superconductivity and Novel Magnetism, 30 (2017) 441.

[13] Yadav, R.S., Kuritka, I., Vilcakova, J., Havlica, J., Kalina, L., Urbánek, P., Machovsky, M., Masar, M. and Holek, M., Journal of Materials Science: Materials in Electronics, 28 (2017) 9139.

[14] Kumar, L. and Kar, M., Ceram. Inter., 38 (2012) 4771.

[15] Karimi, Z., Mohammadifar,Y., Shokrollahi, H., Asl, S.K., Yousefi, G. and Karimi, L., J. Magn. Magn. Mater., 361 (2014) 150.

[16] Ghone, D.M., Mathe, V.L., Patankar, K.K. and Kaushik, S.D., J. Alloys Compd., 739 (2018) 52.

[17] Wu, X., Ding, Z., Song, N., Li, L. and Wang, W., Ceram. Int., 42 (2016) 4246.

[18] Neel, L., Ann. Phy., 3 (1948) 137.

Volume 15, Number 1, 2022. pp. 29-36

Jordan Journal of Physics

ARTICLE

Structural and Electrical Studies of Aluminium-doped Nickel-Cobalt Ferrite Nanoparticles

S. P. Waghmare[a], D. M. Borikar[a], M. A. Borikar[b] and K. G. Rewatkar[c]

[a] *Department of Chemistry, Dr. Ambedkar College, Deekshabhoomi, Nagpur, India.*
[b] *Department of Chemistry, St. Vincent Palloti College of Engg.& Tech., Nagpur, India.*
[c] *Department of Physics, Dr. Ambedkar College, Deekshabhoomi, Nagpur, India.*

Doi: **https://doi.org/10.47011/15.1.4**

Received on: 01/08/2020; *Accepted on: 29/6/2021*

Abstract: Aluminium-doped Nickel-Cobalt ferrite nanoparticles with general formula $Ni_{0.5}Co_{0.5}Al_xFe_{2-x}O_4$ (x = 0 and x = 0.5) were synthesized by microwave-assisted sol-gel auto-combustion method. The X-ray diffraction analysis of the samples confirms single phase with cubic spinel structure belonging to space group Fd3m. The average crystallite size calculated using Debey-Scherrer formula was found to be in the range of 19-36 nm. XRD studies revealed that the lattice parameter (a), the particle size (D) and X-ray density (d_x) decrease, whereas porosity increases with Al substitution. Energy Dispersive X-ray (EDX) was used to confirm the elemental composition of synthesized powders. TEM micrograph suggests that the particle size is in nanometric range, which confirms the nanocrystalline nature of the samples. The electrical resistivity and dielectric constant have been studied as functions of temperature. It was observed that the electrical resistivity decreases with increasing temperature, exhibiting the semiconducting nature of the sample. The dielectric constant increases with increase in temperature up to transition temperature and then decreases, which is explained on the basis of hopping mechanism.
Keywords: Ni-Co ferrites, Sol-Gel, XRD, Resistivity, Dielectric constant.

Introduction

Nanostructured spinel ferrites play an important role in the technological applications because of their interesting chemical stability, electric and dielectric properties [1]. Recent research reports that mixed nanoferrites usually have better performance than conventional nanoferrites and nanospinel ferrite nickel-cobalt ferrites are of technical importance due to their unique electrical and dielectric properties. They have been used for numerous applications, including microwave devices, gas sensors, magnetic fluids, recording media, ferro-fluids, high-density information storage and catalysis [2]. The general chemical formula of spinel ferrites is MFe_2O_4, where M is the divalent metal cation. The spinel ferrite structure consists of close-packed oxygen arrangement in which tetrahedral (A) sites and octahedral (B) sites are occupied by the cation [3]. This structure allows incorporation of different metallic ions without altering the basic crystal structure of spinel ferrites [4]. Substitution of non-magnetic ions in spinel ferrites was found to alter their electric and magnetic properties [5]. Al^{3+}- substituted nickel-cobalt ferrite shows high stability and high electrical resistivity [6]. Such materials can be used in data-storage devices [7]. To our best knowledge, structural and electrical properties of aluminium-substituted nickel-cobalt ferrite were not documented yet. By keeping this fact into consideration, we have chosen Al-substituted nickel-cobalt ferrite to study these properties.

Corresponding Author: D. M. Borikar **Email**: drdmborikar@gmail.com

Many methods have been reported for the synthesis of spinel nanoferrites. Among the several methods, microwave-assisted Sol-Gel auto-combustion method is primarily selected because of many advantages, such as rapid heating, shorter processing time, fast reaction, efficient energy transformation and volume heating, high purity, high yield, easy reproducibility, particle size and shape control, homogeneity and improved characteristics [8].

In the present work, we have reported the synthesis of nickel-cobalt ferrite with aluminium substitution using microwave-assisted sol-gel auto-combustion method and investigation of their structural, electrical and dielectric properties.

Experimental

Synthesis Technique

Nano-crystalline powders of $Ni_{0.5}Co_{0.5}Al_xFe_{2-x}O_4$ (x = 0 and x = 0.5) have been synthesized *via* microwave-assisted sol-gel auto-combustion method. The stoichiometric amounts of AR grade nickel nitrate $Ni(NO_3)_2.6H_2O$, cobalt nitrate $Co(NO_3)_2.6H_2O$, iron nitrate $Fe(NO_3)_2.9H_2O$ and aluminium nitrate $Al(NO_3)_2.9H_2O$ were used, while urea $Co(NH_2)_2$ was used as fuel. The mixture of metal nitrate and urea was dissolved in minimum quantity of distilled water. Condensation reaction occurs between the adjoining metal nitrates and urea, yielding a polymer network in colloidal dimensions known as 'sol'.

The beaker containing 'sol' is continuously stirred using a hot-plate magnetic stirrer and constantly maintained at temperatures of 70 ^{0}C - 80 ^{0}C in order to evaporate water in excess. The resulting viscous liquid foams ignite and undergoes a self-sustained combustion, producing 'gel' by slows drying process. Further, the wet gel is fired in a specially designed microwave oven, to get the resultant ash powder. The ashes of raw substances obtained were ground in a pestle and mortar for 4 hrs. Finally, these samples were annealed at 800 ^{0}C for several hours at a heating rate of 100 ^{0}C/hr so as to obtain single-phase nano-spinel ferrite.

X-ray Diffraction (XRD) Analysis

Structural analysis and phase identification of the synthesized samples were carried out by Philips X-ray diffractometer (Model 3710) using CuKα radiation of wavelength λ = 1.54 Å at room temperature. In this present research study, the expected sample structure is of spinel ferrite having cubic crystal lattice and therefore, the unit cell is characterized by the value of lattice parameter 'a', which is calculated from the equation:

$$a = [d^2 (h^2 + k^2 + l^2)]^{½} \quad (1)$$

where, *d* is the value of *d*-spacing of line in XRD pattern and *h, k, l* are the corresponding indices to each line in the XRD pattern.

The X-ray density (d_x) and bulk density (d_b) were also determined using the following formulae:

$$d_x = \frac{Z\,M}{N_A\,V} \quad (2)$$

$$d_b = \frac{m}{\pi\, r^2 h} \quad (3)$$

where, M is the molecular mass of the sample, Z is the number of formula units in a unit cell which is 8 for spinel ferrite, N_A is the Avogadro's number,V is the unit cell volume, m is the mass of the pellets, r is the radius of the pellets, *h* is the thickness of the pellet.

By comparing the X-ray density with bulk density, the % porosity (P) of the materials was calculated by using the equation:

$$P = 1 - \frac{d_x}{d_b} \times 100. \quad (4)$$

The average crystalline size of the samples was determined from the most intense peak (311) in the X-ray patterns using Debye-Sherrer's formula [9]:

$$D = \frac{K\lambda}{\beta\, Cos\theta} \quad (5)$$

where, λ is the wavelength of X rays which is equal to 1.54 Å, *K* is the shape factor which is equal to ~ 0.9 for nano-spinel ferrites, β is the line broadening at the full width at half maximum (FWHM) intensity in radians.

Energy Dispersion X-ray (EDX) Spectroscopy

Elemental analysis has been conducted and chemical characterization of synthesized samples has been determined using energy dispersive X-ray spectroscopy EDX which was carried out by SEM-JSM-7600F operating at an accelerating voltage of 0.1 to 30 kV.

Transmission Electron Microscopy (TEM) Analysis

TEM analysis was carried out by the instrument of make PHILIPS, Model CM200, having an operating voltage of 20-200 kV and a resolution of 2.4 Å for nickel-cobalt ferrite nanoparticles.

Electric and Dielectric Measurements

For studying the electrical resistivity and dielectric constant of the samples, the samples were made in pellet form with a thin layer of silver pasted on both the flat faces to provide a better electrical contact and by applying a D.C. voltage across the pellet in four-probe Precision Impedance Analyzer 6500B Wayn Kerr at the frequency of 100 Hz. The measurements of electric resistivity (ρ) were carried out over the temperature range 250K-500K. The variation of dielectric constant (ε′) was measured from 300K-800K.

Results and Discussion

XRD Analysis

The X-ray diffraction patterns of $Ni_{0.5}Co_{0.5}Al_xFe_{2-x}O_4$ (x = 0 and x = 0.5) are shown in Fig.1. The XRD patterns were analyzed using X- Powder software and the crystalline phases were identified by comparison with reference data from the JCPDS card No.89-4927 for nickel ferrite and 22-1086 for cobalt ferrite. XRD pattern revealed the formation of single phased cubic spinel structure belonging to space group Fd3m. Bragg's reflections were indexed which confirmed the formation of a well-defined single phase cubic structure without any trace of impurity. The diffraction peaks can be indexed for the Miller Indices (111), (220), (311), (400), (422), (511) and (440), which are all allowed peaks.

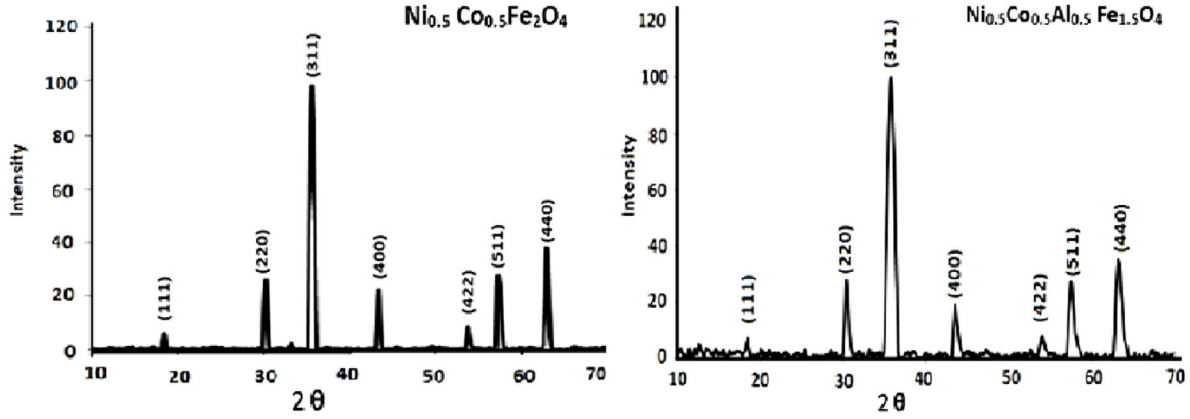

FIG. 1. X- ray diffraction pattern of $Ni_{0.5}Co_{0.5}Al_xFe_{2-x}O_4$ (x = 0 and x = 0.5).

The particle size of the synthesized ferrite samples has been calculated from the most intense peak corresponding to (311) using the classical Debey-Scherrer formula. The values of lattice constant, X-ray density, bulk density, porosity and particle size were deduced from the X-ray data and are given in Table1. It is found that doping of Al^{3+} in the nickel-cobalt nanoferrite results in the decrease of lattice constant, which obeys the Vegard's law [10].

This decrease in lattice constant causes the XRD peaks to be shifted to the higher 2θ values, which can be clearly seen in Table1.The shifting of peaks towards higher angles and the decrease of lattice parameter 'a' show that Al atoms have been incorporated into the spinel structure of nickel-cobalt ferrite [11] .

The peak intensities of (220) and (440) signals are more responsive to the cations in tetrahedral and octahedral sites, respectively [12, 13]. From Table 1, it is clearly seen that the intensity of (440) decreases with the addition of Al^{3+} ions, whereas the increase in intensity of (220) is due to migration of Fe^{3+} ions from octahedral site to tetrahedral site as Fe^{3+} ions are replaced by Al^{3+} ions [14]. This decreasing behavior of lattice constant is explained on the basis of difference in the ionic radii of Al^{3+} and Fe^{3+}. In the present study, larger Fe^{3+} ions having an ionic radius of 0.67 Å are replaced by smaller Al^{3+} ions having an ionic radius of 0.51 Å. Therefore, a decrease in lattice constant is observed which causes the shrinking of unit cell dimensions. Similar behavior of lattice constant was reported by A. Amirabadizadeh*et al.*[15].

TABLE 1. X-ray diffraction parameters for the samples of $Ni_{0.5}Co_{0.5}Al_xFe_{2-x}O_4$ (x = 0 and x = 0.5).

Sr. No.	Al content (x)	a (Å) ± 0.002	2θ (311) ± 0.01	I (220)	I (440)	dx (gm/cm^3)	d_b(gm/cm^3)	P (%)	D (nm)
1	x = 0	8.352	35.64	26.7	22.0	5.347	2.4870	52.92	36
2	x = 0.5	8.311	35.81	27.9	18.8	5.147	2.3591	53.23	20

The X-ray densities and bulk densities are found to decrease with the addition of dopant Al^{3+}. This is due to replacement of heavier Fe^{3+} (55.85 amu) atoms by lighter Al^{3+} (26.98 amu) atoms [16]. From Table 1, it is also observed that x-ray densities of both samples are greater than the corresponding bulk densities due to the presence of pores in the synthesized sample [17].

The values of porosity of the synthesized sample are calculated using x-ray densities and bulk densities. From Table 1, it is observed that porosity of the samples increases with addition of aluminium. This may be due to the decrease in density with aluminium substitution and evolution of gases like N_2, H_2O and CO_2 during the combustion process favoring increased porosity. It has been found from Table 1 that the crystallite sizes are in the nanometer range of 19-36 nm and show a decrease with addition of aluminium. This observation resembles the reported results [15].

Energy Dispersion X-ray (EDX) Analysis

The EDX spectra of nickel-cobalt and aluminium-substituted nickel-cobalt ferrites are shown in Fig. 2. The weight percentage and atom percentage of different elements present in the samples are given in Table 2.

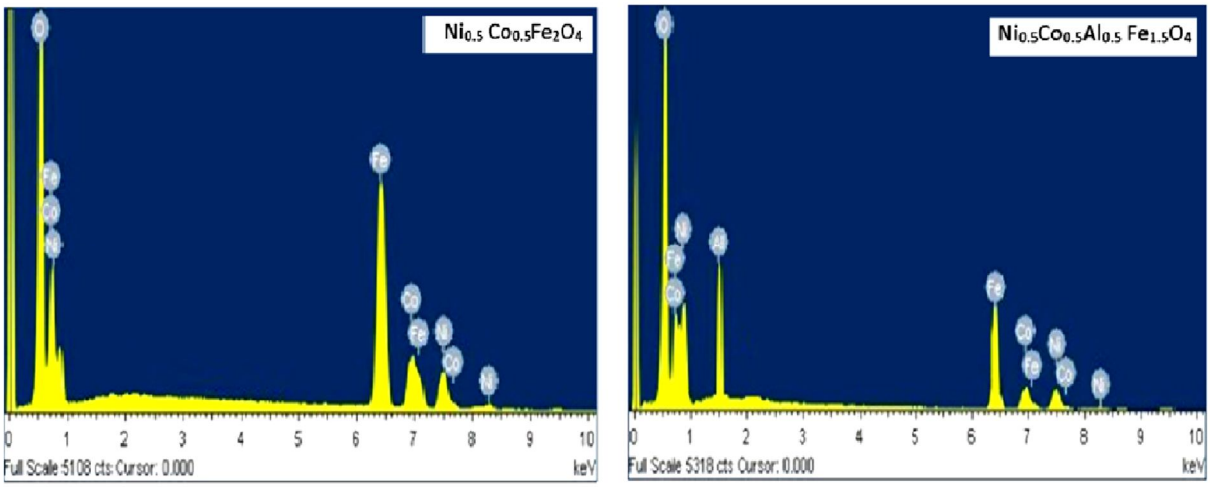

FIG. 2. EDX spectra of $Ni_{0.5}Co_{0.5}Al_xFe_{2-x}O_4$ (x = 0 and x = 0.5).

TABLE 2. Elemental composition of $Ni_{0.5}Co_{0.5}Al_xFe_{2-x}O_4$ (x = 0 and x = 0.5).

Sr. No.	Al content(x)	Elements	Weight%	Atom%
1	x = 0	Ni	12.51	7.14
		Co	12.57	7.14
		Fe	47.63	28.55
		O	27.29	57.14
		Total	100.00	99.97
2	x = 0.5	Ni	13.34	7.14
		Co	13.39	7.14
		Al	6.13	7.14
		Fe	38.06	21.44
		O	29.08	57.15
		Total	100.00	100.01

From EDX plots and values given in Table 2, it is clear that there is no trace of impurity and no loss of any ingredient was found in the compounds. The characteristics peaks of Ni, Co, Fe, O and Al elements were observed in EDX spectra confirming the presence of all constituting elements in the prepared nano-spinel ferrite. EDX study also suggests that all the precursors have undergone a complete reaction to produce the nickel-cobalt and aluminium substituted nickel-cobalt spinel nanoferrites [18].

Transmission Electron Microscopy (TEM) Analysis

TEM was employed to confirm the details about the shape and size, microstructure, morphology and nanocrystalline nature of alumimium-substituted nickel-cobalt ferrite.

Fig. 3(a)shows the TEM micrograph of alumimium-substituted nickel-cobalt ferrite nanoparticles. It is clear from the figure that nanoparticles of synthesized alumimium-substituted nickel-cobalt ferrites are uniform in morphology and crystalline size with some clustering/agglomeration between the particles.

The average particle size observed from the TEM micrographs is found to be in good agreement with the size calculated from the XRD analysis, confirming the formation of single-phase cubic structure.

The crystalline structure and detailed morphology of aluminium-substituted nickel-cobalt ferrite were further investigated by TEM bright-field images with corresponding Selected Area Electron Diffraction (SAED) patterns. SAED patterns of these samples are shown in Fig 3(b), which indicates that SAED pattern consists of well-defined spotted concentric rings, indicating the polycrystalline nature of synthesized nanoferrites. Similar observations have been reported by M. Lakshmi *et al.*[3].

The average particle size observed from the TEM micrograph is found to be in the range equal to that estimated from the XRD analysis, suggesting the formation of single crystals.

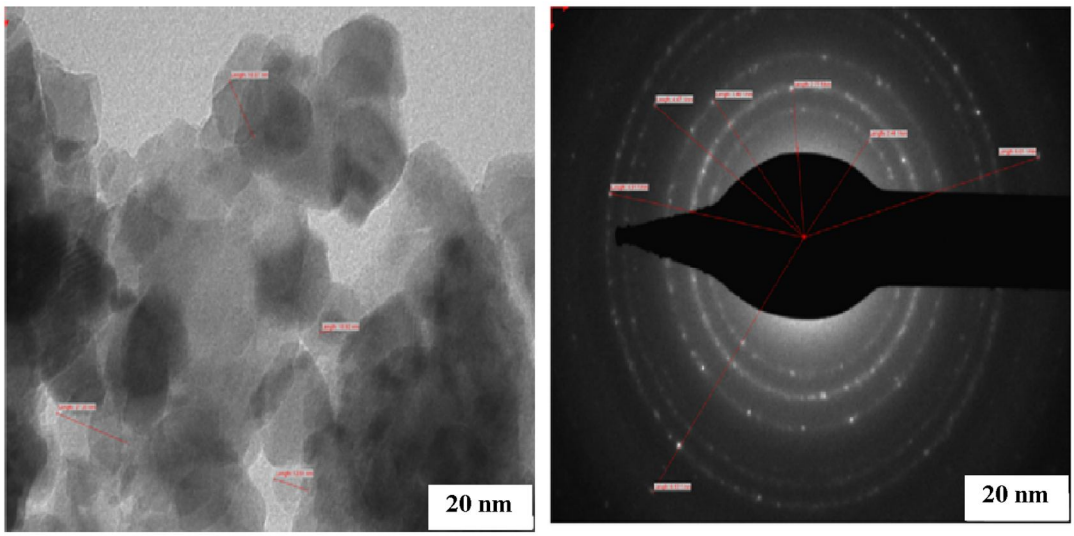

FIG. 3. (a) TEM image of $Ni_{0.5}Co_{0.5}Al_{0.5}$ $Fe_{1.5}O_4$.FIG. (b) SAED image of $Ni_{0.5}Co_{0.5}Al_{0.5}$ $Fe_{1.5}O_4$

Electric Resistivity

Fig. 4 shows the variation of electric resistivity with temperature for undoped and doped nickel-cobalt ferrites. From the figure, it is observed that electrical resistivity decreases exponentially with temperature, exhibiting semiconductor behavior. Similar behavior of electrical resistivity with temperature was reported by A. M. Bhavikatti*et al.* [19]. This decrease in electrical resistivity or increase in conductivity can be explained by Verwey's hopping mechanism.

According to Verwey [20], the conduction in ferrite is because of the exchange or hopping of electrons between ions of the same element with different valence states. In the present nickel-cobalt ferrites, conduction is due to simultaneous presence of ferrous (Fe^{2+}) and ferric (Fe^{3+}) ions on equivalent crystallographic sites usually the octahedral (B) sites and when electrons exchange from ferrous (Fe^{2+}) to ferric (Fe^{3+}) ions, conduction takes place. The extra electron which is present on a ferrous ion (Fe^{2+}) **r**equires very small energy for exchange to ferric (Fe^{3+})

ion. With increase in temperature, charge carriers gain thermal energy, resulting in the increase in hopping rate and hence these extra electrons can be considered to be responsible for the increase in conductivity or decrease in resistivity.

From Fig. 4, it is also clear that resistivity increases with the addition of dopant Al^{3+}. The addition of aluminium in nickel-cobalt ferrite replaces the equal number of Fe^{3+} ions from the octahedral B-sites. The decrease in number of Fe^{3+} ions in octahedral sites results in the decrease of Fe^{2+}/ Fe^{3+} pairs contributing to the conduction which hinders the electron hopping between Fe^{3+} and Fe^{2+} ions and consequently increases the resistivity with the addition of aluminium. Similar type of behavior in resistivity with Al^{3+} was reported by Le-Zhong Li [21]. As reported in the literature [22], resistivity of nanoparticles is dependent on the grain size and increases with decrease in grain size. Thus, in the present study, as the grain size decreases with addition of aluminium, the increase in resistivity is observed. Similar variation in electrical resistivity with Zn^{2+}doping in cobalt ferrite [5] and Al^{3+} in nickel ferrite is observed [23].

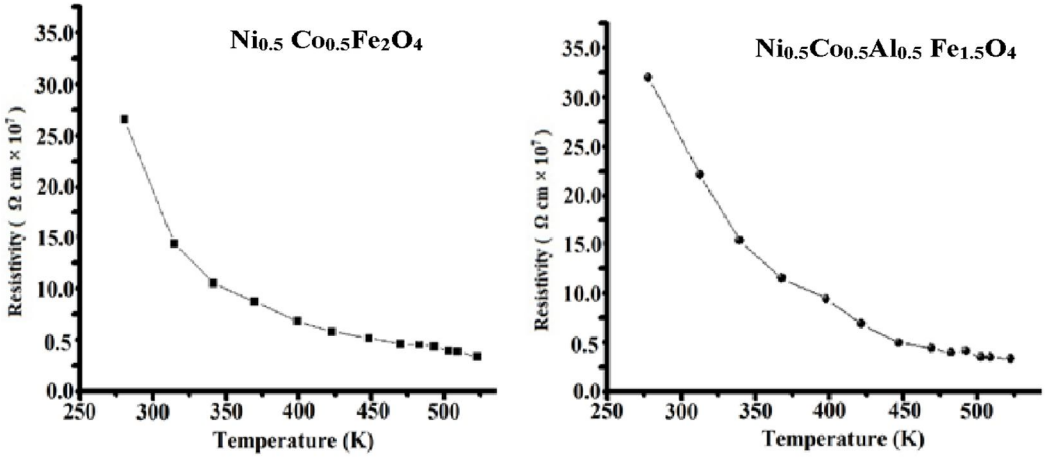

FIG. 4. Variation of electrical resistivity with temperature.

Dielectric Constant

Fig.5 shows the variation of dielectric constant with temperature at 100 Hz for undoped and doped nickel- cobalt ferrite. The figure shows that the dielectric constant increases steadily with increasing temperature up to the certain point of temperature, which is called the dielectric transition temperature (T_d). However, beyond this transition temperature, the dielectric constant is found to decrease. Similar variation of dielectric constant with temperature was observed by G. Sathish Kumar *et al*. [14] and G. R. Mohan *et al.* [24].

The variation of dielectric constant with temperature can be explained on the basis of hopping mechanism which is similar to that of mechanism of dielectric polarization. The electronic exchange between Fe^{2+} and Fe^{3+} in octahedral sites results in local displacements determining the polarization of charges in these ferrites.

With increase in temperature, charge carriers gain thermal energy and hopping of electrons is thermally activated, resulting in an increase in polarization and thus dielectric constant increases. But, with further increase in temperature beyond dielectric transition temperature, charge carriers are less oriented towards the direction of the applied field and thus decrease the dielectric constant as reported by G. Sathish Kumar *et al*. [14] and G. R. Mohan *et al*. [24].

It can be understood from Fig. 5 that the dielectric constant decreases with the addition of aluminium in nickel-cobalt ferrite. The addition of Al^{3+} replaces the Fe^{3} ions from the octahedral sites. Therefore, there will be a decrease in number of Fe^{3+} ions at B- site which plays a dominant role in dielectric polarization. Thus, electron exchange between Fe^{2+} and Fe^{3+} ions will be obstructed i.e., polarization will also decreased. As a result, dielectric constant decreases with addition of dopant aluminium. Similar behavior was observed by B. Vara Prasad for indium-substituted Ni–Zn ferrite system [25]. Similar type of behavior in dielectric constant with Zn^{2+} doping in cobalt

ferrite [5] and Al^{3+} doping in nickel ferrite was observed [23].

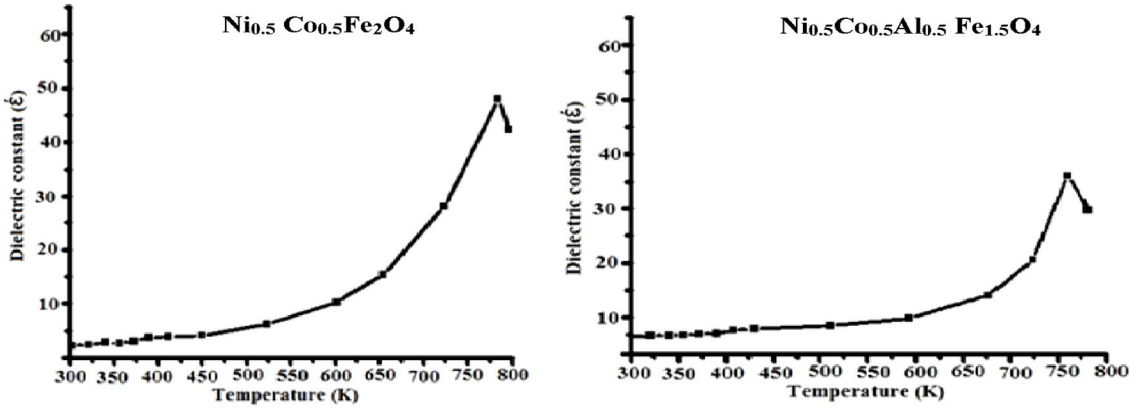

FIG. 5. Variation of dielectric constant with temperature.

Conclusion

$Ni_{0.5}Co_{0.5}Al_xFe_{2-x}O_4$ (x = 0 and x = 0.5) nanoparticles have been effectively and successfully synthesized by microwave-assisted sol-gel auto-combustion method. The XRD analysis confirms single-phase cubic spinel structure with space group Fd3m. Lattice parameter, particle size and X-ray density decrease, whereas porosity increases with Al substitution.EDX spectra confirmed the compositional formation of synthesized samples.

TEM confirmed the formation of nanocrystalline nature with single-phase spinel structure. Decreasing electrical resistivity with temperature shows semiconducting nature. The dielectric constant increases with temperature and afterword decreases, which is due to the fact that electronic exchange between Fe^{2+} and Fe^{3+} and does not follow the direction of the applied field.

Acknowledgment

The authors acknowledge the Department of Nanoscience and Nanotechnology and the Department of Physics, Dr. Ambedkar College, Deekshabhoomi, Nagpur, for providing facilities and support to carry out this work.

References

[1] Dabagh S., Ati A., Ghoshal S. K., Zare S., Roshan R. M., Jbara A. and Othaman Z., Bull. Mater. Sci., 39(2016) 1029.

[2] Patil R. P., Delekar S. D., Mane D. R. and Hankare P. P., Results in Physics, 3 (2013)129.

[3] Lakshmi M., Kumar K. V. and Thyagarajan K., Advances in Nanoparticles, 5 (2016)103.

[4] Khan S. B., Irfan S. and Long Lee S., Nanomaterials, 9 (1024) (2019) 1.

[5] Bayoumi W., J. Mater. Sci., 42 (2007)8254.

[6] Kumar K. V., Paramesh D. and Reddy P. V., World Journal of Nano Science and Engineering, 5 (2015)68.

[7] Singh H. S., Sangwa N. and Chauhan R., International Journal of Scientific and Engineering Research, 6 (12)(2015)765.

[8] Venkattesha M., Kumara G. S., Vijia S., Karthib S. and Girijab E. K., Modern Electronic Materials, 2 (2016)74.

[9] Cullity B. D., "Elements of X-ray Diffraction", 2rd edition, (Addsion-Wesley Publishing Company, 1978).

[10] Denton A. R. and Ashcroft N.W., Vedard's Law, Physics Review, A 43 (1991)3161.

[11] Birajdar A. A., Shirsath S. E., Kadam R. H., Mane M. L. and Shitre A. R., Journal of Applied Physics, 112 (2012)053908.

[12] Ladgaonkar B. P. and Vaigainkar A. S., Materials Chemistry and Physics, 56 (3)(1998)280.

[13] Narasimhan C. S. and Swamy C. S., Physica Status Dolidi (a), 59 (1998)817.

[14] Sathish Kumar G., Venkataraju C. and Sivakumar K., Materials Sciences and Applications, 1(2010) 19.

[15] Amirabadizadeh A. and Amirabadi T., World Journaul of Condensed Matter Physics, 3 (2013)131.

[16] Arvind G. and Aranind D., Int. Journal of Engineering Research and Applications, 3 (6)(2013)1414.

[17] Paramesh D., Kumar K. V. and Reddy P. V., Processing and Applications of Ceramics, 10 (3)(2016)161.

[18] Lakshmi M., Kumar K. V. and Thyagarajan K., Journal of Nanostructure Chemistry, 5 (2015)365.

[19] Bhavikatti A. M. and Mugli M., Proceedings of NCRIET-2015 & Indian Journal Science Research, 12 (1)(2015)232.

[20] Verwey E. J. W., Haayman P. W. and Romeijn C.W., J. Chem. Phys.,15 (1947)181.

[21] Li L.-Z., Zhong X.-X., Wang R., Tu X.-Q., He L., Guob, R. D. and Xu,Z.-Y., RSC Advances, 7 (2017)39198.

[22] Wang Y. Z., Qiao G. W., Liu X.D., Ding B. Z. and Hu, Z. Q., Mater. Lett., 17(1993)152.

[23] Waghmare S. P., Kakde A. S., Sisyawar A. C., Borikar D. M. and Rewatkar K. G., International Journal of Researchers in Bioscience, Agricultural & Technology, Special Issue (2) (2015) 2347.

[24] Mohan G. R., Ravinder D., Ramana Reddy A. V. and Boyanov B. S., Materials Letters, 40 (1999)39.

[25] Vara Prasad B. B.V. S., J. Theor. Appl. Phys., 9 (2015)267.

Volume 15, Number 1, 2022. pp. 37-42

Jordan Journal of Physics

ARTICLE

Optical, P-XRD & U-V Properties by Varying the Concentration of L-valine Amino Acid in Pure KDP

Nitesh D. Shambharkar[a] and **Vijay R. Raghorte**[b]

[a] *Assistant Professor, Department of Physics, Vidya Vikas Arts, Commerce and Science College, Samudrapur, Wardha-442305 Maharashtra, India.*

[b] *Assistant Professor, Department of Physics, Narayanrao Kale Smruti Model College, Karanja(Gh.),Wardha-442203,Maharashtra,India.*

Doi: **https://doi.org/10.47011/15.1.5**

Received on: 01/08/2020; *Accepted on: 27/1/2021*

Abstract: H_2PO_4 potassium dihydrogen phosphate crystals (KDP) were prepared for dopant L- valine amino acid. The bulk growth was reported along <011> and <101> plane by seed rotating crystal method and solution growth method. The doping concentrations in the mother solution were 0.4 mole%, 0.6 mole% and 0.8 mole% and the corresponding seed rotation rates were 30 rpm, 60 rpm and 100 rpm for 15 to 20 days. KDP crystal of dimensions 102 x 23 mm, 72 x 23 mm and 102 x 35 mm size has been grown. FTIR spectra showed the presence of functional groups in the crystal. Powder X-ray diffraction analysis of transparent bulk nonlinear optical crystal doped with LV confirms the formation of the tetragonal system. Energy Dispersive X-ray analysis (EDAX) confirms the elemental analysis of potassium and phosphate radicals in the reported crystal. Optical transmission increases with the increase of concentration of L-valine in KDP crystals.

Keywords: Crystal growth, Symmetry, FTIR, UV, EDAX.

1. Introduction

The non-linear property of a single crystal is very useful for optoelectronics, acousto-optics, laser, telecommunication technologies, medical instrumentation, … etc. KDP single crystal possesses important piezoelectric, ferroelectric, electro-optic and mainly NLO properties [1, 2]. NLO property of matter is essential for frequency conversion in laser devices. KDP is suitable for higher harmonic generation of a huge laser system of fusion experiments, because it can be grown to larger sizes and KDP has a high laser damage threshold. Some of the crystal-like KTP used in Nd: YAG laser by frequency doubling to get green light; lithium borate, potassium beryllium boro-fluoride, strontium beryllium borate, … etc. are promising for UV generation because of their wide bandgap and adequate optical nonlinearity. Many researchers have attempted to enhance the properties and growth rate of KDP crystal by varying the concentration of dopant or by changing the growth conditions [3-6]. The doping of organic impurities like amino acid improved the NLO properties of the KDP crystal [7].

In the present investigation, the kinetic mechanism of growth of prismatic faces of pure and doped KDP solutions was studied. The crystal morphology depends on the expansion rates of the various crystallographic faces. The study shows that the prismatic face (1 0 0) type is much more sensitive to some impurities than the (1 0 1) pyramidal faces [8].

Corresponding Author: Vijay R. Raghorte **Email**: vijayphy26@rediffmail.com

2. Methods

2.1 Solution Growth

A bulk-size transparent crystal which has high solubility and has variation in solubility with temperature when the material decomposes at the melting point and a suitable solvent are available to make a saturated solution at the desired temperature [9]. The basic concept of this method is to achieve a super-saturated solution first and then to have it crystallized. The low-temperature solution crystal growth method is extremely popular in the production of many technologically important crystals compared with high-temperature growth methods. It is the most widely used method for the growth of single crystals having solubility up to 1000C. This method is a long lived method. Most electro-optic and ferroelectric single crystals have been produced by solution growth technique [10-12].

2.2 Seed Rotating Crystal Method

In this method, seeds shown in Fig. 1a of solution method of pure KDP are used for harvesting bulk crystal by the rotating method. The mother solution was prepared under saturation condition and thoroughly stirred for 5 to 6 hours for homogenization at 40°C. The c-axis direction <101> plane of the seed crystal was selected for this method to grow a crystal. Firstly, processed seed is placed on a cylindrical platform (Fig. 1b) which was made by using an acrylic sheet. The cylindrical platform was attached with a rotating unidirectional DC motor, which was controlled by an electronic dc power supply of 12 V at about 30 rpm. The whole assembly was placed on a rectangular constant temperature bath (Fig. 2) which was made by a glass plate. In this method, seed crystal mounted on a cylindrical platform is allowed to rotate in the forward direction in an estimated time interval. The complete assembly is placed inside the crystallizer. Constant temperature bath controller is maintaining the temperature at 40°C with an accuracy of 0.01°C. The solution is prepared according to the solubility curve at a particular temperature. The amount of solute is calculated according to the solubility curves at different temperatures. The temperature of the crystallizer was reduced by 1°C per day to maintain the supersaturation level. This process increased the growth rates of the seed crystal. Good-quality transparent and bulk size of KDP crystal is harvested within two weeks, as shown in Fig. 1c. The sizes of grown crystals are 102 x 23 mm, 72 x 23 mm and 102 x 35 mm.

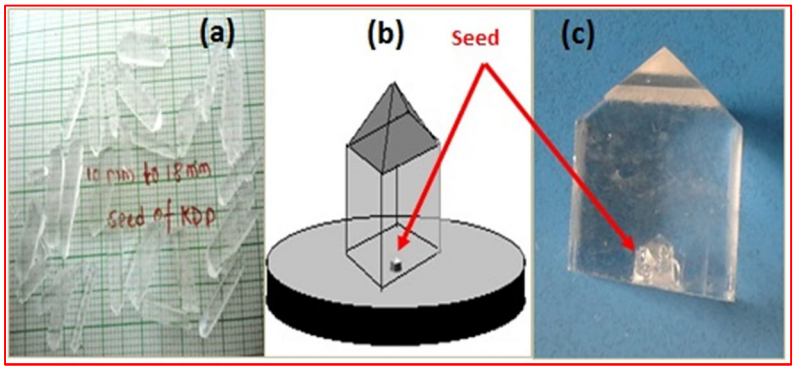

FIG. 1. (a) Seeds of pure KDP, (b) Schematic diagram of cylindrical platform and (c) Grown crystal.

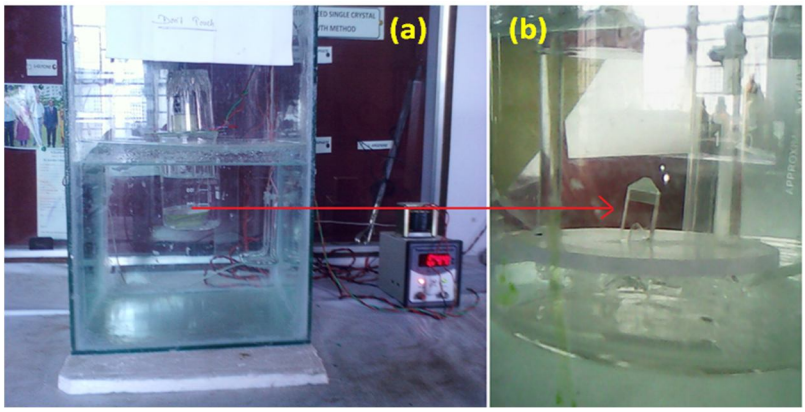

FIG. 2. (a) Constant temperature bath for seed rotating crystal method and (b) Grown crystal.

3. Results

3.1 Structural Analysis by XRD

Crystalline phase characterization of the powder samples is carried out by using a Bruker AXS D8 Advance (λ=1.5406 Å) Vertical, Theta/2 Theta geometry, X-ray diffractometer. The powder sample is scanned over the range 100-700 at a scan rate of 10/min. The XRD patterns of the single crystals are further refined by the Origin 8 SRO v8.0725 (B725) and CELREF Beta version (2000) software. The standard International Centre Diffraction Data (ICDD) and calculated ICSD diffraction file are used to match the evolving phases of the single crystals. The JCPDS card No. 35-0807 is used to compare the interplanar spacings and intensities of the powder pattern [13, 14]. The observed and calculated lattice parameters of pure and doped KDP are shown in Table 1. The single-crystal study reveals that the grown crystal belongs to the tetragonal system with space group I42d, where the number of molecules per unit cell is 4 [15]. The recorded Powder X-ray diffraction patterns of doped KDP crystals for different concentrations of L-valine dopant as 0.4 mole %, 0.6 mole % and 8.0 mole % are shown in Fig. 3.

TABLE 1. Observed and calculated lattice parameters of pure and doped KDP.

Sr. No.	Compound	Observed lattice parameters	Lattice parameters by using CELREF Beta Version	Lattice parameters by using X-powder
1	Pure KDP	a =b=7.4077 Å, c=6.9389 Å, Cell volume=380.76 Å^3	a=b =7.3977 Å, c =6.8789 Å, Cell volume= 376.45 Å^3	a=b = 7.3963 Å, c = 6.8808 Å, Cell volume=376.418 Å^3
2	0.4 mole %+ KDP	a =b=7.4098 Å, c=6.9335 Å, Cell volume=380.68 Å^3	a=b =7.3998 Å, c =6.8335 Å, Cell volume=374.182 Å^3	a=b =7.4000 Å, c =6.8356. Cell volume=374.317 Å^3
3	0.6 mole %+ KDP	a =b=7.4280 Å, c=6.8738 Å, Cell volume=379.26 Å^3	a=b =7.428 Å, c =6.934 Å, Cell volume= 382.58 Å^3	a=b = 7.4221 Å, c = 6.9599 Å, Cell volume=383.408 Å^3
4	0.8 mole %+ KDP	a =b=7.4377 Å, c=6.8356 Å, Cell volume=378.14 Å^3	a=b =7.4377 Å, c =6.9612 Å, Cell volume=385.0893 Å^3	a=b =7.444 Å, c =6.9612 Å, Cell volume= 385.74 Å^3

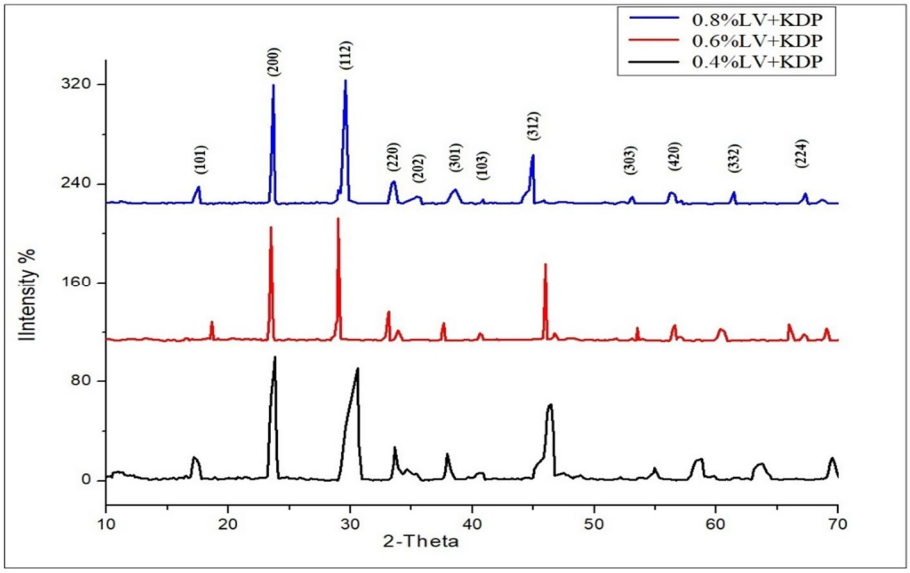

FIG. 3. Powder XRD pattern of L-valine-doped KDP crystals.

3.2 UV-Vis NIR Spectral Analysis

UV-Vis-NIR spectral transmittance was studied using a model Varian, Cary 5000 spectrophotometer with a single crystal of 5 mm thickness in the range of 200 – 1600 nm. Recorded spectrum (Fig. 4a) reveals that the percentage of optical transmission increases with the increase of concentration of L-valine in KDP

crystals about 90 % for the highest dopant concentration. The results of L-valine-doped KDP have good agreement with the results reported in [7]. The crystal has sufficient transmission within the entire visible and IR region. The lower stop wavelength is around 224 nm. The transmission spectra reveal that a higher concentration of amino acid additives has not destroyed the optical transparency of the crystals which have sufficient transmission in the entire UV- visible and IR regions [16]. Hence, it could be concluded that L-valine doping plays a vital role in improving the optical quality of KDP crystals [17-19].

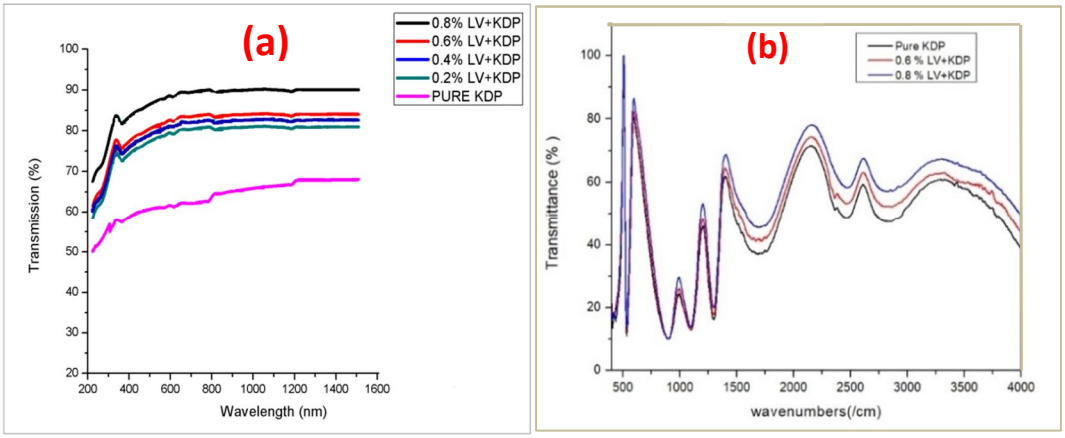

FIG. 4. (a) UV- spectra and (b) FTIR spectra of pure and doped KDP.

3.3 EDAX Analysis

Energy Dispersive X-ray analysis (EDAX) utilized in conjunction with all types of microscope has become an important tool for characterizing the weather present within the crystals. During this work, the grown crystal was subjected to EDAX analysis using the instrument JEOL Model JED - 2300 energy dispersive X-ray micro analyzer. The load percentage (wt %) of C, N, K, P and O as obtained from EDAX analysis shown in Table 2 is concurrent with the theoretical values [20-22].

TABLE 2. Weight percentage (wt %) of (a) 0.6 mole % LVKDP and (b) 0.8 mole % LVKDP.

Element	0.6 mole % LVKDP (a)				0.8 mole % LVKDP (b)			
	(keV)	Mass%	Atom%	K	(keV)	Mass%	Atom%	K
C K	0.277	5.37	12.1	2.9183	0.277	2.56	6.06	2.9183
O K	0.525	14.95	25.31	1.1103	0.525	14.5	25.81	1.1103
P K	2.013	40.81	35.68	1	2.013	40.4	37.14	1
K K	3.312	38.87	26.92	1.2645	3.312	42.54	30.98	1.2645
Total		100	100			100	100	

3.4 FTIR Spectral Analysis

The spectra were recorded in the infrared region of range 400- 4000 cm^{-1} using a Thermo Nicolet, Avatar 370 FTIR spectrometer by KBR beam splitter as shown in Fig. 4b. The vibration frequencies of functional groups of additives used in KDP crystal have been identified by FTIR spectroscopy. The values of bond length and bond angles were taken from Sutton's table (Internal coordinates for the out of plane torsional vibrations are defined as recommended by IUPAC). The spectrum confirms the interaction between KDP and organic amino acid by additional peaks corresponding to the functional groups of L-valine. There are high similarities between the spectra of pure and L-valine-doped KDP. It is found that the optical properties of pure and doped KDP changed due to the weak force of attraction of the bond between O-H and P=O. Also, low concentrations of dopant pure KDP peaks are predominant over valine peaks. Overall, the vibration spectra reveal the incorporation of impurities in the host crystals [21].

The band which appeared at 3672 cm^{-1} assigned to free O–H stretching is analogous with calculated wave number 3605 cm^{-1}, but this is absent in 0.6 and 0.8 mole % due to low concentration of dopant in pure KDP. The broad absorption bands that appeared at 3372 and 3472

cm^{-1} were assigned to hydrogen-bonded O–H stretching frequencies in 0.8 mole%-doped KDP. These peaks are absent in 0.6 mole%. This leads to a decrease in the frequency of O–H stretching and confirms the non-linear optical property of pure and doped KDP. This property is also reflected in the P=O, P–O, P– OH stretching and HO–P–OH bending vibrations shown in Table 3. The vibration assignments show that hydrogen bonding leads to stretching frequencies of the O-H group of KDP and therefore the carboxyl of L-valine molecules. This confirms the presence of L-valine in pure KDP crystal [7, 23].

TABLE 3. Assignment of vibrational wave numbers.

Sr. No.	Calculated frequencies (cm^{-1})	Pure KDP (cm^{-1})	0.6% LV+KDP (cm^{-1})	0.8% LV+KDP (cm^{-1})	Assignment
1	3605	--	--	--	Free O-H stretching; hydrogen bonding of KDP
2	3333	--	---	3472.45	O-H stretching; hydrogen bonding of KDP
4	2839	2844.65	2836.73	2824.74	P-O-H symmetric stretching
5	2461	2484.24	2464.90	2468.90	NH_3^+ bending superimposed with P–O–H stretching
6	2358		2362.94	2362.94	P-O-H bending of KDP
7		1718.49	--	--	C=O stretching
	1650		1681.25	1671.25	O=P-OH stretching of KDP
8	1295	1297.39	1301.42	1297.42	P=O stretching of KDP
9	1100	1095.92	1103.50	1097.51	P-O stretching of KDP
10	904	899.72	899.72	899.72	N-H wagging
11	535	534.66	533.76	537.76	Symmetric HO-P-OH bending
12	416	409.81	411.81	397.82	N-H torsional oscillation

3.5 Second-harmonic Generation Studies

Measurements of second-harmonic generation potency (SHG) were created by victimization of the Kurtz and Perry photography. The input ray of light was more experienced through IR reflector, so incident on the fine powder variety of the KDP specimen, that was packed in a glass tube. The resultant second-harmonic signal (532 nm) was detected once the ray of light was more matured essential amino acid-doped KDP specimen. The second-harmonic generation potency was measured with reference to KDP. From this measurement, we have a tendency to find that the relative SHG potency of essential amino acid-doped KDP slightly changes that of the standard dihydrogen phosphate. For the Nd :YAG optical device, the elemental beam of 1064 nm generates a second-harmonic signal of 532 nm. The output pulses were measured for 0.8 % and 2.0 % with relation to pure KDP (80 mV) and therefore, the results square measure is compiled in Table 4. It's determined that the essential amino acid-doped KDP crystal shows the property of SHG [23].

TABLE 4. SHG in valine-doped KDP.

Sr. No.	Sample	Second-harmonic signal output (mV)	Ratio with pure KDP
1	pure KDP	80 mV	1.00
2	0.8 mole % LV + KDP	80 mV	1.00
3	2.0 mole % LV + KDP	75 mV	0.93

4. Discussion and Conclusion

The calculated unit cell parameters of grown crystals are a = b = 7.428, c = 6.934 which are in good agreement with the results reported in the literature. Single-crystal study reveals that the grown crystal belongs to the tetragonal system with space group I42d. The number of molecules per unit cell is 4. Powder X-ray diffraction

analysis confirmed the crystalline nature of the KDP crystal. Optical absorption of KDP single crystal shows no absorption in the entire UV–visible region. The lower cut-off wavelength is around 224 nm. The transmission percentage of valine-doped KDP crystal is around 90 %. The transmission percentage of valine-doped KDP crystal for highest dopant concentration is higher. As the entire region does not bear any absorption band, it shows good transparency in the visible region. This means that the dopant increases the optical transmission of the crystal. The weight percentage (wt %) of C, N, K, P and O obtained from EDAX analysis is concurrent with the theoretical values. All elements are present in the sample and confirmed by their respective energy peak. The energy peaks were observed in the EDAX spectrum of elements as follows: Oxygen 0.525 keV, Phosphorous 2.013 keV, Potassium 3.312 keV and Carbon 0.277 keV. It was observed that 0.6 and 0.8 mole % of organic amino acid L-valine is incorporated into the crystal. The dopant L-valine is expected to substitute the potassium ions in the KDP lattice compared to pure KDP due to its valency as well as proximity of ionic radius. FT-IR spectra confirmed the presence of organic additive amino acid in potassium dihydrogen phosphate. From second-harmonic generation, the valine-doped KDP crystal shows the property of NLO.

5. References

[1] Prasad, P.N. and Williams, D.J., "Introduction to Nonlinear Optical Effects in Molecules and Polymers", (Wiley-Interscience, New York, 1991).

[2] Chemla, J.Z., "Nonlinear Optical Properties of Organic Molecules and Crystals", (Academic Press, New York, 1987).

[3] Hirota, S., Miki, H., Fukui, K. and Maed, K., J. Cryst. Growth, 235 (2002) 541.

[4] Zekic, A.A. and Mitrovic, M.M., J. Cryst. Growth, 258 (2003) 204.

[5] Sun, X., Xu, X., Gao, Z., Fu, Y., Wang, S., Zeng, H. and Li, Y., J. Cryst. Growth, 217 (2000) 404.

[6] Kumaresan, P., Moorthy Babu, B.S. and Anbarasan, P.M., Mater. Res. Bull., 43 (2008) 1716.

[7] Kumaresan, P., Moorthy Babu, B.S. and Anbarasan, P.M., Opt. Mater., 30 (2008) 1361.

[8] de Vries, S.A., Goedtkindt, P. et al., J. Cryst. Growth, 205 (1999) 202.

[9] Aggarwal, M.D., Batra, A.K. and Lal, R.B., http://ntrs.nasa.gov.

[10] Martin Britto Dhas, S.A. and Natarajan, S., Cryst. Res. Technol., 43 (8) (2008) 869.

[11] Raja, C.R., Gokila, G. and Joseph, A.A., Spectrochimica Acta-Part A, 72 (2009) 753.

[12] Baraniraj, T. and Philominathan, P., Spectrochimica Acta-Part A, 75 (2010) 74.

[13] Xu, D. and Xue, D., Physica B, 370 (2005) 84.

[14] Javidi, S., Faripour, H., Esmaeil Nia, M., Sepehri, K.F. and Ali Akbari, N., Semiconductor Physics, Quantum Electronics & Optoelectronics, 11 (3) (2008) 248.

[15] Rajesh, N.P., Kannan, V., Ashok, M., Sivaji, K., Raghavan, P.S. and Ramasamy, P., J. Cryst. Growth, 262 (2004) 561.

[16] Balamurugan, N. and Ramasamy, P., Cryst. Growth Design, 6 (2006) 1642.

[17] Balamurugan, S., Ramasamy, P., Sharma, S.K., Inkong, Y. and Manyum, P., Materials Chemistry and Physics, 117 (2009) 465.

[18] Bringley, J.F. and Rajeswaran, M., Acta Cryst. E, 62 (2006) m1304.

[19] Richardsonand, J.H., Peterson, R.V., "Systematic Materials Analysis", 2nd Edn., (Academic Press, New York, 1974).

[20] Kumaresan, P., Moorthy Babu, S. and Anbarasan, P.M., Opt. Adv. Mater. Rapid Communication, 1 (2007) 65.

[21] Suresh Kumar, B. and Rajendra Babu, K., I. J. Pure & Applied Physics, 46 (2008) 123.

[22] Balamurugan, S. and Ramasamy, P., Materials Chemistry and Physics, 112 (2008) 1.

[23] Kumaresan, P. and Moorthy Babu, S., Journal of Optoelectronics and Advanced Materials, 9 (5) (2007) 1299.

Volume 15, Number 1, 2022. pp. 43-48

Jordan Journal of Physics

ARTICLE

Study of Acoustic Behaviour of Thiamin Hydrochloride with Methanol at 303K

S. P. Dange[a] and **O. P. Chimankar**[b]

[a] *Department of Physics, Dada Ramchand Bakhru Sindhu Mahavidyalaya, Nagpur (Maharashtra), India.*

[b] *Acoustic Research Laboratory, Department of Physics, RTM Nagpur University, Nagpur (Maharashtra), India.*

Doi: **https://doi.org/10.47011/15.1.6**

Received on: 01/08/2020; *Accepted on: 2/11/2020*

Abstract: In the present study, ultrasonic velocity (u), density (ρ) and viscosity (η) have been measured at 2 MHz frequency in the binary mixtures of thiamin hydrochloride and methanol in the concentration range 0 to 0.1 molar concentration at 303K using ultrasonic interferometer technique. From the basic experimental data, various acoustic and thermodynamic parameters; namely, adiabatic compressibility, free length, free volume and internal pressure, were calculated, with a view to investigate the nature and strength of molecular interaction in the binary liquid mixture of thiamin hydrochloride and methanol. The obtained results support the occurrence of molecular interaction through hydrogen bonding in the binary liquid mixture.

Keywords: Ultrasonic velocity, Binary liquid mixture, Molecular interaction, Hydrogen bonding.

Introduction

The field of ultrasonic technique has grown enormously in scientific studies and has become a subject of active interest during the recent years [1]. Ultrasonic technique is most important and universally accepted to study the physical and chemical properties of solutions [2-6]. Ultrasonic velocity helps to provide qualitative information about the nature of molecular interactions in pure and binary liquid mixtures [7-9]. Literature study shows that a lot of work has been performed on pure and binary liquid mixtures [10-15].

Vitamins are in general biologically active compounds which are needed by cells and organs to sustain good health; so, they are essential dietary components [16-17].

Acoustical properties are important tool to study the behaviour of solute and solvent interaction. The study of acoustical behaviour in liquid mixtures was reported by various researchers. Thirumaran *et al.* [18] determined the acoustical properties of N, N-Dimethyl formamide, (DMF) acetophenone with 1-alkanols. Khan and Bhise [19] measured the acoustical studies of sucrose in aqueous and non-aqueous media. Vanathi, Mullainathan and Nithiyanantham [20] conducted an acoustical study on 1,4-dioxane with chloroform and cyclohexane. Shinde *et al.* [21] studied the acoustical properties of aqueous manganese chloride solutions. Wasnik [22] reported the acoustic properties of prochlorperazine melate drug in 20% DMF-water solution. In literature survey, it has been found that no effort has been made to investigate the acoustical behaviour of binary liquid solution of thiamin hydrochloride with methanol at 303K.

Corresponding Author: S. P. Dange **Email**: dange.sudhir30@gmail.com

In this communication, we reported the ultrasonic velocity, density and viscosity of binary liquid mixture of thiamin hydrochloride and methanol at a fixed temperature of 303K over 0.00 to 0.1 molar concentrations. From these experimental values of ultrasonic velocity, density and viscosity, a number of other thermodynamic parameters; namely, adiabatic compressibility, free length, free volume and internal pressure, have been calculated using standard equations. The variation of these parameters with molar concentration was found to be useful in understanding the nature of interactions between the components.

Experimental Methods

The chemicals thiamin hydrochloride and methanol used in the present study were products from E-Merck. These products were highest commercial and therefore, used without further purification. The binary mixtures of these chemicals were prepared immediately before use by mixing appropriate volume. Double distilled water was used in the preparation of experimental solutions. The solutions of each composition were prepared fresh and all the properties were measured at the same day. The ultrasonic velocities of liquid mixture of thiamin hydrochloride and methanol were measured using an ultrasonic interferometer (Model F-05, with digital micrometer) at a fixed frequency of 2 MHz. The measurements were made at different concentrations from 0 to 0.1 molar at a fixed temperature of 303K. The temperature of liquid mixture can be maintained constant at 303K with an accuracy of 0.1K using a digitally controlled water bath. The viscosity of the liquids was measured by an Ostwald viscometer. The viscometer was suspended in a thermostatic water bath. An electronic digital stopwatch with uncertainty of ±0.01 s was used for flow time measurements. At least three repetitions of each data reproducible to ±0.05 s were obtained and the results were averaged. The density of the pure components and their liquid mixtures was measured with a single-capillary pycnometer made up of borosil glass with a bulb of 8cm^3 and capillary with an internal diameter of 0.1 cm, chosen for the present work. The liquid mixtures were prepared by mass in an air-tight stopped bottle using an electronic balance accurate to ±0.1 mg. The accuracies of density and velocity data were ± 0.02% and ± 0.01%, respectively.

Theory

Adiabatic Compressibility

From the ultrasonic velocity (U) and density (ρ) of the medium, the adiabatic compressibility values of the solution were calculated as [23]:

$$\beta_a = \frac{1}{U^2 \rho} \ (\mathbf{Kg^{-1}.m.sec^2}) \quad (1)$$

where:

U: Ultrasonic velocity of the solution (m.Sec^{-1}) at fixed experimental temperature.

ρ: Density of the solution (kg.m^{-3}) at fixed experimental temperature.

Free Length

Jacobson [24] in 1951 established a semi-empirical relation to achieve the concept of intermolecular free length in order to explain the ultrasonic velocity in liquids.

$$L_f = K(\beta_a)^{1/2} \ (\mathbf{m}) \quad (2)$$

where**:**

K is a temperature-dependent constant known as Jacobson's constant. K= 2.131×10^{-6}.

β_a is adiabatic compressibility.

Free Volume

The dimensional relation given by Suryanarayana and Kuppusamy [25] based on ultrasonic velocity (U) and viscosity (η) data is given below.

$$V_f = \left(\frac{M.U}{K\eta}\right)^{3/2} \ (\mathbf{m^3/mole}) \quad (3)$$

where**:**

U: Ultrasonic velocity of the solution (m.Sec^{-1}) at fixed experimental temperature.

η: Viscosity of the solution (Pa.Sec) at fixed experimental temperature.

K: Temperature-independent constant = 4.28 x 10^9.

M: Effective molecular weight of the mixture = $\Sigma(m_i x_i)$

where: m_i and x_i are the molecular weight and mole fraction of individual constituents, respectively.

Internal Pressure

On the basis of statistical thermodynamics, Suryanarayana [26] derived an expression for the

determination of internal pressure by the use of free volume concept as:

$$P_i = bRT \left(\frac{K_j \cdot \eta}{U}\right)^{1/2} \left(\frac{\rho^{2/3}}{M^{7/6}}\right) (\mathbf{N/m^2}) \quad (4)$$

where**:**

b: Cubic packing factor (assumed to be 2 for all liquids and solutions).

R: Universal gas constant.

T: Absolute temperature (in Kelvin).

K_j: Temperature-independent constant = 4.28 x 10^9.

η: Viscosity of the solution (Pa.Sec) at fixed experimental temperature.

U: Ultrasonic velocity of the solution (m.Sec^{-1}) at fixed experimental temperature.

ρ: Density of solution (kg.m^{-3}) at fixed experimental temperature.

M: Effective molecular weight of the mixture = $\Sigma(m_i x_i)$

where: m_i and x_i are the molecular weight and mole fraction of individual constituents, respectively.

Results and Discussion

With a view to understand the effects of concentration, nature of solvent and the structure of thiamin hydrochloride on structure forming and breaking tendency, various acoustical parameters, like adiabatic compressibility, free length, free volume and internal pressure, were determined using experimental data of ultrasonic velocity, density and viscosity of binary liquid solution of thiamin hydrochloride and methanol at 303 K using standard Eqs. 1 to 4. The ultrasonic velocity and related acoustical parameters at 303K are shown in Figs.1 to 5.

The measured experimental values of density (ρ),viscosity (η) and ultrasonic velocity (U) of pure solvent methanol are compared with the available literature data [27-30] at 303 K. These values are reported in Table 1 and a satisfactory agreement was found.

Fig. 1 shows the variation of ultrasonic velocity with increase in molar concentration of thiamin hydrochloride. Initially, the ultrasonic velocity of binary mixture of thiamin hydrochloride and methanol increases and attains a maximum value at a particular concentration of 0.02 M. This is due to the fact that as the density of solution increases, the number of particles in a given region increases leading to quick transfer of sound energy and disrupting the methanol structure with the addition of thiamin hydrochloride [31]. Methanol is monohydric alcohols having a hydroxyl group (OH), which may form hydrogen (O-H..O) bond with thiamin hydrochloride, thus association may be possible between thiamin hydrochloride and methanol molecules through hydrogen bonding. The increase of intermolecular hydrogen bonding between the molecules increases the ultrasonic velocity, which results in structure-making behavior of thiamin hydrochloride.

TABLE 1. Comparison of experimental measured density (ρ), viscosity (η) and ultrasonic velocity (U) values of methanol with literature data at 303 K.

Organic liquid (Solvent)	ρ (kg.m^{-3})		η (Pa.Sec)		U (m/Sec^2)	
	Present work	Literature work	Present work	Literature work	Present work	Literature work
Methanol	782.2	781.9[27] 781.8[30]	0.000512	0.000501[28] 0.000515[29]	1100	1087[27] 1103[28]

The ultrasonic velocity attains a maximum value at 0.02 molar concentration, because at this molar concentration, components' molecules show a strong hydrogen bond. Similar increasing trend of variation of ultrasonic velocity with increase in solute concentrations was reported by various co-workers; Chithralekha and Panneerselvam [1], Raju and Rakkappan [32], Magazu *et al.* [33], Rohman and Mahiuddin [34], Badarayani and Kumar [35]. The ultrasonic velocity further decreases up to 0.04 molar concentration, which indicates structure-breaking properties of interacting molecules. Similar decreasing trend was reported by Mehra and Malav [36], Kannapan, Thirumaran and Palani [37], Kannapan and Hemlata [38], Mistry and Bhandakkar [39]. Ultrasonic velocity again shows an increasing trend from 0.04 molar concentration, which indicates structure-making property of thiamin hydrochloride [40].

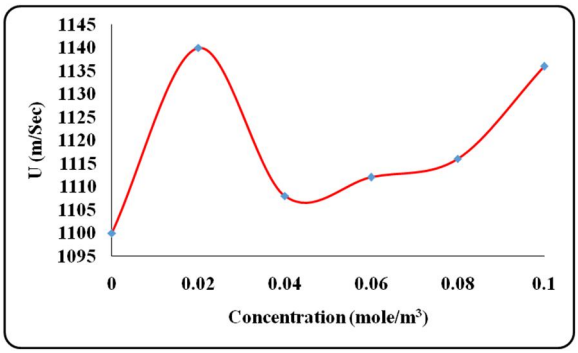

FIG. 1. Variation of ultrasonic velocity with concentration.

The variation of adiabatic compressibility with increase in molar concentration is shown in Fig. 2. The adiabatic compressibility initially decreases up to 0.02 molar concentration and then increases to 0.04 molar concentration. The decrease in adiabatic compressibility implies enhancement in molecular association by increase in thiamin hydrochloride content, as the new entities (formed due to molecular association) become compact and less compressible. It is also suggested that compressibility of the solution will be lesser than that of methanol. As a result, thiamin hydrochloride will have mobility and have more probability of contacting methanol molecules. This may enhance the interaction between thiamin hydrochloride and methanol molecules. Similar kinds of behaviour were observed by researchers at various solute concentrations [41-47]. The increases in adiabatic compressibility up to 0.04 mole concentration suggest molecular dissociation between the thiamin hydrochloride and methanol molecules [48]. Further decrease in adiabatic compressibility from 0.04 molar concentration might be due to aggregation of methanol molecules around thiamine hydrochloride molecules. Nithiyanantham and Palaniappan [49], Hemlata *et al.* [50] and Praharaj and Satapathy *et al.* [51] reported similar trends and observations. The inverse relationship that exists between ultrasonic velocity and adiabatic compressibility clearly indicates association between the thiamin hydrochloride and methanol molecules [52]. The calculated values of ultrasonic velocity and adiabatic compressibility are in good concordance with reported work [53].

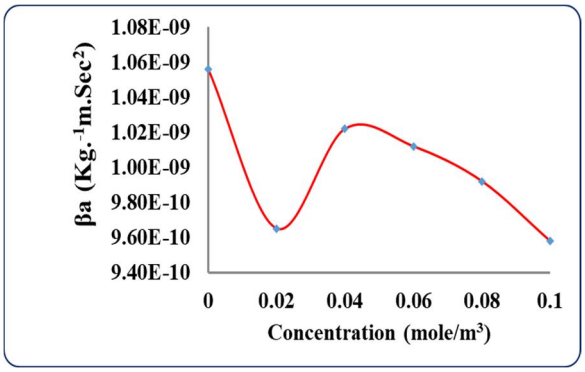

FIG. 2. Variation of adiabatic compressibility with concentration.

The intermolecular free length (L_f) gives the distance between the surfaces of the neighbouring molecules, which mainly affects the sound velocity [54]. The behaviour of free length is analogous to adiabatic compressibility, but inversely reflected by ultrasonic velocity [1]. It has been found that free length initially decreases up to 0.02 molar concentration and then increases to 0.04 molar concentration and again decreases from 0.04 molar concentration. The decrease in free length with increase in concentration of thiamin hydrochloride indicates that there is a significant interaction between thiamin hydrochloride and methanol molecules, suggesting a structure-promoting behaviour on addition of thiamin hydrochloride concentration. This structure-promoting behaviour considerably changed the structural arrangement of interacting molecules of thiamin hydrochloride and methanol. Asghar, Khan and Subramani [55], Thakre and Naik [56], Aswale, Dhote and Tayade [57] reported similar results. The increase in free length with increase in thiamin hydrochloride concentration brings the molecules to a loosely packing, resulting in weakening the molecular association between unlike molecules [48].

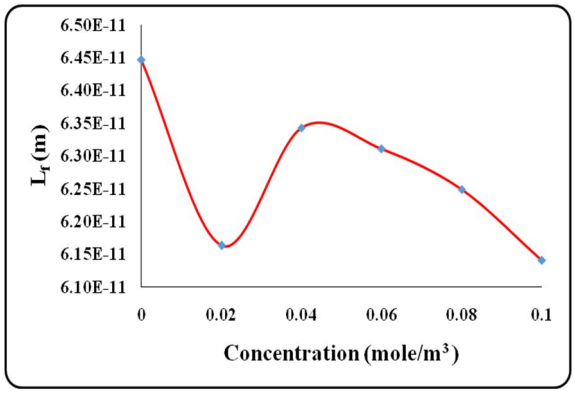

FIG. 3. Variation of free length with concentration.

Free volume gives the measure of cohesive or binding forces between the solute and solvent molecules [58] and internal pressure gives significant information about structural changes in the solution [36]. It has been observed that free volume and internal pressure show no variation up to 0.06 concentration with increase in molar concentration indicating that less amount of intermolecular forces exists during this concentration range. However, from 0.06 M concentration, free volume increases whereas internal pressure decreases. This is due to the fact that at these concentrations, molecules get disordered due to increasing entropy of the system which leads to decrease interactions between molecules of thiamine hydrochloride and methanol [59].

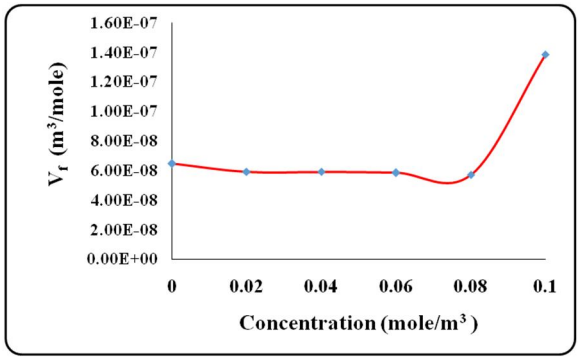

FIG. 4. Variation of free volume with concentration.

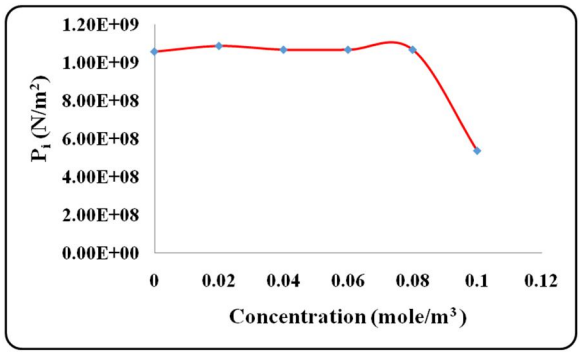

FIG. 5. Variation of internal pressure with concentration.

Conclusion

The results of the present investigation indicate a positive slope of ultrasonic velocity and a corresponding negative slope of adiabatic compressibility (or free length) and *vice versa* with increase in molar concentration of thiamin hydrochloride. The resulting positive slope of ultrasonic velocity is indicated by hydrophobic character, whereas the negative slope is indicated by hydrophilic character. These hydrophobic and hydrophilic characters promote the structure-making and structure-breaking tendency of thiamine hydrochloride due to formation of hydrogen bond between thiamin hydrochloride and methanol molecules.

References

[1] Chithralekha, N. and Panneerselvam, A., Asian J. of Chem., 31 (3) (2019) 674.

[2] Aswale, S.S., Aswale, S.R. and Ganjare, P.J., Asian J. of Chem, 24 (12) (2012) 5957.

[3] Pal, A. and Singh, Y.P., J. Chem. Eng. Data, 42 (1997) 689.

[4] Kumaran, M.K., Fluid Phase Equil., 182 (2001) 313.

[5] Yadava, S.S. and Yadava, A., Ultrason., 43 (2005) 732.

[6] Houkhani, H. and Rostami, Z., J. Chem. Eng. Data, 52 (2007) 921.

[7] Soitkar, V.S. and Jajoo, S.N., Acoust. Lett., 7 (12) (1984) 1991.

[8] Nithya, R., Nithiyanatham, S., Mullainathan, S. and Rajasekaran, M., E-Jou. of Chem., 6 (1) (2009) 138.

[9] Pavai, R.E. and Renuka, S., Int. J. Res. Pure & App. Phys., 1 (2) (2011) 6.

[10] Ali, A., Hyder, S. and Nain, A.K., Acoustics Letters, 21 (4) (1997)

[11] Ali, S.J., J. Chem. and Pharm. Res., 4 (1) (2012) 617.

[12] Babavali, S.K.F., Shakira, P., Rambabu, K., Narendra, K. and Srinivasu, Ch., Res. J. Phar., Bio. and Chem. Sci., 7 (2) (2016) 1344.

[13] Dange, S.P. and Chimankar, O.P., J. Emg. Tech. and Inn. Res., 7 (2) (2020) 555.

[14] Bedare, G.R., Bhandakkar, V.D. and Suryavanshi, B.M., J. of Chem. and Pharm. Research, 4 (2) (2012) 1028.

[15] Dash, U.N., Roy, G.S., Mohanty, S. and Ray, M., Ind. J. Pure Appl. Phys., 45 (2007) 151.

[16] Faizullah, A.T., Dikran, S.B. and Hassan, R.O., Tikrit J. Phar. Sci., 1 (1) (2015) 15.

[17] Ayranci, G., Sahin, M. and Ayranci, E., J. Chem. Thermodyn., 39 (2007) 1620.

[18] Thirumaran, S., Mathammal, R. and Thenmozhi, P., Chem. Sci. Trans., 1 (3) (2012) 674.

[19] Khan, J. and Bhise, M., IOSR J. Appl. Chem., 12 (1) (2019) 34.

[20] Vanathi, V., Mullainathan S. and Nithiyanantham, S., E. J. of Chem., 9 (1) (2012) 415.

[21] Shinde, B.R., Jadhav, S.S. *et al.*, J. Chem. Pharm. Res., 3 (3) (2011) 432.

[22] Wasnik, U., Int. Res. J. Sci. & Eng., A7 (2020) 59.

[23] Das, R., Prakash, K., Muthuri, D. and Hazra K., Acoustics Letter, 18 (1994) 69.

[24] Jacobson, B., Acta Chem. Scand., 5 (1951) 1214.

[25] Surayanarayana, C.V. and Kuppusami, J., J. Acoust. Soc. India, 4 (1976) 75.

[26] Suryanarayana, C.V., J. Acoust. Soc. India, **7** (1979) 131.

[27] Elangovan, S. and Mullainathan, S., Asian J. of Chem., 26 (1) (2014) 137.

[28] Palaniappan, L., Asian J. of Material Sci., 4 (1) (2012) 21.

[29] Bhandakkar, V.D. and Rode, S., Advances in App. Sci. Res., 3 (5) (2012) 3223.

[30] Bahadur, I., Deenadayalu, N. and Ramajugernath, D., Thermochimica Acta, 577 (2014) 87.

[31] Meshram, B., Agrawal, P. *et al.*, Int. J. Emer. Techno. in Comp. and Appl. Sci., 5 (4) (2013) 369.

[32] Raju, K. and Rakkappan, C., Asian J. of Chem., 23 (1) (2011) 19.

[33] Magazu, S., Migliardo, P., Musolino, A.M. and Sciortino, M.T., J. Phys. Chem. B, 101 (1997) 2348.

[34] Rohman, N. and Mahiuddin, S., J. Chem. Soc., Faraday Trans., 93 (1997) 2053.

[35] Badarayani, R. and Kumar, A., J. Chem. Thermodyn., 35 (2003) 897.

[36] Mehra, R. and Malav, B.B., Arabi. J. of Chem., 10 (2017) S1894.

[37] Kannapan, A.N., Thirumaran, S. and Palani, R., J. Phys. Soc., 20 (2) (2009) 97.

[38] Kannappan, V. and Hemalatha, G., Ind. J. Pure Appl. Phys., 43 (2005) 849.

[39] Mistry. A.A., Bhandakkar, V.D. and Chimankar, O.P., J. Chem. and Pharma. Res., 4 (1) (2012) 170.

[40] Tadalkar, A., Pawar, P. and Bichile, G.K., J. Chem. Pharm. Res., 3 (3) (2011) 165.

[41] Das, J., Dash, K., Swain, S.K. and Swain, N., J. Mol. Liquids, 81 (1999) 163.

[42] Kannappan, A.N. and Palani, R., Ind. J. Pure Appl. Phys., 45 (2007) 573.

[43] Kumar, D.S. and Rao, D.K., Ind. J. Pure Appl. Phys., 45 (2007) 210.

[44] Palani, R., Srinivasan, G. and Lakshmi, B.G., Int. J. Chem. Tech. Res., 3 (1) (2011) 284.

[45] Praharaj, M.K., Satapathy, A. and Mishra, S., J. Chem. Pharm. Res., 4 (4) (2012) 1910.

[46] Tirumaran, S. and Job Sabu, K., J. Appl. Sci., 11 (18) (2011) 3258.

[47] Punitha, S. and Uvarani, R., Heliyon, 5 (6) (2019) e01941.

[48] Shanmuga, P., Int. J. Adv. Sci. and Tech., 18 (2010) 59.

[49] Nithiyanantham, S. and Palaniappan, L., Rasayan J. of Chem., 2 (3) (2009) 709.

[50] Hemalatha, B., Vasantharani, P. and Senthilkumar, N., Inter. J. of Adv. Eng. & Tech., 6 (2) (2013) 795.

[51] Praharaj, M.K, Satapathy, A., Mishra, P.R. and Mishra, S., Archives of App. Sci. Res., 4 (2) (2012) 837.

[52] Pund, D.A., Tayade, D.T. and Naik, A.B., Procedia - Technology, 24 (2016) 677.

[53] Roy, M.N., Sinha, A. and Sinha, B., J. Solution Chem., 34 (11) (2005) 1311.

[54] Ubagaramary, D. and Neeraja, P., Int. Ref. J. Eng. and Sci., 1 (4) (2012) 54-77.

[55] Asghar, J., Khan, F.L.A. and Subramani, K., Rasayan J. of Chem., 3(4) (2010) 697.

[56] Thakre, A.R. and Naik, A.B., Chem. Xpress, 9 (6) (2016) 1.

[57] Aswale, S.R., Aswale, S.S., Dhote, A.B. and Tayade, D.T., J. Chem. Pharm. Res., 3 (6) (2011) 233.

[58] Fakruddin, S.K, Srinivasu, C.H. and Kolla, N., Int. J. of App. Sci. Eng. and Tech., 1 (1) (2012) 6.

[59] Godhani, D.R., Dobariya, P.B., Sanghani, A.M. and Mehta, J.P., Ara. J. of Chem., 10 (2017) S422.

Volume 15, Number 1, 2022. pp. 49-56

Jordan Journal of Physics

ARTICLE

Optical, Structural and Electrical Properties of CuS Thin Film on Dielectric Substrate by Spray Pyrolysis Technique

Avish K. Patil[a], Sachin H. Dhawankar[b], Nishant T. Tayade[c]

[a] *Department of Physics, DRB Sindhu Mahavidyalaya, Panchpaoli, Nagpur, Maharastra, India.*

[b] *Department of Physics, Shri JSPM Arts, Commerce and Science College, Dhanora - 442606, Gadchiroli, Maharashtra, India.*

[c] *Department of Physics, Institute of Science, (Formerly) Nagpur, Maharastra, India.*

Doi: **https://doi.org/10.47011/15.1.7**

Received on: 01/08/2020 *Accepted on: 17/01/2021*

Abstract: This paper deals with depositing a CuS thin film on a glass substrate at 380^0C by using spray pyrolysis method. Its optical properties and electric properties are characterized after cooling the sample. Formation for compound, structure and morphology were studied using x-ray diffraction. The optical study comprised the extraction and analysis of calculated optical constants, such as absorption coefficient (α), transmittance, extinction coefficient (k), which revealed the presence of a direct optical energy band gap of 2.0 eV. The temperature-dependent electrical resistivity with other necessary parameters was systematically studied for CuS film in the present work. Overall study confirmed the semiconducting behavior of the film which is useful for many applications, even when the film is touching the substrate at a micrometer scale with spray pyrolysis. This paper also explores the optical conductivity, dielectric constant, Urbach energy, morphology and thermal activation energy of the CuS film with explaining methodological details.

Keywords: Thin film, Spray pyrolysis technique, Electrical and optical properties, XRD.

Introduction

The CuS metal thin film belongs to I – VI compound semiconductor materials. It is used in several applications, such as microwave shielding, photo thermal, photo detector, photovoltaic and solar control coating applicationsas well as its uses as a wide-energy gap semiconductor and as an electro conductive electrode … etc [1-5]. Such metal thin films also have applications in diamond d films, magnetic films, superconducting films, microelectronic devices, surface modification, hard coating, photoconductors, IR detectors, optical imaging, optical mass memories and sensors [3-6]. Different types of methods are used for thin-film deposition, such as chemical bath deposition [4-6], spray pyrolysis [7], successive ionic layer absorption and reaction [1], electrode position [8], atomic layer deposition [9-10], sol gel [11-13] and solution growth [14-15].

The optical band gap energy (Eg) of Cu_XS thin films for 3D solar cell applications has been reported to be 2.41 to 3.1 eV with crystalline phase and found to be temperature-dependent [2]. The thin film exhibited polycrystalline structure when substrate temperature reached 320°C. Direct energy band gap has been reported to be 2.07 to 2.50eV in another work. Cu_xS thin films possess p-type semiconducting behavior [3]. Nascu studied at 150 to 220°C deposited, 0.01 to 0.05μm thickness films and found a 2.2 eV bandgap [16].Adelifard *et al*. reported 2.4 to 2.6eV for substrate temperatures 250, 285 and

Corresponding Authors: S. H. Dhawankar **Emails**: sachindhawankar@gmail.com
N. T Tayade nishanttayade@rediffmail.com

310°C [17]. Firat *et al.* also reported Eg of 2.07 eV for 320°C [18]. For the 380°C substrate temperature-deposited CuS thin film, it is expected to show some changes in structure and optical properties as evident from an overview of previous reports [2, 3, 19]. We observed in literature that the CuS film has not been optically characterized immediately after its synthesis and cooling to room temperature.

Therefore, we proposed to conduct this work to test the optical and electrical properties immediately after the cooling down (to room temperature) of CuS thin film deposited on a glass slide at 380°C substrate temperature. For that, the simple, fast growing, low-cost and convenient deposition spray pyrolysis technique was used.

Experimental Details

Synthesis of CuS Thin Film

The substrate of glass plate was cleaned before depositing the CuS thin film on it. A glass slide was taken as a substrate and it was cleaned with nitrate acid (conc.) for 3 hours, then rinsed with double distilled water and kept in ultrasonicator for several times to remove the impurities on the surface. The cleaned glass slide was weighed before and after deposition using an electron unipan microbalance. For accuracy concerns, four batches of 10 readings were taken and the average was obtained by statistical methods.

The film had been prepared by the following chronological order. The aqueous solution for deposition of CuS thin film consisted of copper chloride (1N) and thiourea (1N) dissolved in double distilled water separately and stirred for 10-12 hours to form a clear solution. Equal amounts of both solutions were mixed and kept stirring for 3 hours. The cleaned glass slide was arranged to use spray pyrolysis for deposition of CuS thin film at 380^0C. After the finish of deposition part, the glass slide was allowed to cool at room temperature. The thickness of CuS thin film is calculated by using the weight difference density method (discussed in a previous paragraph) which is the most convenient method to calculate the thickness of thin film.

Spray pyrolysis deposition was done by using a laboratory-designed glass atomizer, which has an output nozzle of <1 mm. The period between spraying processes was about 2 to 3 min. This period is enough to avoid excessive cooling of the glass substrate. The carrier gas (compressed air) was maintained at a pressure of 100 Nm^2. Distance between nozzle and substrate was about 30 cm and solution flow rate was 5 ml/min. The five sample slides were prepared this way and immediately characterized for optical study using manual microscopic observation to select good films by surface uniformity and the best CuS thin film was selected for the full study first using electrical characterization and then XRD characterization.

Characterization Methods

Thin film was characterized by XRD preferentially to check whether the CuS phase was successfully formed or not formed. XRD data was recorded from 20 to 60 degrees for the Cu Kα radiation of 1.54060 Å. The indexing information (and plot provided by technician along with background subtraction) was post-processed manually for the unit cell refinement using the CELREF software, rendering the calculation for microstructure.

Optical characterization was conducted immediately after the cooling of the prepared thin film to room temperature. Optical properties of the deposited CuS thin film were studied by using UV – VIS Spectrophotometer (ELCO SL-159) at wavelengths ranging from 380 – 1000 nm, using four-probe technique. Optical absorption spectra of CuS thin film are studied on ELCO – SL 159 UV – VIS Spectrophotometer in the optical range from 380to1000 nm.

A high-impedance digital electrometer KEITHLEY 6514 system was used to measure the floating potential between second and fourth probes of the four-probe apparatus. 'DFP 03' oven was used to adjust the temperature for the range from 300K to 380K. K-type thermocouple with accuracy of 0.75% above 400K was used to measure temperature. The AGRONIC-92D was used as a constant-current source for this system.

Results and Discussion

Thickness of Thin Film

The thickness of CuS thin film was estimated at 1.0973 μm. The thickness (d) is calculated from Eq. (1) using the mass of the film (M) deposited on the substrate, where $\rho$is the density

of the deposited substance and A is the area of the deposited film.

$$d = \frac{M}{\rho A} \quad (1)$$

Structure by XRD

X-ray diffraction pattern is shown in Fig. 1. The prominent and good peaks were indexed to (102), (103), (006), (110) and (116), which confirms the formation of hexagonal phase. The symmetry has been found present for the 194 space group, which is also indicated by H-M standard symbol P63/mmc (Hall symbol –P 6C 2C). These patterns seem to be likely in agreement with JCPDS Card Number 06 – 0464.Broadening of peak and very large background noise proposes the nano-dimension case and confirms the crystallites or grains having nano size at microstructure. It is well known that the thin film is confined into one direction in nm size. Thus, characterization confirms the formation of polycrystalline CuS compound deposited on the substrate as a thin film. The unit cell refinement reveals its lattice parameters, volume and density as presented in Table 1 and details of analysis are given in a supplement as Table S1. All values are comparatively slightly lower values than in the work done for 320°C [18]. Our results are found slightly shifting to lower 'a' and 'c' constants of the TF1 sample in the paper. This confirms that close packing is tight. The zero error correction has been also done in refinement and was found to be -0.520 further reduction in the volume of unit cell.

TABLE S1. XRD outcomes of refinement at final cycle of iteration.

(a): Refined Parameters

Parameters	Zero	a	b	c	alpha	beta	gamma	volume
Value	-0.520	3.7738	3.7738	16.3431	90.00	90.00	120.00	201.57
Std. Error	0.0393	0.0084	0.0000	0.1104	0.000	0.000	0.000	1.434

(b): Corrected 2Th corresponding to hkl planes

h	k	l	2Th(obs)	2Th_obs-shift	2Th(Calc)	diff.
0	1	2	28.8900	29.3936	29.3939	-0.0003
0	1	3	31.3560	31.8567	31.8874	-0.0307
0	0	6	32.3730	32.8724	32.8339	0.0385
1	1	0	47.7100	48.1856	48.1433	0.0423
1	1	6	58.9850	59.4376	59.4855	-0.0479

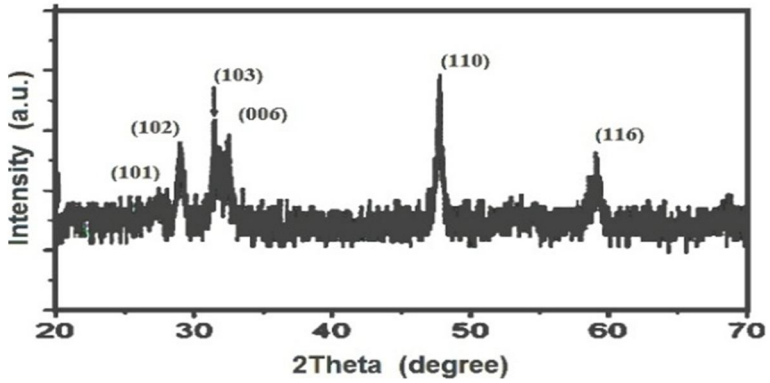

FIG. 1. P-XRD of CuS thin film compound.

The aim of XRD was only for the formation of compound and phase, since data was not suitable for deep structural study. However, we have estimated the size of grain (D) 14nm and the dislocation density (δ) 0.005032 nm^{-2} from the peak width (β_{hkl}) of good orientation. The microstructure strain (ε), due to imperfection and distortion (in crystal structure), is found 0.44, which is significant. All these parameters were calculated by using the following formulae and are given in Table 1.

Debye's formula -

$$D = \frac{K\lambda}{\beta_{hkl}\cos\theta} \quad (2)$$

$$\delta = \frac{1}{D^2} \quad (3)$$

$$\varepsilon = \frac{\beta_{hkl}}{4\tan\theta} \quad (4)$$

Where, k is the shape parameter which is 0.89 for spherical considerations, λ is the wavelength of x-ray of Cu-$K_\alpha$and β_{hkl} is the peak width in radians.

TABLE 1. XRD results (unit cell refinement and analysis of microstructure).

Unit Cell and Microstructure	Parameter	Refined /Calculated Values
Lattice Constant	a & b	3.77(0.008) (Å)
	C	16.34(0.110)(Å)
Unit Cell Volume	V	201.57(1.434) (Å^3)
Unit Cell Density	D	4.74(gcm^{-3})
Microstructure	D	14±1.36 nm
	δ	0.005032 nm^{-2}
	ε	0.44±0.089

Note: Bracket () terms indicate deviation.

Optical Properties

Optical properties of CuS thin film are observed as the absorbance (A) and percentage of transmission (%T) (transmittance) parameters from the data obtained from the spectrometer and their characteristics are shown in Fig. 2 and Fig 3. The peak of absorbance is observed maximum just above 400 nm which is also conversely observed in %T. Data was post-processed for the absorption coefficient (α) and extinction coefficient (k) parameters and plotted as a function of photon energy as shown in Fig 4 and Fig 5. The maximum of absorption coefficient (peak) lied around 2.96 eV, whereas extinction coefficient's maximumlied around 2.64 eV. These 'α' and 'k' values are calculated from the relations given in Eq. (5) and in Eq. (6),respectively as follow.

$$\alpha = \frac{2.303 \times A}{t} \quad (5)$$

$$k = \frac{\alpha\lambda}{4\pi} \quad (6)$$

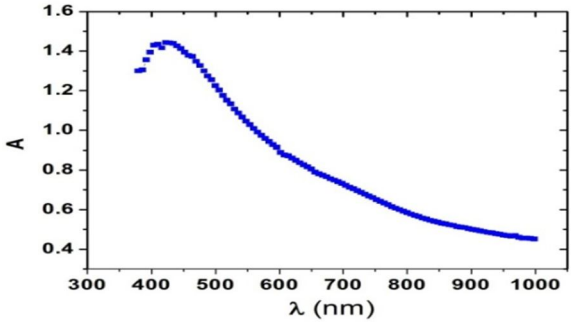

FIG. 2. Absorption spectrum of CuS thin film.

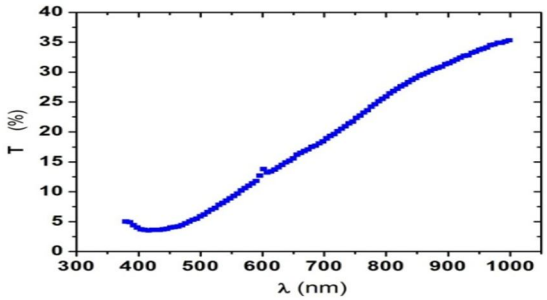

FIG. 3. Transmission spectrum in percentage.

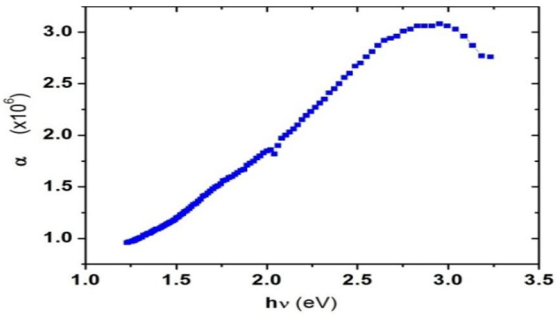

FIG.4. Absorption coefficient as a function of photon energy.

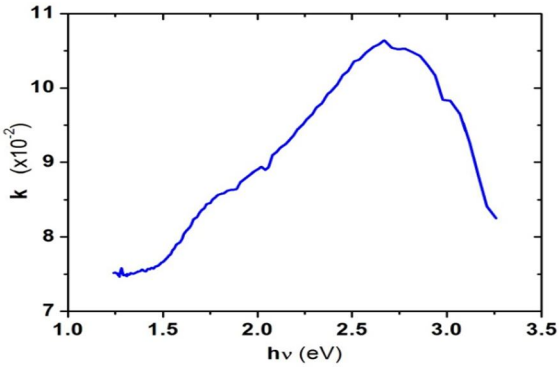

FIG.5. Extinction coefficient as a function of photon energy.

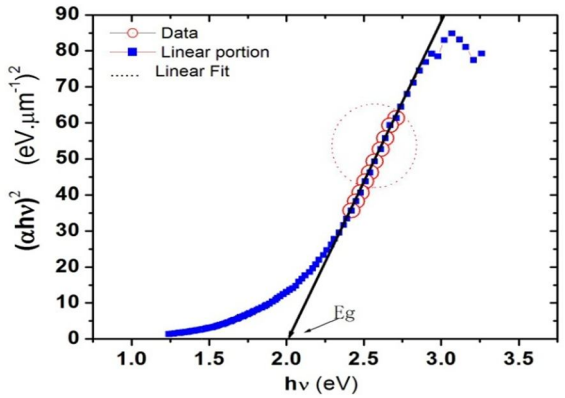

FIG. 6. Optical energy gap of CuS thin film.

An important characteristic property of material extracted from optical data is the energy band gap (Eg). Eg of CuS thin film is obtained from the x-intercept of an extrapolation of the linear part of the tail of data plotted in the graph in Fig. 6. The graph has been plotted $(\alpha.hv)^2$ *versus* photon energy representing Eq. (7) by (Tauc method) [7-15, 19].

$$(\alpha.hv)^2 = K(hv - Eg)^2 \quad (7)$$

where, v = the frequency of radiation, h = Planck's constant, hv is photon energy, K = constant. The allowed transition is possible for the found band gap of 2.01 eV which is non-interrupted by phonon. This Eg is in the order of reported 2.07 eV band gap in another work[18]. The transition in which the phonon vibrations of the lattice took part for the band gap can be tested by Eq. (8).

$$(\alpha.hv)^{\frac{1}{2}} = K(hv - Eg)^2 \quad (8)$$

But, it was avoided and is not presented in this paper due to the observed peak in Fig. 2 and the observed linear portion in Fig. 6. Probably, this implies that the thin film is free from impurities. Therefore, the CuS thin film possesses direct band gap energy and allows transition due to photon absorption only. We observe differences in the preparation method when compared with literature, such as that spray pyrolysis method gave lower-band gap thin film material compared to the chemical bath deposition and dip coating deposition synthesis methods which reported 2.2 eV for t=11nm and 2.5 eV for t=13nm, respectively[20]. Localized defect states are observed (which can effectively influence the conduction and valence bands' edges) from the presence of the Urbach tail (i.e, absorption tail). It is calculated in the form or Urbach energy [21], which is nothing but the slope of the Ln(α) *versus* hυ graph above the band gap energy region. It is found to be 313 meV.

Four-probe Electrical Study

Electrical response of thin film material at different temperatures has been obtained in four-probe experiment and used to calculate the bulk resistivity and the conductivity of CuS thin film. Conductivity is calculated from the reciprocal of the bulk resistivity and the bulk resistivity is calculated from the Voltage-Current (V-I) characteristics measured in a four-probe experiment using Eq. (9) [22].

$$\rho = 4.532\,\mathrm{t}\left(\frac{\mathrm{V}}{\mathrm{I}}\right) \quad (9)$$

where, t is thickness, V is voltage measured as a function of temperature and I is current kept constant at 0.49 μA and four-probe correction factor for thin film sheet is $\left(\frac{\pi}{\ln 2}\right) = 4.532 \times \mathrm{t}$.

The bulk resistivity and conductivity data plots are not seen smooth; instead, they are observed as steps. This is illustrated in Fig. S1 and Fig. S2 in the supplement. Data is significantly irregular at 320 to 330 K and around 360 K. But, for the full range of 300 to 380 K, the linear character is observable and hence we performed linear fit in resistivity case. The resistivity was found decreasing with increasing temperature with a rate of $1.5\text{x}10^{-5}$ Ωm/K, which determines the semiconducting nature. Fig. S2 reveals that the film has increasing conductivity, which supports literature [23]. For electrical property response, natural log of conductivity as a function of 1000/T was plotted and fitted to a straight line as shown in Fig 7 in accordance with Eq. (10).

$$\sigma = \sigma^{o} \exp\left(\frac{\mathrm{E_a}}{\mathrm{KT}}\right); \quad (10)$$

Where, $\mathrm{E_a}$ is the thermal activation energy and K is Boltzmann's constant. The data fitted showed decrement with reducing temperature. It does not show increment as the semiconducting to metallic transformation in one reported work [24]. The slope of graph is found to be -0.4618 which is $\left(\frac{\mathrm{E_a}}{\mathrm{KT}}\right)$. $\mathrm{E_a}$ is estimated to be 0.0398 eV from this. It is in good agreement with 0.03 eV of the silar-prepared 278 nm thick thin film having Eg= 2.28eV and grain size of 17 nm which has a resistivity of 0.05Ωcm at 303 K [25]. Using Hall effect method, Ea was estimated at 0.007 eV for 100°C and 0.013 eV for 150 and 200°C in case of 13nm grain size thin film.

Therefore, for the range of 300 to 380K, it is confirmed that the film is becoming more and more conductive as temperature rises upto 375K.

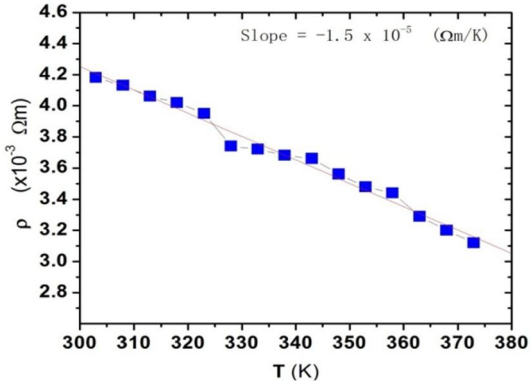

FIG. S1. Variation in electrical resistivity of CuS thin film.

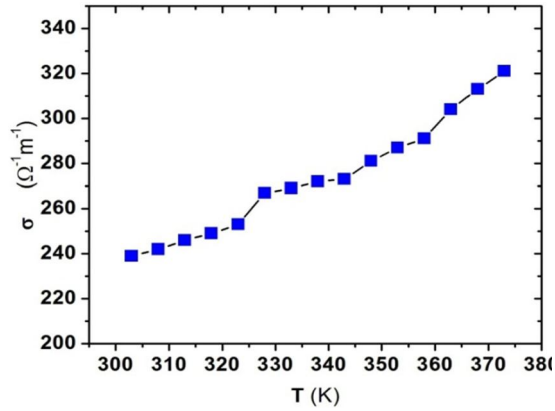

FIG. S2. Variation in electrical conductivity of CuS thin film.

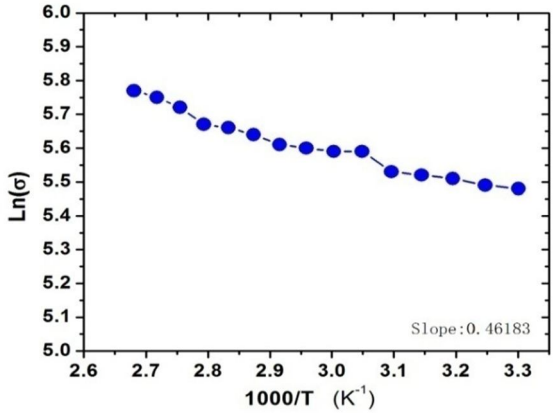

FIG.7.Natural log of conductivity as a function of (1000/T).

Morphology and Dielectric Properties

1- Morphology

All the above optical and electrical properties are concerned with film's material surface morphology. We have tracked it from the XRD data of FWHM (Full Width Half Maxima) of the peak in term of the morphological index (M.I.). M.I is calculated using the highest broadening $(FWHM_h)$ and particular broadenings$(FWHM_{hkl})$ by the following formula [26].

$$M.I. = \frac{FWHM_h}{FWHM_h + FWHM_{hkl}} \quad (11)$$

The smaller index to higher index (for eg. 0.5 to 0.99) refer the blocks to platue type morphologies as per[27]. In Cu thin film, we observed that M.I. is ranging from 0.5 to 0.59, as shown in Table 2 and found proportional to the crystallites domain size with a correlation coefficient of 0.9904. It shows good morphology which is tending toward uniformity at the size of grains/crystallites. Inter-planar spacing and size corresponding to particular orientations are also provided in Table 2.

TABLE 2: Plane spacings, morphology and grain size corresponding to particular (hkl) orientations.

hkl	d (Å)	Size (nm)	MI
(102)	3.036	15.27569	0.590
(103)	2.804	14.90345	0.583
(006)	2.725	14.16049	0.570
(110)	1.888	14.34639	0.561
(116)	1.553	11.79916	0.500

2-Optical Conductivity and Dielectric Constant

We extend our optical study to optical conductivity (σ_{opt}) by using the following formula:

$$\sigma_{opt} = \frac{\alpha nc}{4\pi} \quad (12)$$

Where, R is the reflectance of CuS thin film and c is the speed of light in SI unit. The$\sigma_{opt}$is plotted as a function of photon energy (shown in Fig. 8) illustrating that optical conductivity increases with photon energy up to 2.92 eV. Conductivity was found more at 423nm.

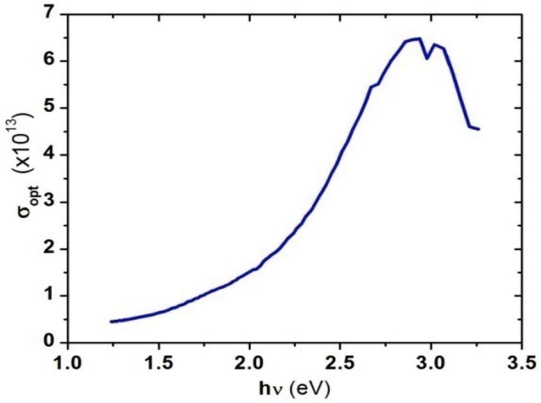

FIG.8. Optical conductivity as a function of wavelength.

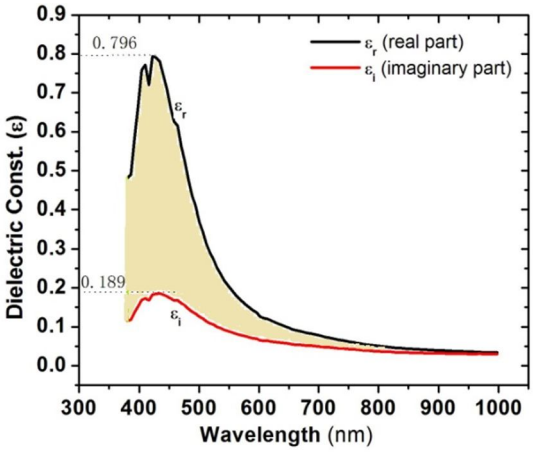

FIG.9. Dielectric constant variation with wavelength.

We have also examined the optical data for dielectric properties as shown in Fig. 9.It is characterized by real-part (ε_r) and imaginary-part (ε_i) constants which are calculated by the following formulae [27].

$$\varepsilon_r = n^2 + k^2 \quad (13)$$

$$\varepsilon_i = 2nk\,; \quad (14)$$

where n is the refractive index calculated as per [27]. The real part of dielectric constant is maximum 0.796 at a wavelength of 423 nm and decreases toward the higher wavelength (lower photon energy). Compared to this, the imaginary part is maximum 0.189 at 432 nm and showsthe same decreasing phenomenon. Fig. 9 clearly identifies the comparison $\varepsilon_r > \varepsilon_i$and the difference between them reduces toward larger wavelengths.

Conclusion

The CuS thin film is successfully deposited on a glass slide at 380^0C by spray pyrolysis technique and observed as a good semiconductor. It is polycrystalline in nature and has a 14 nm grain size with unit cell of hexagonal symmetry. This work has reported 2.01 eV direct band gap energy with the presence of localized states for 1.0973µm film thickness at 380^0C substrate temperature. The optical study for the region 380 – 1000 nm revealed the good electronic nature of the CuS thin film material in terms of absorption, transmission character and optical constants. We are possibly the first to successfully present the immediately-characterized optical and electrical study of CuS thin films after synthesis and cooling. Electric conductivity is increasing and thermal activation occurred. Optical conductivity and dielectric constant also confirm the similar nature with photons for nearly uniform morphology of the film.

References

[1] Pathan, H.M. and Lokande, C.D., Bull. Mater. Sci., 27 (2004) 85.

[2] Sagadevan, S. and Murugasen P., International Journal of Chemtech Research, 6 (14) (2014) 5608.

[3] Dhawankar, S.H. and Suryavanshi, B.M., International Journal of Physical Research, 4(2) (2016) 58.

[4] Singh, A.K., Mehra, S. and Thool, G.S., European Chemical Bulletin, 2(8) (2013) 518.

[5] Dhawankar, S.H., Patil, A.K. and Suryavanshi, B.M., Applied Physics Letter, 1 (2) (2014).

[6] Kassim, A., Min, H.S., Haron, M.J. and Nagalingam, S., Int. J. of Pharm. & Life Sci., 2 (11) (2011) 1190.

[7] Isac, L.A., Duta, A., Kriza, A., Enesca I.A. and Nanu, M., Journal of Phys. Conf. Series, 61 (2007) 477.

[8] Thanikaikarasan, S., Mahalingam, T., Kathalingam, A., Moon, H. and Kim, Y.D., J. of New Materials for Electrochemical Systems, 12 (2009) 29.

[9] Alex, B.F., Martinson, S.C., Thimsen, R.E., Elam, J.W. and Pellin M.J., Energy and Environmental Science, 6 (2013) 1868.

[10] Dhawankar, S.H., Patil, A.K., Lad, J.S. and Suryavanshi, B.M., Scholars Research Library, Archives of Physics Research, 4(3) (2013) 7.

[11] Johansson, J., Kostamo, J., Karppinen, M. and Niinisto L., Journal of Material Chemistry, 12 (2002) 1022.

[12] Dhawankar, S.H., Patil, A.K., Lad, J.S. and Suryavanshi, B.M., International Journal of Innovative and Applied Research,2(8) (2014) 67.

[13] Wu, Y., Wadia, C., Ma, W., Sadtler, B. and Alivisatos, P., Nano Letters, 8(8) (2008) 2551.

[14] Sagade, A.A. and Sharma, R., Sensors and Actuators B, 133 (2008) 135.

[15] Dhawankar, S.H., Patil, A.K., Suryavanshi, B.M. and Tirpude, M.P., International J. of Phys. Res., 5(1) (2017) 1.

[16] Nascu, C., Pop, E., Ionescu, V., Indrea, E. and Bratu, I., Material Letters, 32 (1997) 73.

[17] Adelifard, M., Eshghi, H. and Mohagheghi M.M.B, Applied Surface Sci., 258 (15) (2012) 5733.

[18] Firat,Y.E., Yildrim,H., Erturk,K. and Peksoz,A., Scanning, 2017 (2017) 2625132.

[19] Tayade, N.T., Dhawankar, S.H. and Arjuwadkar, P.A., Journal of Physical Sciences, 22 (2017) 137.

[20] Chaki, S.H., Deshpande, M.P. and Tailor, J.P., Thin Solid Films, 550 (2014) 291.

[21] Grozdanov, E. and Najdoski, M., J. of Solid State Chem., 114(2) (1995) 469.

[22] Cruz, J.S., Hernandez, S.A.M., Delgado, F.P., Angel O.Z., Perez, R.C. and Delgado, G.T., International J. of Photoenergy, 2013 (2013) 9.

[23] Choudhury, B. and Chaudhary, A., Phys. E., 56 (2014) 364.

[24] Gaikawad, P.D., Shirale, D.J., Gade, V.K., Savale, P.A., Kharat, H., Kakade, K.P., Hussaini, S.S., Dhumane, N.R. and Shirsat, M.D., Bull. Mater. Sci., 29 (2006) 169.

[25] Ubale, A.U., Bhute, M.V., Malpe, G.P., Raut, P.P., Chipade, K.S. and Ibrahim S.G., J. of Saudi Chemical Society, 20(2) (2016) 227.

[26] Sarkar, S. and Das, R., Indian J. Pure and Appl. Phys., 56 (2018) 765.

[27] Jacob, R., Nair, H.G. and Isac, J., Int. Lets. Chem., Phys. and Astronomy,2 (2015) 100.

Volume 15, Number 1, 2022. pp. 57-60

Jordan Journal of Physics

ARTICLE

Study of Structural and Magnetic Properties of Co-doped M-Type Sr-Hexaferrite Nanoparticles

Sunil N. Kamde[a], **Amar K. Nandanwar**[b], **Purushottam G. Agone**[a] and **Kishor G. Rewatkar**[c]

[a]*Department of Physics, Rajiv Gandhi College of Engineering, Chandrapur - 442403, India.*

[b]*Department of Physics, VMV College, Wardhaman Nagar, Nagpur - 440008, India.*

[c]*Department of Physics, Dr. Ambedkar College, Deekashbhoomi, Nagpur – 440010, India.*

Doi: **https://doi.org/10.47011/15.1.8**

Received on: 01/08/2020; *Accepted on: 08/07/2021*

Abstract: The aim of this work is to synthesize nanocrystalline $SrFe_{10}Co_3O_{19}$ with M-type hexaferrites *via Sol-gel* auto-combustion method. The synthesized powders were consequently subjected to calcination at 900°C for 6h. The synthesized samples are characterized by X-ray diffraction (XRD) to find structural parameters. The XRD results exposed single hexagonal magnetoplumbite phase formation in the heated samples. The morphology of the compound was revealed by Field Emission Gun Scanning Electron Microscopy (FEG-SEM). Vibration Scanning Magnetometer (VSM) provides the magnetic nature of the compound. It shows that the decrease in coercivity was affected by doping of Co^{2+} ions.

Keywords: M-type hexagonal ferrites, SEM, Sol-gel, VSM, XRD.

Introduction

The M-type hexaferrite $SrFe_{12}O_{19}$ (Sr-*M*) was discovered in the early 1950s. In view of the large volume of the market and over this long time, many attempts have been made to improve the key magnetic properties by various techniques, including doping on the Co^{2+} sub-lattices [1].

Magnetic properties of calcium hexaferrite strongly depend on the preparation technique and nature of applied precursors. In recent years, magnetic nanoparticles have been subjected to intense research, because finite-size effects dominate the magnetic properties of nano-sized particles and become more important with the decrease of the particle size. These properties lead to the large application of nanomaterials in loading coils, magnetic storage media and biosensor devices. This critical diameter typically lies in the range of a few tens of nanometers and depends on the material [2, 3].

Five different positions of iron ions define the magnetic structure of the M-type hexaferrite crystals and replacing one or more iron ions by other elements changes the magnetic and microwave material properties dramatically [2]. Hexaferrites are widely used in microelectronics because of their possible modification. The most prospective materials for electronics are lead, barium, strontium M-type hexaferrites and their doped compositions [4, 5]. The Cobalt divalent ions diffuse into magnetoplumbite hexaferrites with other divalent materials with heating treatment then found distribution of ions in tetrahedral and octahedral sites which gives its possible applications [13]. The prime objective of the present study is to achieve higher magnitudes of M_S and maximum value of [B-H]

Corresponding Author: Sunil N. Kamde **Email**: sunilkamde.kamde@gmail.com

curve without significant drop in H_C for the sintered isotropic $SrFe_{12}O_{19}$ [6].

This paper is devoted to structural and magnetic study of Sr-M-type hexaferrites.

Experimental

Sr-M hexaferrites compound was synthesized in polycrystalline form by the *Sol-gel* auto-combustion method. Strontium Nitrate (0.8827 gm), Cobalt Nitrate (7.284 gm), Ferric Nitrate (13.48 gm) and Urea (8.4355 gm) with molar concentrations were mixed with 30 ml. of deionized water to form a solution. Here, Urea is used as a fuel and works as a catalyst. The metallic ions solution is gradually heated on a metallic hot plate for 4 hours for the formation of a gel. This mixture of metallic gel is further burnt in microwave oven for very short period of time to get better molecular homogeneity. Finally, extracted burnt dry ash is grained mechanically by a pestle and mortal and calcinated in a muffle furnace at 900°C for 6 hours [7].

Results and Discussion

X-Ray Diffraction (XRD) Analysis

The prepared sample of $SrCo_3Fe_{10}O_{19}$ was examined by X-ray diffraction graphs in order to study the ferrite phase and to determine the particle size. Powder method was used where X-rays are diffracted, not by a single crystal, but a sample consisting of a very large number of randomly oriented crystalline particles ; i.e.,in powder form.

The XRD patterns for the $SrCo_3Fe_{10}O_{19}$ ferrite are shown in Fig 1. Phase formation studied by XRD (MDI-Jade) revealed the identification of hexagonal ferrite phases similar to JCPDS card no. 27-1029. It is evident from the XRD plots that the samples are composed of magnetoplumbite crystal structure ; namely, hexagonal M-phase ferrite. There were no metal oxide phases in the burnt powder and no extra lines were detected, hence confirming the single magnetoplumbite phase in the reported samples. The space group for the samples is observed to be P_6mmc [7].

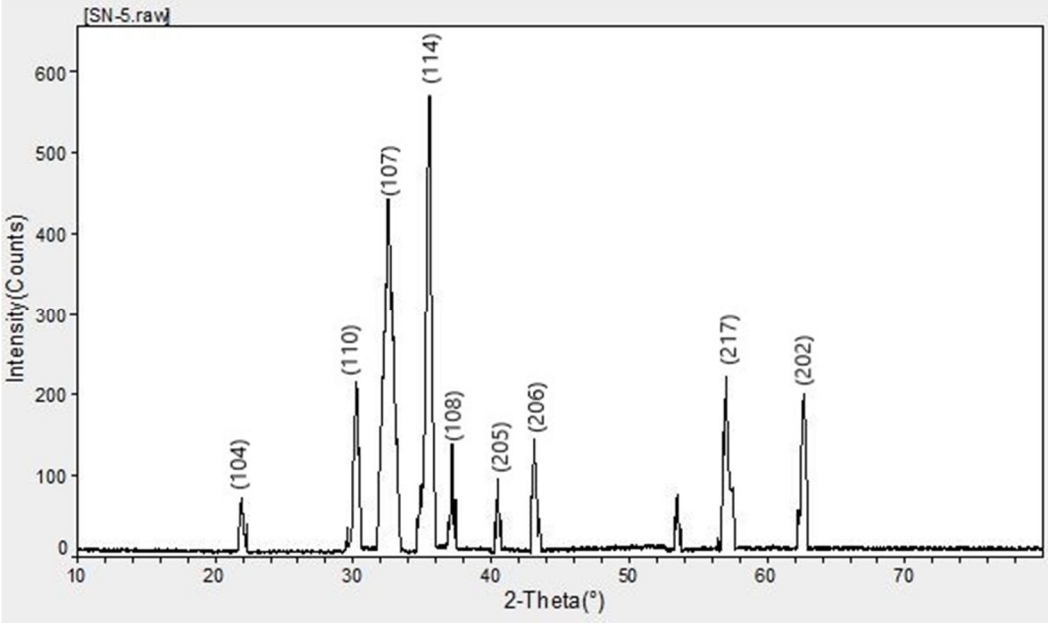

FIG. 1. XRD pattern of $SrFe_{10}Co_3O_{19}$hexaferrite.

The structure and crystallite size were evaluated from XRD measurements. The crystallite size of the nano-crystalline samples was measured using Debye-Scherer formula [8] :

$$D_{XRD} = 0.98\lambda/\beta \text{ Cos } \theta \qquad (1)$$

where, λ is the wavelength of X-ray used in Å, β is the full width at half-maximum (FWHM) in radians for 2θ scale, θ is the Bragg angle, D_{XRD} is the crystallite size in nm. The burnt powders were calcined at 900 ºC for 6 hrs to get a more crystalline homogeneous hexagonal phase. The average crystallite size of calcined powder was 22 nm.

Morphological Study by Scanning Electron Microscopy (SEM)

In this section, morphological properties of the synthesized samples are recorded and studied. Typical FE-SEM image [JSM-7600F] at IIT Bombay Powai, of the sample Sr-M hexaferrite synthesis *via* Sol-gel method annealed at 900°C, is shown in Fig 2. The image reveals that the particles have an almost regular shape and homogeneous distribution. It is also observed that the nanoparticles have nearly spherical morphology and are agglomerated with each other with average particle size and particle size distribution from SEM analysis is found to be from 20 to 40 nm.

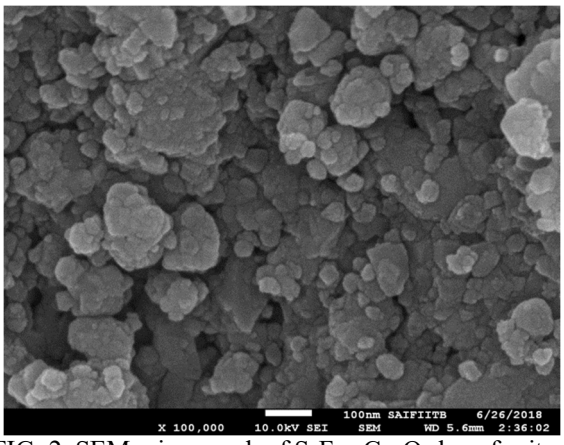

FIG. 2. SEM micrograph of $SrFe_{10}Co_3O_{19}$hexaferrites.

TABLE 1. Tabular representation of sample parameters.

Composition	a Å	c Å	c/a	Average Particle Size (nm)
$SrFe_{10}Co_3O_{19}$	6.13	23.05	7.76	22

Magnetic Study by VSM

The magnetic properties of the synthesized nanoparticles are analyzed using a Vibrational Sample Magnetometer (Lakeshore VSM 7410, SAIF IIT Madras) at room temperature (300 K) in the range of approximately −1500 to +1500 Gauss. Fig. 3 shows the M-H curves of the prepared $SrFe_{10}Co_3O_{19}$ nanocrystals. The coercivity (H_C) and saturation magnetization (M_S) values have been directly extracted from these curves and have been listed for x = 3 concentrations of Co^{+2} ions.

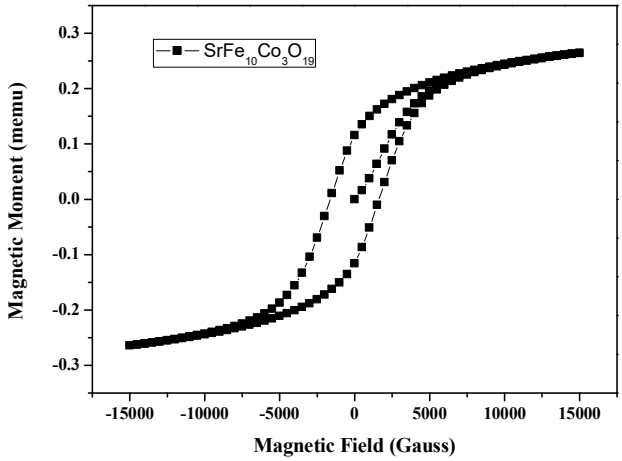

FIG. 3. VSM pattern of $SrFe_{10}Co_3O_{19}$ hexaferriite.

Strontium hexaferrite, with the chemical formula $SrFe_{10}Co_3O_{19}$, is one of the M-type hexagonal ferrites and belongs to the magneto-plumbite group of oxides. In magneto-plumbite, the interaction between two close sites, such as 2a-12k, 2a-4f_1 and 4f_1-12k, has been decisive for the strong magnetic character [10-12].

In this section, magnetic properties of samples directly extracted from VSM data, like

magnetization (M_S), remanence magnetization (M_r), coercivity (H_C), … etc. are presented in Table 2. The graphical variations of these magnetic characters have helped point out some typical nature and behavioral tendencies of such Strontium Hexaferrite Nanoparticles under the influence of the applied field [15, 16].The large value of coercivity shows that the sample belongs to the hard ferrite category.

TABLE 2. Tabular representations of magnetic parameters.

Composition	a Å	c Å	c/a	Retentivity Mr(emu)	Magnetization Ms (emu/g)	Coercivity Hc (Gauss)	Particle Size (nm)
$SrFe_{10}Co_3O_{19}$	6.13	23.05	7.76	0.11549	36.28	1625	22

Conclusion

Nanoparticles of cobalt-doped strontium hexaferrite have been successfully synthesized using the sol-gel technique. Cobalt substitution has brought about remarkable improvements in the structural and magnetic properties of strontium ferrite.

The XRD analysis confirmed the formation of nanocrystalline hexagonal magnetoplumbide structure. The crystallite size of the synthesized nanoparticles was calculated by Debye-Scherer formula and found to be 22 nm. The values of crystallite size and particle size are calculated from the XRD. The high saturation magnetization value can be explained by the fact that the particles are single domain with higher magnetic moments.

References

[1] Nandanwar, A.K, Sarkar, N.N., Sahu, D.K., Choudhary, D.S. and Rewatkar, K.G., Materials Today: Proceedings, 5 (10) (2018) 22669;Yang,C., Wang,M., Zhou,J.and Chi,Q., Mater. Sci. Eng. C, 82 (2018) 42.

[2] Fang, C.M., Kools, F., Metselaar, R., DeWith, R.and Groot, R., J. Phys.: Condens. Matter, 15 (2003) 6229.

[3] Nandanwar, A.K., Meshram, N.S., Korde, V.B., Choudhary, D.S. and Rewatkar, K.G., Integrated Ferroelectrics, 203 (1) (2019) 12.

[4] Rewatkar, K.G., Solid State Phenomena, Trans. Tech. Publications, 241 (2016) 177.

[5] Nandanwar, A. K., Chaodhary, D. L., Kamde, S. N., Choudhary, D. S., & Rewatkar, K. G. (2020). Materials Today: Proceedings, 29, 951-955.

[6] Amiri, S.and Shokrollahi, H., Materials Science and Engineering: C, 33(1)(2013)1.

[7] Raghasudha, M., Ravinder, D.and Veerasomaiah, P., Journal of Nanostructure in Chemistry, 3(1)(2013)63.

[8] Rewatkar, K.G., Journal of Magnetism and Magnetic Materials, 316 (1) (2007) 19.

[9] Sable, S.N., Rewatkar, K.G. and Nanoti, V.M., Materials Science and Engineering B, 168 (2010) 156.

[10] Gawali, S.R., Moharkar, P.R., Rewatkar, K.G.and Nanoti, V.M.,J. of Bio-nano Fontier, 5 (2012) 26.

[11] Dahal, J.N., Wang, L., Mishra, S.R., Nguyen, V.V.and Liu, J.P., Journal of Alloys and Compounds, 595 (2014) 213.

[12] Gorter, E.W., Proc. IEEE, 104B (1957) 255S.

[13] Bertaut, E.F., Deschamps, A., Pauthenet, R.and Pickart, S., J. Phys. Rad., 20 (1959) 404.

[14] Van Wieringen, J.S., Philips Tech. Rev., 28 (1967) 33.

[15] Ghatak, S., Chakraborty, G., Sinha, M., Pradhan, S.K.and Meikap, A.K., Physica B: Condensed Matter, 406(17)(2011)3261-6.

[16] Tehrani, F.S., Daadmehr, V., Rezakhani, A.T., Akbarnejad, R.H.and Gholipour, S., Journal of Superconductivity and Novel Magnetism, 25(7)(2012)2443.

Volume 15, Number 1, 2022. pp. 61-66

Jordan Journal of Physics

ARTICLE

A Brief Review on Structural, Morphological, Magnetic and Dielectric Behavior of Divalent Cation-substituted Nanocrystalline Cobalt Ferrite

Y. S. Bopche[a], **A. M. Shahare**[a], **A. V. Bagde**[b] and **D. S. Choudhary**[a]

[a] *Department of Physics, Dhote Bandhu Science College, Gondia 441614, India.*
[b] *Chintamani College of Science, Pobhurna 441224, India.*

Doi: **https://doi.org/10.47011/15.1.9**

Received on: 01/08/2020; *Accepted on: 14/12/2020*

Abstract: Spinel ferrites nanoparticles have received much more focus due to their promising applications in various technologies, such as magnetic refrigerators, microwave devices, colour imaging, high-density recording media and magnetic fluids. Nano-crystalline cobalt ferrite has been widely studied for its distinctive properties, like cubic magneto crystalline anisotropy, high coercivity, reasonable saturation magnetization, great chemical constancy, wear resistance and electrical insulation. Thus, cobalt ferrite has its own applications in the arena of high-frequency devices, magneto-optical devices, memory cores, recording media and spintronics and also in the biomedical sector, such as MRI, drug delivery schemes and magnetic hyperthermia. Reduced dimensionality of ferrite nanoparticles is having differences in properties when compared to its bulk counterparts. Size modulation of the physico-chemical properties of cobalt ferrite gives a distinctive response in the nanosized scale, permitting for material engineering in order to meet different necessities while addressing its different applications. The present study gives a brief review of significant effects on structural, dielectric and magnetic properties of cobalt spinel ferrite with different cation substitutions, like Mg^{2+}, Ni^{2+}, Zn^{2+}, Cu^{2+}, In^{2+} ...etc. This study regarding the size and its dispersity, core shell design, shape, crystallinity and surface decoration with hybrid derivatives opens up a wide variety of prospects for elementary studies as well as for growth and revolution in the field of ferrites.

Keywords: Spinel ferrite, Structural properties, Microstructural properties, Magnetic properties, Dielectric properties.

Introduction

Spinel ferrite has the general formula $(A)\,[B_2]\,O_4$, with the larger oxygen anions forming a close-packed FCC structure with the smaller metal cations occupying interstitial sites: the tetrahedral (A) sites and the octahedral [B] sites. In cubic spinel MFe_2O_4 structure, the cations will locate at tetrahedral (A) and octahedral (B) interstitial sites. Generally, in the normal spinel ($MnFe_2O_4$, $ZnFe_2O_4$), divalent cations (Zn^{2+}, Mn^{2+}) occupy tetrahedral A sites, while octahedral B sites are occupied by trivalent cations Fe^{2+}. However, in inverse spinel ($CoFe_2O_4$, $NiFe_2O_4$, $MgFe_2O_4$), divalent cations Co^{2+}, Ni^{2+}, Mg^{2+} occupy octahedral sites and trivalent cations Fe^{3+} are distributed equally at A and B sites. So, the formula of MFe_2O_4 ferrites can be stated as $(M_{1-x}^{2+}Fe_x^{3+})\ [M_x^{2+}Fe_{2-x}^{3+}]O_4$, where round and square brackets denote tetrahedral and octahedral sites, respectively. The interaction between these two sub-lattices A and B, in a spinel structure(AB_2O_4), comprise inter-sublattice super exchange (A-B) interactions and intra-sublattice exchange

Corresponding Author: Y. S. Bopche **Email**: ysbopche@dbscience.org

interactions; i.e., (A-A) and (B-B) interactions. The super-exchange interactions (A-B) are more dominant than intra-sub lattice exchange interactions [1]. The type of spinel structure (inverse, normal and mixed) decides the lattice occupancy of the divalent metal ions and hence, these metal ion occupancy on lattice sites influences the properties of ferrite nanoparticles. The structural, electrical and magnetic properties of two sub-lattice ferrites can be evaluated by using tools such as elemental category, composition with concentration and preparation methods as well as outer perturbations such as temperatures and pressures. Correspondingly, octahedral and tetrahedral sub-lattices antiferromagnetic coupling is a key source for the magnetic moment of the spinel ferrite. In normal spinel ferrite structure of $CoFe_2O_4$, the tetrahedral A-site is occupied by divalent (Co) atoms, whereas the octahedral B-site is filled by trivalent (Fe) atoms. While, in an inverse spinel structure of $CoFe_2O_4$, A-site is populated by Fe^{3+} ions, while B-site is equally populated by Co^{2+} and Fe^{3+} ions. Therefore, the structural, transport and magnetic properties of $CoFe_2O_4$ are highly based on the synthesis method and crystallite size [2]. Cobalt ferrite exhibits ferromagnetic behavior at the transition temperature around 790 K and crystallizes in tetrahedral A-site coordination ($Co_{1-\delta}Fe_{\delta}O_4$) and octahedral B-site coordination ($Co_{\delta}Fe_{1-\delta}O_4$), where δ is the degree of inversion whose value depends on the thermal treatment during the synthesis process. δ=1 corresponds to the formation of inverse spinel structure and δ=0 corresponds to the formation of normal spinel structure. The cation redistribution leads to the microstructure variation, which further affects the magnetic properties of the ferrite nanoparticles. Hence, the internal structure with cation distribution can be well controlled by using appropriate synthetic methods. Thus, by tuning the microstructure and cation distribution within the ferrites, the magnetic properties will be strongly influenced.

Literature Review and Discussion

Microstructure and magnetic properties of MFe_2O_4 (M = Co, Ni, Mn) ferrite nanocrystals were studied by Wei Wang *et al.* [3] who found that all the obtained samples exhibit higher saturation magnetization (Ms). SEM and TEM images indicate that $CoFe_2O_4$ and $MnFe_2O_4$ samples contain nanosphere, whereas $NiFe_2O_4$ samples consist of big cauliflower-like nanoparticles and small nanoplatelets.

Structural and magnetic properties of cobalt ferrite nanoparticles were studied by C. R. Stein *et al.* [4] confirming the inverse cubic spinel structure with Fd-3m space group with diameters in nano-size range (below 10 nm). In the field of magnetic recordings, a large value of magnetic moment is demanded for video and audio modes. Tailhades *et al.* [5] tried to substitute Cu into the $CoFe_2O_4$ to increase magnetization, but found cation migration during annealing. Reports [6] are also existing on Al- as well as Ti-substituted $CoFe_2O_4$ prepared by sol-gel method with obtained saturation magnetization of 72.1 and 62.6 emu/gm, respectively, which shows low values of magnetization as compared to Ni-substituted $CoFe_2O_4$ and mismatch of the synthesized particle size.

The effect of nickel on cobalt ferrite was studied by Ninad B. Velhal *et al.* [7] confirming the formation of cubic-phase spinel structure with 30-44 nm crystallite size variation with nickel content. Porous agglomerated morphology of powder samples was shown in the SEM and dispersion behavior, which shows the high resistance of cobalt nickel ferrite. The saturation magnetization with maximum value of 92.87 emu/gm was observed at 30K temperature by substituting cobalt ferrite with 0.4 nickel concentration. The dielectric constant and loss tangent decrease with frequency, whereas conductivity increases with increase in frequency. As we increase Ni content, the magnetic moment of the sample decreases, due to which Ms, Mr, Hc and Mr/Ms decrease at constant temperature. As we decrease the temperature of the sample, all these magnetic values decrease.

Zinc-doped cobalt ferrite nanoparticles were synthesized by Khalid M. Batoo *et al.* [8] using sol-gel method and approved the formation of single-phase cubic structure with an average particle size between 55.38 and 32.87 nm, which was also authorized by transmission electron microscopy. As we increase the doping concentration of Zn, the lattice parameter was found to increase. The sample display of Maxwell-Wagner type of interfacial polarization with normal dielectric behavior decreases with increasing the applied field frequency. With the doping of non-magnetic Zn, the ac conductivity, dielectric constant and loss tangent were found

to decrease. Also, the same type of change was observed for other magnetic parameters; i.e., saturation magnetization, remanence and coercivity.

In doped cobalt ferrite nanoparticles studied by Razia Nongjai *et al.* [9] for magnetic and electrical properties, the major dependence of magnetic and electric properties on grain size was found. The variation of dielectric properties, *tan δ* and as conductivity with frequency exposes, the dispersion is owed to Maxwell-Wagner type of interfacial polarization in general and the hopping of charge between $\boldsymbol{Fe^{2+}}$ -$\boldsymbol{Fe^{3+}}$ and between $\boldsymbol{Co^{2+}}$ - $\boldsymbol{Co^{3+}}$ ions at B-sites.

S. Muthurani *et al.* [10] synthesized nanostructured $Cu_xCo_{1-x}Fe_2O_4$ by auto-combustion method to sense the magnetic and humidity properties and observed a significant increase in saturation magnetization (M_s) and remanence magnetization (M_r) due to the substitution of Cu^{2+} ions in cobalt ferrite, while coercivity (H_c) decreases. The temperature variation of electrical conductivity shows a thermal hysteresis and definite break in conductivity, which corresponds to ferromagnetic-paramagnetic transition and exhibits highest sensitivity for humidity.

Comparative Observations

The different cation substitutions and their significant effects on the characteristics (structural, dielectric, magnetic) of ferrites have been intensively studied. In particular, the effect of partial interstitial substitution of divalent cations like Cu^{2+}, Ni^{2+}, Zn^{2+}, Mg^{2+}… etc. was studied.

Cu Substitutions

A. Samavari *et al.* [11] results showed that increasing Cu concentration causes a reduction in the nanoparticle size. Saturation magnetization (Ms), remanence magnetization (Mr) and coercivity (Hc) of the cobalt ferrite diminished by the substitutions of Cu^{2+} ions. B. Chandra Sekhar *et al.* [12] confirmed the cubic spinel structure and improved strain derivatives standards as compared to pure cobalt ferrite, thus making them suitable for the application of stress sensing. N. Sanpo *et al.* [13] also reported the same results. M. Margabandhu *et al.* [14] synthesized Cu^{2+}-substituted cobalt ferrite magnetic nanoparticles by chemical co-precipitation method. The VSM results showed that the magnetic parameters coercivity (Hc) and retentivity (Mr) decrease with increase in Cu^{2+}substitution. Saturation magnetization (Ms) shows increment and decrement with Cu^{2+} substitution. Rakesh K. Singh *et al.* [15] synthesized copper-substituted cobalt ferrite nanoparticles using citrate precursor method and observed a cubic spinel structure with sharp changes in particle size, lattice constant, magnetization and retentivity with respect to Cu content.

Ni Substitutions

Sonal Singhal *et al.* [16] prepared nano-size nickel-substituted cobalt ferrite using aerosol route with a particle size of 10 nm which rises up to 80 nm on annealing at 1200^0C. With the nickel concentration, the unit cell parameter decreases linearly due to smaller ionic radius of nickel. Won-Ok Choi *et al.* [17] used sol-gel method and found that when the nickel-substitution was increased, the lattice constant and size of particles of the ferrite powders decreased. The nickel-substituted cobalt ferrites showed lower coercivity and saturation magnetization than the pure cobalt ferrite powders, due to cation distribution, magnetic moment and magneto crystalline anisotropy constant of the substituted ions. The variation of lattice parameter from 8.350 to 8.300 Å was observed by Mozaffari *et al.* [18] with the increase of Ni content. Saturation magnetization (Ms) and coercive forces drops with increase in nickel content, but the Curie temperature increases, which was explained by the changes in magneto crystalline anisotropy. Abdul Gaffor *et al.* [19] manufactured nickel-cobalt nanoparticles by citrate gel auto-combustion method and confirmed cubic spinel structure of ferrites. For magnetic data storage purpose, the crystallite size in the range of 20 nm to 31 nm is desirable. N. B. Velhal *et al.* [20] reported the cubic spinel phase using the auto-combustion technique at low temperature. Due to the lower magnetic moment of nickel, the magnetic properties; i. e., Ms, Mr, Hc and Mr/Ms decrease with the increase of Ni content and show a temperature-dependent behavior. Nickel-substituted cobalt ferrite was prepared by Uday Bhasker Sontu *et al.* [21] using self-combustion method at low temperatures and observed the tuning of magnetic and electrical properties of the ferrites from hard magnetic and lower-resistivity cobalt ferrite to soft magnetic and

high-resistivity nickel ferrite. Ajaypal Singh *et al.* [22] synthesized nanoscale ferrite particles by using solution combustion method and exposed single-phase spinel structure to X–ray diffraction studies. Magnetic studies showed the variation of coercivity and saturation magnetization with nickel substitution and observed higher values of coercivity and saturation magnetization than in pure nickel ferrites. The single cubic spinel phase for all the samples was also observed by P. P. Hankare *et al.* [23]. It is also noticed that as we increase the nickel content in the cobalt ferrites, the lattice parameter decreases and the crystallite size of the ferri-spinel increases. The size of the synthesized nanoparticles lies between 20 and 25 nm.

Zn Substitutions

Faheim, A. S. *et al.* [24] synthesized zinc-substituted nano-crystalline cobalt ferrite powders, $Co_{1-x}\ Zn_xFe_2O_4$ by the co-precipitation method. X-ray analysis tells that the samples were in cubic spinel. Bond length between the magnetic ions, lattice constant, X-ray density and ionic radii were found to increase as we increase the zinc concentration. The crystallite size is within the range of 6-24 nm, approved by XRD & HR-TEM. The saturation magnetization and coercivity decrease with the increase in zinc content. The chemical composition of $\boldsymbol{Co_{0.3}Zn_{0.7}}Fe_2O_4$ sample exhibits super-paramagnetic behavior. EI-Saaey *et al.* [25] showed the same results and exhibited super-paramagnetic behavior. The single-phase spinel cubical structure was confirmed by S. Nasrin *et al.* [26] who observed that the average grain size increases with the sintering temperature and decreases with the increase of zinc content. Thus, the sintering temperature and zinc content both affect the lattice constant. The saturation magnetization, remanent magnetization, coercivity and magnetic moment have been found to show a decreasing behavior with the increase of Zn content. Experimental data shows that Curie temperature increased with the increase of sintering temperature and decreased with the increase of Zn content. S. Jadhav *et al.* [27] also confirmed the decrease in Curie temperature with the increase in Zn concentration. Polina Yaseneva *et al.* [28] also reported the effect of Zn substitution on the Curie temperature and found that Zn substitution decreases the Curie temperature from around 440 ^oC for the pure sample to 180 ^oC for the doped sample with x = 0.5. Coppola, P. *et al.* [29] found structural and morphological changes in the sample with respect to zinc substitution. The shapes of the nanoparticles vary from spheres, cubes to octahedrons as per TEM analysis. In the nanoparticle composition, the proportions of Zn and Co strongly influence the properties of hysteresis loop. G. Vaidyanatham *et al.* [30] studied $\boldsymbol{Co_{1-x}Zn_x}Fe_2O_4$ nanoparticles and showed that the samples were cubic spinel with average crystallite size varying from 6.92 to 12.02 nm with the increase of zinc concentration; therefore, the lattice constant increases with zinc. Magnetic factors such as M_s, M_r and H_c were found to reduce with the increase of zinc content. M. T. Jamila *et al.* [31] studied the effect of Zn content on the structural parameters and confirmed single-phase face center cubic structure. They revealed that the crystallite size was found in the range 30-70 nm while lattice parameter and X-ray density decrease with the increase of Zn concentration. Linear growth of unit cell parameter with the increase in zinc concentration was investigated by Swati Tapdiya *et al.* [32] due to the larger ionic radii of Zn^{2+} ion and they also found an increase in saturation magnetization owing to the variation of exchange interaction among the tetrahedral and octahedral sites. Sonal Singhal *et al.* [33] synthesized zinc-substituted cobalt ferrite *via* sol-gel method, characterized using IR spectroscopy, TEM, X–ray diffractometry (XRD) and magnetic measurements. It is observed that the lattice parameter and X-ray density increase with increasing Zn concentration. The saturation magnetization first increases and then decreases. C. Nlebedim *et al.* [34] studied the temperature dependence of structural and magnetic properties of zinc-substituted cobalt ferrite from 50 K to 300 K and found no observable changes in the crystal structure. At all temperatures, magnetization increased with x, indicating A-site Zn substitution. An inverse relation was seen between magnetic susceptibility and coercive field, while a direct relationship was seen between coercive field and magnetocrystalline anisotropy coefficient.

Mg Substitutions

Vithal Vinayak *et al.* [35] & Shaik Jesus Mercy *et al.* [36] successfully synthesized the nanocrystalline $Co_{1-x}Mg_xFe_2O_4$ by sol gel auto-combustion method and showed the formation of

single-phase cubic spinel structure by X-ray technique. The lattice constant was found to decrease with increasing Mg^{2+} concentration. The particle size of the sample was obtained in the range of 11-24 nm by Debye-Scherrer formula. The tetrahedral and octahedral bond lengths and edges decrease as Cu^{2+} content increases. In overall, the substitution of magnesium in cobalt ferrite influences the structural properties. V. V. Dhole *et al.* [37] synthesized the nanocrystalline $Co_{1-x}Mg_xFe_2O_4$ by sol-gel auto-combustion technique. X-ray diffraction results showed the formation of single-phase cubic spinel structure. The lattice constant is found to decrease with increasing Mg^{2+} concentration. The particle size of the sample calculated using Debye-Scherrer formula was obtained in the range of 12-32 nm. The average grain size determined from scanning electron microscopy technique is of the order of 45-66 nm. The signs of modification in structural and magnetic properties due to substitution of Mg for Ni in $Co_{0.5}Ni_{0.5}Fe_2O_4$ sample were also observed by S.V. Bhandare *et al.* [38].

Conclusion

In the present paper, different cation substitutions like Ni^{2+}, Zn^{2+}, Cu^{2+}, Mg^{2+}… etc. in cobalt ferrite and their significant effects on structural, dielectric and magnetic properties of the ferrites have been intensively studied. Hysteresis study of the curve shows enrichment in coercivity and remanence, which is attributed to the shift from multidomain to single-domain environment and reduction in saturation magnetization with the substitution of divalent metal ions into cobalt ferrite materials. The variation of dielectric properties, tan δ and ac conductivity with frequency reveals the dispersion relation due to Maxwell-Wagner (two-layer models) type of interfacial polarization that decreases with increasing the frequency of the applied field. The lattice parameter is found to increase with increasing divalent metal ion doping concentration into the cobalt ferrite crystals. Porous and agglomerated morphology of the bulk sample was displayed in the scanning electron microscopy (SEM). The dispersion behavior of the doped sample shows high resistance of cobalt-nickel ferrite with ferromagnetic nature. X-ray diffraction pattern of the doped sample reveals single-phase cubic spinel structure. It is also seen that increment or decrement in these properties depends on the dopant concentration, the type of dopant, sintering temperature and also on the method of preparation of the sample.

References

[1] Shirsath, S. E., Jadhav, S. S., Toksha, B. G., Patange, S. M. and Jadhav, K. M., Scripta Materialia, 64 (2011) 773.

[2] Mooney, K. E., Nelson, J. A. and Wagner, M. J., Chemistry of Materials, 16 (2004) 3155.

[3] Wang, W., Ding, Z., Zhao, X., Wu, S., Li, F., Yue, M. and Li, J. P., Journal of Applied Physics, 117 (2015) 17A328.

[4] Stein, C. R., Bezerra, M.T.S., Holanda, G.H.A., Andre-Filho, J. and Morais, P. C., AIP Advances, 8 (2018) 056303.

[5] Tailhades, P., Villette, C., Rousset, A., Kulkarni, G. U., Kannan, K. R., Rao, C. N. R. and Lenglet, M., Journal of Solid State Chemistry, 141 (1998) 56.

[6] Chae, K. P., Lee, J.-G., Kweon, H. S. and Lee, Y. B., Journal of Magnetism & Magnetic Materials, 283 (2004) 103.

[7] Velhal, N. B., Patil, N. D., Shelke, A. R., Deshpande, N. G. and Puri, V. R., AIP Advances, 5 (2015) 097166.

[8] Batoo, K. M., Raslan, E. H., Yang, Y., Adil, S. F., Khan, M., Imran, A. and Al-Douri, Y., AIP Advances, 9 (2019) 055202.

[9] Nongjai, R., Khan, S., Asokan, K., Ahmad, H. and Khan, I., Journal of Applied Physics, 112 (2012) 084321.

[10] Muthurani, S., Balaji, M., Gautam, S., Chae, K. H., Song, J. H., Padiyan, D. P. and Asokan, K., Journal of Nanoscience & Nanotechnology, 11 (2011) 5850.

[11] Samavati, A., Mustafa, M. K., Ismail, A. F., Othman, M. H. D. and Rahman, M. A., Materials Express, 6 (2016) 473.

[12] Sekhar, B. C., Rao, G. S. N., Caltun, O. F., Lakshmi, B. D., Rao, B. P. and Rao, P. S. V., Journal of Magnetism and Magnetic Materials, 398 (2016) 59.

[13] Sanpo, N., Wang, J. and Berndt, C. C., Journal of Nano Research, 25 (2013) 110.

[14] Margabandhu, M., Sendhilnathan, S., Senthilkumar, S. and Gajalakshmi, D., Brazilian Archives of Biology and Technology, 59 (2016) e161046.

[15] Singh, R. K., Rai, B. C. and Prasad, K., International Journal of Advanced Materials Science, 3 (2012) 71.

[16] Singhal, S., Singh, J., Barthwal, S. K. and Chandra, K., Journal of Solid State Chemistry, 178 (2005) 3183.

[17] Choi, W.-O., Lee, J,-G., Kang, B.-S. and Chae, K. P., Journal of Magnetics, 19 (2014) 59.

[18] Mozaffari, M., Amighian, J. and Darsheshdar, E., Journal of Magnetism and Magnetic Materials, 350 (2014) 19.

[19] Abdul-Gaffoor, D. R., International Journal of Engineering Research and Applications, 4 (2014) 73.

[20] Velhal, N. B., Patil, N. D., Shelke, A. R., Deshpande, N. G. and Puri, V. R., AIP Advances, 5 (2015) 097166.

[21] Sontu, U. B., Yelasani, V. and Musugu, V. R., Journal of Magnetism and Magnetic Materials, 374 (2015) 376.

[22] Singh, A., Singh, J. and Dosanjh, H. S., Journal of Chemical and Pharmaceutical Research, 7 (2015) 612.

[23] Hankare, P. P., Sanadi, K. R., Garadkar, K. M., Patil, D. R. and Mulla, I. S., Journal of Alloys and Compounds, 553 (2013) 383.

[24] Faheim, A. S., Abd El Fattah, M. K. E., Abdul Rahman, A. H. and Badawi, A., Journal of Nanomaterials & Molecular Nanotechnology, 4 (1) (2014) 1000155.

[25] Faheim, A. S., Abd El Fattah, M. K. E. and Badawi, A., IOSR Journal of Applied Chemistry, 7 (2014) 30.

[26] Jadhav, S. S., Shirsath, S. E., Patange, S. M. and Jadhav, K. M., Journal of Applied Physics, 108 (2010) 09920.

[27] Nasrin, S., Manjura Hoque, S., Chowdhury, F.-U.-Z. and Moazzam Hossen, M., IOSR Journal of Applied Physics, 6 (2014) 58.

[28] Yaseneva, P., Bowker, M. and Hutchings, G., Physical Chemistry-Chemical Physics, 13 (2011) 18609.

[29] Coppola, P. and da Silva, F.G., Journal of Nanoparticle Research, 18 (2016) 138.

[30] Vaidyanatham, G., Sendhinatham, S. and Arulmurugan, R., Journal of Magnetism and Magnetic Materials, 313 (2007) 293.

[31] Jamila, M. T., Ahmada, J., Bukharia, S. H., Sultanb, T., Akhterc, M. Y., Ahmadd, H. and Murtaza, G., Journal of Ovonic Research, 13 (2017) 45.

[32] Tapdiya, S. and Shrivastava, A. K., International Journal of Innovative Research in Science, Engineering and Technology, 5 (5) (2016) 6681.

[33] Singhal, S., Namgyal, T. S., Bansal, S. and Chandra, K., Journal of Electromagnetic Analysis and Applications, 2 (2010) 376.

[34] Nlebedim, I. C., Vinitha, M., Praveen, P. J., Das, D. and Jiles, D. C., Journal of Applied Physics, 113 (2013) 193904.

[35] Vinayak, V., Khirade, P. P., Birajdar, S. D., Gaikwad, P. K., Shinde, N. D. and Jadhav, K. M., International Advanced Research Journal in Science, Engineering and Technology, 2 (3) (2015) 55.

[36] Mercy, S. J., Murali, N., Ramakrishna, A., Ramakrishna, Y., Veeraiah, V. and Samatha, K., Applied Physics A,126 (2020)873.

[37] Dhole, V. V., Khirade, P. P., Kale, C. M., Patil, V. G., Shinde, N. D. and Jadhav, K. M., International Journal of Innovative Science, Engineering & Technology, 2 (2015) 387.

[38] Bhandare, S. V., Kumar, R., Anupama, A. V., Mishra, M., Kumar, R. V., Jali, V. M. and Sahoo, B., Materials Chemistry and Physics, 251 (2020) 123081.

Volume 15, Number 1, 2022. pp. 67-79

Jordan Journal of Physics

ARTICLE

Natural Extracts-mediated Biosynthesis of Zinc Oxide Nanoparticles and Their Multiple Pharmacotherapeutic Perspectives

A. G. M. Haldar[a], **D. Kar Mahapatra**[b], **K. M. Dadure**[c] and **R. G. Chaudhary**[d]

[a] *Department of Applied Chemistry, Priyadarshini Bhagwati College of Engineering, Nagpur 440009, Maharashtra, India.*

[b] *Department of Pharmaceutical Chemistry, Dadasaheb Balpande College of Pharmacy, Nagpur 440037, Maharashtra, India.*

[c] *Department of Chemistry, J. B. College of Science, Wardha 442001, Maharashtra, India.*

[d] *Post-graduate Department of Chemistry, S. K. Porwal College, Kamptee, Nagpur 441001, Maharashtra, India.*

Doi: **https://doi.org/10.47011/15.1.10**

Received on: 01/08/2020; *Accepted on: 01/09/2021*

Abstract: Eco-friendly green syntheses of nanoparticles (NPs) have involved the natural biomass contents since over a decade. The NPs of zinc oxide (ZnO) have important applications in diagnostics, detection of biomolecules, opto-electronic devices, microelectronics like electromagnetic coupled sensor laser devices, neutralization of environmental hazard pollutants as well as pharmaceutical components from water. ZnO-NPs play a pivotal role in drug delivery, exhibiting biomedical activities, such as anti-pathogenics, diagnosis of various diseases, anti-oxidants etc. The interest in synthesizing ZnO-NPs *via* the biological method (plant extracts) has increased considerably in the last few decades. The development of this new approach and the significant interest in it are mainly related to the absence of toxic chemicals or high-energy applied methods to the biological synthesis which develop more environmentally friendly and cost-effective methods. This review article focuses on recent (January 2020 to May 2020) plant-mediated green synthetic methods which are highlighted comprehensively in this review article.

Keywords: Zinc, Nanoparticles, Natural, Synthesis, Plant, Extract.

Introduction

Nanotechnology has been a subject of great research and enthusiasm for researchers in recent years [1]. Nanomaterials having nanoscale dimensions possess unique properties as compared to their micro-molecules. The most current approach focuses on more cost-effective techniques for creating and manipulating materials at the nanometer scale [2]. The research on nanomaterials is one of the most demanding and greatly growing areas in the branch of science and engineering. Nanoparticles (NPs) of different noble metals have been already in practice for therapeutic purposes since centuries ago. These NPs proved to be very valuable for pharmaceutical, biomedical and tissue engineering [3].

Synthesis of NPs is conducted by biological or green technology and physical and chemical methods. The two end processes of developing NPs have been accompanied by costly and environmentally hazardous effects. In chemical synthesis, toxic and hazardous chemicals are involved in NP synthesis, which causes various ecological risks and serious diseases.

Corresponding Author: A. G. M. Haldar **Email**: animesh2477@gmail.com

Pharmacological importance of zinc oxide (ZnO) nanoparticles has been studied for their unique characteristics [4]. Due to the large surface area of the ZnO-NPs, they are used to remove hazardous chemicals, like chromium and lead from effluents [5], as well as hazardous components from radioactive effluents [6]. The nanoparticles of ZnO have important applications in diagnostics, detection of biomolecules, opto-electronic devices, microelectronics like electromagnetic coupled sensor laser devices [7], neutralization of environmental hazard pollutants as well as pharmaceutical components from water [8-10]. In the area of pharmacological research, ZnO-NPs play a pivotal role in drug delivery, exhibiting biomedical activities, such as anti-pathogenics, diagnosis of various diseases, anti-oxidanst, … etc. These NPs of ZnO are very prominent against pathogenic species such as *E. coli, Salmonella*, *S. aureus* and *B. subtilis* using different susceptibility test protocols, as has been reported [11].

Plausible Mechanism(s) of ZnO Nanoparticle Formation

Eco-friendly green syntheses of NPs have involved the plant contents since over a decade. Since the early twentieth century, it has been found out that the plant extracts have the capability to reduce metal ions to their reduced form. This has come in the limelight of experimental form only a few decades ago for the reduction of metal salts. The different bioactive molecules, like phenols, alkaloids, citric acid, terpenes, polyphenolic, flavonoids, ascorbic acid, and many more present in the plant extract, play an important role as reducing agents. The biosynthesis of nanoparticles through plant biomass is very important in the field of nanotechnology, because the plant extract acts as both a capping and a reducing agent. The development of this new approach and the significant interest in it are mainly related to the absence of toxic chemicals or high-energy applied methods to the biological synthesis, which develop methods that are more environmentally friendly and cost-effective. The plant-oriented mechanism involves an intracellular and an extracellular pathway to synthesize the nanoparticles. In the intracellular pathway, the metals are absorbed through the roots by utilizing growing media of plant with the metal-rich organic component, metal-enriched soil and hydroponic solution with high metal contamination [12-15]. The extracellular pathway involved the synthesis of NPs by using the extracts (by boiling and crushing) of different parts of the plants (Fig. 1) [16].

Plant-mediated Biosynthesis of ZnO Nanoparticles and Their Applications

In the last several decades, there has been a surge in interest in biologically manufacturing ZnO-NPs. Literature indicates that the biosynthesis of metal oxides or reduced to metallic NPs is more eco-friendly than the conventional physicochemical methods used presently. These fabrciated ZnO-NPs of varied shapes, like spherical, hexagonal, quasi-spherical, rod, … etc. demonstrate diverse pharmacological applications ranging from anti-fungal (*Alternaria mali*, *Aspergillus fumigatus*, *Aspergillus niger, Candida albicans*), anti-bacterial (*Bacillus pumilus*, *Bacillus subtilis*, *Escherichia coli*, *Pseudomonas aeruginosa*, *Salmonella typhi*, *Staphylococcus aureus*, and *Vibrio cholera*), anti-nociceptive, anti-proliferative, anti-mitotic, anti-inflammatory, anti-diabetic, anti-leishmanial, osteoclast inhibition, anti-oxidant, dressing element, local anesthetics, muscle relaxants, … etc. The plant-mediated green synthetic methods or biological methods are highlighted comprehensively.

Anti-microbial Applications of ZnO-NPs

Sara Zafar *et al.* have synthesized eco-friendly ZnO-NPs by utilizing $ZnSO_4.7H_2O$ with the help of aqueous extract of seeds of sesame. They have developed spherical-shaped 9.07 nm particles of ZnO. The anti-bacterial activity of newly synthesized Zn-NPs possesses greater values against various bacteria compared to the std. gentamicin. The zone of inhibition produced by Zn-NPs against various strains of Bacteria is: *P.aeruginosa* (12.6mm), *E.coli* (10.4mm), S.*pneumonia* (8.6 mm) and *S.aureu* (4.1mm) with respect to 120µg/l [17].

Velsankar *et al.* conducted an experiment to prepare cost-effective and environment-friendly ZnO-NPs by biogenic reduction of $Zn(CH_3COO)_2.2H_2O$ through deionized water and ethanol mixed extract of grain powder of *Echinochloa frumentacea* which produced nanoparticles of hexagonal shape and size of 35-85 nm. The antibacterial activity of ZnO-NPs has a higher antibacterial effect against *Bacillus pumilus* and *Salmonella typhi* than a standard

drug of ciprofloxacin. Results showed that the zone of inhibition rate was perceived at 18, 20, 23, 24, 26 and 29 mm (against *Bacillus pumilus* bacterium) and at 13, 16, 18, 21, 25 and 27 mm (against *Salmonella typhi* bacterium) for 25, 50, 100, 250, 500 and 1000 µg/mL concentrations, respectively. Nature of the diversity in the cell wall structure is responsible for different zones of inhibition rate against *Bacillus pumilis* and *Salmonella typhi* [18].

Ahmad *et al.* have studied the green synthesis of ZnO-NPs with the help of *Euphorbia hirta* leaves extract which acted as a reducing and capping agent with zinc nitrate ($ZnNO_3$) as a precursor of the reaction. The newly formed ZnO-NPs have a spherical shape with 20-25 nm size. The antibacterial study of synthesized nanoparticles clearly revealed that the zone of inhibition increases with increasing the conc. of ZnO-NPs (20-100 mg/ml), which may be due to the increase of H_2O_2 concentration from the surface of ZnO-NPs. In measuring zone of inhibition, *Streptococcus aureus* (29 mm) was found to be highest when compared to other bacteria, like *Streptococcus mutans* (28 mm), *Clostridium absonum* (27 mm), *Escherichia coli* (24 mm) against the std. drug streptomycin which was used as a control [19].

Di *et al.* have reported the biosynthesis of ZnO-NPs by treating radish root (*Raphanus sativus*) extract with zinc acetate dihydrate [$Zn(CH_3CO_2)_2 \cdot 2H_2O$] as the initiator of the reaction. The reported NPs have hexagonal-shaped morphology with 15-25 nm size. Antibacterial property of synthesized ZnO-NPs, displayed on multidrug-resistant bacteria along with ATCC microbial strains, correlated with the zone of inhibition (mm). MDR-*Staphylococcus aureus* showed highest zone of inhibition (21.23 ± 1.16 mm) and *S.aureus* ATCC 29213 showed an inhibition zone of (21.32 ± 1.53 mm) when compared with ZnO-NPs and plant extract. Lowest zone of inhibition was observed by *E.faecalis* ATCC 29212 (11.23 ± 0.58 mm). Excellent antibacterial activity towards microbes isolated from diabetic foot ulcers, like *P.aeruginosa* ATCC 27853, MDR-*E.coli*, *S.aureus* ATCC 29213, MDR-MRSA, *E.coli* ATCC 25922, *E.faecalis* ATCC 29212, MDR-*P.aeruginosa* and MDR-*A.baumannii*, was shown using the disc diffusion method [20].

Fahimmunisha *et al*. have revealed an interesting fact regarding flora-mediated synthesis of ZnO-NPs employing an aqueous extract of *Aloe socotrina* leaf by utilizing zinc acetate dihydrate as the precursor. The spherical-shaped NPs of 15-50 nm size exhibited interesting pharmacological activity. The antibacterial action showed that *Aloe socotrina(As)*-ZnO-NPs had dynamic dose-dependent activity against UTI pathogens, such as *Escherichia coli*, *Klebsiella pneumonia, Proteus vulgaris* (HQ640434), *Pseudomonas aeruginosa* (ATCC) and the maximum zone of inhibition was shown against *E. coli* (19.2± 0.8mm) and *P. vulgaris* (25.0±0.9mm). The *As* extract and *As*–ZnO-NPs showed bacteriostatic activity against *Proteus vulgaris* and *Pseudomonas aeruginosa* at low concentrations of 75 µg/mL and 50 µg/mL, respectively. The synthesized ZnO nanoparticles have anti-biofilm properties [21].

Maruthupandy *et al.* have synthesized eco-friendly ZnO-NPs by utilizing zinc nitrate hexahydrate [$Zn(NO_3)_2 \cdot 6H_2O$] and reducing it with the help of aqueous extract of *Camellia japonica* leaf. The synthesized NPs were spherical-shaped and 15-30 nm in size. The antibacterial activity of ZnO-NPs against gram-positive bacteria was found to be 21mm and 11.5mm for *S. pneumoniae* and *B. subtilis* at 100 µg/mL concentration, respectively. The NPs showed better activity at 100 µg/mL concentration against gram-negative bacteria with zone of inhibition of 10.5, 18 mm and 11, 12 mm for *E. coli* and *S. typhimurium*, respectively. The size of inhibition zone was concentration-dependent of ZnO-NPs. The results revealed that the sensitivity of *S. pneumoniae* was higher at the lowest concentration of ZnO-NPs. The maximum zone of inhibition of *S. pneumoniae* (21 mm) was higher at the highest concentration of ZnO-NPs when compared to other pathogens [22].

Rasli *et al.* have reported the fresh *Aloe vera* leaf-mediated ZnO-NPs with the help of aqueous extract by utilization of zinc nitrate used as the precursor. The research revealed the fabrication of rod-shaped 16-nm NPs. The antibacterial action was measured by the active inhibition zone around 1.325mm^2 against *E. Coli* after 24 h of incubation. The inhibition zone clearly indicates that membrane disruption leads to the death of pathogens. ZnO is a well-known antibacterial agent and is effective at very low

concentration of bacteria as compared to the standard [23].

Mydeen *et al.* synthesized ZnO-NPs from the precursor zinc acetate dihydrate through an eco-friendly approach utilizing the aqueous extract of *Prosopis juliflora* leaf. The spherically shaped NPs of 83 nm size demonstrated notable anti-pathogenic activities. The antibacterial activities have been carried out (*in vitro*) against four different pathogens *viz E.coli, R. rhodochrous, B. subtilis* and *V.cholera* against streptomycin sulfate as standard. A higher zone of inhibition of 25 mm was perceived in the gram-negative bacteria *V.cholera* similar to other gram-positive bacterial strains. Observations concluded that the synthesized ZnO-NPs had an antibacterial character confirmed by clear zone of inhibition representing biocidal behavior. They were distributed in the bacterial membranes and the formation of surface oxygen species from ZnO led to bacterial cell death [24].

Uma *et al.* have studied the potentials of flora-mediated synthesis of ZnO-NPs by reducing the precursor zinc acetate with aqueous extract of fresh plum fruits. From antibacterial activity of ZnO-NPs, it can be inferred that the growth of bacterial cells was lower than that of cells in the control, indicating that ZnO-NPs could inhibit the growth of bacterial cells. The percentage of bacterial growth decreased to 5.1-100% for *E.coli* and 23.43-99.48% for *S.aureus*, respectively. Maximum and minimum growth reduction was at 80 ppm and 20 ppm, respectively. Results concluded that *S.aureus*, being the gram-positive bacteria having single peptidoglycan layer, seemed to be more sensitive to the ZnO-NPs as compared to the *E.coli* having two outer membranes; i.e., peptidoglycan and outer lipid membrane. There was a sharp reduction in the growth of *S.aureus* with the increase in concentration of ZnO-NPs [25].

Awwad *et al.* applied an eco-friendly aqueous extract of *Ailanthus altissima* fruits and synthesized spherical-shaped ZnO-NPs of size 5-18 nm from the precursor zinc nitrate hexahydrate [$Zn(NO_3)_2 \cdot 6H_2O$]. Antibacterial activity of synthesized ZnO-NPs was tested on gram-negative bacteria *E.coli* and gram-positive bacteria *S.aureus.* As the concentration of ZnO-NPs increases, the zone of inhibition also increases against the bacteria strains. ZnO-NPs (0.5mg/ml) have a significant growth inhibition effect against *S.aureus and E.coli* bacteria. This effect is due to high surface area of ZnO-NPs and their small particle size of 12 nm. ZnO-NPs performed antimicrobial activities when tested against *Staphylococcus aureus, Bacillus subtilis, Proteus vulgaris, Pseudomonas aeruginosa, Candida albicans and Aspergillus niger* and gave good inhibition results [26].

Ansari *et al.* revealed the interesting potentials of flora-mediated synthesis of ZnO-NPs from an aqueous extract of *Cinnamomum verum* by utilizing [$Zn(NO_3)_2 \cdot 6H_2O$] as the precursor. The synthesized spherical NPs of 45-nm size showed promising antibacterial activity. The green synthesized ZnO-NPs showed significant inhibition against the test pathogens (*S.aureus* and *E.coli*) compared to the control. ZnO-NPs offered a maximum zone of inhibition of 16.75 mm and 13.25 mm observed against *S.aureus* and *E.coli*, respectively. Observations resulted in that the gram-positive (*S.aureus*) bacteria showed to be more sensitive to the green synthesized ZnO-NPs compared to the gram-negative (*E.coli*) bacteria. The green synthesized ZnO-NPs inhibited the growth of *E.coli* and *S.aureus* with an MIC of 125µg/mL and 62.5 µg/mL, respectively. The results concluded that the synthesized ZnO-NPs can be used as a potential antimicrobial agent against harmful pathogens [27].

Ahmad *et al.* have designed and synthesized environmentally friendly originated ZnO spherical NPs of size 52-70 nm from the aqua extract of *Eucalyptus globules* leaf by utilizing zinc nitrate hexahydrate [$Zn(NO_3)_2 \cdot 6H_2O$] as the precursor. The aqueous broth was observed to be an effcient reducing agent, leading to the rapid formation of ZnNPs of varied shapes with sizes ranging between 52–70 nm. In addition, antifungal activity of the biosynthesized ZnNPs was evaluated against major phytopathogens of apple orchards. The fungal growth inhibition rate was found to be 76.7% for *Alternaria mali*, followed by 65.4 and 55.2% inhibition rate for *Botryosphaeria dothidea* and *Diplodia seriata*, for 100ppm of ZnNPs, respectively [28].

Anti-diabetic Applications of ZnO-NPs

Bayrami *et al.* have synthesized eco-friendly ZnO-NPs by utilizing [$Zn(NO_3)_2 \cdot 6H_2O$] as a precursor with the aid of aqueous leaf extract of nettle (*Urtica dioica*). The antidiabetic activity of ZnO and ZnO-extract samples was examined through injection to alloxan-diabetic rats for a period of 16 days. The levels of insulin, FBS,

TG, TC and HDLC were measured in the blood serums of the treated rats before and after treatment. A statistical comparison was carried out for the level of insulin in rats suffering from diabetes, prior to and following the treatment. The level of insulin in non-diabetic healthy rats was 1.66 mg/L. This level was significantly reduced to 0.6 mg/L in rats with diabetes [29].

Anti-nociception Applications of ZnO-NPs

Xu *et al.* have reported the biosynthesis of ZnO-NPs with the help of deionized water extract of fresh leaves of *Selaginella convolute* by utilization of the precursor zinc acetate for bioreduction. This research highlighted the formation of spherical-shaped 40-nm ZnO-NPs. The ZnO-NPs and *S.convolute* extract possess an important antinociceptive operation (where $P < 0.001$) at the studied concentrations. For both ZnO-NPs as well as *S.convolute* extract, they have a dose-dependent impact. The percentage of *S.convolute* extract analgesic impact at 50 mg/kg was 66.45%, whereas at 100 mg/kg, it was 78.98%. Likewise, at levels of 5 and 10 mg/kg, the percentage of acetic acid attenuation caused writhes for ZnO-NPs of 72.87 and 80.76 %. The muscle relaxant impact of ZnO-NPs as well as *S.convolute* extract resulted in that post 20 min of administration, *S.convolute* extract at 50 and 100 mg/kg generated an important muscle relaxant activity (where $P < 0.05$) in both the traction and chimney studies. In the traction study, ZnO-NPs showed equally important (where $P < 0.05$) muscle relaxant impacts at 5 and 10 mg/kg, but the impact was noticed to be more pronounced in the chimney experiment at 10 mg/kg (where $P < 0.01$). The normal 0.25 mg/kg injection of diazepam generated an important muscle relaxant activity (where $P < 0.01$) in both studies [30].

Wang *et al.* have synthesized eco-friendly approach-based ZnO-NPs from $Zn(CH_3COO)_2.2H_2O$ with the help of aqueous extract of *Fraxinus rhynchophylla* wood. The ecosynthesized ZnO-NPs of 100-200 nm size were assessed for anti-nociceptive property by using different models. The sedative effect of synthesized ZnO-NPs was evaluated with an open field test. Results of both thermal stress-induced methods (hot-plate and tail-immersion nociception tests) verified that the synthesized ZnO nanoparticles are a potent antinociceptive drug. ZnO nanoparticles effectively reduced the abdominal writhes in acetic acid-induced nociception and significantly decreased the nociception activity in other glutamate-, capsaicin- and formalin-induced nociception models. Open-field experiment proved that synthesized ZnO nanoparticles are less sedative compared to the standard antinociceptive drug morphine [31].

Wound Healing Applications of ZnO-NPs

Zhang *et al.* have reported the plant-mediated synthesis of ZnO-NPs by using *Allium saralicum* R.M. Fritsch leaf extract with zinc nitrate hexahydrate $Zn(NO_3)_2.6H_2O$ as the initiator of the reaction. The reported spherical-shaped NPs have 19 nm of average size. In search of wound healing effects of zinc nitrate, *A.saralicum(As)* and ZnNPs-As, 0.2% ointments were formulated and compared with the control and untreated groups. The use of ZnNPs-As ointments significantly ($P \leq 0.01$) raised the wound contracture, vessel, hydroxyl proline, hexuronic acid, hexosamine, fibrocyte, fibroblast and fibrocytes/fibroblast rates and significantly ($P \leq 0.01$) decreased the wound area, total cells, neutrophil, macrophage and lymphocyte compared to other groups in rats. As per observation, ZnNPs-*As* may be consumed for the treatment of cutaneous wounds and infectious diseases in humans [32].

Local Anesthetic Applications of ZnO-NPs

Cui *et al*. have reported the biosynthesis of ZnO-NPs by using aqueous extract of *Cinnamon zeylanicum* leaf with $Zn(CH_3COO)_2.2H_2O$ as initiator for bioreduction. The reported spherical-shaped NPs of 20 nm size expressed potent local anaesthetic properties. The activity of local anaesthesia was tested in frog models and it was observed that withdrawal reflex of frog's foot time of anaesthesia onset was 8.17, 15.00, 6.5 and 10.50 min at a dosage of 40 mg, 12 mg, 80 mg and 20 mg of the methanolic ZnO-NPs, respectively. ANOVA (one-way analysis of variance) displays that local anaesthetic activity was extremely significant [33].

Bone (Osteo) Applications of ZnO-NPs

Dongyan *et al.* synthesized spherical-shaped ZnO-NPs of 20-nm size from precursor zinc acetate dihydrate by an environmentally friendly approach through an aqueous extract of *Artemisia annua* stem barks. The synthesized NPs have worked as an inhibitor of osteoclast formation related to bone deformities and bone-related diseases. The viability of MG-63 cells

was assayed by MTT test and osteogenic-related assays, like real-time PCR and mineralization assay, were adopted to determine the effects of *A. annua* ZnO-NPs on the multiplication and differentiation of human osteoblast-like MG-63cells. The synthesized *A.annua* ZnO-NPs enhanced the proliferation, differentiation and mineralization without causing significant cytotoxic impact on MG-63 cells. These effects indicate that *A.annua* ZnO-NPs can both stimulate bone formation *via* the differentiation of MG-63 cells. Hence, it was concluded that *A. Annua* ZnO-NPs can be a promising agent for the treatment of bone deformities and bone-related diseases [34].

Anti-cancer Applications of ZnO-NPs

Duan *et al.* have demonstrated the flora-mediated generation of ZnO-NPs through water and alcoholic extracts of leaves of *Cardiospermum halicacabum(CH)*. The NPs of spherical shape and 10-20 nm size expressed promising cytotoxic capacity. The cell adhesion assay showed better adherent results for the time of 24 hr and 12 hr, respectively. *C.halicacabum* ZnO-NPs (12.5 µg/mL) exposed moderate (12 hr incubation) and much adhesion (24 hr incubation) to the adherent cells and the standard doxorubicin (2 µM/mL).The mRNA expression of apoptotic genes like caspase 3, 8 and 9 was elevated followed by the exposure to ZnO nanoparticles and it was narrowly proved that ZnO nanoparticles stimulate the apoptotic cell necrosis at the transcriptional stage. CH-ZnO nanoparticles persuaded programmed cell necrosis *via* elevated ROS levels in cells. CH-ZnO-NPs further stimulates the markers of apoptosis and aggravates necrosis of cancerous cells, toxicity to cells and increase of ROS. With observations, this might accomplished that CH-ZnO-NPs complexed with *CH* appreciably possessed a toxicity to human melanoma cells (A375) *via* provoking the apoptotic cell necrosis [35].

Zheng *et al.* have revealed interesting facts about the biosynthesis of ZnO-NPs in the presence of an aqueous solution of *Rhizoma paridis* saponins extract with zinc acetate initiator. The results found that spherical-shaped 100nm NPs were produced. The *R. paridis* saponins-based ZnO NPs (RPS-ZnO NPs) have been seen to destroy the mitochondria and cause necrosis of cells by increasing intracellular anti-oxidant generation. The research revealed that supplementation of RPS-ZnO NPs changed the morphological linkage with Molt-4 cells, which resulted in the induction of apoptosis [36].

Tang. *et al.* have developed ZnO-NPs of 100 nm size through an eco-friendly process by employing [$Zn(NO_3)_2 \cdot 6H_2O$] as the precursor along with water extract of leaves of *Morus nigra(MN)*. The synthesized spherical-shaped NPs have been reported to exhibit the anticancer effect against AGS cells and were analyzed through cell viability, apoptotic morphological variations by AO/EtBr, alterations of mitochondrial membrane potential (MMP), cell cycle arrest, lipid peroxidation status (TBARS), antioxidants (SOD, GSH and CAT) and generation of ROS. The status of apoptosis genes, such as bax, caspase-9, caspase-3 and Bcl-2 expressions, was analyzed by using RT-PCR techniques. Observation revealed that gastric cancer cells demonstrated cell death by MN-ZnO-NPs treatment. The MN-ZnO-NPs induced apoptosis by enhanced formation of ROS, decreased MMP, increased lipid peroxidation, decreased antioxidants and induced cell cycle arrest, as was observed [37].

Mohammad *et al.* utilized the precursor zinc acetate dihydrate $Zn(CH_3COO)_2.2H_2O$ for the synthesis of ZnO-NPs by using aqueous extract of Hyssop (*Hyssopus officinalis*) leaf. The obtained spherical NPs demonstrated impressive anti-cancer activity. The green synthesis of *Hy*-ZnO-NPs affects PC3 cell line and BALB/c mice model. The cytotoxicity of ZnO-NPs was assessed on PC3 cell line by MTT test and apoptotic effect of ZnO-NPs was determined by *in vitro* AO/PI staining. The expression of major genes involved in spermatogenesis and sperm maturation (Adam3, Prm1, Spata19, Tnp2 and Gpx5) was also analyzed. The obtained results showed that the IC_{50} for PC3 cell line was reported to be 8.07 and 5 µg/ml (24 and 48h). Meanwhile, the induced apoptosis was recorded as 26.6% ± 0.05, 44% ± 0.12 and 80% ± 0.07 of PC3 cells. The percentage of induced apoptosis by ZnO-NPs was reported as 80% apoptosis in PC3 cells treated with 19.53 µg/ml of green-synthesised ZnO-NPs. These results indicated that along with the increment of treatment duration and concentration of green-synthesised ZnO-NPs, apoptosis may increase [38].

Selim *et al.* revealed an interesting biosynthesis approach for ZnO-NPs through an aqueous extract of *Deverra tortuosa* plant by

utilizing [$Zn(NO_3)_2 \cdot 6H_2O$] as the precursor. The reported NPs have a spherical shape with a size range of 9.26-31.18 nm. The potential anticancer activity was investigated against two cancer cell lines "Caco-2" and "A549" compared to their activities on the human lung fibroblast cell line (WI38) using the MTT assay. Both the aqueous extract and ZnO-NPs showed a remarkable selective cytotoxicity against the two examined cancer cell lines investigated using doxorubicin as the positive control, and the untreated cells as the negative control. This effect was concentration-dependent, IC_{50} values of A549 cells were 193.12 and 83.47, while IC_{50} values of Caco-2 cells were 136.12 and 50.81 µg/mL by the extract and ZnO-NPs, respectively. Significantly higher IC_{50} values of 902.83 and 434.60 µg/ml were obtained from the treatment of the normal lung epithelial cell (WI38) with the respective materials [39].

Nilavukkarasi *et al.* have reported the biosynthesis of ZnO-NPs by using *Capparis zeylanica* leaf extract with zinc acetate dihydrate [$Zn(CH_3CO_2)_2 \cdot 2H_2O$] as an initiator of the reaction. The reported NPs were of spherical-shape and 32-40 nm size. Observation exposed that microbial growth decreases with increase in the concentration of synthesized ZnO-NPs investigated against gram-positive bacteria (*Staphylococcus epidermidis*, *Enterococcus faecalis*), gram-negative bacteria (*Salmonella paratyphi*, *Shigella dysenteriae*) and fungi (*Candida albicans*, *Aspergillus niger*) by well diffusion method. Cytotoxicity of biosynthesized ZnO nanoparticles treated with lung cancer cell line (A549) was analyzed by cell proliferation assay. Synthesized ZnO-NPs could reduce cell viability after 48 h with significant decreases in cell viability at 22% and 38%. The morphological changes of A549 cells were exposed in higher concentrations of treated cells including cell shrinkage and extensive detachment of the cells. Therefore, bio-mediated ZnO nanostructures proved to be an excellent novel antimicrobial and anticancer material [40].

Multiple Applications of ZnO-NPs

Mohamed *et al.* have reported an interesting way of biosynthesizing ZnO-NPs from the aqueous extract of *Hyphaene thebaica* fruit by utilizing zinc acetate dihydrate as the precursor. The synthesized quasi-spherical-shaped NPs of size of 8-23 nm demonstrated dose-dependent promising results against anti-microbial potential, anti-oxidant potential, anti-leishmanial potential and cytotoxicity dependence. Excellent protein kinase (PK) inhibition and varying antimicrobial potential against different bacterial and fungal strains are reported. *E.coli* and *A.flavus* were found the most susceptible microbial strains. MTT assay revealed an IC_{50} of 106 µg/mL against *Leishmania tropica*. Antifungal activities of the ZnO-NPs across different test concentrations (4–250 µg/mL) were reported. ZnO-NPs indicated varying antifungal potential against the tested fungal strains. *A. flavus* and *A. niger* revealed highest susceptibility to the nanoparticles (4 mg/mL) and zones of 11.8 mm and 10 mm were obtained, respectively. Excellent protein kinase inhibition potential is reported with the highest zone of inhibition reported as 12 mm at 4 mg/mL and the diameter of the zones gradually declined with the decrease in concentration. Streptomycin control revealed an inhibition zone of 31.5 mm. Different antioxidant assays indicated the antioxidant potential of ZnO-NPs. The DPPH radical scavenging activity was 55% at 400 µg/mL and 22% at 25 µg/mL. Total antioxidant capacity was recorded as 39.6 µg AAE/mg at 400 µg/mL. The highest value recorded for the reducing power was 79 µg AAE/mg at 400 µg/mL [41].

Karunakaran *et al.* have synthesized eco-friendly ZnO-NPs by utilizing zinc nitrate hexahydrate [$Zn(NO_3)_2 \cdot 6H_2O$] with the help of aqueous extract of flower of *Hylotelephium telephium* subsp. The synthesized NPs have an oval to spherical shape with 83 nm size. The developed NPs have antioxidant (free radical scavenging activity) and anti-pathogenic activity. The percentage of free radicals scavenged by the ZnO-NPs increased with an increase in their masses, exhibiting 18% (1 mg), 35% (5 mg), 50% (10 mg) and 75% (100 mg). The clear zone around the nanoparticles indicates their antibacterial activity against the tested bacteria *S.aureus* and *K.pneumoniae*. Streptomycin was used as a standard. The ZnO-NPs showed 16 ± 0.24 mm and 14 ± 0.38 mm, respectively. The antibacterial activity of the tested nanoparticles might be due to their interaction with the peptidoglycan layer mediated by electrostatic interaction [42].

Jayappa *et al.* have reported the biosynthesis of ZnO-NPs by employing the air-dried leaves of *Mussaenda frondosa* extract with zinc nitrate

hexahydrate [$Zn(NO_3)_2 \cdot 6H_2O$] as the initiator for developing NPs. The spherical-shaped ZnO-NPs had a 5-20 nm size. The ZnO-NPs expressed exceptional pharmacological activities, like anti-diabetic, anti-oxidant, anti-cancer and anti-microbial activities. The IC_{50} values of ZnO-NPs for quenching DPPH radical was found to be 824 µg/ml (L-ZnO-NP), 752 µg/ml (S-ZnO-NP) and 857 µg/ml (C-ZnO-NP). The S-ZnO-NPs (from stem) exhibited effective antioxidant activity compared to L-ZnONP (from leaf) and C-ZnO-NP (from callus). It was observed that all the ZnO-NPs showed inhibition against all the tested strains except for *P.vulgaris*. Among the tested strains, *E.coli* was found to be more susceptible to S-ZnO-NPs with 28.64 mm zone of inhibition ($p < 0.05$) compared to the standard. The highest mean zone of inhibition observed against *P. aeruginosa*, *S.aureus* and *B. subtilis* was found to be 20.31 mm (S-ZnO-NP), 21.51 mm (C-ZnO-NP) and 19.13 mm (S-ZnO-NP), respectively at $P < 0.05$. Highly significant MIC was recorded against *E.coli* at 19.23 µg/ml with $P < 0.05$, which was followed by the activity against *P.aeruginosa, S.aureus* and *B.Subtilis*, showing MIC values of 35.46, 54.13 and 93.14 µg/ml. as compared with MIC values of the standard (8.44 to 22.13 µg/ml) [43].

Dhandapani *et al.* revealed the biosynthesis of ZnO-NPs through an aqueous extract of *Melia azedarach* leaf by utilizing [$Zn(NO_3)_2 \cdot 6H_2O$] as the precursor. The synthesized spherical-shaped NPs of 33-96 nm size represented promising anti-oxidant and anti-bacterial properties. ZnO-NPs and *M.azedarach* aqueous leaf extract revealed divergent levels of superoxide anion radical scavenging activity in the ranges between 25, 50, 100, 150, 200 µg/mL concentrations compared with the standard Butylated Hydroxyl Toluene (BHT). Superoxide anion radical scavenging activity of ZnO-NPs shows 27.58%, 37.40%, 43.93%, 48.07% and 52.28% compared with the standard BHT exhibiting 34.82%, 37.08%, 46.78%, 55.10% and 58.92% of hydroxyl radical scavenging activity [44].

Vidhya *et al.* reported an environmentally friendly way of synthesis of spherical-shaped ZnO-NPs of 45 nm size by using *O.americanum* leaf extract with $Zn(CH_3COO)_2.2H_2O$ as the initiator of the reaction. The novel ZnO nanomaterials displayed bacteriocidal, fungicidal and anti-proliferative activity against human skin cancer cell line. Bio-inspired ZnO-NPs have performed activity against skin disease-causing pathogens, such as *B.cereus, C.penfrigens, K.pnemoniae, S.paratyphi, C.albicans* and *A.niger*, resulting in that ZnO-NPs displayed excellent antimicrobial activity with the highest inhibition zone with *C.penfrigens* (30 mm), followed by *K.pnemoniae* (27 mm), *B.cereus* (25 mm) and *S.paratyphi* (24 mm). The antifungal activity with ZnO-NPs shows a maximum zone of inhibition with *C.albicans* (28 mm), followed by *A.niger* (24 mm). The nanoparticles can enter the microbial cell membrane due to immediate electrostatic interactions formed at the interface to release reactive oxygen species to promote cell damage [45].

Eaton *et al*. revealed an interesting fact about the biosynthesis of ZnO- NPs from the precursor [$Zn(NO_3)_2 \cdot 6H_2O$] using the aqueous extract of *Melia azedarach* leaf. The synthesized spherical-shaped NPs have a size range of 35-129 nm. ZnO-NPs presented significant inhibition towards yeasts of the genus *Candida*, particularly *Candida parapsilosis* which is an important emerging pathogen, with no toxicity against red blood cells, which indicates a promising material that could be safely used in medical devices or in pharmaceutical formulations as a support to antifungal treatments. In terms of antifungal activity at different concentrations tested, bulk ZnO exhibited inhibition of *C.krusei*, only at the high concentration of 1,000 µg/mL. On the other hand, the ZnO-NPs synthesized showed improved antifungal potential against yeasts, demonstrating that ZnO-NPs improve their antifungal capacity at lower concentrations [46]

Abbasi *et al.* synthesized spherical ZnO-NPs of 18 nm size from the aqueous extract of *Geranium wallichianum* leaves with the precursor zinc nitrate hexahydrate [$Zn(NO_3)_2 \cdot 6H_2O$]. The fabricated NPs showed anti-pathogenic potentials, free radical scavenger capacities and inhibition of α-amylase and protein kinases. Antileishmanial potential of ZnO-NPs was evaluated using *L.tropica* (KMH23) parasites which were evaluated at various doses (1–200 µg/mL) of ZnO-NPs. ZnO-NPs showed a significant antileishmanial potential against *L.tropica* promastigotes with IC_{50} of 15.60 µg/mL. Similarly, ZnO-NPs also showed a significant potential against *L.tropica* amastigotes with IC_{50} of 34.5 µg/mL. Fungicidal potential of ZnO-NPs was evaluated using

various fungal strains (FS) compared with drug amp-B as a positive control. A dose-dependent inhibition response was reported. *A.flavus* was the least susceptible fungal strain with MIC of 250 µg/mL, while *A.niger* and *M.racemosus* were the most susceptible strains with MIC of 31.25 µg/mL. The PK inhibition activity was tested using different doses of ZnO-NPs ranging from 31.25-1000 µg/mL. The highest ZOI was measured as 15 mm at 1000 µg/mL, which shows an important protein kinase inhibition potency of ZnO-NPs compared with surfactin as a positive control [47].

Miri *et al.* have studied the interesting facts of developing ZnO-NPs from the aqua extract of *Prosopis farcta* fruit by utilizing zinc sulfate as the precursor. These NPs have a spherical shape with a size range of 40-50 nm. The produced NPs showed better antifungal activity and inhibition of breast cancer proliferation as compared to the ionic form. The MIC and MFC of ZnO-NPs against *C.albicans* have been surveyed *via* turbidimetric antifungal assay and calculated to be 32–64 and 128–512 µg/ml, respectively Results showed that ZnO-NPs possess a good antifungal activity against *C.albicans*. Then, cytotoxic activity of synthesized NPs was evaluated by using WST-1 assay on MCF7 cell line. Cell viability of synthesized NPs was observed to be 50.23% at 500 µg/ml concentration of NPs [48].

Sarlia *et al.* studied the potentials of ZnO-NPs developed from the aqueous extract of leaves, trunks and shells of *Taxus baccata* plant by utilizing [$Zn(NO_3)_2 \cdot 6H_2O$] as the precursor. The reported NPs had a spherical shape with 60-80 nm size, resulting in promising anti-bacterial activity. The antimicrobial activities of the *Taxus baccata* extract, zinc nitrate solution and Zn nanoparticles (Zn-NPs) were examined by the well diffusion method.The extract and solution did not show antimicrobial effects against *Staphylococcus aureus*, *Escherichia coli* and *Pseudomonas aeruginosa*. In negative control wells, no bacterium was grown, while in positive control wells, a very good growth of bacteria was observed [49].

Hemanth *et al.* have fabricated an environmentally benign method to synthesize (aqueous extract of *Simarouba glauca* DC leaves)-based hexagonal ZnO-NPs of size range 17-37 nm by utilizing $Zn(NO_3)_2 \cdot 6H_2O$ salt as the precursor. The antioxidant potential of the synthesized ZnO-NPS was estimated by DPPH, ABTS, H_2O_2 and superoxide radical scavenging methods. The RSA of ZnO-NPs was found between 5 and 59% (among different methods) and the antioxidant potential increased with increase in the concentration of ZnO-NPs. The half-maximal inhibitory concentration (IC_{50}) of RSA varied between 400 and 500 µg mL^{-1} among the test methods. The standard control (ascorbic acid) offered 75% inhibition at 50 µg mL^{-1}.The antimitotic activity of green synthesized ZnO-NPs was studied using allium assay. Onion is considered as a good bioindicator for genotoxicity and clastogenicity studies by UNEP and USEPA. In this study, the mitotic index was decreased from 43.06 to 17.46% with an increase in the concentration of ZnO-NPs compared to the control [50].

Narain *et al.* have produced eco-friendly approach-mediated spherical ZnO-NPs of an average size of 81 nm from *Phoenix loureiroi* aqueous fruit by using zinc nitrate hexahydrate [$Zn(NO_3)_2 \cdot 6H_2O$] as the precursor. The antioxidant and cytotoxic properties were investigated in the biologically and chemically synthesized zinc oxide (ZnO)-B and chitosan (CTS)-encapsulated ZnO (ZnO–CTS) nanoparticles. The synthesized (B-ZnO and B-ZnO–CTS) nanoparticles showed higher free radical scavenging ability in DPPH (IC_{50} = 445.94 and 419.32 µg/mL), ABTS (37.95 and45.61%), NO (20.52 and 21.28%) and OH· (74.09 and 77.10%) assays. Hemolytic test was performed by using RBCs *in vitro* for the study of interaction of fruit extract and nanoparticles with membranes, because this test is a good indicator of destruction of RBC cells. The results showed that the gradual increase of hemolytic activity (0.65–1.43%) was in a dose-dependent manner in methanolic extracts. Results showed that C-ZnO nanoparticles have a higher percentage (7.85%) of hemolysis at 2.50 mg/mL. Thus, up to 1.50 mg/mL concentration, the nanomaterial can be used as a biocompatible material [51].

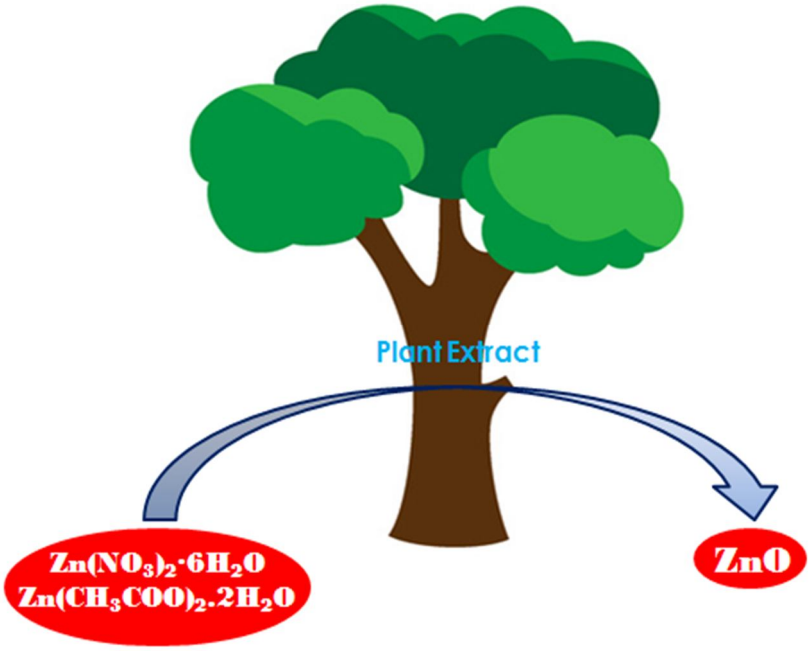

FIG. 1. Fabrication of zinc nanomaterials from various zinc salts employing different plant extracts.

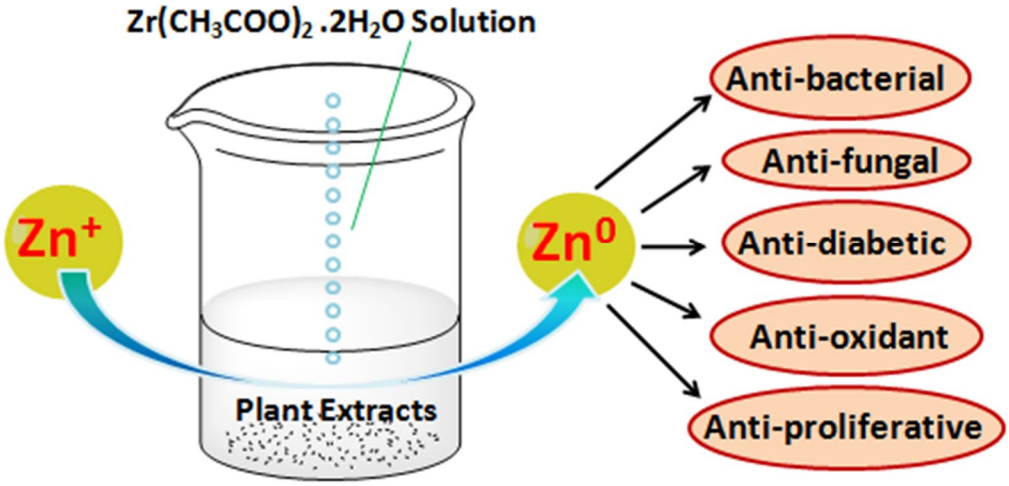

FIG. 2. Zinc nanomaterials formation from different plant extracts and their pharmacotherapeutics.

TABLE 1. Fabrication of zinc nanomaterials through various plant biomasses.

Plant	Family	Part used	Average size (nm)	Shape	Therapeutic applications	Precursor	Reference
Sesamum indicum	Pedaliaceae	seeds	9.07	Spherical	Anti-bacterial	$ZnSO_4.7H_2O$	[17]
Echinochloa frumentacea grains	Poaceae	grain	35-65	Hexagonal shape	Anti-bacterial	$Zn(CH_3COO)_2.2H_2O$	[18]
Euphorbia hirta	Euphorbiaceae	leaf	20-25	Spherical shape	Anti-microbial	Zinc nitrate	[19]
radish root (Raphanussativus) extract	Brassicaceae	root	15-25	Hexagonal structure	Dressing agents for diabetic foot ulcers	$Zn(CH_3COO)_2.2H_2O$	[20]
Aloe socotrina	Asphodelaceae	leaf	15-50	Spherical	Anti-bacterial	$Zn(CH_3COO)_2.2H_2O$	[21]
Camellia japonica	Theaceae	leaf	15-30	Spherical shape	Anti-bacterial, Anti-fungal	$Zn(NO_3)_2 \cdot 6H_2O$	[22]
Aloe vera	Asphodelaceae	leaf	18-61	Rod shape	Anti-bacterial	Zinc nitrate	[23]

Plant	Family	Part used	Average size (nm)	Shape	Therapeutic applications	Precursor	Reference
Prosopis juliflora	Leguminosae	leaf	65	Spherical shape	Anti-bacterial	$Zn(NO_3)_2{\cdot}6H_2O$	[24]
Plum fruits	Rosaceae	fruit	60-80	Cylindrical	Anti-bacterial	$Zn(CH_3COO)_2.2H_2O$	[25]
Ailanthus altissima	Simaroubaceae	fruits	5-18	Spherical shape	Anti-bacterial	$Zn(NO_3)_2{\cdot}6H_2O$	[26]
Cinnamomum verum J. Presl	Lauraceae	bark	~45	Spherical	Anti-bacterial	$Zn(NO_3)_2{\cdot}6H_2O$	[27]
Eucalyptus globules	Myrtaceae	leaf	52-70	Spherical	Anti-fungal	$Zn(NO_3)_2{\cdot}6H_2O$	[28]
Nettle *(Urtica dioica)*	Urticaceae	leaf	NA	NA	Anti-diabetic	$Zn(NO_3)_2{\cdot}6H_2O$	[29]
Selaginella convolute	Selaginellaceae	leaf	40	Spherical	Muscle relaxant, Anti-nociceptive	$Zn(CH_3COO)_2.2H_2O$	[30]
Fraxinus rhynchophylla	Oleaceae	wood	100-200	NA	Anti-nociceptive	$Zn(CH_3COO)_2.2H_2O$	[31]
Allium sar alicum R.M. Fritsch	Amaryllidaceae	leaf	19	Spherical	Anti-oxidant, Anti-bacterial, Anti-fungal	$[Zn(NO_3)_2{\cdot}6H_2O$	[32]
Cinnamon zeylanicum	Lauraceae	leaf	20	Spherical shape	Local anaesthetics	$Zn(CH_3COO)_2.2H_2O$	[33]
Artemisia annua	Asteraceae	stem, bark	20	Spherical shape	Inhibition of osteoclast formation, Treatment of bone deformities and bone-related diseases	$Zn(CH_3COO)_2.2H_2O$	[34]
Cardiospermum halicacabum	Sapindaceae	leaf	10-20	Spherical shape	Anti-cancer activity in human melanoma cells (A375)	$Zn(CH_3COO)_2.2H_2O$	[35]
Rhizoma paridis saponins	Liliaceae	leaf	100	Spherical shape	Anti-carcinogenic	$Zn(CH_3COO)_2.2H_2O$	[36]
Morus nigra	Moraceae	leaf	100	Spherical shape	Anti-cancer, gastic cancer	$Zn(NO_3)_2{\cdot}6H_2O$	[37]
Hyssop (Hyssopus officinalis)	Lamiaceae	leaf	NA	NA	Anti-cancer	$Zn(CH_3COO)_2.2H_2O$	[38]
Deverra tortuosa extract	Apiaceae	aerial parts	9.26-31.18	Spherical shape	Anti-microbial, Anti-cancer	$Zn(NO_3)_2{\cdot}6H_2O$	[39]
Capparis zeylanica	Capparaceae	leaf	32-40	Spherical sizes	Anti-proliferative, Anti-cancer	$Zn(CH_3COO)_2.2H_2O$	[40]
Hyphaene thebaica	Arecaceae	fruit	8-23	Quasi-spherical	Anti-microbial Anti-leishmanial	$Zn(CH_3COO)_2.2H_2O$	[41]
Hylotelephium telephium subsp.	Crassulaceae	flower	83 nm	Spherical	Anti-bacterial	$[Zn(NO_3)_2{\cdot}6H_2O$	[42]
Mussaenda frondosa	Rubiaceae	leaf, stem and callus	5-20	Spherical	Anti-oxidant, Anti-inflammatory, Anti-diabetic, Antimicrobial, Anti-cancer	$Zn(NO_3)_2{\cdot}6H_2O$	[43]
Melia azedarach	Meliaceae	leaf	33-96	Spherical shape	Anti-oxidant, Anti-bacterial	$Zn(NO_3)_2{\cdot}6H_2O$	[44]
Ocimum americanum	Lamiaceae	leaf	45	Spherical shape	Anti-microbial, Anti-cancer	$Zn(CH_3COO)_2.2H_2O$	[45]
Cashew Gum	Anacardiaceae	gum	35-129	Round-shaped	Anti-fungal	$Zn(NO_3)_2{\cdot}6H_2O$	[46]
Geranium wallichianum	Geraniaceae	leaf	~18	Spherical	Anti-cancer, Anti-leishmanial	$Zn(NO_3)_2{\cdot}6H_2O$	[47]
P. farcta	Fabaceae	fruit	40-50	Hexagonal	Anti-microbial	$ZnSO_4$	[48]

Plant	Family	Part used	Average size (nm)	Shape	Therapeutic applications	Precursor	Reference
Taxus baccata	Taxaceae	leaves, trunks and shells	20-27	Hexagonal	Anti-bacterial, Anti-cancer	$Zn(NO_3)_2{\cdot}6H_2O$	[49]
Simarouba glauca	Simaroubaceae	leaf	17-37	Hexagonal	Anti-oxidant, Anti-mitotic	$Zn(NO_3)_2{\cdot}6H_2O$	[50]
Phoenix loureiroi fruit	Arecaceae	fruit	81	Spherical shape	Anti-oxidant, Anti-cancer	$Zn(NO_3)_2{\cdot}6H_2O$	[51]

Conclusion

This article provided information to active researchers on the recent advances in the area of zinc oxide (ZnO) nanoparticles development of diverse morphologies (hexagonal, spherical, quasi-spherical, rod, cylindrical, … etc.) from various precursor zinc salts [$Zn(NO_3)_2{\cdot}6H_2O$, $Zn(CH_3COO)_2.2H_2O$ and $ZnSO_4$] using the extracts of plant parts (leaf, stem, bark, fruit, flower, seed, wood, trunk and grain). The pharmacological perspectives of these nanomaterials, such as anti-oxidant, anti-inflammatory, anti-leishmanial, anti-diabetic, anti-bacterial, anti-fungal, anti-cancer, local anaesthetic, muscle relaxant, anti-nociceptive, dressing agents, osteoclast formation inhibitor, … etc., have opened new avenues of therapeutic applications. This literature opened new future perspectives for researchers in developing zinc-based nanomaterials which will have multifarious applications.

References

[1] Marcelo, G.A. *et al*., Mater. Sci. Eng. C, 106 (2020) 110104.

[2] Choudhury, H. *et al*., Mater. Sci. Eng. C, 112 (2020) 110925.

[3] Chandra, H. *et al*., Biocatal. Agric. Biotechnol., 24 (2020) 101518.

[4] Bandeira, M. *et al*., Sustain. Chem. Pharm., 15 (2020) 100223.

[5] Gu, M. *et al*., Chem. Phys., 534 (2020) 110750.

[6] Hu, H. *et al*., J. Hazard. Mater., 387 (2020) 121670.

[7] Sachdeva, A. *et al*., Mater. Today Proc., (2020) in Press.

[8] Bhattacharya, P. *et al*., J. Environ. Chem. Eng., 8 (3) (2020) 103803.

[9] Chandra, N. *et al*., Groundw. Sustain. Dev., 10 (2020) 100325.

[10] Chakrabarti, S., Banerjee, P., Mitra, P. and Roy, A., "Zinc Oxide–based Nanomaterials for Environmental Applications". (Elsevier, 2020).

[11] Pillai, A.M. *et al*., J. Mol. Struct., 1211 (2020) 128107.

[12] Nasrollahzadeh, M., Sajadi, S.M., Issaabadi, Z. and Sajjadi, M., "Biological Sources Used in Green Nanotechnology", 1st Ed., vol. 28, (Elsevier, 2019).

[13] Jose Varghese, R., Zikalala, N., Sakho, E.H.M. and Oluwafemi O.S., "Green Synthesis Protocol on Metal Oxide Nanoparticles Using Plant Extracts", (Elsevier, 2020).

[14] Shrivastava, M. *et al*., Environ. Nanotechnology, Monit. Manag., 11 (2019) 100218.

[15] Das, G. *et al*., Mater. Sci. Eng. C, 114 (2020) 111011.

[16] Alharbi, F.A. and Alarfaj, A.A., J. King Saud Univ. Sci., 32 (2) (2020) 1346.

[17] Zafar, S. *et al*., J. King Saud Univ. Sci., 32 (1) (2020) 1116.

[18] Velsankar, K. *et al*., Mater. Chem. Phys., 239 (2020) 121976.

[19] Ahmad, W. and Kalra, D., J. King Saud Univ. Sci., 32 (4) (2020) 2358.

[20] Liu, D. *et al*., J. Drug Deliv. Sci. Technol., 55(23) (2020) 101364.

[21] Fahimmunisha, B.A. *et al*., J. Drug Deliv. Sci. Technol., 55 (2020) 101465.

[22] Muthuchamy, M. *et al*., Mater. Today Commun., 22 (2020) 100766.

[23] Rasli, N.I. *et al*., Heliyon, 6 (1) (2020) e03156.

[24] Sheik Mydeen, S. *et al*., J. Saudi Chem. Soc., 24 (5) (2020) 393.

[25] Singhal, U. *et al*., Mater. Today Proc., 28 (1) (2020) 261.

[26] Awwad, A.M. *et al*., Chem. Int., 6 (3) (2020) 15.

[27] Ansari, M.A. *et al*., Biomolecules, 10 (2) (2020) 1.

[28] Ahmad, H. *et al*., Biomolecules, 10 (3) (2020) 1.

[29] Bayrami, A. *et al*., Adv. Powder Technol., 31 (5) (2020) 2110.

[30] Xu, K. *et al*., J. Photochem. Photobiol. B Biol., 202 (2020) 111700.

[31] Wang, Z. *et al*., J. Photochem. Photobiol. B Biol., 202 (2020) 111668.

[32] Zhang, C. *et al*., Appl. Organomet. Chem., 34 (2020) e5564.

[33] Cui, P. *et al*., J. Drug Deliv. Sci. Technol., 57 (29) (2020) 101740.

[34] Wang, D. *et al*., J. Photochem. Photobiol. B Biol., 202 (2020) 111652.

[35] Duan, X. *et al*., J. Photochem. Photobiol. B Biol., 202 (2020) 111718.

[36] Xu, Z. *et al*., J. King Saud Univ. Sci., 32 (3) (2020) 1865.

[37] Tang, Q. *et al*., J. Photochem. Photobiol. B Biol., 202 (2020) 111698.

[38] Mohammad, G.R.K.S. *et al*., Andrologia, 52 (1) (2020) e13450.

[39] Selim, Y.A. *et al*., Sci. Rep., 10(1) (2020) 1.

[40] Nilavukkarasi, M. *et al*., Mater. Sci. Energy Technol., 3 (2020) 335.

[41] Mohamed, H.E.A. *et al*., J. Inorg. Organomet. Polym. Mater., 30 (2020) 3241.

[42] Karunakaran, G. *et al*., Jom, 72 (3) (2020) 1264.

[43] Jayappa, M.D. *et al*., Appl. Nanosci., 10 (2020) 3057.

[44] Dhandapani, K.V. *et al*., Biocatal. Agric. Biotechnol., 24 (2020) 101517.

[45] Vidhya, E. *et al*., Gene Reports, 20 (2020) 100688

[46] Souza, J.M.T. *et al*., J. Clean Prod., 247 (2020) 119085.

[47] Abbasi, B.A. *et al*., Biomolecules, 10 (1) (2020) 1.

[48] Miri, A. *et al*., Green Chem. Lett. Rev., 13 (1) (2020) 27.

[49] Sarli, S. *et al*., Eurasian Chem. Commun., 2 (3) (2020) 302.

[50] Hemanth Kumar, N.K. *et al*., J. Clust. Sci., 31 (2) (2020) 523.

[51] Narain, M. *et al*., Arab. J. Sci. Eng., 45 (1) (2020) 15.

Volume 15, Number 1, 2022. pp. 81-88

Jordan Journal of Physics

ARTICLE

Half a Decade Progress of Biomass-assisted Development of Zirconium Nanomaterials: Anti-microbial Potentials

D. Kar Mahapatra[a], **A. G. M. Haldar**[b], **K. M. Dadure**[c] and **R. G. Chaudhary**[d]

[a]*Department of Pharmaceutical Chemistry, Dadasaheb Balpande College of Pharmacy, Nagpur 440037, Maharashtra, India.*

[b]*Department of Applied Chemistry, Priyadarshini Bhagwati College of Engineering, Nagpur 440009, Maharashtra, India.*

[c]*Department of Chemistry, J. B. College of Science, Wardha 442001, Maharashtra, India.*

[d]*Post-graduate Department of Chemistry, S. K. Porwal College, Kamptee, Nagpur 441001, Maharashtra, India.*

Doi: **https://doi.org/10.47011/15.1.11**

Received on: 01/08/2020; *Accepted on: 01/07/2021*

Abstract: Nanotechnology has revolutionized all fields across the globe and opened up several frontiers in nanobiotechnology, nanopharmacotherapeutics, material and applied sciences, biomedical sciences, drug delivery, tumor therapy imaging, biosensing, electronics, bactericidal activity, catalysis, optics and photoelectrochemistry. Nature has provided abundant biological resources to synthesize NPs eco-friendly. Over the past few years, purified extracts of bacteria, fungi, algae, seaweeds and viruses have received adequate attention for the development of energy-proficient, non-toxic, economic nanoparticles (NPs). The present review article exclusively focuses on the last 5 years (January 2016 to December 2020) progress in the area of green synthesis of zirconium nanomaterials (zirconium NPs (Zr-NPs), zirconium dioxide (ZrO_2) and zirconium/metal nanocomposites, Cu/ZrO_2) by utilization of plant extracts, fungal extracts and seaweed extracts. The probable mechanism(s) of the formation of NPs by reduction with bioreductants is (are) also described briefly.

Keywords: Zirconium, Nanoparticles, Plant, Fungi, Seaweed, Anti-microbial potentials.

Introduction

Nanotechnology has revolutionized all fields across the globe and opened up several frontiers in nanobiotechnology, nanopharmacotherapeutics, material and applied sciences, biomedical sciences, drug delivery, tumor therapy imaging, biosensing, electronics, bactericidal activity, catalysis, optics and photoelectrochemistry [1-2].

Diversity of chemical and physical processes has been reported for the synthesis of metallic nanoparticles (NPs) [3]. However, several methods subsisted, but many problems are associated with these processes, like utilizing toxic solvents, expensive production of harmful by-products, …etc [4]. Chemicals, like hydrogen peroxide, hydrazine hydrate, polyvinylpyrrolidone, sodium borohydride, ethylene glycol and dimethylformamide, are generally used for the production of NPs, but they get absorbed on the surface of NPs formed, thereby producing toxicity [5]. Thus, there is a need to explore eco-friendly synthetic protocols for the synthesis of nanomaterials [6-15].

Corresponding Author: D. Kar Mahapatra **Email**: dkmbsp@gmail.com

Nature has provided copious biological resources to fabricate NPs in an eco-friendly manner [16]. With the improvement in technologies, a new way for research and development in the field of biology towards nanomedicine has been ascertained [17]. The use of biological resources in the synthesis of nanomaterials is swiftly developing due to their emergent success, economics, ease of formation and eco-friendly nature [18]. Over the past few years, purified extracts of bacteria, fungi, algae, seaweeds and viruses have received sufficient consideration for the development of non-toxic, economic and energy-proficient NPs [19].

Typically, a bio-organism-mediated metallic salt reduction process occurs when the aqueous extract of the bio-organism reacts with an aqueous solution of the metal salt [20]. The whole reaction occurs at room temperature within a few minutes [21]. Due to the occurrence of an extensive selection of chemicals, the bioreduction process is relatively complex. Biological synthesis of NPs using plant extracts is relatively scalable and less expensive compared with microbial processes [22]. The nature of plant extract, pH, its concentration, temperature, the concentration of metal salt, contact time, …etc. affect the quantity, rate of production and characteristics of the NPs [23]. The source of the plant extract also influences the characteristics of NPs because of varying concentrations and combinations of organic reducing agents. For the green synthesis of NPs, the following points must be considered (i) selecting appropriate bioresources for the reduction of metal salts and (ii) providing optimal reaction conditions for NP formation [24].

The present review article exclusively focuses on the last 5 years (January 2016 to December 2020) progress in the area of green synthesis of zirconium nanomaterials (zirconium NPs, ZrO_2 and zirconium/metal nanocomposites, Cu/ZrO_2) by utilization of plant extracts, fungal extracts and seaweed extracts (Fig. 1). The probable mechanism(s) of the formation of NPs by reduction with reductants is (are) also described briefly.

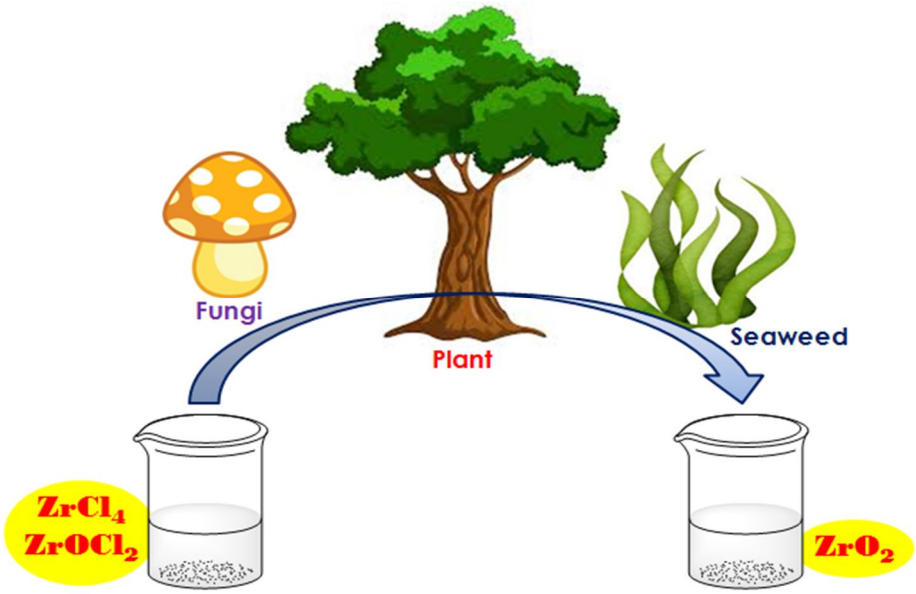

FIG. 1. A simple summary or graphical representation of zirconium nanomaterials fabrication using plant extracts, fungi extracts and seaweed extracts.

Fabrication of Zirconium Nanomaterials

Plant Extracts-mediated Synthesis

The leaf extracts of *Moringa oleifera*, *Rosmarinus officinalis* and *Lagerstroemia speciosa* have been successfully utilized for preparing ZrO_2-NPs of size 9 nm-10 nm (spherical), 12 nm-17 nm (semi-spherical) and 56.8 nm (oval) which presented utility as nanocomposite films, anti-bacterial agents (*Bacillus subtilis*, *Escherichia coli*, *Pseudomonas aeruginosa* and *Staphylococcus aureus*) and photocatalytic ally active NPs [25-27].

The root extracts of *Euclea natalensis* were utilized by Silva *et al*. in fabricating ZrO_2-NPs of the size range from 5.9 nm to 8.54 nm and further employed the produced NPs in adsorbing

tetracycline for preventing environmental pollution. Sophisticated techniques, such as FTIR, XRD and TEM techniques, have been utilized for characterization [28].

Two plants of the Euphorbiaceae family; *Acalypha indica* and *Jatropha integerrima*, have been reported to play a crucial role in the fabrication of ZrO_2-NPs. Aqueous leaf extract of the former plant was utilized for obtaining cube-shaped NPs of the size range from 20 nm to 100 nm. The NPs were comprehensively characterized by Scanning Electron Microscopy (SEM), Fourier Transform Infrared Spectroscopy (FT-IR) and Energy Dispersive X-ray studies [29].

The aqueous flower extract of the latter plant was employed for obtaining nano-sized materials and characterized by XRD, FT-IR spectroscopy, and UV-Vis spectroscopy. The produced NPs demonstrated better reduction (degradation) of malachite green as compared to conventional reduction [30].

Recently, hybrid ZrO_2-NPs with cerium and copper for multifarious applications has been fabricated through green approaches by model investigators. Nithya *et al*. fabricated agglomerated nano stick-like (20 nm to 45 nm) core metal NPs of CeO_2/ZrO_2 utilizing ionic liquid-mediated *Justicia adhatoda* extract. The bioreductants, such as *N*, *N*-dimethylglycine and vasicinone, present in the extract played a vital role in reducing the ionic form into the elemental form. The hybrid NPs expressed anti-bacterial [higher activity against *S. aureus* (Gram-positive) than *E. coli* (Gram-negative)], anti-oxidant and anti-biofilm (violacein inhibition assay, prodigiosin inhibition assay and biofilm inhibition assay) activities [31].

Similarly, the leaf extract of *Rubia tinctorum* was utilized by Nasrollahzadeh *et al*. for developing Cu/Zr silicate nanocomposite which has a crucial role as a catalyst in the N-benzylation reaction of arylcyanamides. The researchers established the structure of the nanocomposite through techniques, like FESEM, XRD, EDS, BET, FT-IR, TEM and elemental mapping [32].

Azadirachta indica has been utilized for the fabrication of ZrO_2 by two independent groups of Indian researchers. In the former case, the extract produced nano-sized particles that were characterized exclusively by UV-Vis spectroscopy technique with a calculated band gap of 5.80 eV [33].

In another report, the former extract was utilized along with *Aloe barbadensis* in producing nano-zirconium. The authors stated that the obtained NPs showed strikingly high concentration-dependent anti-fungal activity against *Candida albicans*, *Aspergillus fumigatus* and *Aspergillus niger* as evidenced by the zone of inhibition (Fig. 2) [34].

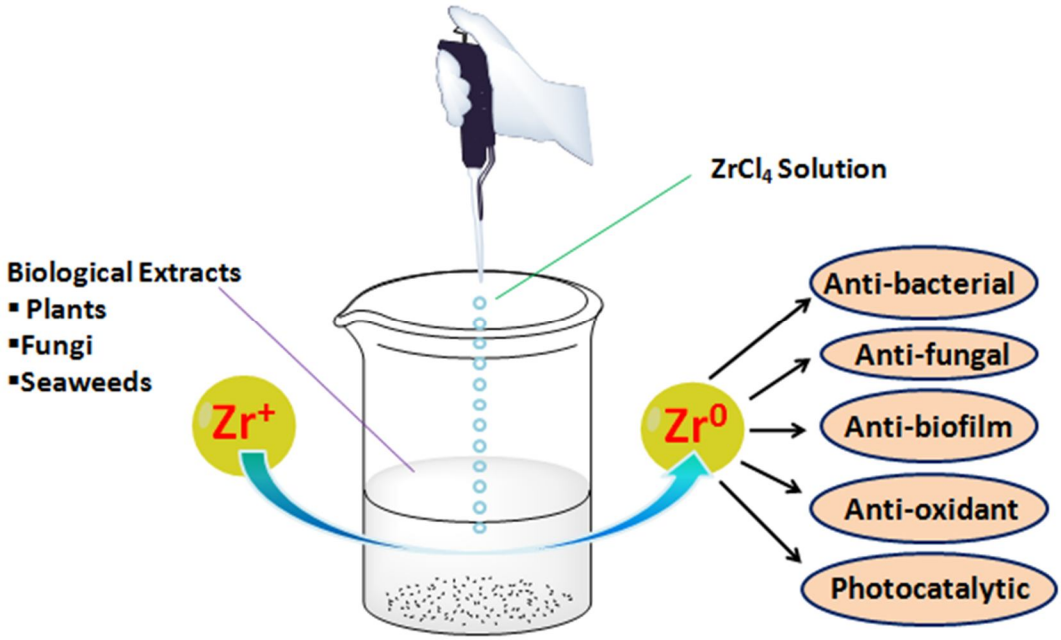

FIG. 2. Formation of zirconium nanomaterials from diverse biomasses and their applications.

Bacteria-mediated Synthesis

Bacteria are having the best biofactory, where several protein-based elements play a pivotal role in the bioreduction processes. They are often regarded as the most trusted comrades for numerous biotechnological products creation in several pharmaceutical industries. However, it is shocking to state that there are no interesting reports available at present for the biosynthesis of ZrO_2-NPs. Though, it is expected that in the near future, enthusiastic researchers will definitely explore the zirconium salt bioreduction potentials of various bacterial species.

Seaweed Extract-mediated Synthesis

Kumaresan and co-workers synthesized tetragonal ZrO_2-NPs of average size of 4.8 nm by utilizing the whole extract of *Sargassum wightii* (Sargassaceae) marine brown algae (Table 1). The prepared NPs were thoroughly characterized through sophisticated analytical tools, such as HR-TEM, XRD, PL spectroscopy, FTIR spectroscopy and UV–Vis spectroscopy. The NPs expressed tremendous anti-bacterial activity against *Salmonella typhi*, *B. subtilis* and *E. coli* with an impressive MIC value. The high bactericidal activity of the NPs is mediated by the large surface area offered by these nanomaterials (Table 1) [35].

TABLE 1. Green synthesized zirconium nanomaterials from various biomasses in the last 5 years.

Biomass	Family	Part used	Type	Size (nm)	Shape	Applications	Ref.#
Acalypha indica	Euphorbiaceae	Leaves	ZrO_2	20-100	Cube	-	19
Aloe barbadensis and *Azadirachta indica*	Meliaceae / Asphodelaceae	Leaves	ZrO_2	350	Spherical	Anti-fungal	24
Azadirachta indica	Meliaceae	Leaves	ZrO_2	-	-	-	23
Euclea natalensis	Ebenaceae	Roots	ZrO_2	5.9-8.54	Spherical	Adsorption of tetracycline	18
Jatropha integerrima	Euphorbiaceae	Flowers	ZrO_2	-	-	Malachite green reduction	20
Justicia adhatoda	Acanthaceae	Leaves	CeO_2/ ZrO_2	25-45	Stick	Anti-bacterial, anti-oxidant and anti-biofilm	21
Lagerstroemia speciosa	Lythraceae	Leaves	ZrO_2	56.8	Oval	Photocatalytic activity	17
Moringa oleifera	Moringaceae	Leaves	ZrO_2	9-10	Spherical	Anti-bacterial	15
Penicillium chrysogenum, *Penicillium pinophilum*, *Penicillium aculeatum*, *Penicillium notatum*, and *Penicillium purpurogenome*	Trichocomaceae	Whole	ZrO_2	< 100	Spherical	Anti-bacterial	22
Rosmarinus officinalis	Lamiaceae	Leaves	ZrO_2	12-17	Semi-spherical	Nanocomposite films	12
Rubia tinctorum	Rubiaceae	Leaves	CuO/ ZrO_2	15-25	Spherical	*N*-benzyl-*N*-arylcyanamides preparation	18
Sargassum wightii	Sargassaceae	Whole	ZrO_2	4.8	Tetragonal	Anti-bacterial	21

Fungi Extract-mediated Synthesis

Ghomi and researchers synthesized spherical ZrO_2-NPs through an eco-friendly extracellular development procedure employing various species of Penicillium (*Penicillium pinophilum*, *Penicillium chrysogenum*, *Penicillium notatum*, *Penicillium purpurogenome* and *Penicillium aculeatum*). These biosynthesized NPs were duly characterized through Dynamic Light Scattering (DLS), Fourier Transform Infrared (FT-IR), Atomic Force Microscope (AFM), Energy Dispersive X-ray (EDX) and Scanning Electron Microscopy (SEM). The screening of these NPs against a range of Gram-negative bacteria (*S. typhi*, *B. subtilis* and *E. coli*) presented a notable activity owing to smaller dimensions which resulted in a better access to the biological target(s) [36].

Role of Various Phytochemicals in the Bioreduction

Although the precise mechanism of ZrO_2-NP production is unknown, a number of studies strongly suggest that nitrate reductase is a crucial enzyme in NP synthesis in bacteria, with bioreduction being linked to metabolic activities that use nitrate by converting it to nitrite and ammonium [37].

In general, ZrO_2-NPs are made in two steps: first, bulk ions are reduced into NPs and then the produced NPs are capped. The first step in fungal-mediated synthesis includes trapping ions on the surface of the fungal cells and then a 32 kDa protein, which may be a reductase produced by the fungal isolate, reduces ions into NPs. In a later stage, 35 kDa proteins bind to NPs and provide stability [38]. Protein-NP interactions have the potential to help NPs maintain their stability. Fungal proteins play an important role in the reduction of metal salts to their elemental forms. *Volvariella volvacea* proteins are an example of a natural bioreductants. Bioreduction occurs in *Fusarium oxysporum* through NADPH-dependent sulfite reductase (35.6 kDa) and phytochelatin components, while compactin is the bioreductant in *Penicillium brevicompactum* [39-40].

For the formation of ZrO_2-NPs from zirconium salt, the process of bioreduction may be performed by the various prominent phytochemicals (alizarin, aloe emodin, aloin A, aloin B, asiatic acid, azadirachtin, azadirone, betulin, biorobin, corosolic acid, ellagic acid, gedunin, kaempferol, nimbidinin, nimbin, nimocinol, quercetin, ursolic acid and vasicine) present in the plant extract which acted as reducing agent as well as capping agent (Fig. 3). Since plant extracts have hundreds of bioactive components belonging to diverse classes, such as alkaloids, glycosides, proteins, sugars, tannins, anthraquinones, saponins, flavonoids, steroids, terpenes, … etc., there is a possibility that apart from the above-mentioned phytochemicals, some others may take part in the bioreduction process. It is extremely difficult to predict the reducing agent as well as capping agent present in seaweeds and fungi because of large multi-cellular complex system.

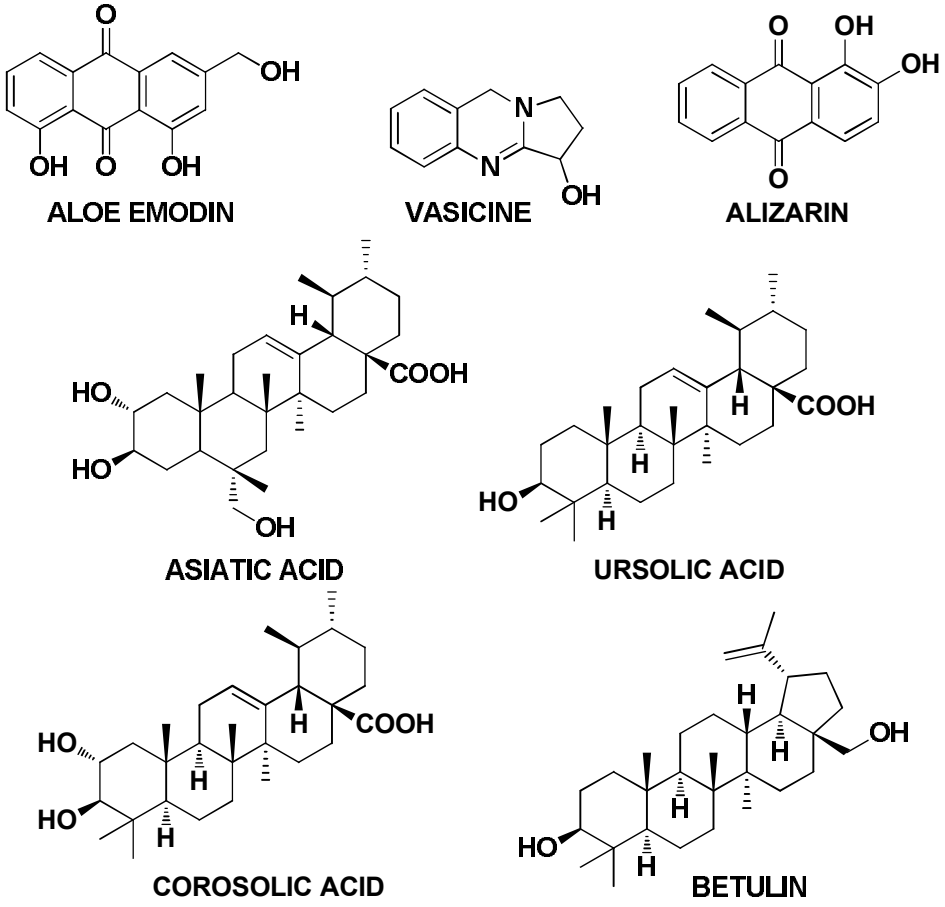

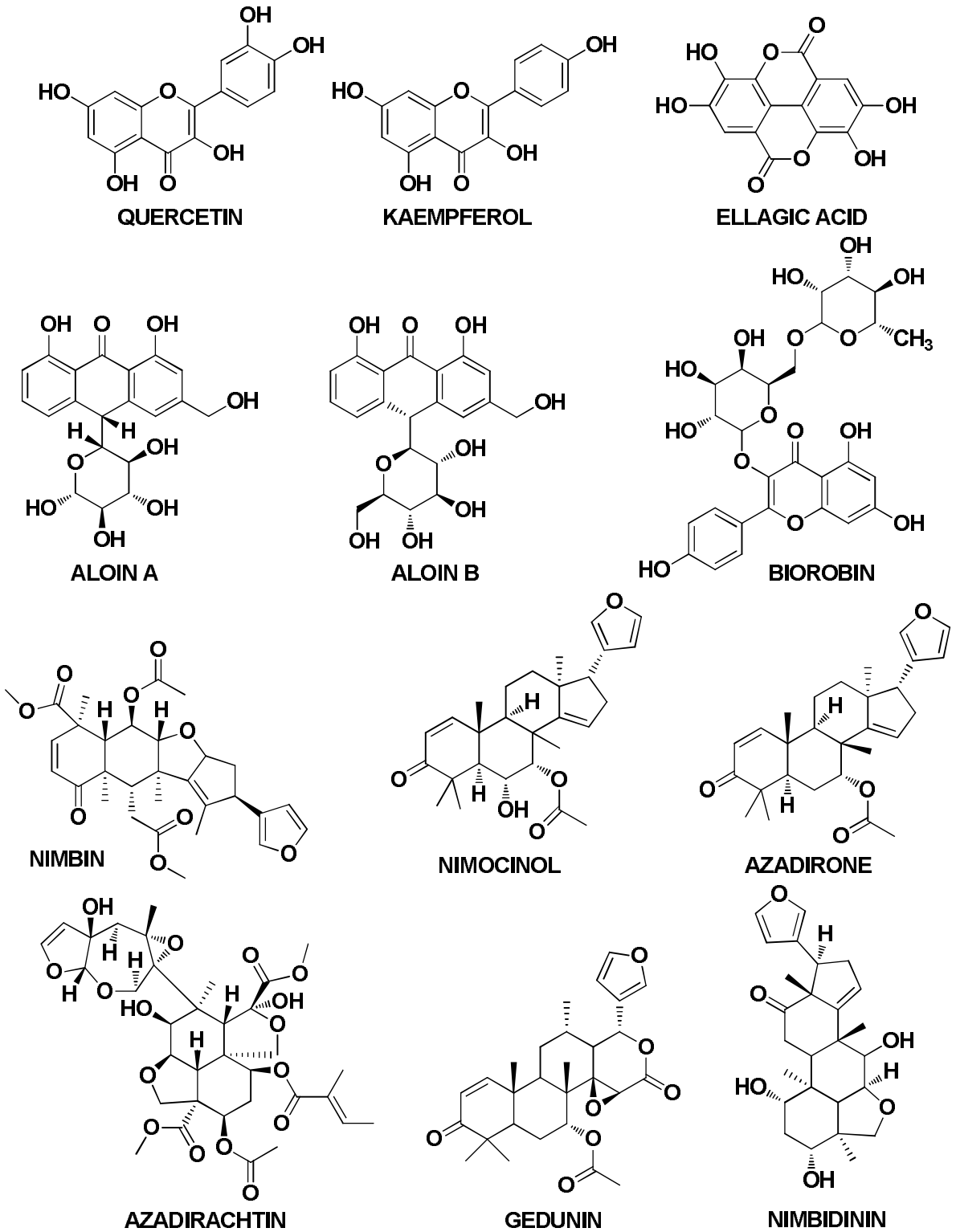

FIG. 3. Structures of some prominent reducing and capping agents.

Applications of Zirconium Nanoparticles

These fabricated ZrO_2-NPs have diverse pharmacological applications ranging from anti-fungal (*A. fumigatus*, *A. niger*, *C. albicans*), anti-bacterial (*S. aureus* ATCC 25923, *S. aureus* ATCC 29213, *E. coli* ATCC 27853, *B. subtilis*, *S. typhi* and *P. aeruginosa* ATCC 27853), anti-biofilm forming agents, anti-oxidant agents… etc. Under non-pharmacological mode, applications are restricted to nanocomposite films, photocatalytic agents, catalysts in *N*-benzyl-*N*-arylcyanamides preparation, assisting

adsorption of tetracycline, facilitating malachite green dye reduction and many more.

Conclusion

Nature has provided plentiful bio-resources that can reduce Zr ions into Zr-NPs. In the field of nanotechnology, a reliable and eco-friendly process for the synthesis of NPs is the foremost demand. In order to achieve this goal, the use of natural sources for the green synthesis of NPs becomes crucial. This approach has numerous advantages over conventional methods as a cost-effective, environmentally safe and efficient approach. Though, there are a few shortcomings connected with the biosynthesis of NPs employing green chemistry approach. It is comparatively a slow progression, somewhat complicated to manage the size/shape of NPs employing the biological sources, the precise mechanism for NPs formation is indefinite and non-specific conjugation of proteins/phytoconstituents during the synthesis of NPs. The microorganism (bacteria and fungi)-mediated synthesis is somewhat trouble-free, but there is a need to explore the biochemical and molecular mechanisms of NPs synthesis by these organisms. Algae and seaweeds are comparatively newer bio-resources that are not explored passably and necessitate supplementary exploration. The wide variety of biological activities and imaging properties of biosynthesized NPs may offer a foundation for the progress of future nanomedicine. Additionally, purification and proper character-ization of these NPs are the imperative steps to be taken into contemplation before the nanomaterials to be used commercially in healthcare. Despite all the foremost challenges and concerns, the biosynthesized NPs may be potential nanomedicines for the pharmacotherapeutics of a variety of diseases in the near opportunities.

References

[1] Rao, C.N.R. *et al*., "Nanomaterials Chemistry: Recent Developments and New Directions", (John Wiley & Sons, 2007).

[2] Pantidos, N. and Horsfall, L.E., Journal of Nanomedicine Nanotechnology, 5 (5) (2014) 233.

[3] Iravani, S, Green Chemistry, 13 (2011) 2638.

[4] Khan, I. et al., Arabian Journal of Chemistry, 12 (7) (2019) 908.

[5] Mahapatra, D.K. *et al*., Research and Reviews: A Journal of Pharmacognosy, 5 (1) (2018) 20.

[6] Nasrollahzadeh, M. *et al*., Materials Research Bulletin, 102 (2018) 24.

[7] Sajadi, S. *et al*., ChemistrySelect, 3 (4) (2018) 12274.

[8] Barzinjy, A.A. *et al*., Journal of Materials Science: Materials in Electronics, 31 (14) (2020) 11303.

[9] Barzinjy, A.A. *et al*., Eurasian Journal of Science and Engineering, 4 (2019) 74.

[10] Barzinjy, A.A. *et al*., Inorganic and Nano-Metal Chemistry, 50 (8) (2020) 620.

[11] Barzinjy, A.A. *et al*., Current Organic Synthesis, 17 (7) (2020) 558.

[12] Azeeza, H.H. *et al*., Desalination and Water Treatment, 190 (2020) 179.

[13] Barzinjy, A.A. *et al*., Micro & Nano Letters, 15 (6) (2020) 415.

[14] Barzinjy, A.A. *et al*., SN Applied Sciences, 2 (5) (2020) 1.

[15] Barzinjy, A.A. *et al*., Eurasian Journal of Science and Engineering. 4 (1) (2018) 82

[16] Dhabarde, D.M. *et al*., Asian Journal of Pharmacy and Pharmacology, 5 (3) (2019) 456.

[17] Khandel, P. *et al*., Journal of Nanostructure in Chemistry, 8 (2018) 369.

[18] Telrandhe, R. *et al*., International Journal of Pharmaceutics and Drug Analysis, 5 (9) (2017) 376.

[19] Mahapatra, D.K. *et al*., Current Nanomedicine, 7 (1) (2017) 5.

[20] Hutchison, J.E. *et al*., ACS Nano, 2 (3) (2008) 395.

[21] Mahapatra, D.K. and Bharti, S.K., "Recent Advances in Bio-organism-mediated Green Synthesis of Silver Nanoparticles: A Way Ahead for Nanomedicine". In: Paurhashemi, A., Deka, S.C. and Haghi, A.K., Editors, Research Methods and Applications in Chemical and Biological Engineering, (New Jersey: Apple Academic Press, 2019).

[22] Li, X. et al., Journal of Nanomaterials, 2011 (2011) 270974.

[23] Mahapatra, D.K. *et al.*, "Research Progress and New Insights in Biosynthesis of Silver Nanoparticles with Particular Applications". In: Torrens, F., Haghi, A.K. and Chakraborty, T, Editors, Chemical Nanoscience and Nanotechnology: New Materials and Modern Technology, (New Jersey: Apple Academic Press, 2019).

[24] Telrandhe, R. *et al*., "Anti-Proliferative Potentials of Silver Nanoparticles Synthesized from Natural Biomass". In: Mahapatra, D.K., Talele, S.G. and Haghi, A.K., Editors, Applied Pharmaceutical Science and Microbiology: Novel Green Chemistry Methods and Natural Products, (New Jersey: Apple Academic Press, 2020).

[25] Annu, A. *et al*., Materials Today: Proceedings, 33 (8) (2020) 5317.

[26] Saraswathi, V.S. and Santhakumar, K., Journal of Photochemistry and Photobiology B: Biology, 169 (2017) 47.

[27] Davar, F. *et al*., Ceramics International, 44 (16) (2018) 19377.

[28] da Silva, A.F. *et al*., Colloids and Surfaces A: Physicochemical and Engineering Aspects, 583 (2019) 123915.

[29] Tharani, S.S., International Journal of Engineering and Applied Sciences, 3(4) (2016) 23.

[30] Matheswari, P.P. *et al*., The Pharma Innovation Journal, 8 (6) (2019) 968.

[31] Pandiyan, N. *et al*., Journal of Photochemistry and Photobiology B, 178 (2018) 481.

[32] Nasrollahzadeh, M. *et al*., Applied Organometallic Chemistry, 33(2) (2019) e4705.

[33] Nimare, P. and Koser, A.A., International Journal of Engineering and Technology, 3 (2016) 1910.

[34] Santhanam, P. *et al*., International Journal of Research in Pharmaceutical Sciences, 10 (4) (2019) 2864.

[35] Kumaresan, M. *et al*., Microbial Pathogenesis, 124 (2018) 311.

[36] Golnaraghi, G.A.R. *et al*., Iranian Journal of Pharmaceutical Research, 18 (4) (2019) 2101.

[37] Lengke, M.F. *et al*., Langmuir, 23 (2007) 2694.

[38] Jain, N. *et al*., Nanoscale, 3 (2011) 635.

[39] Kumar, S.A. *et al*., Biotech Letters, 29 (3) (2007) 439.

[40] Shaligram, N.S. *et al*., Process Biochemistry, 44 (200) 939.

Volume 15, Number 1, 2022. pp. 89-99

Jordan Journal of Physics

ARTICLE

Utilization of Mother Nature's Gift for the Biofabrication of Copper/ Copper Oxide Nanoparticles for Therapeutic Applications

K. M. Dadure[a], D. Kar Mahapatra[b], A. G. M. Haldar[c], A. K. Potbhare[d] and R. G. Chaudhary[d]

[a] *Department of Chemistry, J. B. College of Science, Wardha-442001, Maharashtra, India.*
[b] *Department of Pharmaceutical Chemistry, Dadasaheb Balpande College of Pharmacy, Nagpur-440037, Maharashtra, India.*
[c] *Department of Applied Chemistry, Priyadarshini Bhagwati College of Engineering, Nagpur-440009, Maharashtra, India.*
[d] *Post-graduate Department of Chemistry, Seth Kesarimal Porwal College of Arts, Science and Commerce, Kamptee-441001, Maharashtra, India.*

Doi: **https://doi.org/10.47011/15.1.12**

Received on: 01/08/2020; *Accepted on: 04/07/2021*

Abstract: This review enumerates the green *cum* biosynthesis of copper/copper oxide nanoparticles (Cu/CuO NPs) using plant and biogenic extracts. Moreover, it explores the biogenic synthesis of Cu/CuO NPs using different methods and elaborates on biological and eco-friendly modes of synthesis using different plant species. The survey revealed that biological methods involve the use of plant extracts, bacteria, protozoa and fungi. However, plant mediated nanomaterials synthesis is the best technique. Some of the microscopic characterization techniques, like XRD, SEM, TEM, FTIR, XPS, BET and UV–Vis, have been discussed to explore the size, shape, structure, composition and porosity of Cu NPs. The current review highlights the phytosynthesis, characterization and therapeutic applications of Cu/CuO NPs. The therapeutic applications of Cu/CuO NPs, like antimicrobial, anti-parasitic and anticancer activities against a variety of gram-negative and positive bacteria, fungi and human cancer cells, respectively, have been discussed.

Keywords: Biosynthesis, Phytosynthesis, Cu/CuO NPs, Microscopic techniques; Therapeutic applications.

Introduction

Research all over the world on green nanotechnology enhanced the scientific revolution of the twenty-first century. Metal nanoparticles have varieties of applications, like catalytic, energy storage, environmental remediation, biological, and so forth [1]. There are various chemical and synthetic routes that have been employed to synthesize nanoparticles due to their various applications in scientific, technological, pharmacological and biomedical sectors [2]. One of the interesting and human beneficial biogenic synthesized metallic nanoparticles is copper nanoparticles (Cu NPs). In the synthesis of Cu NPs, low-cost chemicals and plant extracts as precursors are used, several of which have advanced chemical and physical properties [3]. Cu NPs are among the most useful elements in medical sciences that can be used in numerous therapeutic effects, such as anti-inflammatory, anticancer, analgesic and antimicrobial effects [6]. Cu NPs have greater applications in heat transfer systems, such as sensors as well as catalysts [7]. Nanotechnology has greater applications in research area. In the past, chemical methods of the synthesis of Cu NPs were used which are known to be expensive

Corresponding Author: K. M. Dadure **Email**: kdadure@gmail.com

and toxic due to usage of expensive hazardous chemicals, thus posing a threat to health as well as the environment issue. This has led to the utilization of safe methods of NP synthesis, such as the biological method through which various plant extracts can be used as precursors in the green synthesis. According to literature survey, Cu/CuO NPs were biosynthesized using *Neriumoleander, Punicagranatum*, *Aegle marmelos*, *Ocimum sanctum* and *Zingiber officinale*. As-synthesized Cu NPs were studied against gram +ve bacteria, like *Staphylococcus aureus,* and showed good results. [4] NPs are recognized for their large surface area to volume ratio, small size and other physicochemical parameters which make them useful to man in applications, such as dye removal [5], antioxidant, antidiabetic, anti-inflammatory [6] and antibacterial activities [8]. The Cu NPs also possess remarkable properties due to their specific qualities, like tunable size, shape, and distribution as compared to bigger particles. Nanoparticles generally possess remarkable catalytic, optical, magnetic, electronic and thermal properties. Amongst the various noble ionic-based NPs, Cu NPs remain the most explored and have potential in catalysis. Similarly, silver is one of the common antimicrobial agents like copper owing to its strong toxicity against various microorganisms [9]. However, Cu NPs attract a great deal of attention due to the availability of the Cu precursor and their distinguished exceptional properties, as mentioned earlier, in addition to their versatile applicability in many fields, including - but not limited to - agricultural, industrial, environmental and medical applications [10]. Synthesis methodologies are considered of utmost importance in the field of nanotechnology. In this regard, the methodologies which have been adopted in the synthesis of Cu NPs using plant extracts are shown in (Fig. 1) [11].

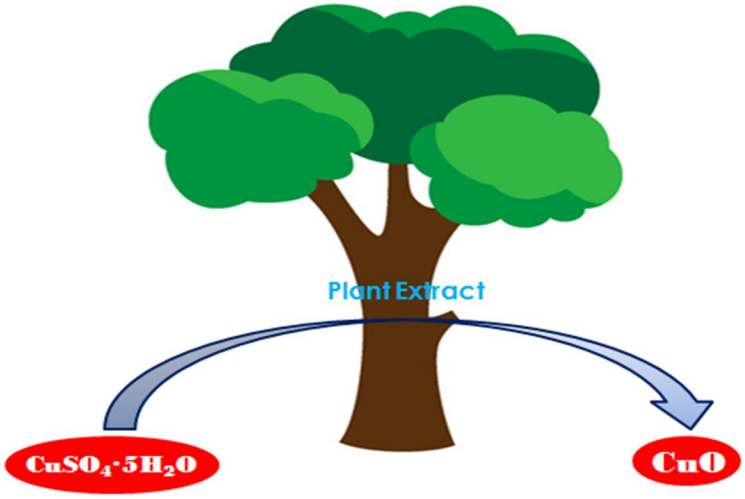

FIG. 1. Fabrication of Cu NPs from various zinc salts employing different plant extracts.

Plant-mediated Biosynthesis of Cu/Cuo Nps

The objective of the present work is the introduction of a quick and simple literature survey on the biosynthesis of Cu NPs. The green methodologies' utilization has increased considerably in the last few decades [12-14]. The literature survey reveals that the eco-friendly preparation methods using different plant species and their properties and potential applications serve as a good alternative in nanotechnology. The development of this new approach and the significant interest in it are mainly related to the absence of toxic chemicals or high-energy applied methods to the biological synthesis, which led to develop methods which are more environmentally friendly and cost-effective. This review enumerates the classification of nanomaterials in general, green biosynthesis of NPs using plant extracts and its advantages over using bacteria and fungi. Many researches in the literature indicate that the biosynthesis of metal oxides reduced to metallic nanoparticles is more eco-friendly than the conventional physiochemical methods used presently. Therefore, these biological methods have become more popular as green synthesis. The recent developments of plant-mediated biosynthesis of Cu NPs have been dissected in the subsequent paragraphs and are listed in Table 1.

S. Nasreen *et al.* have synthesized low-cost eco-friendly Cu NPs. A naturally available precursor with the help of plant extract *Aloe barbedensis* was used to develop the biocompatible NPs and the antibacterial activity was evaluated against gram-negative and gram-positive pathogens. Also, the results found more enhanced activity towards the gram-negative bacteria [15].

T. Saleh *et al.* used a biological extract of *Cynomorium coccineum* for the synthesis of Cu NPs using copper sulphate as a starting material and reported 14.2 nm as the size of the NPs [16].

Nadri *et al.* used *C. spinosa* fruits extract to prepare Cu NPs and obtained particle size between 17 and 41 nm. The results demonstrated the analgesic effects of Cu NPs, especially in combination with morphine and provided a new strategy for producing new antinociceptive medications in the future [17].

Bharadvaja *et al.* have synthesized environment-friendly Cu NPs with size of 1.54 nm which were also cost-efficient at different concentrations with the help of plant leaves of *Centella asiatica* and produced spherical shape of 323 nm size [18].

Ji-Ming Song *et al.* synthesized Cu NPs through biological route and environmentally friendly approach using *Camellia japonica* plant leaf extract, which were tested for antimicrobial properties against *Pneumoniae*, *Streptococcus pneumonia*, *Bacillus subtilis* and gram-negative (*Escherichia coli, Salmonella typhimurium*) bacterial pathogens as well as fungal strains of *Aspergillus flavus, Aspergillus fumigates*, *Aspergillus niger* and *Candida albicans* [19].

A. Mohamed reported a green method for synthesis of Cu NPs using the extract of seedless dates, which is simple, cost-effective and environment-friendly, obtaining spherical-shaped particles with size of 78 nm [20].

N. Ildiz *et al.* have demonstrated the plant-mediated synthesis of Cu NPs using a plant extract and enhanced antimicrobial activities towards standard bacterial (*E.coli, S.typhi, P.aeruginosa* and *S.aureus*) and fungal pathogens (*C.albicans*) compared to other extracts and reported flower-shaped 11±1 and 8±1nm nano-size particles. The results suggest that green synthesis of NPs presents a promising potential for development of eco-friendly antimicrobial agents for specific nasocomial human pathogens [21].

A. Zangeneh *et al.* performed biosynthesis of Cu NPs using *A. biebersteinii* leaf aqueous extract and reported crystal-shaped NPs of 10.1 nm and 23.4 nm size. According to these results, it seems that Cu NPs could be administrated as a neuroprotective supplement or drug for the treatment of central nervous system disorders in clinical trials and have shown antispermatogenic, antidiabetic, antibacterial, antiviral, antiparasitic, antifungal, antiulcer, anti-inflammatory, antispasmodic and especially neuroprotective effects [22].

Li,Burn *et al.* also reported a biosynthesis of Cu NPs from the bioreduction of $CuSO_4$ solutions using *A. eriophyllum* leaf extracts and produced spherical-shaped NPs of 31.34 nm size. The environment-friendly method used also indicated high antifungal, antibacterial, antibiotic, antiviral and antiparasitic effects against all the tested fungi and bacteria species [23].

Similarly, Al. Haddad *et al.* developed a cost-effective, non-toxic green technique to produce high-quality Cu NPs. This green synthesis of Cu bimetallic NPs was performed using extracts from date palm tree (*Phoenix dactylifera*) leaves. The results showed the FCC structure of 26 nm size having significant pharmacological and antibacterial activities against *Bacillus subtilis* (gram-positive) and *Escherichia coli* (gram-negative) bacteria [24].

Moreover, extensive work was published on copper oxide nanoparticles (CuO NPs) for various clinical applications. The CuO NPs were biosynthesized by M.T. Pelegrino *et al.* using green tea extract, which acts as a reducing and capping agent and reported NPs with the size of 6.6 nm. CuO NPs were highly stable in aqueous suspension. Toxicity of bioassays has shown that at low concentrations (up to 40 $\mu g\ mL^{-1}$), the CuO NPs did not affect or even enhance seed germination enhancing plant growth and the involvement of nitric oxide signaled the phytotoxic effects induced by high concentrations of this formulation [25].

Next, Karunakaran *et al.* have demonstrated flower extract-mediated biosynthesis of CuO using *Hylotelephium telephium*. The study confirmed the formation of spherical-shaped of

size 83nm NPs and found great antioxidant and antimicrobial activities on the tested bacteria. It is cleared that *H.telephium* flower extract-mediated biosynthesis of NPs is a new approach with prospects for eco-friendly NP synthesis [26].

Similarly, S. Shah *et al.* have reported green synthesis of nano-sized CuO NPs using *Carica papaya* leaves extract. They obtained a growth of crystalline-shaped with size of 270 nm nanoparticles. The CuO NPs-coated cotton fabric displays greater antibacterial activity against *E.coli* and exhibits superior antimicrobial activity, indicating that it has a higher potential to be employed in medical textile to avoid cross-infection within a clinical environment. The NPs also exhibited good antimicrobial activity against gram-negative *E.coli* [27].

Likewise, Chandrasekaran *et al.* have studied the green synthesis of CuO NPs using an aqueous extract of *Beta vulgaris* beetroots. The synthesized NPs appeared crystalline in shape with a range of 35-95 nm size. Subsequently, anticancer efficacy of the CuO NPs was studied in A549 cells through cell viability assay. The CuO NPs induced apoptosis in the A549 cell line with an IC_{50} value of 25 lg/mL, as revealed by cytometer analysis. Therefore, it is presumed that CuO NPs could be developed as a nano-drug for infectious diseases and tumor studies [28].

S. Suresh *et al.* have revealed the biosynthesis of CuO nanostructures, which were synthesized using *Cynodon dactylon* and *Cyperus rotundus* grass extracts. The reported NPs had clusters of sponge-like shape with 500 nm size, having a significant antibacterial activity against bacterial species *B.cereus*, *S.aureus*, *E.coli* and *K.pneumoniae* [29].

Moreover, Lin Yuanhua *et al.* used the peels extract to mediate the synthesis of Cu NPs (ETP-Cu NPs) using *Citrus reticulata* (tangerine) and obtained round shape with 54 and 72 nm particles. The crystal structure, morphology, surface and chemical properties were experimentally confirmed. The nano-formulation was found to inhibit both acid and microbial corrosion of X80 steel [30].

Getu Weldegebrie has revealed the study of biosynthesis of CuO NPs using *Verbascum thapsus* extract and their characteristics study showed NPs having a spherical shape with 219 to 500nm size. They also exhibited antibacterial properties against both *S.aureus* and *E.coli* bacteria [31].

J. Sackey *et al.* have revealed that CuO NPs were successfully synthesized *via* a cost-effective approach using aqueous extracts obtained from red flowers of *Euphorbia pulcherrima* and further characterization study of NPs showed a cubic shape with 153.7 and 16.3nm particle size [32].

D. Padmanabhan Nambiar *et al.* synthesized CuO NPs using *Caesalpinia bonducella* seed extract *via* a green synthetic pathway. The study introduces a convenient and inexpensive method to synthesize CuO NPs as a novel reducing and stabilizing agent. They obtained rice-shaped NPs with 3.13−56.3 nm particle size. The antibacterial properties of CuO NPs were investigated against *S.aureus* gram-positive and gram-negative bacteria by the agar diffusion method. Each bacterial strain was smeared evenly on the sterilized agar Petri plates and allowed to dry the synthesized nano-particles, thus proving to be an interesting material for electrochemical and biological studies (Fig. 2) [33].

Fatih Erci *et al*. prepared cost-effective and environment friendly Cu NPs by biogenic reduction of $CuSO_4.5H_2O$ solution through deionized water and ethanol mixed extract of leaf powder of *Thymbra spicata*. They have produced spherical-shaped and 26.8 nm and 21 nm size nanoparticles. The bacterial inhibition of the developed NPs against *S.typhi* and biofilm activity against *S.aureus* showed promising results. In addition, the reported particles showed a significant anti-oxidant property [34].

Jaswanth Seetha *et al.* have reported the biosynthesis of CuO NPs with the help of de-ionized water extract of fresh leaves of *Moringa oliefiera* (MO) by utilization of precursor $CuSO_4.5H_2O$ as a reductant for bioreduction. This research resulted in the growth of spherical-shaped, 110 nm NPs having a significant pharmacological activity against *S. aureus* and pathogenic bacteria *Klebsiella pneumonia* (*K.pneumonia*) in a disc diffusion test [35]. D. Balakrishnan *et al*. have demonstrated the flora-mediated generation of CuO NPs through water and alcohol extraction method of the leaves of *Euphorbia cyathophora*. The NPs were spherical-shaped with 40 nm to 55 nm size range. The developed nanoparticles showed promising antioxidant capacity [36].

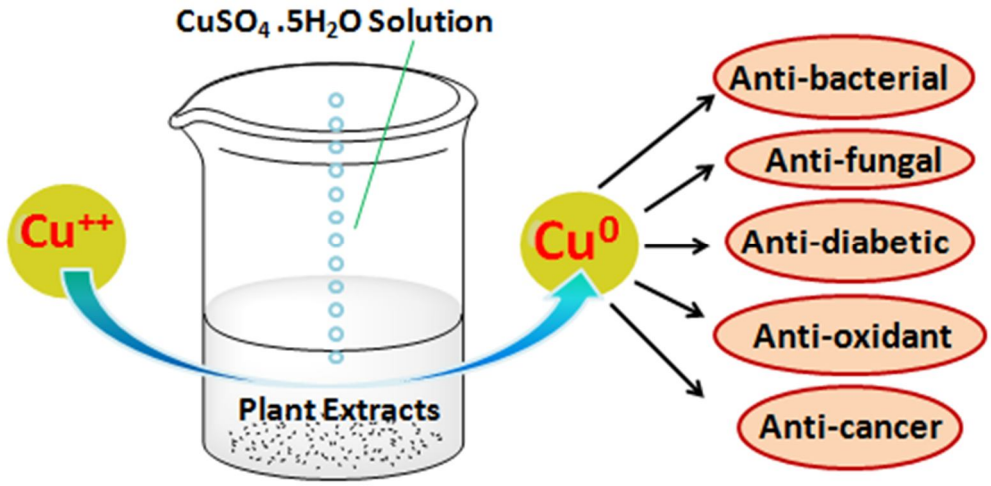

FIG. 2. Biosynthesis of Cu NPs and their pharmacological applications.

Similarly, A.M. Awwad *et al*. have revealed interesting facts about biosynthesis of CuO NPs in the presence of aqueous solution of *Ailanthus altissima* leaf extract with copper acetate initiator. Spherical-shaped NPs with 20 nm size were produced. The CuO NPs have revealed antibacterial activity against *S.aureus* using chloromphenical as a control for the antimicrobial agent in a disc diffusion method [37].

Sharmila Pradhan Amatya *et al*. have studied the green synthesis of CuO NPs with the help of *Euphorbia hirta* leaves extract as reducing and capping agent with $CuSO_4 \cdot 5H_2O$ as the precursor of the reaction. The newly formed Cu NPs were spherical-shaped with size between 20-25 nm. The synthesized NPs appeared to be effective against various standard strains of micropathogens, like *S.aureus* and *E.Coli* by taking ofloxacin as a standard for zone of inhibition [38].

Adeyemi, D. K. *et al*. have reported the biosynthesis of CuO NPs by using *Spondias mombin* leaves extract with copper acetate as reductant of the reaction. The reported NPs have a triangular shape with 65-90 nm size. The newly synthesized NPs were found to have exceptional pharmacological activity, like antibacterial inhibition towards common micropathogens *E.Coli*, *Pseudomonas aeruginosa* and *S. aureus* against standard drug ciprofloxacin [39-40].

Suresh Ghotekarb *et al*. have revealed some interesting facts about flora-mediated synthesis of CuO NPs in aqueous extract of *Moringa oleifera* leaf by utilising copper acetate monohydrate as the precursor. The synthesized NPs, as observed, were quasi-spherical-shaped with 35-95 nm size. The newly reported particles have interesting antifungal activity against some selected strains (*C.albicans*, *A.niger*, *A.clavatus*, *T.mentographyte* and *E.floccosum*) with reference standard of griseofulvin [41].

Akhilesh Kumar Singh *et al*. have synthesized eco-friendly CuO NPs by utilizing $CuSO_4$ as reductant with the help of aqueous extract of leaf of *Mangifera indica* (L.). The synthesized NPs were spherical-shaped and 4-7 nm size. They have found to be efficient in the detection of cysteine and NADH. The newly synthesized NPs have revealed antimicrobial inhibition against *E.coli* KT45/45A and *S.aureus* KT68, as well as antioxidant activity [42].

Anbuvannan Mari *et al*. have reported the flora-mediated synthesis of CuO NPs with the help of aqueous extract of fresh leaves of *Catharanthus roseus* by utilization of copper nitrate used as the precursor. The research revealed the development of rod-shape 23-nm nanoparticles having promising anti-micropathogenic activity against *E.coli* [43].

Rakesh Chowdhury *et al.* have reported the synthesis of CuO NPs by an alkaline hydrolysis process in the presence of the flower extract of *Lantana camara*, an invasive weed, followed by calcination in air at 400 ^{o}C. They noted crystalline shape with 10 nm size [44].

Olga Długosz1 *et al.* have revealed a green method for synthesis of Cu NPs using extract of hawthorn dried fruit having been reported for the

reduction of copper ions. The synthesized NPs have a spherical shape and 200 nm size. The NPs showed roughly similar antibacterial activity against the tested pathogenic microorganisms, *A.niger*, *E.coli* and *S.cerevisiae* (below 100 mg/l) [45].

Elias E. Elemike *et al.* have reported the synthesis of Cu_2O/CuO NPs, prepared using *Alchornea cordifolia* leaf extract. The average size of the NPs in the composites was estimated at 3.54 nm having spherical shape and toxicity against cervical cancer using MTT assay method. The *in vitro* cytotoxicity tests of the nanomaterials was conducted on cervical *Hela* cell lines [46].

T. Venkatappa Rao *et al*. reported a green synthesis of Cu NPs, with aqueous extract of *Curcuma longa* powder by using a simple and cost-effective method. The size of the particles was in the range of 5–20 nm having a crystalline structure. The antibacterial activity of the obtained Cu NPs is tested for both gram-positive and gram-negative microorganisms. The zone of inhibition of Cu NPs for gram-negative bacteria is higher as compared to that for gram-positive bacteria due to their distinct cell wall structure. The cell wall of negative bacteria does not have an outer membrane envelope. The NPs equally showed antimicrobial, antifungal and anticancer activity [47].

Sukumar Kayalvizhi *et al*. have explored eco-friendly green synthesis of CuO NPs using *Annona muricata* leaf extract to investigate cytotoxic property on human breast cancer cell lines (MCF-7) *via in-vitro* studies. The NPs were exposed to cancer cells in a dose-dependent manner. The synthesized CuO NPs showed 30-40 nm particle size range and spherical shape [48].

R M. Mahmoud *et al*. have explored an efficient biosynthesis of CuO NPs by utilizing two precursors of waste plant extracts; namely, pomegranate peel and date stones. The biogenic CuO NPs as cytotoxic agent were applied against human breast cancer (MCF7) cell lines and compared with the normal BJ1 cell line. The synthesized Cu NPs were reported to be crystalline in nature having particle size of 6 to 20 nm [49].

Abu-Yousef *et al.* in their study revealed the biosynthesis of Cu NPs using an extract of *M.oleifera* leaves treated with $CuSO_4.5H_2O$ solution. This *oleifera* leaves extract exerts considerable anti-bacterial activity against *E.coli*, *Klebsiella pneumoniae*, *S.aureus* and *Enterococcus faecalis* and anti-fungal activity against *A.niger*, *A.flavus*, *Candida albicans* and *Candida glabrata*. Besides, it reported antioxidant, anti-bacterial and anti-fungal activities [50].

Joy Sarkar *et al.* have reported the biosynthesis of CuO NPs with the help of de-ionized water extract *Adiantum lunulatum* whole plant extract by utilization of precursor $CuSO_4.5H_2O$ as a reductant for bioreduction. This research resulted in the growth of spherical-shaped, 6.5 - 1.5 nm NPs. The NPs have significant antioxidant activity [51].

Ashutosh Sharma *et al.* conducted a study to prepare cost-effective and environment-friendly CuO NPs by biogenic reduction of $CuSO_4.5H_2O$ solution through de-ionized water and ethanol mixed extract of leaf and flower powder of *Galphimia glauca*. They have produced spherical-shaped and 5-10 nm sized particles. The cytotoxicity assays of developed nanoparticles were also determined using MRC-5 and HeLa cell lines for CuO NPs and it was found that the NPs are non-toxic to the normal cells and are relatively toxic to cancer cells [52].

Mehran Moradi *et al*. have reported the biosynthesis of CuO NPs with the help of deionized water extract of fresh fruit of mulberry (*Morus alba* L.) by utilization of precursor copper nitrate trihydrate ($Cu(NO_3)_2 \cdot 3H_2O$) as a reductant for bioreduction. The research resulted in the growth of spherical-shaped, 50 to 200 nm NPs having a significant pharmacological activity and superior antibacterial activity against *E.coli* O157:H7 and *Listeria monocytogenes* [53].

D Renuga *et al*. prepared cost-effective and environment-friendly CuO NPs by biogenic reduction of copper (II) acetate solution through deionized water and ethanol mixed extract of leaf powder of *Brassica oleracea.* They have produced spherical-shaped and 26-nm size particles. The bacterial inhibition of the developed NPs against *E.coli* showed enhanced effect. Likewise, the nanocomposites exhibited strongest antifungal activity against *Aspergillus niger* and *Candida albicans* (Table 1) [54].

TABLE 1. Plant-mediated synthesis of Cu/CuO NPs.

S/ No.	Plants	Family	Part Used	Average Size of Cu/CuO NPs (nm)	Shape	Characterizations	Therapeutic Applications	Ref.
1	*Aloe barbedensis*	Apiaceae	Plant	NA	--	SEM-EDX, FTIR	Antibacterial	[12]
2	*Cynomorium coccineum*	Balanophoraceae	Whole plant	14.2	--	FTIR, SEM, EDX, XRD, TG	Biosorption, Water purification, Photocayalysis, Textile printing	[13]
3	*Copperas spinosa*	Capparaceae	Fruit	NA	--	FTIR, EDX, SEM	Anti-nociceptive	[14]
4	*Centella asiatica*	Mackinlayaceae		323	Spherical	SEM. UV	NA	[15]
5	*Camellia japonica*	Theaceae	Leaf	1.54	--	UV–Vis, FTIR, XRD, SEM, TEM	Antimicrobial, Antifungal	[16]
6	*Seedless dates*	Palmaceae	NA	78	Spherical	TEM, DLS, XRD, UV-Vis, FTIR	NA	[17]
7	*Artemisia*	Asteraceae	Whole Plant	11±1, 8±1	Flower	FTIR, SEM, XRD, EDX	Antimicrobial activity, Antibacterial, Antifungal	[18]
8	*Achillea biebersteinii*	*Achillea*	Leaves	10.1,23.4	Crystalline	FTIR, EDS, SEM, TEM	Antispermatogenic, Antidiabetic, Antibacterial, Antiviral, Antiparasitic, Antifungal, Antiulcer, Anti-inflammatory, Antispasmodic	[19]
9	*Allium eriophyllum*	Asteraceae	Leaf	crystal size of 31.34	Spherical	UV–Vis, FE-SEM, TEM	Antioxidant, Antibacterial, Antiviral, Anti-Parasitic	[20]
10	*Date palm tree*	Arecaceae	Leaves	26	FCC structures	SEM, EDX, XRD	Antibacterial	[21]
11	*Lactuca sativa* L.	Asteraceae	Commercial green tea	6.6	NA	NA	Antioxidant activity	[22]
12	*Hylotelephium telephium*	Crassulaceae	Flower	83	Spherical	SEM and TEM, XRD	Antioxidant, Antibacterial	[23]
13	*Carica papaya*	Caricaceae	Leaves	270	Crystalline nature	UV–Visible, FTIR, XRD, SEM, TEM	Antioxidant, Antibacterial	[24]
14	*Beta vulgaris*	Amaranthaceae.	Beetroot	310	NA	FTIR, TEM EDAX,AFM,	Anticancer, Antibacterial	[25]
15	*Cynodon dactylon*	Poaceae	Grass	500	Clusters of sponge-like	FTIR, TEM EDAX, XRD	Antibacterial	[26]
16	*Citrus reticulata*	Rutaceae	Peels	54, 72	Round	UV–Vis, FTIR, XRD, SEM/EDAX, TEM	Inhibition of acid and bio-corrosion in the oil field	[27]
18	*Verbascum thapsus*	Scrophulariaceae	Leaves	219-500	Spherical	UV–Vis, FTIR, SEM	Photocatalytic, Antibacterial	[28]
19	*Euphorbia pulcherrima.*	Euphorbiaceae	Red flowers	153.7, 16.3	Cubic	XRD (SEM) OPM, HRTEM EDS (FTIR/ATR) (XPS DR UV–Vis, PL CV, EIS)	NA	[29]
20	*Caesalpinia bonducella*	Caesalpiniaceae	Seed	3.13−56.3	Rice shape	UV–Vis, FTIR, XRD, SEM/EDAX, TEM XPES,SEM	Antibacterial	[30]

S/ No.	Plants	Family	Part Used	Average Size of Cu/CuO NPs (nm)	Shape	Characterizations	Therapeutic Applications	Ref.
21	*Thymbra spicata*	Lamiaceae	Leaf	26.8, 21	Spherical	UV-Vis,XE,AFM, FTIR, EDX, SEM, TEM	Antibacterial Antibiofilm	[31]
22	*Moringa oliefiera*	Moringaceae	Leaf	NA	Globular	FTIR, XRD, SEM, EDAX,	Antibacterial.	[32]
23	*Euphorbia cyathophora*	Euphorbiaceae	Leaf	40-55	Spherical	UV-Vis, FTIR, SEM	Antioxidant	[33]
24	*Ailanthus altissima*	Simaroubaceae	Aqueous leaf	20	Spherical	UV-Vis, SEM, TEM, FTIR	Antibacterial, Antimicrobial	[34]
25	*liliales*	Alliaceae	Garlic *Allium sativum*	NA	---	UV-Vis,XE,AFM, FTIR, EDX	Antibacterial, Antifungal, Antiparasitic, Antiviral, Antioxidant, Anti-cancerous	[35]
27	*Spondias mombin*	Anacardiaceae	Leaf	65-90	Triangular	UV-Vis, FTIR, SEM	Anxiolytic, Antiepileptic, Antipsychotic, Antioxidant, Antimicrobial	[37]
28	*Moringa oleifera*	Moringaceae	Leaf exract	35-95	Grain size	XRD, SEM, EDS. UV-DRS, PL	Antiatherosclerotic, Antioxidant,Anti-inflammatory, Anticancer, Antimicrobial	[38]
29	*Phyllanthus Reticulatus/Conyza Bonariensis*	Euphorbiaceous	Leaf	4-14	Microspher	UV-Vis, XRD, FTIR, XPS, BET	Antibacterial, Antioxidant	[39]
32	*Catharanthus roseus*	Apocynaceae	Leaf	23	Crystalline	UV-Vis-DRS PL, XRD, FTIR, SEM-EDS,TEM	Antibacterial, Antimicrobial	[40]
33	*Lantana camara*	Verbenaceae	Flower	10	Crystalline	XRD, FTIR, SEM,TEM,XPS,BET	NA	[41]
34	*Hawthorn*	Rosaceae	Fruits	200	Spherical	UV–Vis, LSPR, DLS, SEM, STEM	Antioxidant, Antimicrobial	[42]
35	*Alchornea cordifolia*	Euphorbiaceae	Leaf	3.54	Spherical	UV-Vis, XRD, FTIR, SEM, EDX, TEM	Anticancer	[43]
37	*Curcuma longa*	Zingiberaceae	*Curcuma longa* powder	5-20	Crystalline	FTIR, FE-SEM, EDS, XRD, TEM	Antimicrobial, Antifungal, Anticancer	[44]
38	*Annona muricata*	Annonaceae	Leaf	30-40	Spherical	UV-Vis, XRD, FTIR, SEM, EDX, BIO-TEM	Cytotoxic	[45]
39	*pomegranate peel*	Lythraceae	Peels	6.0-20	Crystal	FTIR, XRD, SEM, TEM,TGA, SPSS, TGA, DTA, Zetasizer	Cytotoxic inhibition of cancer cell growth	[46]
40	*Moringa oleifera*	Moringaceae	Leaves	35.8-49.2	Amorphous	UV-Vis, XRD, SEM,TEM, ALPHA-E, FTIR, FEG, HRTEM	Antioxidant, Anti-bacterial,Anti-fungal	[47]
41	*Adiantum lunulatum.*	Adiantaceae	Whole plant	6.5-1.5	Quasi-spherical	UV-Vis, XRD, FTIR, TEM, DLS, EDX, BIO-TEM	Antioxidative enzyme	[48]
42	*Galphimia glauca*	Malpighiaceae	Leaves and flowers	5-10	Crystalline	FTIR, TEM,XRD,GCMS	Anticancer	[49]

S/ No.	Plants	Family	Part Used	Average Size of Cu/CuO NPs (nm)	Shape	Characterizations	Therapeutic Applications	Ref.
44	*Mulberry*	*Moraceae*	Fruit	50-200	Spherical	UV-Vis, FTIR, TEM, DLS, ICP, OES	Antibacterial, Antimicrobial	[50]
45	*Brassica oleracea var. italic*	Brassicaceae	Whole plant	26	More or less uniform	FTIR, FESEM, EDAX, XRD, UV –Vis, FESEM	Antifungal activity	[51]

Applications of Cu/CuO NPs

Nanoparticles are generally synthesized in various sizes and shapes. Copper-based NPs, such as Cu NPs and CuO NPs are fabricated into varied shapes, like spherical, hexagonal, quasi-spherical, rod … etc. and demonstrated diverse pharmacological applications ranging between anti-fungal (*Aspergillus fumigatus*, *Aspergillus niger* and *Candida albicans*), anti-bacterial (*S.aureus*, *E.lmonella typhi* and *Pseudomonas aeruginosa*), anxiolytic, antiepileptic, antipsychotic, anti-oxidant, anti-inflammatory, anti-ulcer, anti-spasmodic, anti-viral, anti-parasitic, anti-spermatogenic, anti-diabetic, anti-biofilm, anti-atherosclerotic activities … etc.

A variety of plant parts was employed to biosynthesize Cu NPs and CuO NPs and their characterizations and applications are tabulated in Table 1.

Conclusion and Future Aspects

In conclusion, this article provided a perspective view on the active research area of biogenic synthesis, especially Cu NPs and CuO NPs for clinical applications. In the present work, we discussed the diverse morphologies (hexagonal, spherical, tetragonal, oval, cubic … etc.) of Cu NPs and CuO NPs which were obtained from different plant parts (leaf, stem, bark, fruit, flower, seed and trunk). Also, the pharmacological perspectives of these nanomaterials were discussed, like anti-oxidant, anti-inflammatory, anti-leishmanial, anti-diabetic, anti-bacterial, anti-fungal, anti-cancer, anti-viral, muscle relaxant, anti-nociceptive activities … etc. which opened new avenues in research for therapeutic applications. This literature opened new future perspectives for researchers in developing copper-based nanomaterials which will have multifarious applications. The future aspect of this technique is impactful. Moreover, more emphasis will be paid by young researchers as this technique is cheap and easy. Therefore, this technique could be sustainable, as it is eco-friendly, toxic-free, convenient and straightforward. Nonetheless, around the globe, researchers are always striving for green synthesis, as it is the best technique for nanomaterials' synthesis.

References

[1] Senanayake, S.D., Stacchiola, D. and Rodriguez, J.A., Acc. Chem. Res., 46 (2013) 1702; Chemical Methodologies, 3 (2019) 457.

[2] Cao, G., "Nanostructures and Nanomaterials: Synthesis, Properties and Applications", (576 London: Imperial College Press, 2004).

[3] Mittal, A.K., Chisti, Y. and Banerjee, U.C., Biotechnol. Adv., 31 (2013) 346.

[4] Padma, P.N., Banu, S.T. and Kumari, S.C., Ann. Res. Rev. Biol., 23 (1) (2018) 1.

[5] Saleh, T.A. and Al-Absi, A.A., Journal of Molecular Liquids, 248 (2017) 577.

[6] Govindasamy, R., Muthu, T., Govindarasu, M., Thandapani, G. and Ill- Min, C., Bioprocess Biosyst. Eng., 41 (2018) 1.

[7] Tanna, J.A., Chaudhary, R.G., Gandhare, N.V., Rai, A.R., Yerpude, S. and Juneja, H.D., Journal of Experimental Nanoscience, 11 (2016) 884.

[8] Sun, H., Yang, Z., Pu, Y., Dou, W., Wang, C., Wang, W., Hao, X., Chen, S., Shao, Q., Dong, M., Wu, S., Ding, T. and Guo, Z., J. Colloid Interf. Sci., 547 (2019) 40.

[9] Ravindran, A., Chandran, P. and Khan, S.S., Colloids Surf. B: Biointerfaces, 105 (2013) 342; Roy, A., Res. Rev. Biosci., 12 (4) (2017) 138.

[10] Lee, B., Kim, Y., Yang, S., Jeong, I. and Moon, J., Appl. Phys., 9 (2) (2009) e157.

[11] Shende, S., Ingle, A.P., Gade, A. and Rai, M., World J. Microbiol. Biotechnol., 31 (6) (2015) 865.

[12] Catalano, P.N., Chaudhary, R.G., Desimone, M.F. and Santo, P.L., Current Pharmaceutical Biotechnology, 22 (2021) 813.

[13] Umekar, M.S., Bhusari, G.S., Potbhare, A.K. and Chaudhary, R.G., Emerging Materials Research, 10 (2021) 75.

[14] Chaudhary, R.G., Chouke, P.B., Potbhare, A.K., Dadure, K.M., Mungole, A.J., Meshram, N.P. and Chaudhary, R.R., Materials Today: Proceedings, 29 (2020) 815.

[15] Abbas, S. *et al*. Saudi Journal of Biological Sciences, 27 (2020) 1016.

[16] Sebeia, N. *et al*. Arabian Journal of Chemistry, 13 (2) (2020) 4263.

[17] Mahmoudvand, H. *et al.*, Annals of Medicine and Surgery, 51 (2020) 31.

[18] Raina, S., Roy, A. and Bharadvaja, N., Environmental Nanotechnology, Monitoring & Management, 13 (2020) 100278.

[19] Muthuchamy, M. *et al*., Materials Today Communications, 22 (2020) 100766.

[20] Mohamed, E.A., Heliyon, 6 (1) (2020) e03123.

[21] Devi1, H.S. and Singh, T.D., Advance in Electronic and Electric Engineering, 4 (2014) 83.

[22] Wang, G. *et al*., Applied Organometallic Chemistry, 34 (4) (2020) e5488.

[23] Zhao, H. *et al*., Applied Organometallic Chemistry, 34 (2020) e5587.

[24] Al-Haddad, J. *et al*., Clean Technologies and Environmental Policy, 22 (1) (2020) 269.

[25] Pelegrino, M.T. *et al*., Environmental Monitoring and Assessment, 192 (4) (2020) 1.

[26] Karunakaran, G. *et al*. JOM, 72 (3) (2020) 1264.

[27] Turakhia, B. *et al*., Journal of Coatings Technology and Research, 172 (2020) 531.

[28] Chandrasekaran, R., Yadav, S.A. and Sivaperumal, S., Journal of Cluster Science, 31 (1) (2020) 221.

[29] Suresh, S. *et al*., Journal of Coatings Technology and Research, 17 (2020) 531.

[30] Ituen, E. *et al*. International Biodeterioration & Biodegradation, 149 (2020) 104935.

[31] Chawla, P. *et al*., International Journal of Biological Macromolecules, 146 (2020) 232.

[32] Weldegebrieal, G.K., Optik, 204 (2020) 164230.

[33] Sackey, J. *et al*., Materials Chemistry and Physics, 244 (2020) 122714.

[34] Sukumar, S., Rudrasenan, A. and Nambiar, D.P., ACS Omega, 5 (2020) 1040.

[35] Erci, F. *et al*., Preparative Biochemistry & Biotechnology, 50 (6) (2020) 1.

[36] Seetha, J. *et al*., Inorganic and Nano-metal Chemistry, 50 (9) (2020) 1.

[37] Rajendran, M. *et al*., Inpokra Research, 9 (2020) 103.

[38] Awwad, A. and Amer, M., Chemistry International, 6 (2020) 210.

[39] Potbhare, A.K., Chaudhary, R.G., Sonkusare, V., Mondal, A., Rai, A.R. and Juneja, H.D., Materials Science & Engineering C, 99 (2019) 783.

[40] Liliana, A.-F. *et al*., Progress in Natural Science: Materials International, 24 (4) (2014) 321.

[41] Adeyemi, D.K. *et al*., African Journal of Clinical and Experimental Microbiology, 21 (2) (2020) 106.

[42] Pagar, K. *et al*., Asian Journal of Nanosciences and Materials, 3 (1) (2020) 15.

[43] Rani, H. *et al*., Materials Chemistry and Physics, 239 (2020) 122052.

[44] Mari, A. *et al*., Chemical Methodologies, 4 (4) (2020) 424.

[45] Chowdhury, R., Khan, A. and Harunar Rashid, M.D., RSC Advances, 10 (24) (2020) 14374.

[46] Długosz, O., Chwastowski, J. and Banach, M., Chemical Papers, 74 (1) (2020) 239.

[47] Elemike, E.E., Onwudiwe, D.C. and Singh, M., Journal of Inorganic and Organometallic Polymers and Materials, 30 (2) (2020) 400.

[48] Jayarambabu, N. *et al*., Materials Letters, 259 (2020) 126813.

[49] Mahmoud, N.M.R. *et al*., Chemical Papers, 74 (2020) 1.

[50] Das, P.E. *et al*., Molecules, 25 (3) (2020) 555.

[51] Sarkar, J. *et al*., Nanomaterials, 10 (2) (2020) 312.

[52] Oza, G. *et al*., Applied Nanoscience, 10 (2) (2020) 541.

[53] Razavi, R. *et al*., Applied Nanoscience, 10 (2) (2020) 465.

[54] Renuga, D. *et al*., Materials Research Express, **7** (2020) 045007.

Volume 15, Number 1, 2022. pp. 101-106

Jordan Journal of Physics

ARTICLE

Two-color Emission in Dy^{3+}-activated $CaZnP_2O_7$ Pyrophosphate for White LED

R. L. Kohale[a], **A. N.Yerpude**[b] and **S. J. Dhoble**[c]

[a] *Department of Physics, Sant Gadge Maharaj Mahavidyalaya, Hingna, Dist-Nagpur, MH, India.441110*

[b] *Department of Physics,N.H.College,Bramhapuri - 441206, MH, India.*

[b] *Department of Physics, R.T.M. Nagpur University, Nagpur-440033, India.*

Doi: **https://doi.org/10.47011/15.1.13**

Received on: 01/08/2020; *Accepted on: 01/08/2021*

Abstract: $CaZnP_2O_7$ pyrophosphate phosphor doped with Dy^{3+} ions was synthesized by modified solid-state reaction. The crystalline phases were recognized using X-ray diffraction. Surface morphology was studied by scanning electron microscopy. Furthermore, the chromaticity coordinates' values were estimated from the emission spectra of $CaZnP_2O_7$:Dy^{3+}. The phosphor photoluminescence emission spectra were found to have an excitation at around 353 nm showing two distinguishing bands centered at about 482 nm (Blue) and 575 nm (Yellow) corresponding to $^4F_{9/2}\rightarrow{}^6H_{15/2}$ and $^4F_{9/2}\rightarrow{}^6H_{13/2}$ transitions of Dy^{3+}, respectively. These phosphors have strong absorption in the near-UV region. The intact study reveals that the present phosphors are suitable for color converter using UV light as the primary light source, which can be used as a blue/yellow phosphor excited by the n-UV LED chip and mixed with other color emission phosphors to obtain white light.
Keywords: Chemical synthesis, Luminescence, X-ray diffraction, Optical properties.

Introduction

Luminescent materials doped with Dy^{3+} have drawn much interest for their white emission (WLED), since they can produce white emission by adjusting the yellow to blue intensity ratio value [1,2] and can be used as one of the components in tricolor fluorescent lamps as well as potential white phosphors [3]. Several researchers are engaged in studying the luminescent properties of Dy^{3+} doped with different compositions. Recently, Shinde et al. [4] reported some Dy^{3+}-activated phosphate-based phosphors $X_6AlP_5O_{20}$ (where X= Sr, Ba, Ca and Mg) and Kim et al. [5] studied the photoluminescence properties of $BaMgP_2O_7$ doped with different rare earth metals as a potential phosphor for white emission. However, it is challenging to fabricate persistent phosphors RGB/YB [6] which have similar emission ratios to ensure white-light-emitting phosphors all the time. Dy^{3+} ions, which have a luminescence appearance in the 470–500 nm region due to $^4F_{9/2}$–$^6H_{15/2}$ transition and in the 570–600 nm region due to $^4F_{9/2}$–$^6H_{13/2}$ [7-9], consequently Dy^{3+} ions with emission lines in the visible (400–600 nm) region, have attracted much attention because of their white-light emissions [10-13]. Dy^{3+} has emissions due to the self-atomic energy levels and due to the acceptor levels of defect sites formed by Dy^{3+}.

The objective of this work is to carry out a detailed investigation of structural, morphological and photoluminescence properties of the newly synthesized $CaZnP_2O_7$:Dy^{3+} pyrophosphate phosphor to examine its

Corresponding Author: R. L. Kohale **Email**: riteshkohale@gmail.com

suitability as a potential candidate for phosphor-converted n-UV white-LEDs and solid-state lighting. A modified solid-state diffusion reaction prepared entitled phosphors. Significantly, $CaZnP_2O_7:Dy^{3+}$ phosphors were intensely studied for the effect of doping of rare earth ions Dy^{3+} to obtain various phosphors for w-UV LEDs. A detailed study was carried out on the luminescence properties and the concentration quenching mechanism of Dy^{3+}. The investigations on surface morphology were carried out by scanning electron microscopy (SEM). Furthermore, the color coordinates were calculated using color chromaticity diagrams. The entire study reveals that this phosphor system could be considered an alternative approach for white-light emission and solid-state lighting due to its excellent luminescent properties, more straightforward manufacturing procedure, lower production cost, and mercury-free excitation nonhygroscopic and environmental-friendly characteristics.

Experimental Details

Synthesis of $CaZnP_2O_7:Dy^{3+}$ Phosphor

The Dy^{3+}-activated $CaZnP_2O_7$ phosphor was prepared by chemical synthesis *via* modified solid-state diffusion. The starting AR grade materials (99.99% purity) were taken as follows:

Calcium Carbonate $CaCO_3$ (Merck, 99.999%), Zinc Carbonate $ZnCO_3$ (Merck, 99.990%), Ammonium dihydrogen phosphate $NH_4H_2PO_4$. (Merck 99.99% pure). The molar ratio of rare earth dysprosium oxide Dy_2O_3 (Aldrich, 99.999%) varied from 0.3 mol% to 1 mol% in $CaZnP_2O_7$ phosphor relative to Ca ions. The mixture of reagents was ground together to obtain a homogeneous powder and Dy^{3+} ions were introduced as Dy_2O_3 in solid-powder form. After being ground thoroughly in stoichiometric ratios using an agate mortar, the powder was transferred to silica crucible and then heated in a muffle furnace to ensure the best homogeneity and reactivity at 350 °C for 1 hr to decompose $NH_4H_2PO_4$. Afterward, the mixture was reground and heated in a furnace at 700 °C for 12 hrs. The temperature was cooled to 500°C and air-quenched to room temperature. All samples were found out to be purely white. Several complementary methods were used to characterize the prepared phosphors. The prepared host lattice was characterized for phase purity and crystallinity by X-ray powder diffraction (XRD) using a PAN-analytical diffractometer (Cu-Ka radiation). The photoluminescence measurements of excitation and emission were recorded on the Shimadzu RF5301PC spectrofluorophotometer. The same amount of sample (2 g) was used for each measurement. Emission and excitation spectra were recorded using a spectral slit width of 1.5 nm. The morphological studies were examined by scanning electron microscopy (SEM, JEOL 6380A)

The basic chemical reactions for $CaZnP_2O_7$ can be described as follows:

$$Ca\ (CO_3) + Zn\ (CO_3) + 2(NH_4H_2PO_4) \rightarrow CaZnP_2O_7 + 2NH_3 + 3H_2O + 2CO_2.$$

Results and Discussion

XRD Patterns of $CaZnP_2O_7$ Pure and $CaZnP_2O_7:Dy^{3+}$ Phosphor

In the present work, polycrystalline samples of $CaZnP_2O_7$ phosphor were obtained as described above in the experimental section. The phase purities of all the samples were checked by powder X-ray diffraction using PAN-analytical diffractometer (Cu-Kα radiation) at a scanning step of 0.010, with a continue time of 20s, in the 2θ range from 10^0 to $60^{0.}$ The XRD pattern for $CaZnP_2O_7$ pure samples is presented in Fig. 1. The sample XRD pattern is in good agreement with the standard PDF 50-0361, indicating that $CaZnP_2O_7$ powder was formed with no impurity phases. It gives the complete formation of the homogeneous product. The XRD patterns of these samples described above did not indicate constituents like Ca (CO_3), Zn (CO_3) or $NH_4H_2PO_4$, which forms a direct evidence for the formation of the desired compound.

Surface Morphology of $CaZnP_2O_7:Dy^{3+}$

In order to obtain insight information about the surface morphology of $CaZnP_2O_7$ phosphor, SEM analysis was performed. The particle morphology of the synthesized sample was observed by (SEM, JEOL 6380A) and the typical morphological images for $CaZnP_2O_7$ are represented in Fig.2.

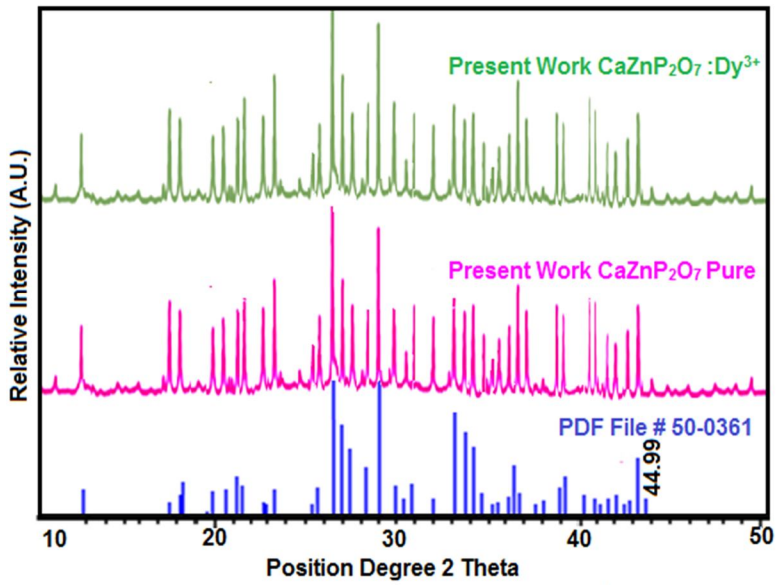

FIG. 1. XRD pattern of $CaZnP_2O_{7\ and}$ $CaZnP_2O_7$:Dy^{3+} materials.

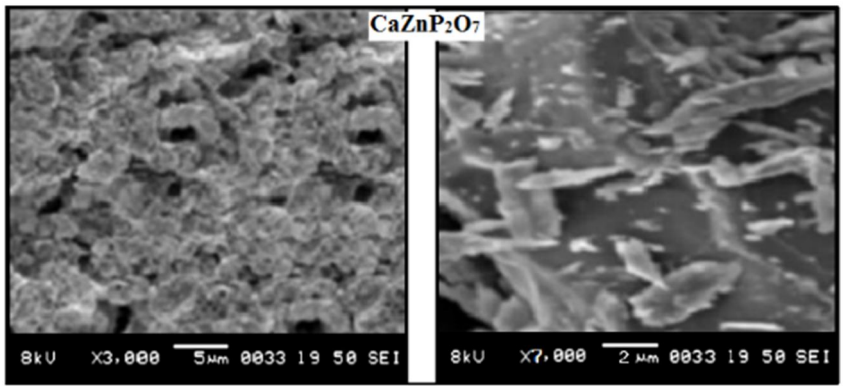

FIG. 2. SEM images of $CAZnP_2O_7$ phosphor.

SEM micrographs of the compound (Fig. 2) confirmed the polycrystalline nature of the material. Highly distinctive, nearly uniform and compact grain distributions are the unique features of the micrograph. Rod-shape and needle-shape morphologies could be visibly observed in the SEM micrographs. The sample size was moderately uniform and estimated in the micrometer range of 2-5 µm as seen in the SEM images. The size of the particles for $CaZnP_2O_7$ is around 1-4 µm (Fig.2). This shows that the solid-state reactions of the mixtures took place well. The sample $CaZnP_2O_7$ revealed a fine structure formed from highly agglomerated crystallites. Most particles showed a rod-shaped structure and sizes of a few micrometers. The sample revealed sintered structures in which individual particles could hardly be distinguished. These characteristics are advantageous when considering their application as phosphor powders to fabricate white LED and solid-state lighting [14].

Photoluminescence Spectra of Dy^{3+}-activated $CaZnP_2O_7$

Measurement of excitation and emission spectra was made by monitoring the peak wavelength of the Dy^{3+} emission of blue and yellow bands, respectively. The excitation spectra of the $CaZnP_2O_7$:Dy^{3+} phosphor monitored at around 575nm are shown in Fig. 3. The excitation spectrum monitored at yellow emission from Dy^{3+} ions indicates several bands in the wavelength region of 200 - 400 nm, which are due to excitation of the f–f shell transitions of Dy^{3+} [15]. The several peaks at 290 nm and 353 nm correspond to the transitions from the ground state $^6H_{15/2}$ to the excited states; $^4P_{7/2}$; $^4P_{3/2}$ and $^4F_{7/2}$, respectively. Maximum PL intensity for the excitation wavelength is located at 353 nm, which is a characteristic of solid-state lighting and hence, it has been selected for further photoluminescence investigation [16].

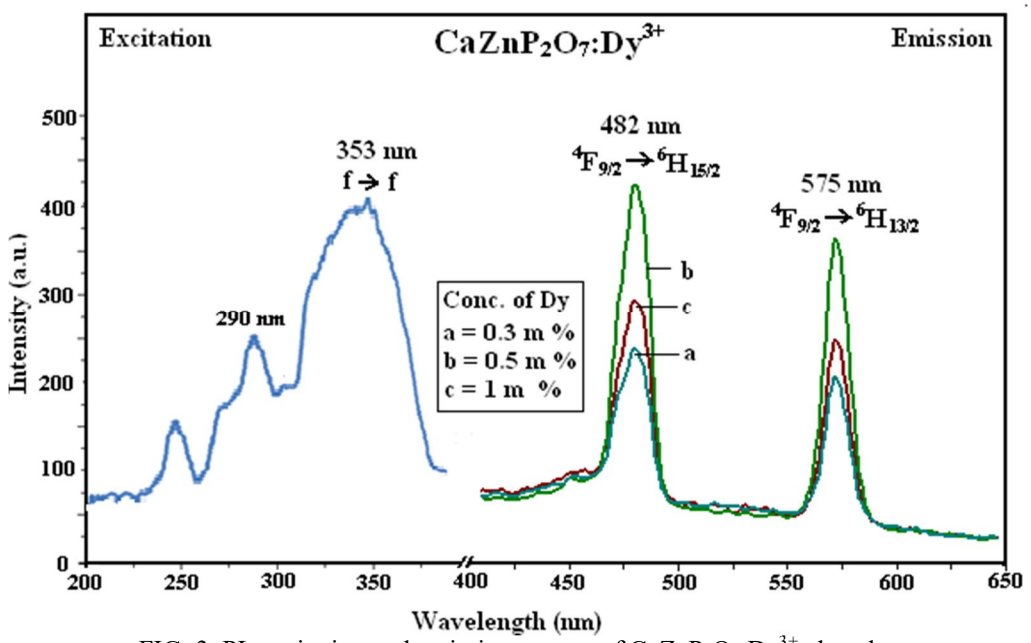

FIG. 3. PL excitation and emission spectra of $CaZnP_2O_7:Dy^{3+}$ phosphor.

Furthermore, Fig. 3 shows the emission spectra of the $CaZnP_2O_7:Dy^{3+}$ phosphors with around 353-nm excitation. The emission spectra were measured between 400–700 nm. Two emission bands peaked at 482 nm and 575 nm are observed. The blue emission at 482 nm is related to $^4F_{9/2}\rightarrow{}^6H_{15/2}$ magnetic dipole transition, while the yellow emission at 575 nm is ascribed to $^4F_{9/2}\rightarrow{}^6H_{13/2}$ electric dipole transition [17, 18]. Within these emission transitions, the yellow and the blue band is the predominant transition. The $^4F_{9/2}\rightarrow{}^6H_{13/2}$ transition is hypersensitive (ΔL-*2;* ΔJ-*2*) and it can be influenced by its microscopic environment, so its intensity strongly depends on the host. As a result, the entire characteristic indicates that Dy^{3+}-doped $CaZnP_2O_7$ phosphor is a good candidate for solid-state lighting devices (mercury-free excited lamp phosphor) and is suitable as a color converter using UV light as the primary light source.

Chromatic Properties of $CaZnP_2O_7:Dy^{3+}$

The CIE diagram of chromaticity for $CaZnP_2O_7:Dy^3$ is presented in Fig. 4. In the CIE diagram, every natural color could be identified by (x, y) coordinates disposed inside the 'chromatic shoe' representing the saturated colors [19]. Luminescence colors of dysprosium-activated $CaZnP_2O_7:Dy^{3+}$ phosphor are placed in the blue and yellow corners. The location of the color coordinates for $CaZnP_2O_7:Dy^{3+}$ phosphate-based phosphor on the CIE chromaticity diagram presented in Fig.4 indicates that the color properties of the phosphor powder prepared by the solid-state diffusion method are approaching those required for emission displays. The dominant wavelength can be determined by drawing a straight line from one of the CIE white illuminants (*C*s (0.3101, 0.3162)), through the (*x*, *y*) coordinates to be measured, until the line intersects the outer locus of points in Fig. 4. The CIE chromatic diagram shows the chromatic coordinates along the spectral edge of the 1931 CIE chromatic diagram.

The color purity was compared to the 1931 CIE Standard Source C (illuminant *C*s (0.3101, 0.3162)). The chromatic coordinates (*x*, *y*) were calculated using the color calculator program radiant imaging [20]. The coordinates of the $CaZnP_2O_7:Dy^{3+}$ phosphor of color range blue ($x\approx0.085$, $y\approx0.159$) and yellow ($x\approx0.475$, $y\approx0.518$) for 483 and 575 nm emission wavelengths are shown in Fig. 4 by the cross sign (×).

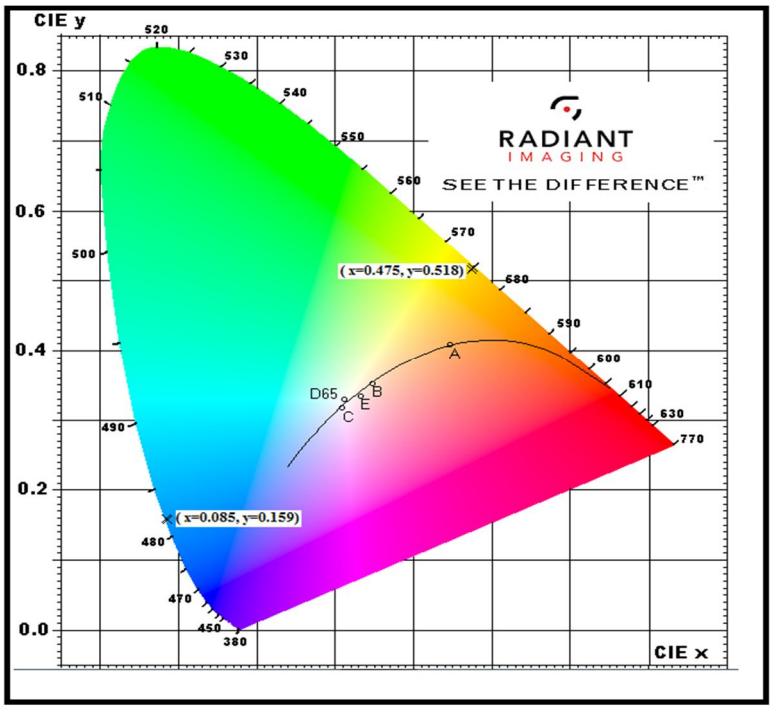

FIG. 4. CIE chromatic diagram showing the chromatic coordinates.

Conclusion

An efficient $CaZnP_2O_7$: Dy^{3+} pyrophosphate phosphor is prepared by modified solid-state diffusion. The XRD pattern for $CaZnP_2O_7$ reasonably agrees with the standard PDF File available. Morphological examination by scanning electron microscope indicates that particles have rod-shape and needle-shape morphologies. The average particle size is in the micrometer range of 2-5 µm and shows uniformity, which is advantageous for fabricating white LEDs (coating purpose). Chromaticity coordinates' values suggest that $CaZnP_2O_7$ pyrophosphate phosphor is suitable for white light-emitting phosphor. In the photoluminescence spectra of present phosphor, under the excitation of 353 nm, only the characteristic transition emissions of Dy^{3+} can be observed, which gives emission at around 482 nm (blue) and 575 nm (yellow). In view of the broad excitation band and excellent luminescent properties, $CAZnP_2O_7$:Dy^{3+} is expected to be a potential candidate for application in n-UV white LEDs and solid-state lighting because of its cost-efficient manufacturing, mercury-free excitation and eco-friendly characteristics.

References

[1] Gu, F., Shu, S.F., Lu, M.K., Zhou, G.J., Liu, S.W., Xu, D. and Yuan, D.R., Chem. Phys. Lett., 380 (2003) 185.

[2] Kohale, R.L. and Dhoble, S.J., AIP Conf. Proc., 1391 (2011) 203.

[3] Pei, Z., Su, Q. and Li, S., J. Lumin., 50 (1991) 123.

[4] Shinde, K.N., Dhoble, S.J. and Kumar, A., J. Lumin., 131 (2011) 931.

[5] Kohale, R.L. and Dhoble, S.J., Journal of Molecular Structure, 1170 (2018) 18.

[6] Kuang, J., Liu, Y. and Zhang, J., J. Solid State Chem., 179 (2006) 2669.

[7] Shinde, N., Dhoble, S.J. and Kumar, A., Journal of Rare Earths, 29 (2011) 527.

[8] Kohale, R.L. and Dhoble, S.J., J. Alloy Compd., 586 (2014) 314.

[9] Yu, M., Lin, J., Wang, Z., Fu, J., Wang, S., Zhang, H.J. and Han, Y.C., Chem. Mater., 14 (2002) 2224.

[10] Duragkar, A., Dhoble, N.S., Kohale, R.L. and Dhoble, S.J., Luminescence, 36 (5) (2021) 1159.

[11] Smets, B., Rutten, J., Hoeks, G. and Verlijsdonk, J., Journal of the Electrochemical Society, 136 (1989) 2119.

[12] Katsumata, T., Sasajima, K., Nabae, T., Komuro, S. and Morikawa, T., J. Am. Ceram. Soc., 81 (1998) 413.

[13] Sommerdijk, J.L. and Bril, A., Journal of the Electrochemical Society, 122 (1975) 9524.

[14] Kohale, R.L. and Dhoble, S.J., J. Lumin., 138 (2013) 153.

[15] Yan, B. and Wang, C., J. Alloys Compd., 462 (2008) 147.

[16] Li, P.L., Yang, Z.P., Wang, Z.J. and Guo, Q.L., Mater. Lett., 62 (2008) 1455.

[17] Yang, C.H., Pan, Y.X. and Zhang, Q.Y., Chin. Rare Metal. Mater. Eng., 37 (2008) 568.

[18] Yan, B., Zhang, X.Q. and Lai, H.S., Chin. J. Lumin., 28 (2007) 531.

[19] Kohale, R.L. and Dhoble, S.J., Journal of Alloys and Compounds, 753 (2018) 111.

[20] Color Calculator, version 2 (a software from Radiant Imaging, Inc., 2007).

المراجع: يجب طباعة المراجع بأسطر مزدوجة ومرقمة حسب تسلسلها في النص. وتكتب المراجع في النص بين قوسين مربعين. ويتم اعتماد اختصارات الدوريات حسب نظام Wordlist of Scientific Reviewers.

الجداول: تعطى الجداول أرقاما متسلسلة يشار إليها في النص. ويجب طباعة كل جدول على صفحة منفصلة مع عنوان فوق الجدول. أما الحواشي التفسيرية، التي يشار إليها بحرف فوقي، فتكتب أسفل الجدول.

الرسوم التوضيحية: يتم ترقيم الأشكال والرسومات والرسومات البيانية (المخططات) والصور، بصورة متسلسلة كما وردت في النص.

تقبل الرسوم التوضيحية المستخرجة من الحاسوب والصور الرقمية ذات النوعية الجيدة بالأبيض والأسود، على ان تكون أصيلة وليست نسخة عنها، وكل منها على ورقة منفصلة ومعرفة برقمها بالمقابل. ويجب تزويد المجلة بالرسومات بحجمها الأصلي بحيث لا تحتاج إلى معالجة لاحقة، وألا تقل الحروف عن الحجم 8 من نوع Times New Roman، وألا تقل سماكة الخطوط عن 0.5 وبكثافة متجانسة. ويجب إزالة جميع الألوان من الرسومات ما عدا تلك التي ستنشر ملونة. وفي حالة إرسال الرسومات بصورة رقمية، يجب أن تتوافق مع متطلبات الحد الأدنى من التمايز (1200 dpi Resolution) لرسومات الأبيض والأسود الخطية، و 600 dpi للرسومات باللون الرمادي، و300 dpi للرسومات الملونة. ويجب تخزين جميع ملفات الرسومات على شكل (jpg)، وأن ترسل الرسوم التوضيحية بالحجم الفعلي الذي سيظهر في المجلة. وسواء أرسل المخطوط بالبريد أو عن طريق الشبكة (Online)، يجب أرسال نسخة ورقية أصلية ذات نوعية جيدة للرسومات التوضيحية.

مواد إضافية: تشجع المجلة الباحثين على إرفاق جميع المواد الإضافية التي يمكن أن تسهل عملية التحكيم. وتشمل المواد الإضافية أي اشتقاقات رياضية مفصلة لا تظهر في المخطوط.

المخطوط المنقح (المعدّل) والأقراص المدمجة: بعد قبول البحث للنشر وإجراء جميع التعديلات المطلوبة، فعلى الباحثين تقديم نسخة أصلية ونسخة أخرى مطابقة للأصلية مطبوعة بأسطر مزدوجة، وكذلك تقديم نسخة إلكترونية تحتوي على المخطوط كاملا مكتوبا على Microsoft Word for Windows 2000 أو ما هو استجد منه. ويجب إرفاق الأشكال الأصلية مع المخطوط النهائي المعدل حتى لو تم تقديم الأشكال إلكترونيا. وتخزن جميع ملفات الرسومات على شكل (jpg)، وتقدم جميع الرسومات التوضيحية بالحجم الحقيقي الذي ستظهر به في المجلة. ويجب إرفاق قائمة ببرامج الحاسوب التي استعملت في كتابة النص، وأسماء الملفات على قرص مدمج، حيث يعلَم القرص بالاسم الأخير للباحث، وبالرقم المرجعي للمخطوط للمراسلة، وعنوان المقالة، والتاريخ. ويحفظ في مغلف واقٍ.

حقوق الطبع

يُشكِّل تقديم مخطوط البحث للمجلة اعترافاً صريحاً من الباحثين بأنّ مخطوط البحث لم يُنْشَر ولم يُقَدَّم للنشر لدى أي جهَة أخرى كانت وبأي صيغة ورقية أو إلكترونية أو غيرها. ويُشترط على الباحثين ملء أنموذج يَنُصُّ على نقْل حقوق الطبع لتُصبح ملكاً لجامعة اليرموك قبل الموافقة على نشر المخطوط. ويقوم رئيس التحرير بتزويد الباحثين بإنموذج نقل حقوق الطبع مع النسخة المُرْسَلَة للتنقيح. كما ويُمنع إعادة إنتاج أيِّ جزء من الأعمال المنشورة في المجلّة من دون إذن خَطِّيٍّ مُسبَق من رئيس التحرير.

إخلاء المسؤولية

إن ما ورد في هذه المجلة يعبر عن آراء المؤلفين، ولا يعكس بالضرورة آراء هيئة التحرير أو الجامعة أو سياسة اللجنة العليا للبحث العلمي أو وزارة التعليم العالي والبحث العلمي. ولا يتحمل ناشر المجلة أي تبعات مادية أو معنوية أو مسؤوليات عن استعمال المعلومات المنشورة في المجلة أو سوء استعمالها.

الفهرسة: المجلة مفهرسة في:

Scopus	ULRICHSWEB GLOBAL SERIALS DIRECTORY

معلومات عامة

المجلة الأردنية للفيزياء هي مجلة بحوث علميّة عالمية متخصصة مُحكمة تصدر بدعم من صندوق دعم البحث العلمي والابتكار، وزارة التعليم العالي والبحث العلمي، عمان، الأردن. وتقوم بنشر المجلة عمادة البحث العلمي والدراسات العليا في جامعة اليرموك، إربد، الأردن. وتنشر البحوث العلمية الأصيلة، إضافة إلى المراسلات القصيرة Short Communications، والملاحظات الفنية Technical Notes، والمقالات الخاصّة Feature Articles، ومقالات المراجعة Review Articles، في مجالات الفيزياء النظرية والتجريبية، باللغتين العربية والإنجليزية.

تقديم مخطوط البحث

تقدم البحوث عن طريق إرسالها إلى البريد الإلكتروني : jjp@yu.edu.jo

تقديم المخطوطات إلكترونيًا: اتبع التعليمات في موقع المجلة على الشبكة العنكبوتية.

ويجري تحكيمُ البحوثِ الأصيلة والمراسلات القصيرة والملاحظات الفنية من جانب مُحكِّمين اثنين في الأقل من ذوي الاختصاص والخبرة. وتُشَجِّع المجلة الباحثين على اقتراح أسماء المحكمين. أما نشر المقالات الخاصّة في المجالات الفيزيائية النَشِطَة، فيتم بدعوة من هيئة التحرير، ويُشار إليها كذلك عند النشر. ويُطْلَب من كاتب المقال الخاص تقديم تقرير واضح يتّسم بالدقة والإيجاز عن مجال البحث تمهيداً للمقال. وتنشر المجلةُ أيضاً مقالات المراجعة في الحقول الفيزيائية النشطة سريعة التغيُّر، وتُشَجّع كاتبي مقالات المراجعة أو مُستَكتبيها على إرسال مقترحٍ من صفحتين إلى رئيس التحرير. ويُرْفَق مع البحث المكتوب باللغة العربية ملخص (Abstract) وكلمات دالة (Keywords) باللغة الإنجليزية.

ترتيب مخطوط البحث

يجب أن تتم طباعة مخطوط البحث ببنط 12 نوعه Times New Roman، وبسطر مزدوج، على وجه واحد من ورق A4 (21.6 × 27.9 سم) مع حواشي 3.71 سم ، باستخدام معالج كلمات ميكروسوفت وورد 2000 أو ما استَجَد منه. ويجري تنظيم أجزاء المخطوط وفق الترتيب التالي: صفحة العنوان، الملخص، رموز التصنيف (PACS)، المقدّمة، طرق البحث، النتائج، المناقشة، الخلاصة، الشكر والعرفان، المراجع، الجداول، قائمة بدليل الأشكال والصور والإيضاحات، ثَمَّ الأشكال والصور والإيضاحات. وتُكْتَب العناوين الرئيسة بخطٍ **غامق**، بينما تُكْتَب العناوين الفرعية بخطٍ *مائل*.

صفحة العنوان: وتشمل عنوان المقالة، أسماء الباحثين الكاملة وعناوين العمل كاملة. ويكتب الباحث المسؤول عن المراسلات اسمه مشارا إليه بنجمة، والبريد الإلكتروني الخاص به. ويجب أن يكون عنوان المقالة موجزا وواضحا ومعبرا عن فحوى (محتوى) المخطوط، وذلك لأهمية هذا العنوان لأغراض استرجاع المعلومات.

الملخص: المطلوب كتابة فقرة واحدة لا تزيد على مائتي كلمة، موضحة هدف البحث، والمنهج المتبع فيه والنتائج وأهم ما توصل إليه الباحثون.

الكلمات الدالة: يجب أن يلي الملخص قائمة من 4-6 كلمات دالة تعبر عن المحتوى الدقيق للمخطوط لأغراض الفهرسة.

PACS: يجب إرفاق الرموز التصنيفية، وهي متوافرة في الموقع http://www.aip.org/pacs/pacs06/pacs06-toc.html.

المقدمة: يجب أن توضّح الهدف من الدراسة وعلاقتها بالأعمال السابقة في المجال، لا أن تكون مراجعة مكثفة لما نشر (لا تزيد المقدمة عن صفحة ونصف الصفحة مطبوعة).

طرائق البحث (التجريبية / النظرية): يجب أن تكون هذه الطرائق موضحة بتفصيل كاف لإتاحة إعادة إجرائها بكفاءة، ولكن باختصار مناسب، حتى لا تكون تكرارا للطرائق المنشورة سابقا.

النتائج: يستحسن عرض النتائج على صورة جداول وأشكال حيثما أمكن، مع شرح قليل في النص ومن دون مناقشة تفصيلية.

المناقشة: يجب أن تكون موجزة وتركز على تفسير النتائج.

الاستنتاج: يجب أن يكون وصفا موجزا لأهم ما توصلت إليه الدراسة ولا يزيد عن صفحة مطبوعة واحدة.

الشكر والعرفان: الشكر والإشارة إلى مصدر المنح والدعم المالي يكتبان في فقرة واحدة تسبق المراجع مباشرة.

Subscription Form

Jordan Journal of PHYSICS

An International Peer-Reviewed Research Journal issued by the Support of the Scientific Research and Innovation Support Fund

Published by the Deanship of Research & Graduate Studies, Yarmouk University, Irbid, Jordan

Name: ..... الأسم:

Specialty:..... التخصص:

Address: ..... العنوان:

P.O. Box:..... صندوق البريد:

City & Postal Code: ..... المدينة/الرمز البريدي:

Country: ..... الدولة:

Phone: ..... رقم الهاتف:

Fax No:..... رقم الفاكس:

E-mail:..... البريد الإلكتروني:

No. of Subscription: ..... عدد الإشتراكات:

Method of Payment:..... طريقة الدفع:

Amount Enclosed:..... المبلغ المرفق:

Signature: ..... التوقيع:

Cheques should be paid to Deanship of Research and Graduate Studies - Yarmouk University.

I would like to subscribe to the Journal
For

- One Year
- Two Years
- Three Years

One Year Subscription Rates

	Inside Jordan	Outside Jordan
Individuals	JD 8	€ 40
Students	JD 4	€ 20
Institutions	JD 12	€ 60

Correspondence

Subscriptions and Sales:

Prof. Mahdi Salem Lataifeh
Deanship of Research and Graduate Studies
Yarmouk University
Irbid – Jordan
Telephone: 00 962 2 711111 Ext. 2075
Fax No.: 00 962 2 7211121

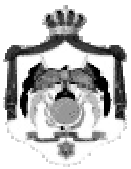

المملكة الأردنية الهاشمية

جامعة اليرموك

المجلة الأردنية
للفيزياء

مجلة بحوث علمية عالمية متخصصة محكّمة

تصدر بدعم من صندوق دعم البحث العلمي والابتكار

المجلد (15)، العدد (1)، آذار 2022م / شعبان 1443هـ

المجلة الأردنية

للفيزياء

مجلة بحوث علمية عالمية محكّمة

المجلد (15)، العدد (1)، آذار 2022م / شعبان 1443هـ

المجلة الأردنية للفيزياء: مجلة علمية عالمية متخصصة محكّمة تصدر بدعم من صندوق دعم البحث العلمي والإبتكار، عمان، الأردن، وتصدر عن عمادة البحث العلمي والدراسات العليا، جامعة اليرموك، إربد، الأردن.

ترسل البحوث إلى العنوان التالي:

الأستاذ الدكتور مهدي سالم لطايفة

رئيس تحرير المجلة الأردنية للفيزياء

عمادة البحث العلمي والدراسات العليا، جامعة اليرموك

إربد ، الأردن

هاتف 7211111 2 962 00 **فرعي** 2075

E-mail: *jjp@yu.edu.jo* **Website**: *http://Journals.yu.edu.jo/jjp*